SELF-CONSISTENT MODELS OF MAGNETIC NEUTRAL SHEETS

by

S. W. H. Cowley

Thesis submitted for the degree of Doctor of Philosophy of the University of London

February 1972

Physics Department
Imperial College
London, S.W.7.

ABSTRACT

Previous theories of magnetic field reconnection at X-type neutral lines of the magnetic field, in the presence of a conducting plasma, are first reviewed. Much existing theory is appropriate only to collision-dominated fluids with scalar conductivities; considerations of self-consistent flow-field models for the collisionless case are different and have been little studied. These require knowledge of particle trajectories in order to obtain the charge and current distributions. However, for many applications in astrophysics and space physics the collisionless case is appropriate. One such case is the Earth's magnetosphere, and evidence that merging with the interplanetary field plays the decisive role in its behaviour is presented. Parameters of the geomagnetic tail are used in later numerical calculations.

As a first step in the development of self-consistent models for the X-type field configuration, only neutral sheet (straight field-line) systems are treated here. It is assumed that the only current source is the plasma contained on the field lines of the neutral sheet system, implying a fixed voltage drop across it. The basic properties are investigated via self-consistency between current and magnetic field, conservation of energy and momentum and charge neutrality in the current sheet. Conservation of momentum and the condition for charge neutrality imply a varying current sheet thickness across the width of the system; model field calculations yield good agreement between the two. The results imply that the voltage drop is localized in a region of dimension the ion plasma

wavelength λ_p in the current sheet, near the boundary where ions leave the system. This in turn implies that ion flow energies above the sheet approach the potential energy across the system, and the theory of plasma drift-flow has been generalized to include this case. The neutral sheet current is carried mainly by a thin electron beam of thickness $(\frac{m_e}{m_i})\ \lambda_p$.

ACKNOWLEDGEMENTS

I would like to thank Professor J.W. Dungey for suggesting the field of study for this thesis, and for much subsequent advice and encouragement. The work benefited from discussions with many members of the Space Physics Group at Imperial College, in particular Drs. T.E. Holzer, E.C. Bowers and E. Gjøen, and Mr. J.W. Eastwood. I would also like to thank my wife, without whose forbearance this work would never have been possible.

Financial support was provided by the Science Research Council.

TABLE OF CONTENTS

page

CHAPTER 1

REVIEW AND DISCUSSION OF PREVIOUS WORK ON THE PROPERTIES OF MAGNETIC NEUTRAL SHEETS AND LINES

(i) Fluid Models

Most of the early work on the theory of field line reconnection and annihilation at (respectively) neutral lines and sheets in the magnetic field was done with special reference to the problem of the solar flare. This phenomenon consists of the sudden release of a considerable amount of energy in the form of electromagnetic radiation (x-rays, optical and radio) and energized particles from a very localized region on the sun, located near sunspot groups. The emission rises to a maximum within about 10 minutes and thereafter declines, with a total life of about half an hour. From considerations of the total energy released it appears that the only reasonable source is in the magnetic field near the site of the flare. This magnetic field is considerably enhanced over the general value, and the complex field structure near sunspots is expected to contain x-type neutral points (Sweet, 1958b). Acceleration of particles during the flare must proceed by an electric field, and if the particles are 'linearly accelerated' by it large currents must result. This is called a 'discharge'. Following earlier suggestions by Giovanelli (1947, 1948) and Hoyle (1949), Dungey (1953, 1958a,b) first quantitatively investigated the possibility of such discharges occuring at neutral points. For simplicity we shall consider two-dimensional problems with $\partial/\partial \ell \equiv 0$

along the neutral line. If the current density is zero in the vicinity of the neutral line then the magnetic field lines are rectangular hyperbolae and the principle axes of the field (i.e. those connected to the neutral point) are orthogonal (see Fig. 1.1(a)). For a non-zero current these axes are no longer orthogonal and the field lines are systems of hyperbolae locally, near the null. (Fig. 1.1(b)). The current must be provided by the presence of a conducting fluid on which acts the electromagnetic force $\underline{j} \wedge \underline{B}/c$. For the field configuration shown in Fig. 1.1(b) the direction of this force is shown in Fig. 1.1(c), and Dungey argued that the fluid must flow in the same general direction. When the fluid is of infinite conductivity the field lines may be regarded as being frozen into the fluid motion so that the flow shown in Fig. 1.1(c) tends to increase the rotation of the principle axes, and with it, increase the current density. Hence the situation in unstable, for a small current will cause motions which in turn increase the current, and a discharge then occurs. This current instability at a neutral point is in direct contrast to the situation where B is non-zero. In this case Lenz's law applies, the electromagnetic force being such as to cause motions which reduce the current.

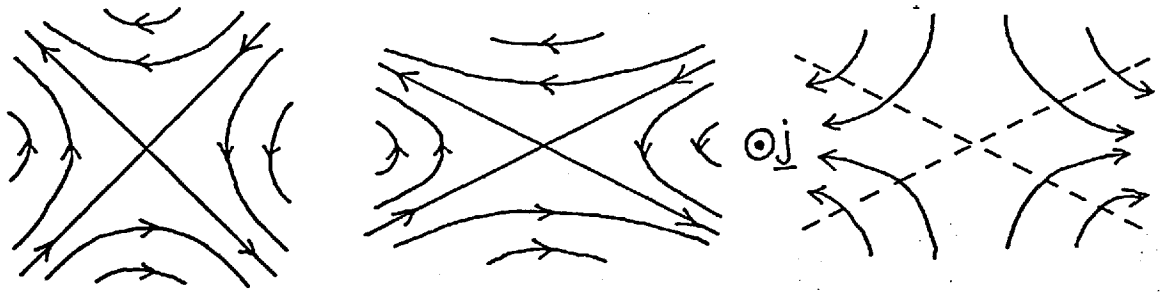

$j = 0$ (a) $j \neq 0$ (b) $\underline{j} \wedge \underline{B}$ lines (c)

Figure 1.1

The equations which govern the system are Maxwell's equations, the hydromagnetic equation of motion

$$\mu \frac{d\underline{u}}{dt} = - \underline{\nabla} p + \frac{\underline{j} \wedge \underline{B}}{c} \qquad (1.1)$$

where μ is the mass density; Ohm's law

$$\underline{E} + (\underline{u} \wedge \underline{B})/c = \underline{j}/\sigma \qquad (1.2)$$

where the Hall term is neglected; and the equation of continuity

$$\frac{d\mu}{dt} = - \mu \, \underline{\nabla} \cdot \underline{u} \qquad (1.3)$$

In these equations $\frac{d}{dt} \equiv \partial/\partial t + (\underline{u} \cdot \underline{\nabla})$. Dungey considers an infinitely conducting fluid ($\sigma = \infty$) so that equation (1.2) becomes

$$\underline{E} + (\underline{u} \wedge \underline{B})/c = \underline{0} \qquad (1.4)$$

and hence the induction equation for the rate of change of the magnetic field is

$$\frac{\partial \underline{B}}{\partial t} = \underline{\nabla} \wedge (\underline{u} \wedge \underline{B}) = - (\underline{u} \cdot \underline{\nabla}) \underline{B} + (\underline{B} \cdot \underline{\nabla}) \underline{u} - \underline{B} (\underline{\nabla} \cdot \underline{u}) \qquad (1.5)$$

From this the 'frozen-in' theorem may be obtained. Dungey now neglects the pressure force in the equation of motion (to be the subject of later discussion), and as is usual the displacement current in Maxwell's equation for curl $\underline{B}$ to obtain from (1.1)

$$\frac{\partial \underline{u}}{\partial t} = - (\underline{u} \cdot \underline{\nabla}) \underline{u} + \frac{(\underline{\nabla} \wedge \underline{B}) \wedge \underline{B}}{4\pi\mu} \qquad (1.6)$$

From equations (1.5) and (1.6) it can be seen that a point

which is initially a neutral point of the magnetic field and a stagnation point of the flow remain so in all subsequent motions. Using Dungey's notation we write $B_{ij} = \partial B_i/\partial x_j$; $u_{ij} = \partial u_i/\partial x_j$ to obtain at the neutral point ($\underline{u} = 0$, $\underline{B} = 0$) the governing equations (from (1.5), (1.6) and (1.3))

$$\frac{\partial}{\partial t} B_{ij} = -u_{kj} B_{ik} + B_{kj} u_{ik} - B_{ij} u_{kk}$$

$$\frac{\partial}{\partial t} u_{ij} = -u_{kj} u_{ik} + (B_{ik} - B_{ki})/4\pi\mu \qquad (1.7)$$

$$\frac{\partial}{\partial t} \mu = -\mu u_{kk}$$

In two dimension we then have nine equations governing nine unknowns. We consider an initial system as shown in Fig. 1.2(a); the coordinate system differs from that used by Dungey, but proves useful in later considerations.

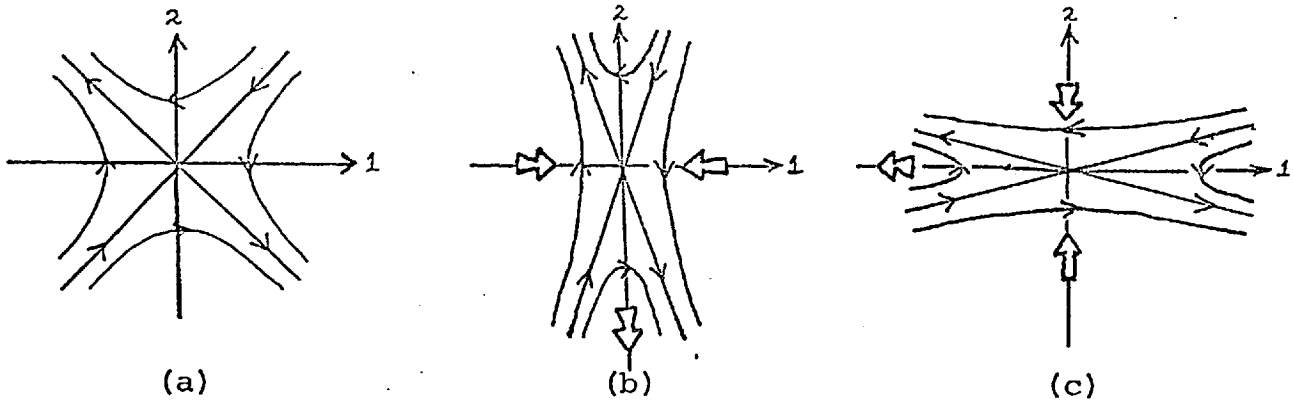

Figure 1.2

By the symmetry of the system $B_{11} = B_{22} = 0$ and $B_{21} < 0$, $B_{12} < 0$ throughout the motion. Also $u_{12} = u_{21} = 0$ throughout, if the system retains its symmetry. Then equations (1.7) become

$$\frac{\partial}{\partial t} B_{12} = -2 u_{22} B_{12} \qquad \text{(a)}$$

$$\frac{\partial}{\partial t} B_{21} = -2 u_{11} B_{21} \qquad \text{(b)} \qquad (1.8)$$

$$\frac{\partial}{\partial t} u_{11} = - u_{11}^2 - (B_{21}-B_{12})\, B_{21}/4\pi\mu \qquad (c)$$

$$\frac{\partial}{\partial t} u_{22} = - u_{22}^2 + (B_{21}-B_{12})\, B_{12}/4\pi\mu \qquad (d) \quad (1.8)$$

$$\frac{\partial}{\partial t} \mu = - \mu\, (u_{11} + u_{22}) \qquad (e)$$

and from these

$$\frac{\partial}{\partial t}(B_{21}-B_{12}) = -2u_{22}(B_{21}-B_{12}) - 2B_{21}(u_{11}-u_{22}) \qquad (f)$$

$$= -2u_{11}(B_{21}-B_{12}) - 2B_{12}(u_{11}-u_{22})$$

$$\frac{\partial}{\partial t}(u_{11}+u_{22}) = -(u_{11}^2+u_{22}^2) - (B_{21}-B_{12})^2/4\pi\mu \qquad (g)$$

$$\frac{\partial}{\partial t}(u_{11}-u_{22}) = -(u_{11}+u_{22})(u_{11}-u_{22}) - (B_{21}+B_{12})(B_{21}-B_{12})/4\pi\mu \qquad (h)$$

From equations (c), (f), (g), (h) and (e) it can be seen that if $u_{11} < 0$ (giving flow towards the null along the '1' direction); $(u_{11}+u_{22})<0$; $(B_{21}-B_{12})<0$; and $(u_{11}-u_{22})<0$ then the sign of the derivatives of each of these quantities is the same as the sign of the quantity, and the instability develops as shown in Fig.2b. From the above conditions we have $-|u_{11}|<u_{22}<|u_{11}|$, so there is no guarantee that $u_{22}>0$ (giving flow away from the null along '2', as shown in Fig.2b), but since initially

$$\frac{\partial}{\partial t} u_{22} \simeq (B_{21} - B_{12})\, B_{12}/4\pi\mu > 0$$

this will be so, at least initially. Also, if it is assumed that the gas is incompressible $u_{22} = -u_{11} > 0$.

Similarly if $u_{22} < 0$; $(u_{11}+u_{22}) < 0$; $(B_{21}-B_{12}) > 0$; $(u_{11}-u_{22}) > 0$ the instability proceeds as is shown in Fig. 1.2c.

Numerical results quoted by Dungey show that u_{11} and $(B_{21}-B_{12})$ initially grow exponentially with time constant

$$\tau \simeq (4\pi\mu)^{1/2}/|B_{21}+B_{12}|$$

(i.e. the time required for an Alfven wave to cross a characteristic length of the system). When perturbation-quadratic terms in equations (1.8 a→h) become of the same magnitude as the linear terms (B_{12} and B_{21} only are non-zero initially) all components become infinite in a time of order τ. That the pressure gradient does not oppose this motion is seen by considering static equilibrium for a system containing an x-type neutral point as shown in Fig. 1.3.

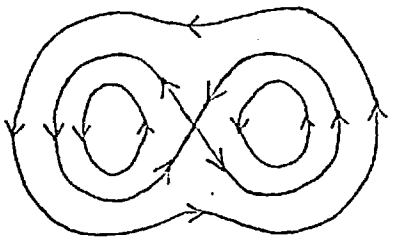

Figure 1.3

The condition for equilibrium is

$$\underline{\nabla}_p = \frac{\underline{j} \wedge \underline{B}}{c}$$

and using this Dungey showed that the current density at the null must be infinite (a step in the magnetic field). Thus if $j_{null} = \infty$ is required for equilibrium it is highly unlikely that pressure forces oppose the instability sufficiently strongly to prevent this equilibrium from being reached. This has been further argued by Dungey (1958b).

The magnetic field at any time is, near the neutral point, taking x ≡ '1' and y ≡ '2'

$$B_1 (y,t) = B_{12} (t)\, y$$
$$B_2 (x,t) = B_{21} (t)\, x \qquad (1.9)$$

such that the field lines are hyperbolae satisfying at time t

$$y^2 = \frac{B_{21}(t)}{B_{12}(t)}\, x^2 + c^2$$

with asymptotes $y = \pm \left(\frac{B_{21}}{B_{12}}\right)^{\frac{1}{2}} x$ (1.10)

The fluid velocity is given by

$$u_1 (x,t) = u_{11} (t)\, x$$
$$u_2 (y,t) = u_{22} (t)\, y \qquad (1.11)$$

so that the flow lines at any time are given by

$$y = \frac{x}{c}^{u_{22}/u_{11}} \qquad (1.12)$$

We note that for an incompressible fluid $u_{22}/u_{11} = -1$ and we obtain a system of rectangular hyperbolae.

The kinetic energy which the fluid derives from the instability must be at the expense of the magnetic field; however, the instability does not depend on field line reconnection at the neutral point. To see this quantitatively we consider the instantaneous fluid velocity on the field lines connected to the neutral point (i.e. the field asymptotes given by equation (1.10)) and compare it to the velocity of the asymptotes themselves. Since the field is 'tied' to the fluid, no reconnection is taking place if these velocities are the same. Refering to Fig. 1.4 we have the fluid velocity perpendicular to the asymptotes

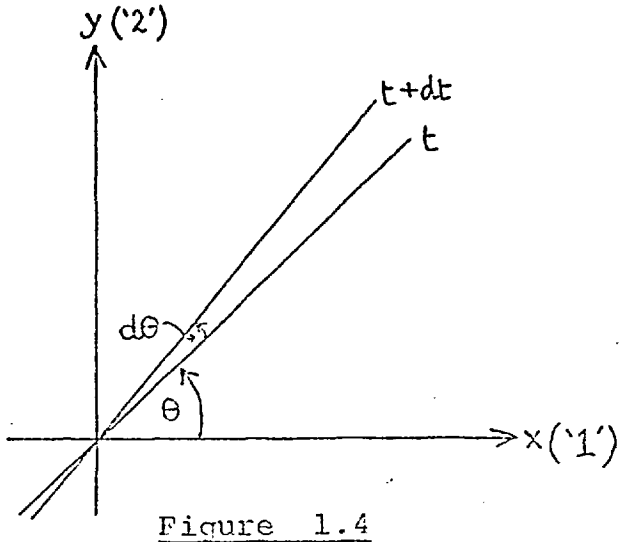

Figure 1.4

$$u^1 = u_2 \cos\theta - u_1 \sin\theta$$

where $\tan\theta = \alpha(t) = \left(\frac{B_{21}(t)}{B_{12}(t)}\right)^{\frac{1}{2}}$.

For any value of x we have, on the asymptote, from equation (1.11)

$$u_2 = u_{22} \tan\theta x = u_{22}\,\alpha x \qquad u_1 = u_{11} x$$

and hence $u^1 = x \sin\theta\,(u_{22} - u_{11}) = \frac{\alpha x}{(1+\alpha^2)^{\frac{1}{2}}}\,(u_{22} - u_{11})$ (1.13)

while the velocity of the asymptote is

$$v^1 = \frac{x}{\cos\theta}\frac{d\theta}{dt} = x\cos\theta\,\frac{d\alpha}{dt} = \frac{x}{(1+\alpha^2)^{\frac{1}{2}}}\frac{d}{dt}\left(\frac{B_{21}}{B_{12}}\right)^{\frac{1}{2}} \qquad (1.14)$$

Now
$$\frac{d}{dt}\left(\frac{B_{21}}{B_{12}}\right)^{\frac{1}{2}} = -\frac{\alpha}{2}\left(\frac{1}{B_{12}}\frac{d}{dt}B_{12} - \frac{1}{B_{21}}\frac{d}{dt}B_{21}\right) = \alpha\,(u_{22}-u_{11}) \qquad (1.15)$$

from equations (1.8a) and (1.8b). Thus we have from (1.13), (1.14) and (1.15)

$$v^1 = u^1 = \frac{\alpha x}{(1+\alpha^2)^{\frac{1}{2}}}\,(u_{22} - u_{11})$$

Thus no field line reconnection occurs in the sense that a fluid element located in one quadrant of the magnetic field structure is never transfered to another quadrant in the course

of the motion.

Exact, non-linear solutions of fluid motion involving this instability have been obtained by Chapman and Kendall (1963, 1966) and by Uberoi (1963, 1966) who consider the motion of a cylinder of fluid, surrounded by a vacuum and located about an x-type neutral line of the magnetic field. The fluid is perfectly conducting and incompressible, hence the flow lines, as shown above, are rectangular hyperbolae. Pressure gradients are included in the analysis, and while these are found to retard the growth of the instability, the growth times found in Dungey's analysis are confirmed. The progress of the instability is shown in Fig. 1.5 (after Chapman and Kendall (1963)).

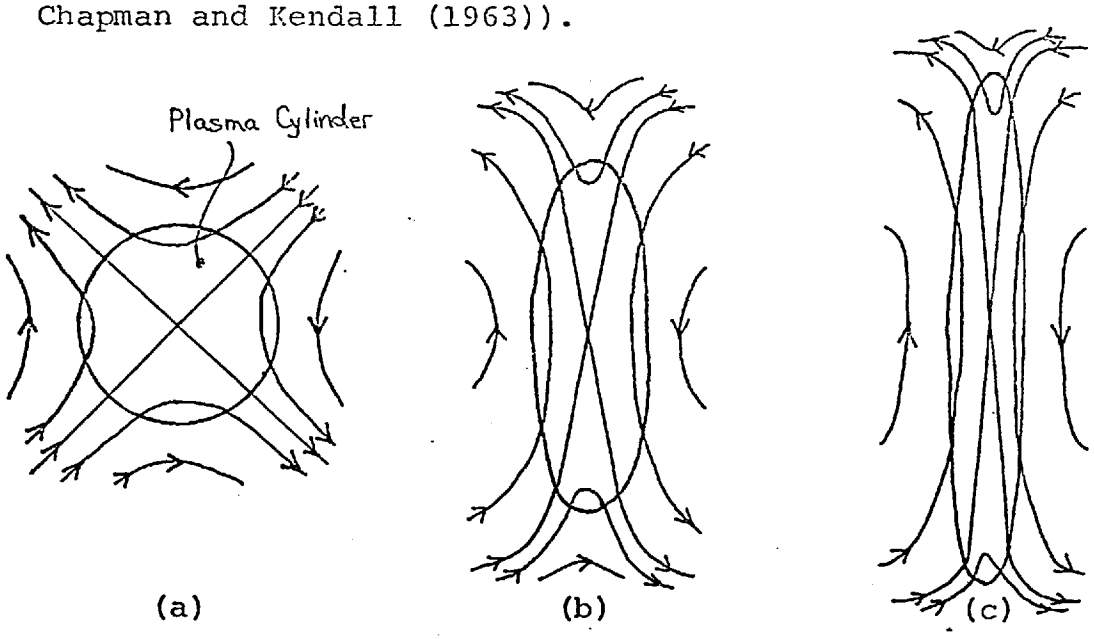

Figure 1.5

Again, as for Dungey's analysis, field line reconnection does not occur, a fact that has also been pointed out by Yeh and Axford (1970). This result was proved above using only the induction equation for an infinitely conducting fluid and does not depend on any details of the instability. It may therefore be considered as a general proof that field line

reconnection cannot occur at an x-type neutral point in the presence of an infinitely conducting fluid.

Thus field line reconnection involves consideration of a plasma with finite conductivity, and from equation (1.2) it can be seen that no matter how large σ is, the term $\underline{j}/\sigma$ becomes important in Ohm's law at some stage as the current goes to infinity at the neutral point. With the inclusion of this term we may then look for steady state situations described by the hydromagnetic equations (1.1) and Ohm's law (1.2). In two dimensions it is first seen that the induction equation requires the electric field to be uniform. Thus

$$\underline{j}/\sigma = \frac{\underline{u} \wedge \underline{B}}{c} + \frac{\underline{j}_{null}}{\sigma} \tag{1.16}$$

and the steady-state hydromagnetic equation is

$$\mu(\underline{u} \cdot \underline{\nabla})\underline{u} = -\underline{\nabla} p + \frac{\underline{j} \wedge \underline{B}}{c} \tag{1.17}$$

As in the discussion of Dungey's neutral point current instability, we consider only the conditions occurring near the neutral point and hence expand in a Taylor series to the lowest order in spatially varying terms

$$\begin{aligned}
\mu &\simeq (u_o + u_{xx}\frac{x^2}{2} + u_{yy}\frac{y^2}{2}) \\
\underline{j} &\simeq (0, 0, j_o + j_{xx}\frac{x^2}{2} + j_{yy}\frac{y^2}{2}) \\
\underline{\nabla} p &\simeq (p_{xx}\, x, p_{yy}\, y, 0) \\
\underline{u} &\simeq (u_{1x}\, x, u_{2y}\, y, 0) \\
\underline{B} &\simeq (B_{1y}\, y, B_{2x}\, x, 0)
\end{aligned} \tag{1.18}$$

where we have chosen axes such that $u_{1y} = u_{2x} = 0$; $B_{1x} = B_{2y} = 0$

and have taken $\underline{\nabla}p = \underline{0}$, $\underline{\nabla}\mu = \underline{0}$ at the neutral point. We have modified the notation slightly such that

$$g_{n_{xy}} \equiv \frac{\partial^2 g_n}{\partial x \partial y} \quad \text{etc.}$$

From the continuity equation we find $u_{1x} = - u_{2y}$ to lowest order such that the fluid flow lines are locally rectangular hyperbolae. Ohm's law gives

$$j_{yy} = \frac{2\sigma}{c} u_{1x} B_{1y} \qquad j_{xx} = \frac{2\sigma}{c} u_{1x} B_{2x} \; ; \qquad (1.19)$$

the hydromagnetic equation gives

$$\mu_o u_{1x}^2 = - (p_{xx} + j_o B_{2x}/c) = - p_{yy} + j_o B_{1y}/c \qquad (1.20)$$

and from Maxwell's equation

$$\frac{4\pi}{c} j_o = B_{2x} - B_{1y} \qquad (1.21)$$

The field lines are given by $y^2 - \frac{B_{2x}}{B_{1y}} x^2 = \text{constant}$, so that for an x-type neutral point B_{2x} and B_{1y} are of the same sign. Let us choose $j_o > 0$; then $B_{2x} > B_{1y}$ and we choose both positive. (Fig. 1.6). Dungey's instability indicates $u_{1x} < 0$ for this situation, and equation (1.19) then indicates that the current decreases away from the neutral point in both directions. The current dies away more quickly in the x-direction (into the large-angled wedge) than in the y-direction. From equations (1.20) we have $p_{xx} + j_o B_{2x/c} < 0$, but since $j_o B_{2x} > 0$ we have $p_{xx} < -|j_o B_{2x}|/c$. Thus a pressure gradient decelerates the flow into the neutral point. We also have $p_{yy} < j_o B_{1y/c}$,

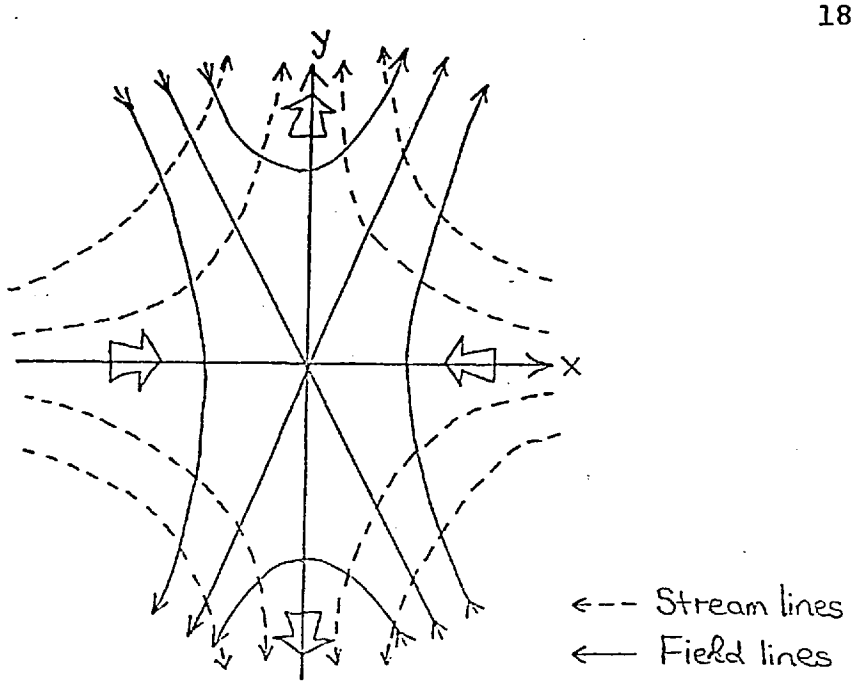

Figure 1.6

and if $p_{yy} < 0$ also, the fluid is accelerated out of the small wedge. The flow situation described here is the same as that given by Yeh and Axford (1970) in their section (4). There appears to be a wide variety of conditions which may occur at a neutral point in the steady state; the properties of the flow at large distances from the neutral point must determine these for any particular problem. The question also remains as to whether such equilibria are stable; the arguments used by Dungey tend to show that they should be unstable to the current instability described above. However, since it is the pressure gradients which hold the mechanical equilibrium of the above system and these were neglected from his stability analysis no quantitative theory is available, and the stability question must remain open.

There exists a degenerate solution of the above equations for $B_{1y} = 0$, when a neutral sheet is formed rather than a neutral line and conditions vary only in the x-direction. In this case field lines are annihilated at the neutral sheet rather than reconnected. Equations (1.19) then give

$j_{yy} = 0$ and $j_{xx} = \frac{2\sigma}{c} u_{1x} B_{2x}$.

Since $u_{1x} < 0$ and $4\pi/c\ j_o = B_{2x}$ we then have

$$j(x) \simeq j_o \left(1 - \frac{4\pi\sigma}{c^2} |u_{1x}| x^2\right)$$

The sheet half-thickness, ℓ, is determined by putting $j \simeq 0$. Writing $u_o \sim |u_{1x}|x$ for the flow velocity external to the sheet we obtain the half-thickness

$$\ell \simeq \frac{c^2}{4\pi\sigma\ u_o} .$$

Of course, the continuity equation cannot be satisfied for this case, and hence we must postulate a plasma sink at the neutral sheet. An equivalent situation has been discussed by Yeh and Axford in which

$$\underline{u} = (-\ \mathrm{sgn}\ (x)\ u_o,\ 0,\ 0) .$$

The induction equation in the steady state is then

$$u \frac{\partial B_y}{\partial x} = \frac{c^2}{4\pi\sigma} \frac{\partial^2 B_y}{\partial x^2} \qquad (1.22)$$

with solution

$$B_y = \pm B_o(1 - e^{4\pi\sigma u x/c^2}) \quad \text{in} \quad x \gtrless 0. \qquad (1.23)$$

The half-thickness of the current sheet is

$$\ell \simeq \frac{c^2}{4\pi\sigma\ u_o} \qquad (1.24)$$

as above, and the field annihilation rate (as given by the flow velocity u_o) is arbitrary. The steady state is set up from a balance between inward convection of the field lines and resistive annihilation at the neutral sheet. The sheet

thickness simply changes in response to changes in the parameters governing these rates. However, if the plasma sink has physical reality, the annihilation rate (u_o) may be obtained from (1.24) if the thickness ℓ can be determined in some fashion from the sink's properties. This is just the situation as discussed by Sweet (1958a) and Parker (1957b, 1963).

Sweet argued that when two oppositely directed fields are pushed against each other in the presence of a highly conducting fluid, the fluid will flow out from the region of contact, along the lines of force. This allows them to approach still closer, and the process continues, until, no matter how large the conductivity, resistive diffusion of the magnetic field becomes important. The field configuration envisaged is shown in Fig. 1.7, which could also be the result of Dungey's current instability rather than just from 'shoving the fields together'.

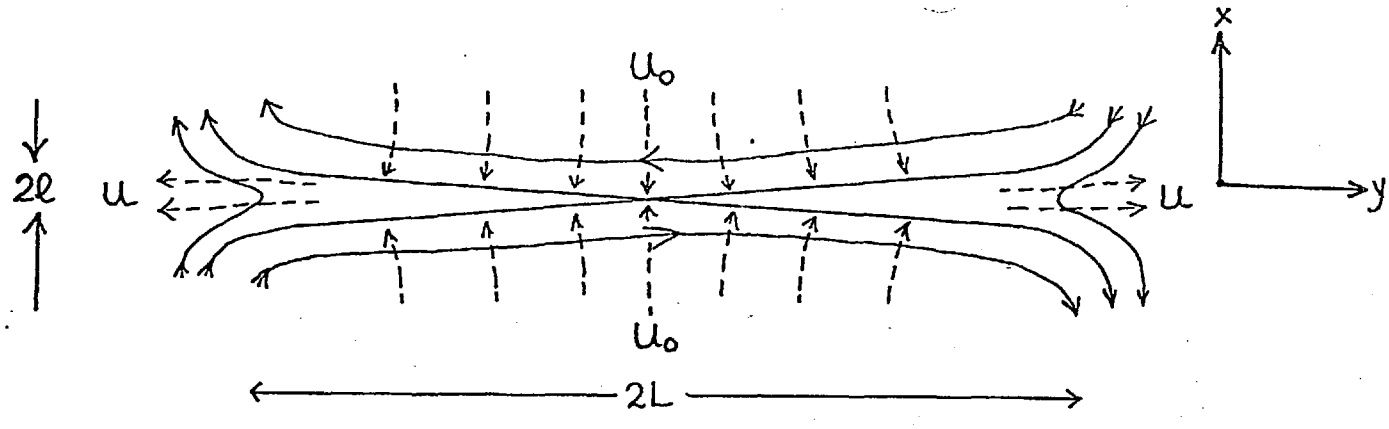

Figure 1.7. (after Parker (1963)).

The particle density in the incoming flow is N_o, pressure p_o and the magnetic field is B_o. In the field annihilation

region the density is n. By conservation of particle flux (see Fig. 1.7) we then have

$$N_o \, v_o \, L = n \, u \, \ell \tag{1.25}$$

The momentum equation yields, for the direction normal to the neutral sheet

$$p + \frac{B^2}{8\pi} \approx \text{constant}$$

for small incoming velocities, so that if $p_o << B_o^2/8\pi$ we have the fluid pressure at the neutral plane

$$p \approx B_o^2/8\pi \tag{1.26}$$

which, together with a temperature, would determine the amount of compression (n/N_o) undergone by the gas. In the direction parallel to the sheet we have

$$nmu \frac{\partial u}{\partial y} = - \frac{\partial p}{\partial y} \tag{1.27}$$

where the magnetic tension force $\frac{cB_x}{4\pi} \frac{\partial B_y}{\partial x}$ accelerating the plasma out of the system is neglected. For an isothermal expansion $n \approx$ constant if (1.26) is satisfied so that from (1.27)

$$\frac{nmu^2}{2} \simeq p - p_o \simeq \frac{B_o^2}{8\pi} \tag{1.28}$$

where we assume the ambient pressure is resumed outside the neutral sheet. Then

$$u \simeq \frac{B_o^2}{\sqrt{4\pi n m}} \tag{1.29}$$

and the gas is expelled at approximately the Alfven velocity computed from the enhanced gas density in the sheet. Thus from (1.24), (1.25), (1.26) and (1.29) we arrive at the governing equations

$$u_o = \frac{c^2}{4\pi\sigma\ell} \qquad N_o u_o L = n u \ell \qquad u = \frac{B_o^2}{\sqrt{4\pi n m}} \qquad nkT = \frac{B_o^2}{8\pi}$$

Parker regards the quantities N_o, B_o, and L as given, so we obtain

$$u_o \simeq V_A \left(\frac{n}{N_o}\right)^{1/4} \left(\frac{c^2}{4\pi\sigma V_A L}\right)^{1/2} \tag{1.30}$$

$$\ell \simeq \left(\frac{N_o}{n}\right)^{1/4} \left(\frac{c^2 L}{4\pi\sigma V_A}\right)^{1/2} \tag{1.32}$$

where V_A is the Alfvén velocity computed from the gas density outside the sheet. We also have, for roughly isothermal conditions

$$\frac{n}{N_o} \simeq \frac{P}{P_o} \simeq \frac{B_o^2/8\pi}{P_o} \gg 1$$

such that gas compression may significantly enhance annihilation rates (u_o) over the incompressible case. Thus, in effect, from equations (1.25) and (1.29) Parker determines the sheet half-thickness ℓ in terms of 'known' quantities L, B_o, N_o, substitution into (1.24) then gives u_o. For any particular situation Parker regards the length L as being given by a typical dimension of the system. However, Yeh and Axford have objected to this, saying that, like ℓ, L should instead be regarded as being determined by (1.30) once u_o is given in

terms of the external flow. The most that can be said is that $L \geq \ell$ and hence

$$u_o \simeq V_A \left(\frac{n}{N_o}\right)^{\frac{1}{2}} \ell/L \leq V_A \left(\frac{n}{N_o}\right)^{\frac{1}{2}}.$$

That the L in equation (1.30) should not be regarded as the scale size of the system was first recognized by Petschek (1964). He suggested that while Parker's analysis may be valid near the neutral point, magnetic field energy can be converted to fluid flow energy by the presence of standing MHD shock waves further away. In his analysis 2L is still the scale length of the system, but the length of the 'diffusion region' is 2y* (hence y* replaces the 'L' in equations (1.30) and (1.31)).

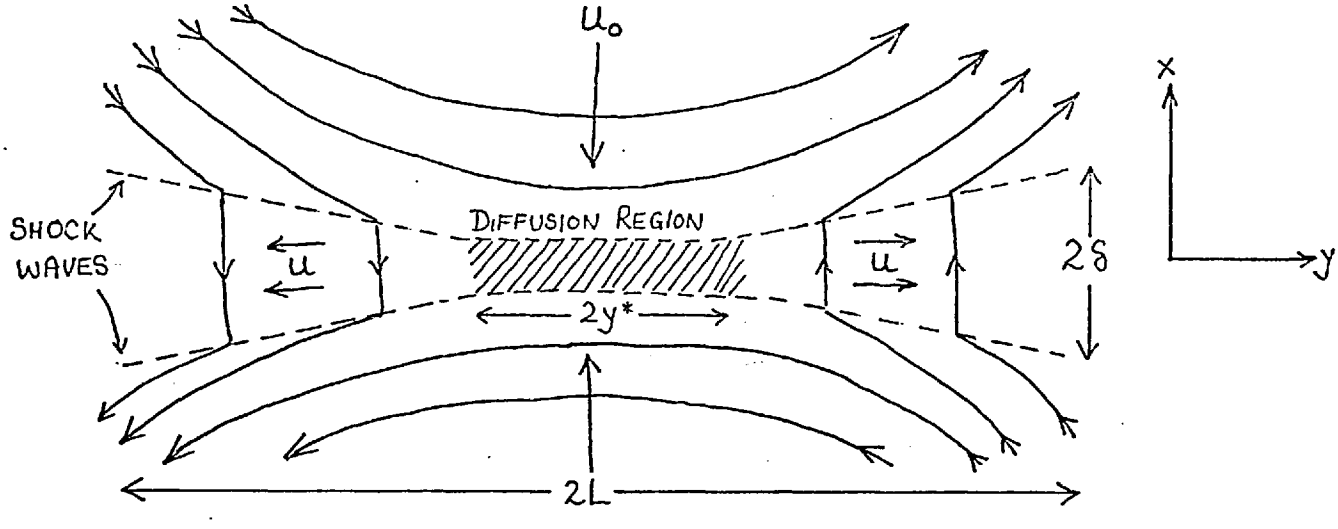

Figure 1.8. (after Petschek (1964)).

We first consider the properties of the fluid flow between the shock waves under the assumption that the external flow and magnetic field are uniform (i.e. a linearized analysis). This solution is matched to a Parker-type diffusive solution near the neutral point. The perturbation of the

external flow by the presence of this "boundary layer" is then considered, and an upper limit on the incoming flow is found such that this perturbation is not too large. Quantities in the external flow have the subscript 'o' while those in the boundary layer are subscripted 'b'.

First, the density is assumed constant throughout the boundary layer, a situation which would occur for an isothermal flow with the pressure $p_b \approx B_o^2/8\pi \approx$ constant. The compression of the gas in the layer is given by

$$\alpha = \rho_o/\rho_b \qquad (1.32)$$

such that $0 < \alpha \leq 1$, and α is regarded as known.
The equation of continuity gives

$$N_o u_o y = n u_b(y) \delta(y)$$

or
$$\alpha u_o y = u_b(y) \delta(y) \qquad (1.33)$$

The momentum equation along the boundary layer is (with $u_{b_x} \approx 0$ and the neglect of the fluid pressure gradient)

$$\rho u_{by} \frac{\partial u_{by}}{\partial y} \simeq \frac{B_x}{4\pi}\left(\frac{\partial B_y}{\partial x} - \frac{\partial B_x}{\partial y}\right) \qquad (1.34)$$

Writing $\frac{\partial B_y}{\partial x} \approx -\frac{B_o}{\delta(y)}$ and $\frac{\partial B_x}{\partial y} \approx \frac{B_x}{L}$ we have for $\delta << L$ $\left|\frac{\partial B_y}{\partial x}\right| >> \left|\frac{\partial B_x}{\partial y}\right|$. Then for constant ρ_b, equation (1.34) becomes

$$\delta(y)\frac{\partial}{\partial y}\left(\frac{\rho_o u_{by}^2(y)}{2}\right) = -\alpha \frac{B_o B_x(y)}{4\pi} \qquad (1.35)$$

Petschek gives $$\frac{\partial}{\partial y}\left(\rho_o \delta(y) u_{by}^2\right) = -\alpha \frac{B_o B_x(y)}{4\pi}$$

which appears difficult to obtain with any reasonable assumptions. Substitution of (1.33) in (1.35) then yields

$$\alpha \left(\frac{u_o}{V_A}\right)^2 \delta(y) \frac{\partial}{\partial y}\left(\frac{y^2}{2\delta^2(y)}\right) = -\frac{B_x(y)}{B_o} \qquad (1.36)$$

where V_A is the Alfvén velocity of the incoming (unperturbed) flow. To maintain a standing shock wave the speed with which the wave propagates relative to the fluid $\simeq |\frac{B_x}{B_o}| V_A$ (away from the boundary) must be matched by the flow of fluid towards the boundary, so that

$$\frac{u_o}{V_A} \simeq |\frac{B_x(y)}{B_o}| \qquad (1.37)$$

Since u_o, V_A and B_o are zero-order constants this requires that B_x is also a constant, i.e. $B_x(y) = -\,\mathrm{sgn}(y)\, B_x$. Then equation (1.36) may be integrated by putting $f(y) = y/\delta(y)$ to obtain

$$\delta(y) = \alpha\left(\frac{u_o}{V_A}\right)|y| \Big/ \left\{\log\left\{\frac{|y|}{y_o}\exp\left(\frac{\alpha u_o}{V_A}\frac{y_o}{\delta(y_o)}\right)\right\}\right\} \qquad (1.38)$$

where y_o, $\delta(y_o)$ may be regarded as being determined by matching to the Parker solution at the origin. Petschek obtains, instead of (1.38)

$$\delta(y) = \alpha\left(\frac{u_o}{V_A}\right)|y| \qquad (1.39)$$

The diffusive solution is obtained from (1.35) by putting $\delta(y) = \delta_D \simeq$ constant, we obtain $B_x(y)$:

$$\frac{B_x(y)}{B_o} \simeq -\alpha\left(\frac{u_o}{V_A}\right)^2 \frac{y}{\delta_D} \qquad (1.40)$$

Note that the fluid is accelerated out of the diffusion region by the tension force neglected in Parker's treatment. The two solutions match when $B_x(y)/B_o$ given by (1.40) reaches the value required for the existence of standing waves (1.37) i.e.

$$|y| = y^* = \frac{\delta_D}{\alpha\left(\frac{u_o}{V_A}\right)} \tag{1.41}$$

For $y < y^*$ the diffusion mechanism dominates, while for $y > y^*$ the wave mechanism is dominant. Thus equation (1.38) becomes

$$\delta(y) = \alpha\left(\frac{u_o}{V_A}\right)|y| \Big/ \left\{1 + \log\left(\frac{|y|}{y^*}\right)\right\} \tag{1.42}$$

Thus Petschek's result (1.39) may be regarded as an approximation valid only for $|y| \sim \mathcal{O}(y^*)$. The flow diverges more slowly according to (1.42) than the linear approximation. From the previous discussion we have $\delta_D = c^2/4\pi\sigma u_o$ so that

$$y^* = \frac{c^2}{4\pi\sigma\, V_A\, \alpha}\left(\frac{V_A}{u_o}\right)^2$$

Petschek gives half this value.

The perturbation of the external flow is caused by currents flowing in the shock waves. Under the assumption that curl $\underline{B} = \underline{0}$ and curl $\underline{u} = \underline{0}$ (where $\underline{u} = c\,\underline{E} \wedge \underline{B}/B^2$) these are calculated for the external flow. The largest perturbation B'/B_o occurs just outside the boundary layer at the origin and is given by

$$\frac{B_y'}{B_o} = -\frac{(1+\alpha)}{\pi}\left(\frac{u_o}{V_A}\right)\log\left(\frac{L}{y^*}\right) \tag{1.43}$$

The maximum allowed perturbation is arbitrarily chosen to be $B_y'/B_o = -\frac{1}{2}$; $(B_y'/B_o \leq -1$ in any case).
Thus we obtain

$$\left(\frac{u_o}{V_A}\right)_{max} \simeq \frac{\pi}{2(1+\alpha)\log\left(\frac{L}{y^*}\right)}$$

Then for $L/y^* \sim 10^3$ say, or greater we find $u_{o_{max}} \simeq V_A/10$ and since logarithms are slowly varying functions this result does not change very much as the parameters vary. Also, from (1.41) we find $y_{min}^* \simeq 10\ \delta_D$. However this assesment of the maximum rate of field annihilation is in reality a condition for the breakdown of Petschek's linearized treatment; whether it has any physical significance is highly questionable.

Yeh and Axford (1970) have obtained exact two-dimensional solutions of the MHD equations for a perfectly conducting, inviscid and incompressible ($\alpha = 1$ in the above analysis) fluid in the region external to the neutral point. The analysis is carried out in terms of the variables Ψ and A where (since div $\underline{B} = 0$ and div $\underline{u} = 0$)

$$\begin{aligned} \underline{B} &= \text{curl } \underline{A} & \underline{A} &= (0, 0, A) \\ \underline{u} &= \text{curl } \underline{\Psi} & \underline{\Psi} &= (0, 0, \Psi) \end{aligned} \qquad (1.45)$$

(The third dimension is perpendicular to the flow). The lines A = constant then define a field line and Ψ = constant a stream line. Using cylindrical polar coordinates it is assumed that

$$\Psi = r\,g(\theta) \quad \text{and} \quad A = r\,f(\theta) \qquad (1.46)$$

It is then found that the curl of the momentum equation

(eliminating the pressure gradient)

$$\rho\, \underline{\nabla} \wedge \left(\underline{u} \wedge (\underline{\nabla} \wedge \underline{u})\right) = \frac{1}{4\pi}\, \underline{\nabla} \wedge \left(\underline{B} \wedge (\underline{\nabla} \wedge \underline{B})\right) \qquad (1.47)$$

and Ohm's law

$$\underline{E} + \frac{\underline{u} \wedge \underline{B}}{c} = \underline{0} \qquad (1.48)$$

(where $\underline{E} = (0, 0, E_0)$ is constant in the steady state) do not depend on r. The above two basic equations are then solved (numerically in the general case) to obtain $f(\theta)$, $g(\theta)$ and hence the field and stream lines. The magnetic field and flow velocity are then obtained from equation (1.45)

$$B_r = \frac{df}{d\theta} \qquad B_\theta = -f(\theta) \qquad u_r = \frac{dg}{d\theta} \qquad u_\theta = -g(\theta) \qquad (1.49)$$

It is found that for general case, each streamline crosses <u>two</u> shocks as it flows from one wedge of the magnetic field into another (discontinuities in the derivatives of $f(\theta)$ and $g(\theta)$ occur). Across these shocks, which lie along θ = constant lines the normal components of the flow velocity, magnetic field and hydromagnetic pressure $(p + B^2/8\pi)$ are continuous, whereas the tangential components are discontinuous and satisfy

$$\rho [u_r]^2 = \frac{1}{4\pi} [B_r]^2$$

The general characteristics of the flow are shown in Fig. 1.9. In order to describe the flow near the neutral point in the steady state a conduction term clearly needs in-

cluding in Ohm's law (1.48) since $\underline{E}$ is constant. The field and flow near the null is the same as that described above by equations (1.18) and (1.20), i.e. hyperbolic field lines and rectangular hyperbolic flow lines. The flow velocity then determines the pressure gradients near the neutral point. While it is not rigorously shown how the two regions match, it is clear from Fig. 1.9 that they are qualitatively similar. The angles between the wedges for the two solutions can be matched by the choice of B_{2x}/B_{1y}. The electric field at the null is the same as that in the external flow giving j_o from $j_o/\sigma = E$, and hence determining $(B_{2x} - B_{1y})$. The pressure gradients are then determined by matching the flow velocity given by u_{1x} at some distance from the neutral point.

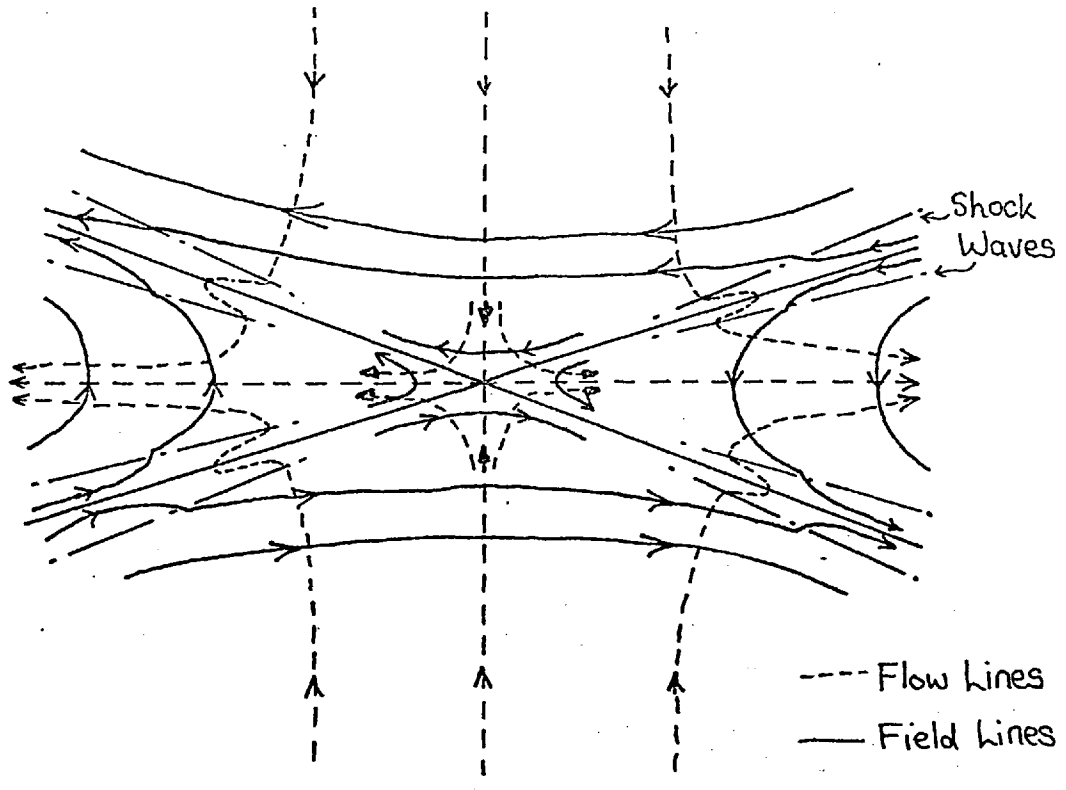

Figure 1.9. (after Yeh and Axford (1970)).

Since for all cases the electric field remains a free parameter of the solutions, they conclude that reconnection

may occur at essentially any speed consistent with the boundary conditions. The higher the velocities the smaller becomes the 'diffusion region' near the neutral point.

Yeh and Axford have compared their external solution with that of Petschek's, since they should be comparable in some regime $y^* < r < L$. They find that the conditions near the shocks cannot be reconciled with Petschek's picture, nor with the later double-shock modifications of Petschek and Thorne (1966). They therefore conclude that Petschek's linearized analysis does not represent a valid solution of the MHD equations "and accordingly that his arguments are less convincing than they seemed originally".

(ii) Summary and Criticism of Fluid Models

The fluid models of magnetic field line reconnection at a neutral line may be summarized as follows, where we consider a nearly neutral-sheet configuration for simplicity (produced perhaps by Dungey's (1953) current instability). If the magnetic field far from the sheet is B_o and the flow velocity is u_o the electric field is $E_o = u_o B_o/c$ and is uniform over the entire system in the steady state. Thus the current at the neutral sheet is $j_o = \sigma E_o$ and for consistency with the magnetic field change $4\pi/c\ j_o\ \ell = B_o$ where ℓ is the half-width of the diffusion region. Then we obtain $\ell = c^2/4\pi\sigma u_o$. While Parker (1963) goes on to determine ℓ in terms of the scale size L of the system by writing $u_o L = v\ell$ and $v \approx B_o/\sqrt{4\pi\rho}$, Petschek (1964) argues that the above L is not the scale size of the system and may be much smaller than

this. Far away from the neutral point field energy may be converted to flow energy across standing shocks, and the 'length' of the diffusion region becomes much smaller than L when u_o is large. An upper limit to the inflow velocity is estimated from a condition of breakdown of his linear analysis. While Petschek's argument is confirmed by the exact analysis of Axford and Yeh (1970) it appears that his linearized theory is not a valid solution of the MHD equations. They further show that the inflow velocity u_o can be comparable with the Alfvén speed in favourable circumstances, though any lower value is possible, depending on the boundary constraints. Whether these steady state solutions are stable (with respect to the current instability) remains an open question.

However, the treatment of the problem in the MHD approximation in the above two-dimensional manner is open to the following objections when the fluid under consideration is collisionless.

(a) In all the models 'diffusion regions' of very small spatial extent occur. For astrophysical and space physics applications ℓ is usually given as being in the range of millimeters to meters, while the gyroradii of electrons and ions may be larger. MHD assumptions then break down (e.g. the pressure tensor $\underline{\underline{P}} = p\underline{\underline{1}}$) and this calls into question the validity of treating with fluid equations the properties of a collision-free plasma near a neutral point.

(b) It has always been assumed that the conductivity of the plasma is homogeneous and isotropic, which is a valid assumption if it is collision-dominated. However, for neutral

sheets and lines in galactic objects, stellar winds or planetary magnetospheres the treatment must be collision-free. The collision mean-free-time is then replaced in the theory of conductivity by the time the particle remains in the system, which depends on the field geometry (see for example Speiser (1970)). The conductivity is then by no means homogeneous or isotropic and the currents should be determined by studies of the particle trajectories, rather than by simply giving a value to σ.

(c) A qualitative study of particle trajectories near neutral sheets was given by Dungey (1953), but this has seemingly been ignored by many succeeding authors. He showed that particles oscillate about the sheet and become accelerated along it by the electric field; positive particles moving in the direction of the electric field, negative particles in the opposite direction. Inclusion of the weak field component normal to the sheet in the 'x' configuration causes them to turn away from the neutral line and move out along field lines as envisaged in the fluid theories. Seymour (1959) obtained exact solutions of the equations of motion for particles moving in a magnetic field of constant gradient containing a neutral sheet, but with no electric fields. (This followed a much shorter investigation by Parker (1957a)). The motion of particles which do not cross the neutral line is described by the usual '$\underline{\nabla}B$' drift of charged particles in a non-uniform magnetic field. Particles crossing the neutral line oscillate symmetrically about it and may travel along it with any velocity (up to the total particle velocity) in either direction, (Fig. 1.10a). Seymour envisaged that such enhanced

drift velocities might give rise to important charge-separation effects in the plasma near the neutral sheet. Particle trajectories in such field configurations together with an electric field along the neutral sheet have been studied by Speiser (1965), (1968) and directly confirm Dungey's (1953) arguments. Particles drift into the region under the action of the electric field from both sides and then oscillate about the sheet, becoming accelerated by the electric field, opposite charges in opposite directions (Fig. 1.10b). Seymour's conjecture about the importance of charge separation effects now takes on added significance. Inclusion of a weak field component perpendicular to the sheet turns the particles away from the neutral line as they accelerate until they are travelling parallel to the field lines emerging from the current sheet, when the particles, too, emerge from the current sheet; (Fig. 1.11).

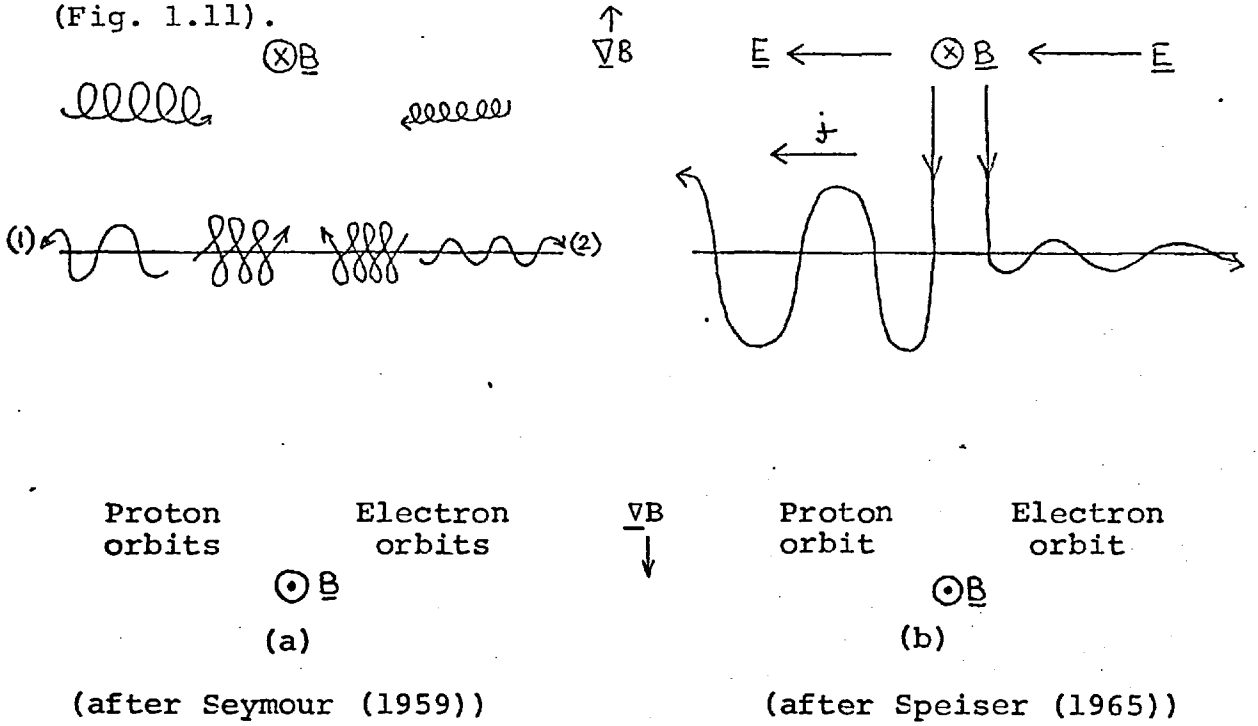

Figure 1.10

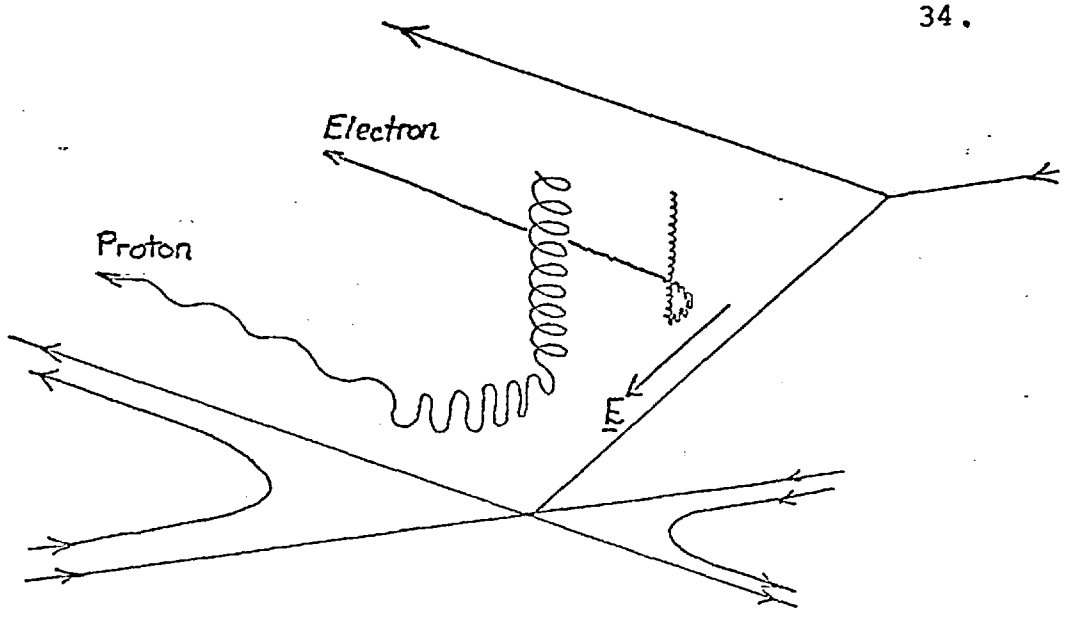

Figure 1.11

It appears from these collision-free discussions that the variations of the system in the third dimension (along the neutral line) may be very important, especially if the normal component of the magnetic field is very small. Indeed, for a strictly neutral sheet the third dimension becomes crucial in the discussion since infinite extent in this dimension with a finite inflow velocity implies an infinite current of oscillating and accelerating particles in the sheet and infinite particle energization. (Speiser (1965) showed that once particles enter the sheet and oscillate about it they never leave it, the amplitude of the oscillations in fact slowly decreases as the energy increases without bound in the electric field).

(iii) Collision-free plasma models.

The first description of the properties of a self-consistent neutral-sheet model for a collision-free plasma was given by Alfvén (1968), and in view of the above comments

it is perhaps not surprising that the considerations involved are rather different from those of the fluid theories. He considers a neutral sheet configuration which is of finite width d in the third dimension (along the electric field), the system being bounded by 'condenser plates', which just represent equipotential boundaries and a sink for charged particles (see Fig. 1.12). The magnetic field outside of the field reversal region is B_o and is constant if appropriate currents flow on the boundary equipotentials. (If the magnetic field outside the system is zero, these boundary currents are just half the neutral sheet current). As a valid first approximation to the motion of cold plasma, the particles drift towards the neutral sheet from both sides under the action of the crossed electric and magnetic fields with velocity $\underline{v} = c\underline{E}\wedge\underline{B}_o/B_o^2$. From flux continuity, we have N/B a constant along a trajectory, and since B is uniform, we may take N (the number density of positive of negative particles) to be uniform in the flow, and equal to N_o. Here, we are generalizing Alfvén's analysis, which assumed a uniform electric field to include non-uniform electric fields. The entire flux of positive (or negative) particles into the sheet is

$$F = 2cN_o\int_C \left|\left(\frac{\underline{E}\wedge\underline{B}_o}{B_o^2}\right)\wedge d\underline{L}\right| = \frac{2cN_o}{B_o}\int_C \underline{E}.d\underline{L} = \frac{2cN_o\Phi}{B_o} \qquad (1.50)$$

where Φ is the total electric potential across the system. 'c' is a contour crossing the system along any path from one boundary equipotential to the other, above or below the neutral sheet, and $\underline{B}_o.d\underline{L} = 0$.

Following Speiser's (1965) analysis of the particle motions, positive particles in the neutral sheet move towards $\phi = \Phi$. Thus at $\phi = 0$ all the current is carried by positive particles while at $\phi = \Phi$ an equal current is carried by electrons. The neutral sheet current is uniform across the system and hence equal to eF (equation 1.50). For self-consistency between the magnetic field and the current we thus have

$$2B_o = \frac{4\pi I}{c} = \frac{4\pi}{c}\left(\frac{2ecN_o\Phi}{B_o}\right)$$

Thus
$$\Phi = \frac{B_o^2}{4\pi N_o e} \tag{1.51}$$

and
$$v \simeq \frac{c\Phi}{B_o d} = \frac{cB_o}{4\pi N_o e d} \tag{1.52}$$

We generalized Alfvén's analysis in the above manner because of the suggestion of the importance of considering charge separation of the plasma at the neutral sheet, with attendant non-uniform electric fields. Far enough away from the sheet, however, we expect a uniform flow so that the drift velocity expression used becomes exact. Hence since contour c is arbitrary, Alfvén's result is also found to be valid in such situations.

If the plasma consists of protons and electrons, the velocity of ejection of the particles after falling through potential Φ is

$$V_p = \sqrt{\frac{2e\Phi}{m_p}} = \left(\frac{m_p+m_e}{m_p}\right)^{1/2}\sqrt{2}V_A \qquad V_e = \left(\frac{m_p+m_e}{m_e}\right)^{1/2}\sqrt{2}V_A$$

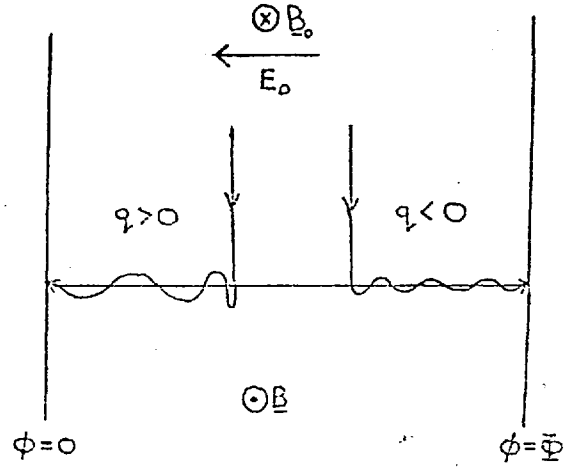

Figure 1.12. (after Alfvén (1968)).

where V_A is the Alfvén velocity in the region external to the neutral sheet and field reversal region. Thus since $m_p >> m_e$

$$V_p \simeq \sqrt{2}\, V_A \qquad \text{and} \qquad V_e \simeq \left(\frac{m_p}{m_e}\right)^{\frac{1}{2}} \sqrt{2}\, V_A \qquad (1.53)$$

The average velocities of ejection (potential drop of $\Phi/2$) are

$$V_p \simeq V_A \quad \text{and} \quad V_e \simeq \left(\frac{m_p}{m_e}\right)^{\frac{1}{2}} V_A .$$

The philosophy of this calculation is simply that from a knowledge of the particle trajectories a self-consistent incoming flux of plasma can be computed to produce the current required by the change in the magnetic field. No knowledge of the detailed structure of the flow or field near the neutral sheet is required, and none is obtained from the calculation. These ideas are somewhat more similar to Parker's calculation of the incoming flow velocity from the properties of the plasma 'sink' (see equation (1.33) and discussion) rather than Yeh and Axford's assertion of arbitrary flow rates for a given system.

It can also be shown (Cowley 1971b) that Alfvén's formula for the total potential across the system also satis-

fies conservation of energy. We have a Poynting flux $\underline{S}$ of electromagnetic energy into the sheet from above and below, while energized particles flow out from the equipotential boundaries. The Poynting flux integrated across the system is

$$W_S = 2\int_C |\underline{S} \wedge \underline{dL}| = \frac{2c}{4\pi} B_o \int_C \underline{E} \cdot \underline{dL} = \frac{2c B_o \Phi}{4\pi} \qquad (1.54)$$

As above the flux of protons or electrons towards the sheet across element $\underline{dL}$ of contour c is

$$dF = N_o \left| \left(\frac{c\underline{E} \wedge \underline{B}}{B^2} \right) \wedge \underline{dL} \right|$$

and by conservation of particle flux dF is the flux of particles from $\underline{dL}$ emerging from the boundary. If $\underline{dL}$ is at potential ϕ, the protons will be accelerated and gain an energy $e\phi$, while electrons gain an energy $e(\Phi-\phi)$ by the time they emerge from the boundary. Adding proton and electron contributions, the particle energy flux from the sides of the sheet from $\underline{dL}$ is $dW_p = e\Phi\, dF$. Integrating dW_p across the system gives W_p, the particle energy per unit time per unit length of system (along the magnetic field) flowing out of the boundaries. Multiplying by two for inflow from both sides we obtain

$$W_p = \frac{2N_o c e \Phi^2}{B_o} \qquad (1.55)$$

Equating W_S and W_p for the steady state gives

$$\Phi = \frac{B_o^2}{4\pi N_o e}$$

regaining Alfvén's formula, equation (1.51).

Alfvén's analysis may be readily extended to the situation with a weak normal component of the field B_1 perpendicular to the current sheet. The electric field may be removed by a frame transformation of velocity $v_T = cE_o/B_1$ parallel to the reversing field component. In this frame the plasma simply streams down the field lines into the current sheet with approximately the transformation velocity. Inside the sheet the particles oscillate about the field minimum while describing a half-circle of radius $r = \frac{cE_o}{B_1}.\frac{mc}{eB_1} = \frac{mc^2E_o}{e\,B_1^2}$ in a plane parallel to the sheet (Speiser 1965, 1968). After describing this half-circle the particles are again moving approximately along a field line and thus leave the sheet from above or below. In order to calculate the current flowing we first draw a 'locus of injection points', which is simply the curve on which particles enter the sheet and pass through point P in the neutral sheet plane. This locus is a semi-circle as are the trajectories in this plane (Fig. 1.13a). The current (or flux of particles) across an element dL of the sheet is simply determined by the flux entering the surface enclosed by the locii of injection points for the end points P_1 and P_2 of the element dL (Fig. 1.13b). However, we note that the flux contribution across dL in the direction of the arrow in Fig. 1.13b is positive for one section of the enclosed area and negative for the other (marked '+' and '-'). The net enclosed area for the evaluation of the current in the direction of the electric field of the untransformed frame is seen to be $2\,r\,dL_1$ and zero for the perpendicular direction. (Fig. 1.13c).

The incoming flux per unit area of the sheet is $2N_ov_1$ where

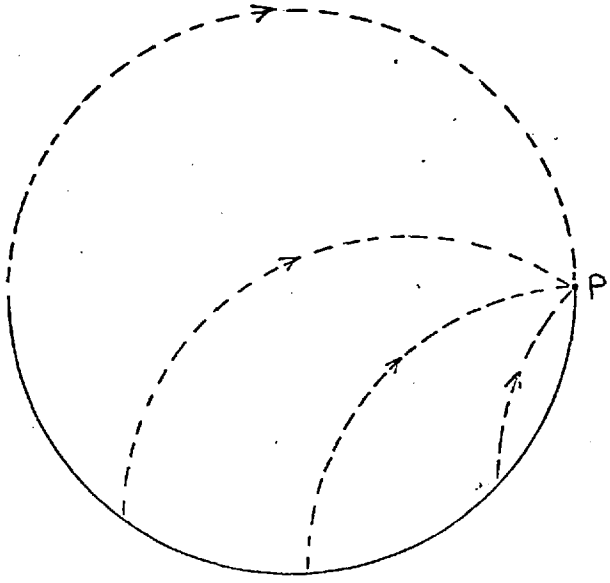

(a)

- - - - Trajectories in the plane of the sheet

——— Locus of injection points

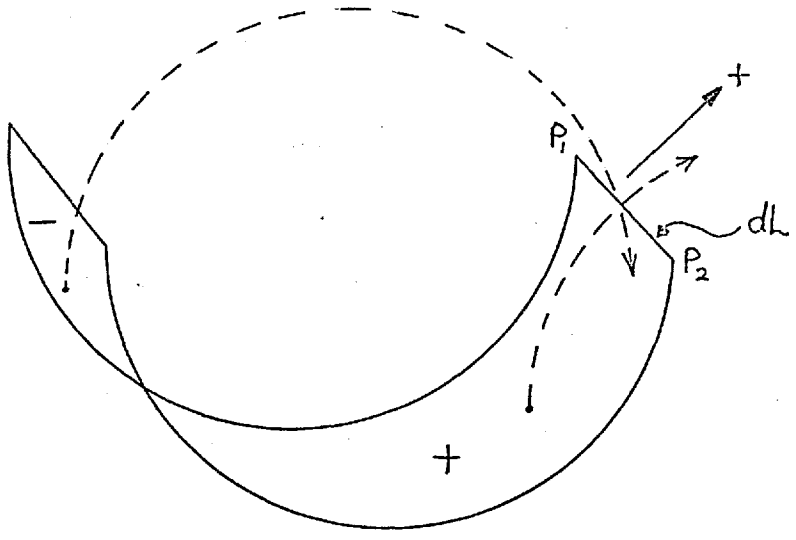

(b)

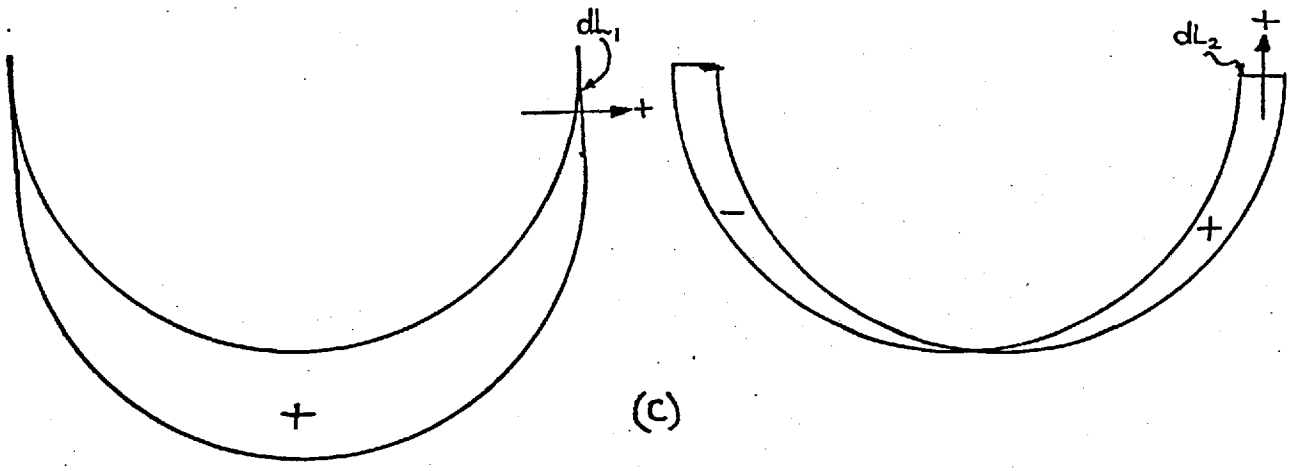

(c)

Figure 1.13

$v_\perp = v_T B_\perp/B_o$, and B_o is the magnitude of the reversing component of the field, outside the sheet. Adding proton and electron contributions to the current per unit length of sheet, we have, by conservation of flux

$$I = 2N_o e v_T \frac{B_\perp}{B_o} \times 2(r_p + r_e) = 2N_o e c \frac{E_o}{B_o} \{2(r_p + r_e)\}$$

and for self-consistency between the current and the field

$$2B_o = \frac{4\pi}{c} \left(\frac{2eN_o c E_o}{B_o} \{2(r_p + r_e)\} \right) \qquad (1.56)$$

Comparison with equation (1.51) now shows that in the untransformed frame the Alfvén potential now falls across a distance which is the sum of the gyrodiameters of the positive and negative particles in the sheet, R. Hence

$$E_o = \frac{\Phi}{R} \quad \text{and} \quad v_\perp = \frac{c\Phi}{RB_o}$$

or, since $R = 2(r_p + r_e) \simeq \frac{2m_p c^2 E_o}{eB_\perp^2}$ we have $E_o = \frac{B_o B_\perp}{\sqrt{8\pi N_o m_p c^2}}$

and $$v_\perp = \frac{B_\perp}{\sqrt{8\pi N_o m_p}} = \frac{v_{A\perp}}{\sqrt{2}} \qquad (1.57)$$

Outside the field reversal region the conductivity may be regarded as infinite, whilst inside it is given by, for Alfvén's case

$$\sigma = \frac{j}{E_o} = \frac{I/\ell}{E_o} = \frac{cB_o d}{2\pi \ell \Phi} = \frac{2N_o e c d}{\ell B_o}$$

where ℓ is the thickness of the field reversal region yet to be determined! (It must ultimately be related to the break-

down of 'frozen-in' infinitely conducting flow due to small scale lengths in the fields). When B_1 is included this just becomes $\sigma = \frac{c\, B_o\, R}{2\pi \ell \Phi} = \frac{2ecN_oR}{\ell\, B_o}$.

There are, however, two assumptions which have been made in Alfvén's analysis. First we have assumed that all incoming particles contribute to the current at the neutral sheet. This must be true if, as in systems of interest here, the particle energy in the incoming flow (thermal plus convective) is much less than the total potential energy across the system $e\Phi$. Then, on energy grounds only very few particles entering near the system boundaries can possibly reach the 'wrong' boundary, and so not contribute to the current. Secondly, and more importantly, we have assumed that the plasma surrounding the neutral sheet is the only source of current, and that no particles can enter the sheet from the 'sides' of the system. Such an injection of plasma from the sides may raise or lower the potential across the system depending on the sign of the current contribution. The orbits of such particles will be similar to those shown in Fig. 1.10a. Protons and electrons which drift across the system such as to enhance the current (orbits (1) and (2)) reduce the potential across the system, while the others give a net reduction of the current and the potential must be enhanced. Of course, for particles of the latter type only those entering with energy greater than $e\Phi$ will be able to drift the whole way across the system. Those of lower energy drift into the neutral sheet before reaching the boundary and are then accelerated back out again, making no net current. (Fig. 1.14). Particle access into a magnetic field region having field gradients and a neutral sheet have

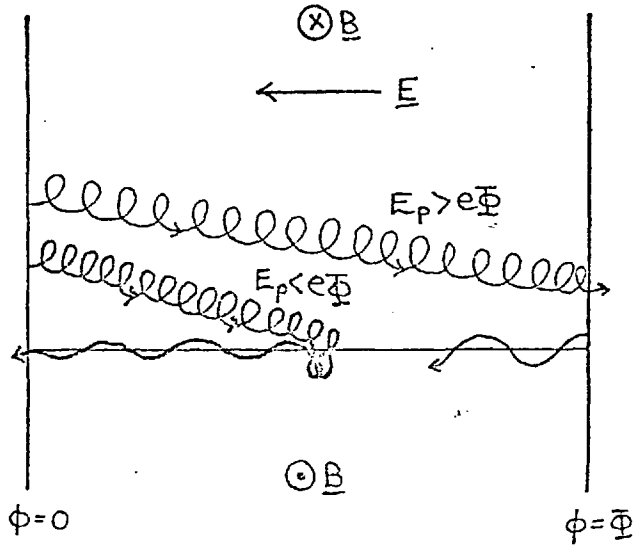

Figure 1.14

been considered by Stevenson and Comstock (1968). They took only a simple plane boundary for the magnetic field, which in any physical situation must be a drastic assumption, the detailed structure of the layer between the two plasma regimes should be taken into account. However, particles entering from the sides can provide the total current in the neutral sheet, and a general method for constructing such solutions has been given by Harris (1962). The equations to be solved are the time-independent Vlasov set

$$\underline{v}.\underline{\nabla} f_j + \frac{q_j}{m_j}\left(\underline{E} + \frac{\underline{v}\wedge\underline{B}}{c}\right).\underline{\nabla}_v f_j = 0 \qquad (1.58)$$

$$\underline{\nabla}.\underline{E} = 4\pi\sum_j q_j \int f_j \, d^3v \qquad \underline{\nabla}\wedge\underline{B} = \frac{4\pi}{c}\sum_j q_j \int f_j \underline{v} \, d^3v \qquad (1.59a,b)$$

where f_j is the distribution function of particle species j. We assume that $\underline{B} = (0,B(x),0)$; $\underline{E} = (E(x),0,0)$ and that $B = 0$ at $x = 0$ (see Fig. 1.15). Since all particles are to be provided from the 'sides' $E_z = 0$. We also have the magnetic vector potential $\underline{A} = (0,0,A(x))$ such that

$$B(x) = -\frac{\partial A}{\partial x} .$$

For a symmetrical sheet A is an even function of x and $A \geq 0$ for the magnetic field configuration shown in Fig. 1.15 if we choose $A(x=o) = 0$.

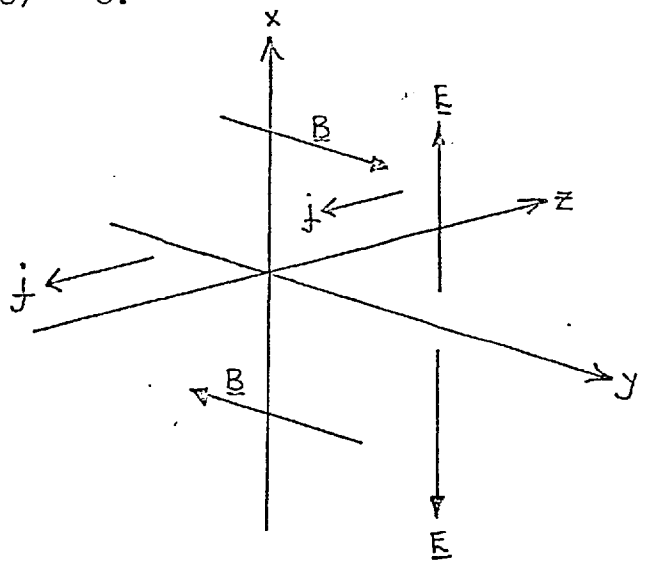

Figure 1.15

For these fields we find the following constants of the motion: the Hamiltonian for the motion in the x-z plane

$$H = v_x^2 + v_z^2 + \frac{2q_j}{m_j} \phi \qquad (1.60)$$

the canonical momentum in the z direction

$$P = v_z + \frac{q_j}{m_j c} A(x) \qquad (1.61)$$

and the velocity in the y-direction (along the magnetic field). It is well known that any distribution function which is a function only of the constants of the motion is a solution of the time independent collisionless Boltzmann equation (1.58). At the neutral sheet $\phi = A = 0$ so that

$$v_z = P \quad \text{and} \quad v_x^2 = H - P^2 .$$

Then, if we choose a distribution function at $x = 0$, i.e. $f_j = f_j(v_z, v_x, v_y)$, then $f_j = f_j(P, \sqrt{H-P^2}, v_y)$ is a solution of (1.58) over all space. Then the currents and charge density can be calculated as functions of ϕ and A; substitution in (59 a,b) then gives the (in general coupled) differential equations for $\phi(x)$ and $A(x)$. Harris chose a Maxwellian distribution at the origin, centred about a mean velocity in the z-direction

$$f_j = \left(\frac{m_j}{2\pi k T_j}\right)^{3/2} N \exp\left\{-\frac{m_j}{2kT_j}\left(v_x^2 + (v_z - V_j)^2 + v_y^2\right)\right\}$$

such that

$$f_j(x,\underline{v}) = \left(\frac{m_j}{2\pi k T_j}\right)^{3/2} N \exp\left[\frac{q_j}{kT_j}\left(\frac{V_j A(x)}{c} - \phi(x)\right)\right] \exp\left[\frac{-m_j}{2kT_j}\left(v_x^2 + v_y^2 + (v_z - V_j)^2\right)\right]$$

The current and charge density of the jth species is then given by

$$J_j = q_j V_j N \exp\left[\frac{q_j}{kT_j}\left(\frac{V_j A(x)}{c} - \phi\right)\right] \qquad \rho_j = \frac{J_j}{V_j} \tag{1.62}$$

and hence we obtain from equations (59 a,b), writing 'p' for protons and 'e' for electrons

$$\frac{d^2A}{dx^2} = -\frac{4\pi e N}{c}\left\{V_p \exp\left[\frac{e}{kT_p}\left(\frac{V_p A}{c} - \phi\right)\right] - V_e \exp\left[\frac{-e}{kT_e}\left(\frac{V_e A}{c} - \phi\right)\right]\right\} \tag{1.63}$$

$$\frac{d^2\phi}{dx^2} = -4\pi e N\left\{\exp\left[\frac{e}{kT_p}\left(\frac{V_p A}{c} - \phi\right)\right] - \exp\left[\frac{-e}{kT_e}\left(\frac{V_e A}{c} - \phi\right)\right]\right\} \tag{1.64}$$

If we transform to a frame such that $\frac{V_p}{T_p} = -\frac{V_e}{T_e}$ then an

obvious solution to (1.64) is $\phi = 0$ (i.e. we will obtain an exact charge-neutral model). Then (1.63) becomes

$$\frac{d^2A}{dx^2} = \frac{4\pi e N}{c} |V_p| \left(1 + \frac{T_e}{T_p}\right) \exp\left[-\frac{e|V_p|}{kT_p c} A(x)\right] \qquad (1.65)$$

For the current shown in Fig. 1.15) , $V_p < 0$. Then with the boundary conditions $A(x=o) = 0$; $B(x=o) = -\frac{\partial A}{\partial x}(x=o) = 0$ we obtain

$$A(x) = \frac{2ckT_p}{e|V_p|} \log \cosh \left(\frac{x}{\lambda}\right) \qquad (1.66)$$

where $$\lambda = \frac{c}{|V_p|}\left(\frac{k T_p}{2\pi e^2 N (1 + T_e/T_p)}\right)^{\frac{1}{2}} \qquad (1.67)$$

Hence $$B_y(x) = -\left[8\pi N k T_p \left(1 + \frac{T_e}{T_p}\right)\right]^{1/2} \tanh\left(\frac{x}{\lambda}\right) \qquad (1.68)$$

where we note that the magnetic pressure at infinity is equal to the total particle pressure at the neutral sheet. The ion and electron densities are given by (see Fig. 1.16)

$$n_i = n_e = N \exp\left(\frac{e\,|V_p|\,A}{k\,T_p\,c}\right) = \frac{N}{\cosh^2\left(\frac{x}{\lambda}\right)} \qquad (1.69)$$

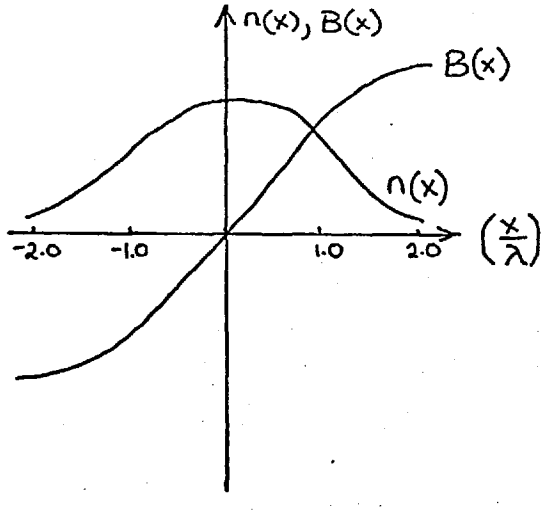

Figure 1.16

Although self-consistent models can be set up, as above, in which particle flow from the 'sides' can provide the neutral sheet current, Dungey (1971) has given a simple argument to show that when a neutral sheet is observed in nature it is clearly a case in which the particle influx is insufficient for this purpose. As above, the condition for equilibrium is $\underline{j} \wedge \underline{B}/c = \nabla p$ or $p + \frac{B^2}{8\pi} \simeq$ constant. This is clearly true in the Harris solution since

$$\frac{B_y^2}{8\pi} = p_o \tanh^2(\tfrac{x}{\lambda}) \quad \text{and} \quad p(x) = \frac{p_o}{\cosh^2(\tfrac{x}{\lambda})}$$

from equations (1.65) and (1.66). (T is constant as may be seen from the equation for $f_j(x,\underline{v})$) hence

$$\frac{B_y^2}{8\pi} + p = \frac{p_o}{\cosh^2(\tfrac{x}{\lambda})} (\sinh^2(\tfrac{x}{\lambda}) + 1) = p_o .$$

However, if the pressure is sufficient at $x = 0$ to satisfy equation (1.68) for a given magnetic field it would also be sufficient to separate the two regions of magnetic field entirely and no neutral sheet system would exist, i.e. the system would have to be very carefully set up at the boundaries in order to maintain such a model. In nature the regions of magnetic field would simply separate, and plasma would fill the region between.

(iv) Discussion and conclusions.

It appears that the considerations involved in a fluid description of magnetic field annihilation and reconnection are rather different from those which have been given for

systems in which particle collisions are unimportant. The latter case is by far the least developed at the present time, but applies in many situations in nature (e.g. the Earth's magnetic tail, solar wind and possibly in interstellar space and other astrophysical objects). It is the aim of this thesis to investigate the field and flow in the situation described by Alfvén (1968), as a first step in the understanding of such systems. Thus we shall neglect any component of the magnetic field perpendicular to the neutral sheet and assume that the only source of current is the plasma above and below it. In addition, such self-consistent configurations must be set up before stability analyses can be performed. At the present time there is no reason to suppose that the system should be grossly unstable, indeed, examples investigated in nature have been notable for their long-term stability and the general 'quietness' of the fields. Although a neutral sheet is known to be unstable to the tearing mode (a breakup of the sheet current into filaments, see, for example, Dobrowolny (1968)) it has recently been found that non-linear effects quickly quench the growth rate, and the instability leads to no more than a little turbulence in the component of the field perpendicular to the sheet (Biskamp et. al. (1970)). The possibility of other micro-instabilities of the two-stream type occuring in current sheets has been investigated by Dungey and Speiser (1969). While it is by no means obvious that a strictly neutral sheet should be unstable to these modes, Dungey (1969) and Gjøen (1971) have shown that, in the event, strong damping occurs by the radiation of cold plasma waves into the surrounding medium. Thus it appears that the self-

consistent steady-state model to be investigated here is not likely to be seriously afflicted by instabilities.

References

Alfvén, H. 1968. Some properties of magnetospheric neutral surfaces. J. Geophys. Res. 73, 4379-4381.

Biskamp, D., Sagdeev, R.Z. and Schindler, K. 1970. Nonlinear evolution of the tearing instability in the geomagnetic tail. Cosmic Electrodyn. 1, 297-310.

Chapman, S. and Kendall, P.C. 1963. Liquid instability and energy transformation near a magnetic neutral line: A soluble nonlinear hydromagnetic problem. Proc. Roy. Soc. Lond. A 271, 435-448.

Chapman, S. and Kendall, P.C. 1966. Comment on 'Some Exact Solutions of Magnetohydrodynamics'. Phys. Fluids 9, 2306-2307.

Cowley, S.W.H. 1971b. Some properties of magnetic neutral sheet systems. Imp. Coll. Sci. Report, June 1971. To be published in Proc. of Advanced Study Institute 'Magnetosphere-Ionosphere Interactions', Norway 1971, U. of Oslo Press.

Dobrowolny, M. 1968. Instability of a neutral sheet. Il Nuovo Cimento 55B, 427-441.

Dungey, J.W. 1953. Conditions for the occurrence of electrical discharges in astrophysical systems. Phil. Mag. 44, 725-738.

Dungey, J.W. 1958a. Cosmical Electrodynamics, Cambridge Univ. Press, 99.

Dungey, J.W. 1958b. The neutral point discharge theory of solar flares. A reply to Cowling's criticism. Electromagnetic Phenomena in Cosmical Physics, (Ed. Lehnert), Cambridge Univ. Press, 135-140.

Dungey, J.W. and Speiser, T.W. 1969. Electromagnetic noise in the current sheet in the geomagnetic tail. Planet. Space Sci. 17, 1285-1290.

Dungey, J.W. 1969. Damping of waves in the current sheet in the geomagnetic tail by radiation. Planet. Space Sci. 17, 1291-1296.

Dungey, J.W. 1971. Theory of neutral sheets. Imp. Coll. Sci. Rept. To be published in Proc. of Advanced Study Inst. 'Earth's Particles and Fields', Italy, 1971.

Giovanelli, R.G. 1947. Magnetic and electric phenomena in the sun's atmosphere associated with sunspots. Month. Not. Roy. Astr. Soc. 107, 338-355.

Giovanelli, R.G. 1948. Chromospheric flares. Month. Not. Roy. Astr. Soc. 108, 163-182.

Gjøen, E. 1971. Radiation damping of waves in the current sheet in the geomagnetic tail. Planet. Space Sci. 19, 635-642.

Harris, E.G. 1962. On a plasma sheath separating regions of oppositely directed magnetic field. Il Nuovo Cimento 23, 115-121.

Hoyle, F. 1949. Some Recent Researches in Solar Physics, Cambridge Univ. Press, 103.

Parker, E.N. 1957a. Newtonian development of the dynamical properties of ionized gases of low density. Phys. Rev. 107, 924-933.

Parker, E.N. 1957b. Sweet's mechanism for merging magnetic fields in conducting fluids. J. Geophys. Res. 62, 509-520.

Parker, E.N. 1963. The solar flare phenomenon and the theory of reconnection and annihilation of magnetic fields. Astrophys. J. Suppl. Ser. 77, 8, 177-212.

Petschek, H.E. 1964. Magnetic field annihilation. AAS-NASA Symposium on the Physics of Solar Flares, (Ed. W.N.Hess), NASA SP-50, 425-439.

Petschek, H.E. and Thorne, R.M. 1966. The existence of intermediate waves in neutral sheets. Astrophys. J. 147, 1157-1163.

Seymour, P.W. 1959. Drift of a charged particle in a magnetic field of constant gradient. Australian J. Phys. 12, 309-314.

Speiser, T.W. 1965. Particle trajectories in model current sheets, 1: Analytical solutions. J. Geophys. Res. 70, 4219-4226.

Speiser, T.W. 1968. On the uncoupling of parallel and perpendicular motion in a neutral sheet. J. Geophys. Res. 73, 1112-1113.

Speiser, T.W. 1970. Conductivity without collisions or noise. Planet. Space Sci. 18, 613-622.

Stevenson, T.E. and Comstock, C. 1968. Particles incident on magnetic field gradients. J. Geophys. Res. 73, 175-184.

Sweet, P.A. 1958a. The neutral point theory of solar flares. Electromagnetic Phenomena in Cosmical Physics, (Ed. Lehnert), Cambridge Univ. Press, 123-134.

Sweet, P.A. 1958b. The production of high energy particles in the solar flares. Nuovo Cimento Suppl. 8, Ser X, 188-196.

Uberoi, M.S. 1963. Some exact solutions of magnetohydrodynamics. Phys. Fluids 6, 1379-1381.

Uberoi, M.S. 1966. Reply to comments by S. Chapman and P.C. Kendall. Phys. Fluids 9, 2307.

Yeh, T., and Axford, W.I. 1970. On the re-connexion of magnetic field lines in conducting fluids. J. Plasma Phys. 4, part 2, 207-229.

CHAPTER 2

FIELD-LINE MERGING AND THE EARTH'S MAGNETOSPHERE

(i) Introduction

Although the model neutral sheet system we shall be considering here is highly idealized (straight field lines contained between parallel equipotential boundaries), this field geometry corresponds quite well to that of the geomagnetic tail. It is the purpose of the present chapter to review the observational evidence concerning the importance of field-line merging as a basic process of magnetospheric physics, and to obtain the tail parameters used in numerical calculations. We shall also consider the applicability of our straight field-line model to the geomagnetic tail.

(ii) The Magnetosphere and Interplanetary Medium

The magnetosphere is the region surrounding the Earth containing and controlled by the geomagnetic field. This region is not of infinite extent due to the presence of plasma radially expanding from the Sun (the solar wind) which is sufficiently highly conducting to prevent the penetration of geomagnetic field lines. The Earth's magnetic field is thus constrained to lie within a magnetospheric cavity around which the solar plasma flows, the dimensions of the cavity being determined by pressure balance across the plasma-field interface (the magnetopause). Shown below are the average near-Earth solar wind properties obtained by the Vela series of

satellites (Montgomery (1971)).

Quantity	Average	90% Range
Proton density $N(cm^{-3})$	7	3 - 15
Bulk velocity V(Km/sec)	410	305 - 550
Proton temperature (^oK)	8×10^4	$2 - 24 \times 10^4$
Electron temperature (^oK)	1.4×10^5	$0.85 - 2.1 \times 10^5$

It should be noted that for protons the energy of the bulk motion (ε_p (bulk) $\simeq$ 1 keV) is much larger than the thermal energy (ε_p (thermal) $\simeq$ 10 eV), while the opposite is true for the electrons (ε_e (bulk) $\simeq$ 0.5 eV ; ε_e (thermal) $\simeq$ 20 eV). From these figures we note that the sound speed ($C_s^2 \simeq \gamma k\ (T_p + T_e)/m_p$) is typically $\simeq$ 50 Km/sec.

The solar wind's magnetic field is found to be 5 to 10 γ near the Earth, and results from 'frozen-in' outward transport of the Sun's field from the base of the corona (of magnitude a few gauss). A solar wind field line should thus be defined by the locus of the plasma stream emitted from a given position on the Sun's surface. Since the sun is rotating ($\sim$ 27 day period) we thus find, on average, a 'garden-hose' pattern of field lines in the solar wind, with an angle near the Earth of about 45^o w.r.t. the Earth-Sun line. The field can, however, point either towards or away from the sun, depending on the surface field direction, and this results in a corotating structure of sectors of definite polarity observed near the Earth. Four sectors were observed at the most recent sunspot cycle minimum (1964-65) and two at the following maximum (1969-70).

Although the average solar wind magnetic field can be described by the corotating garden-hose sector structure, considerable variations can occur, with significant components out of the ecliptic plane, both northward and southward pointing, which may remain steady for periods of an hour or more (or less). In particular, large out-of-the-ecliptic components of magnitude several tens of gamma may occur behind an interplanetary shock-wave triggered by a solar flare on the surface of the sun. It is this component of the field, its duration, sign and strength, which is crucial to field-line merging in the magnetosphere, to be discussed in the next section.

The Alfvén speed in the solar wind, from the above values, is typically 40 to 100 Km/sec, similar to the above value of the sound speed. The wind is therefore supersonic in the Earth's frame with a mach number of $M \simeq 4 - 8$ with respect to the magnetosonic velocity $(C^2 = C_A{}^2 + C_s{}^2)$, and hence a detached bow shock is formed in front of the magnetospheric cavity. Across the shock the plasma velocity is reduced, the density is increased (by a factor $\lesssim 4$), and the total pressure (particle plus field) increased. As this shocked plasma (magnetosheath) expands as it flows around the cavity, the velocity increases again and the density and particle temperatures drop such that plasma conditions similar to the solar wind are resumed downstream (Fig. 2.1). Experimentally, the sheath plasma is found to be highly variable on a scale of a few minutes or less in flow speed and direction, particle temperatures and magnetic field, even when the solar wind is quiet. However, 'typical' parameters for the 'nose' region are $N \simeq 20$ cm^{-3}; ε_p(bulk) $\simeq 0.5$ keV ($v_b \sim 300$ km/sec);

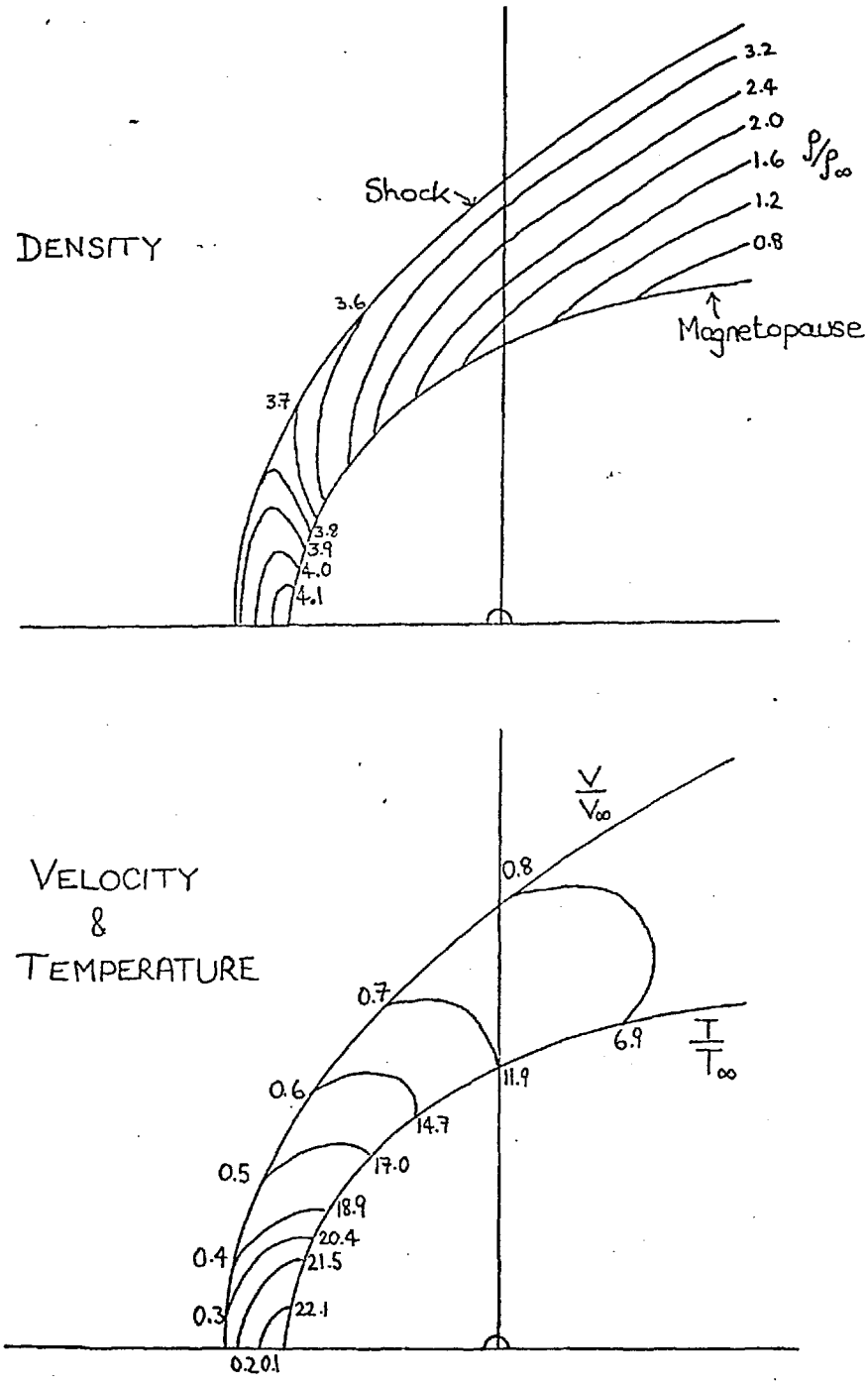

Figure 2.1: Density, velocity and temperature fields for supersonic gas dynamic flow past the magnetosphere; (M = 8, $\gamma = 5/3$). (From Spreiter, J.R., Summers, A.L. and Alksne, A.Y. 1966. Hydromagnetic flow around the magnetosphere, Planetary and Space Sci., 14, 223-253).

ε_p (thermal) ≈ 200 eV (T_p ~ 2 x 10^6 ^oK) ; ε_e (bulk) $\lesssim$ 0.5 eV ; ε_e (thermal) ≈ 50 eV (T_e ~ 5 x 10^5 ^oK) ; B ≈ 10 - 40 γ (B/B_{SW} ≈ 3 - 4). As in the solar wind, the energy density of the magnetic field in the magnetosheath is usually rather smaller than that of the plasma, such that the flow dominates the field, and the field lines may be regarded as being carried along by the flow and 'draped' around the magnetosphere. This has been experimentally confirmed by Behannon and Fairfield (1969).

If we neglect the sheath magnetic field and the magnetospheric particle pressure, then the condition for pressure equilibrium of the magnetopause near the nose may be easily used to obtain its distance from the Earth. Simply substituting sheath parameters into the equation leads to a nose distance of about 12 R_E, a result which changes little with changing interplanetary parameters since the nose distance varies inversely with the sheath pressure (dynamic and thermal) only to the $1/6$ th power. This result is in agreement with observations and establishes a scale of distances for the magnetosphere.

The currents flowing in the magnetopause boundary which 'switch off' the magnetospheric field, and provide the $\underline{j} \wedge \underline{B}/c$ magnetic pressure force on the sheath plasma, form the Chapman-Ferraro current system, shown in Fig. 2.2. The cavity shape expected from these simple pressure-balance considerations would be an asymmetrical 'doughnut', the 'hole' being representative of the dayside magnetopause neutral points to which all the magnetopause field lines are connected (Slutz and Winkelman, 1964). However, there appears to be a second

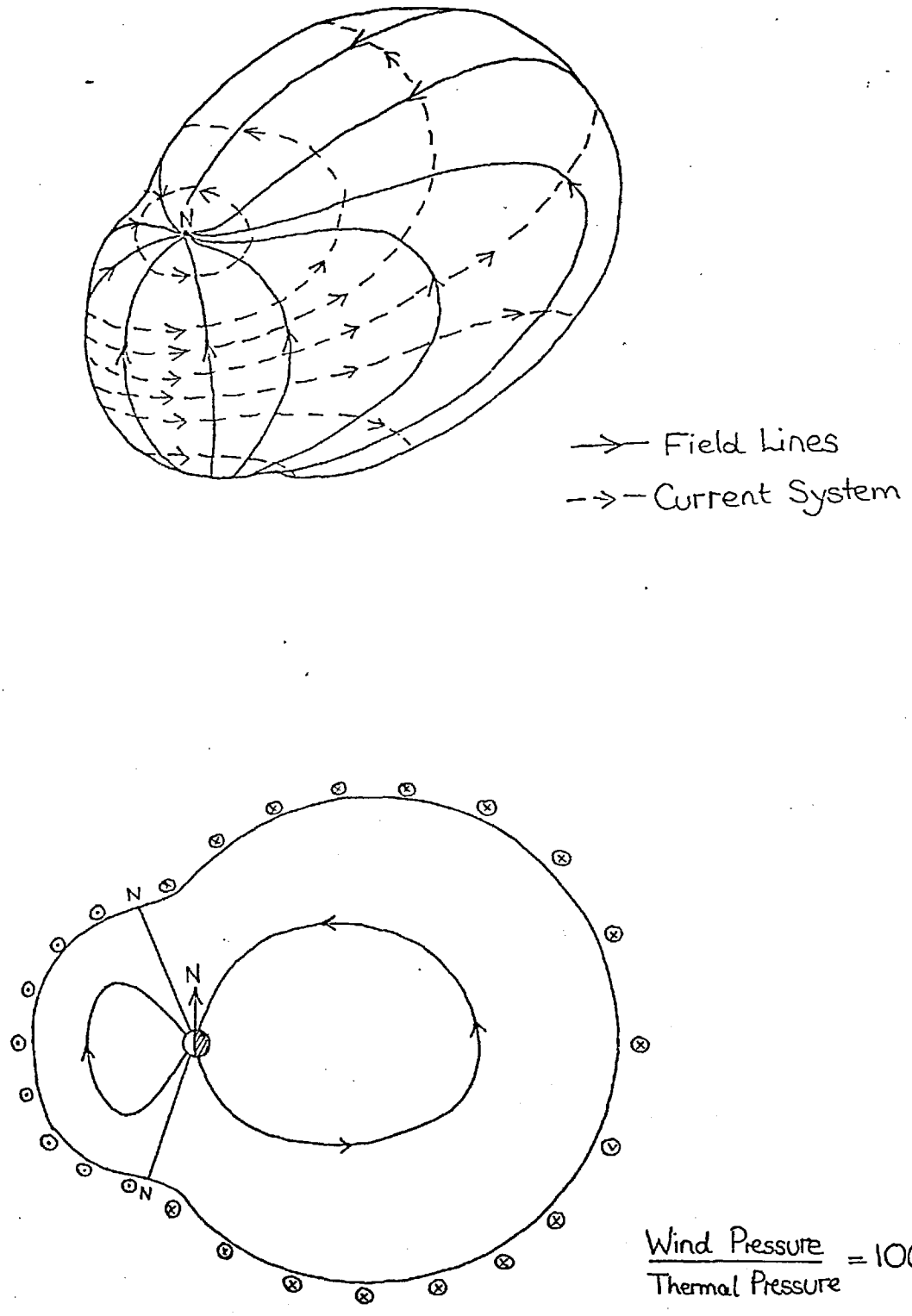

Figure 2.2: The magnetopause Chapman-Ferraro current system, and the asymmetric 'doughnut' magnetospheric configuration obtained by Slutz and Winkelman (1964) from pressure-balance considerations between the magnetosphere and flowing magnetosheath.

magnetospheric current system, resulting in the formation of an elongated magnetic tail, the existence of which was suggested by measurements from Explorer 14 (Cahill (1966)) and confirmed by Ness (1965) on Imp 1. This tail was found to consist of two bundles of oppositely directed magnetic field (connected to the two polar caps) of a quiet and orderly nature, separated by a current sheet of a few thousand Km in thickness (Speiser and Ness (1967)), shown in Fig. 2.3. Since these early measurements (within $X_{SM} = -30\ R_E$), an extensive investigation of the tail structure has been carried out by the Explorer 33 and 35 satellites, showing a well-ordered configuration out to 80 R_E, the average properties of which has been reported by Behannon (1970). The results show the tail to be roughly circular in cross-section, with its radius increasing from about 20 R_E at a distance of ~ 25 R_E from Earth to about 25 R_E at a distance of ~ 60 R_E ; a 'flaring out' consistent with the angle of the boundary with respect to the Earth-sun line required for pressure balance with the flowing magnetosheath plasma. The average field magnitude in the two tail lobes decreases from about 15 γ at a distance of 20 R_E to about 8 γ at a distance of 70 R_E. This decrease can be understood when both the tail flaring, and the small flux across the current sheet (a northward component of a gamma or two is usually observed at least in this near-Earth section of the tail) is taken into account. However, it has recently been shown that the tail configuration is rather variable over time scales of one or two hours and so such 'average' properties are of limited significance.

The length and large distance properties of the tail

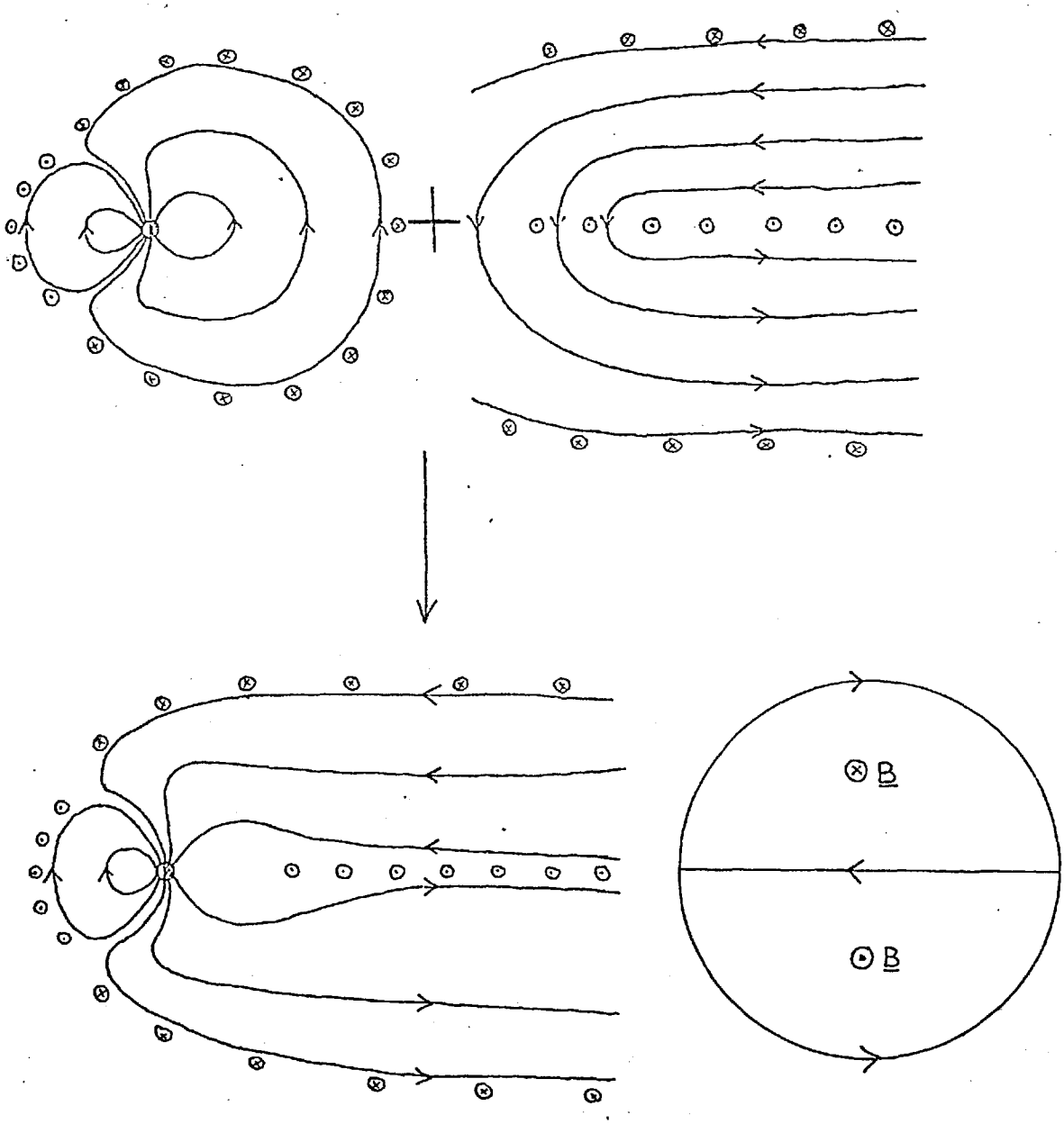

Figure 2.3: The addition of the C-F current system to the 'tail' current system leads to the observed long magnetospheric tail. Note that in the night side outer zone, the north-south 'dipole + CF' field is reduced by the tail current system. A section of the tail current system is also shown, looking towards the earth.

are at the present time undetermined, but evidence of its presence at 500 and 1000 R_E downstream from the Earth have been obtained by the Pioneer 7 and 8 spacecraft (Ness et. al. (1967), Fairfield (1968a), Mariani and Ness (1969)).

The plasma properties within the magnetospheric cavity are in general very complex and highly variable, and may best be discussed within the framework of the convecting magnetosphere, described in the next section.

From this section we will use the following tail parameters in our neutral sheet theory:

$$B \simeq 10\ \gamma \quad \text{and} \quad d\ (\text{width}) = 3 \times 10^{10}\text{cm} \simeq 47\ R_E .$$

(iii) Magnetospheric Convection and Substorms

Both Axford and Hines (1961) and Dungey (1961) suggested the possibility of the convection of magnetic field and plasma within the magnetosphere, an idea involving the transfer of magnetic flux from the dayside magnetopause into the tail, followed by its convective return, throughout the body of the magnetosphere, to the dayside. However, while Axford and Hines postulated that the convection would be driven by a viscous-like drag at the magnetopause (like the convection in a water-drop falling through the atmosphere), Dungey argued that strong convection would be set up when the interplanetary (and hence magnetosheath) magnetic field has a southward component. In such a situation an X-type neutral point is formed between the southward sheath field and the northward dayside magnetospheric field. Merging can then take place (Fig. 2.4), resulting in polar cap field lines becoming directly connected into

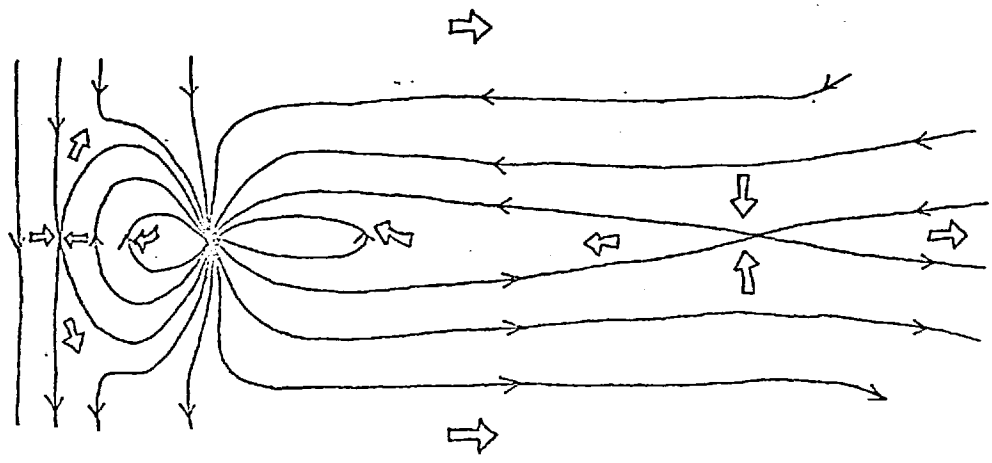

(a)

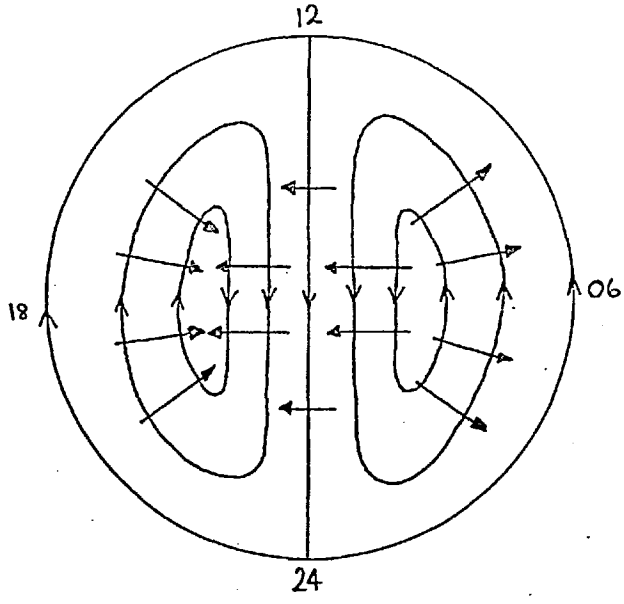

(b)

Figure 2.4 (a): Flow in the reconnection model of the magnetosphere (after Dungey (1961)).

(b): Motion of the field-line feet over the polar cap for uniform convection driven by field-line merging. These paths are electric field equipotentials, so that for a Hall conducting ionosphere the current flows in the opposite direction to the flow. The expected electric field directions are also shown.

the magnetosheath. The flow of the sheath plasma pulls the field lines over the polar cap and into the tail (being presumably responsible for its formation). In the steady-state situation this flux transferred from the 'closed' region of the magnetosphere (topologically a 'doughnut') to the 'open' tail (topologically two cylinders) must be balanced by reconnection at a second X-type neutral line in the tail (see Fig. 2.4(a)). The overall flow may be considered to be driven by an electric field from dawn to dusk across the magnetosphere ($\underline{E} = - \underline{v} \wedge \underline{B}/c$; or $\underline{v} = c\underline{E} \wedge \underline{B}/B^2$), the flow within the 'closed' region being towards the dayside. The expected motion of the feet of the field lines over the polar cap is shown in Fig. 2.4(b), and for a primarily Hall-conducting ionosphere the current is in the opposite direction. This should lead to a well-defined world-wide magnetic disturbance pattern characteristic of the convective state driven by field-line merging.

It was natural that an attempt should be made to give an explanation in terms of this model to one of the magnetosphere's most spectacular phenomena, the magnetospheric substorm. Its effects as observed on the ground are primarily the intensification and breakup of the quiet-time night-side auroral arcs, and the development of an intense westward electrojet in the night auroral oval (10^6 amps across at latitudinal strip 10^o wide, centered on $\Lambda \sim 65^o$) leading to $\sim 500\ \gamma$ negative bays in the H component magnetogram traces. Such phenomena, which start suddenly in a small region near midnight and expand northwards (the auroral 'bulge') and along the auroral oval to east and west, are part of the substorm expan-

sion phase. (See review by Akasofu (1968) and references therein). This was interpreted as being due to an explosive onset, or enhancement of field line reconnection in the tail (Dungey (1968)), although the trigger for this onset was not understood. More recently it has become clear that a well-ordered sequence of events takes place prior to the sudden onset of the expansion phase, all of which may be interpreted in terms of the reconnection model of the magnetosphere, directly confirming Dungey's predictions. During the so-called 'growth phase', we appear to see the evolution of the magnetosphere from a non-convecting (or slowly convecting) state to a strongly convecting equilibrium, in response to the appearance of a southward component of the interplanetary magnetic field. The sudden onset of the expansive phase following the ~ 1 hour duration of the growth phase then represents the effect of some instability or large change in the flow situation which is triggered as the magnetosphere approaches its new equilibrium. The 'trigger' mechanism is still not certain, although instabilities in field-aligned current systems associated with the night-side electrojet which upset the flow pattern, are currently being seriously considered (Coroniti and Kennel (1971)). By comparison with the growth phase, the events following the sudden onset of the expansive phase are ill understood, though it is clear that strong field line reconnection in the tail is involved. An interpretation will be attempted in Chapter 6.

That auroral zone electrojet activity (or DP-1 activity, following the current system nomenclature of Nishida (1971)) is correlated with periods when the interplanetary or magnetosheath field has a southward component has been appreciated for a con-

siderable time, following Dungey's (1961) theoretical prediction. Fairfield and Cahill (1966) first showed that the several substorms they studied occurred during periods of such a southward field, roughly an hour after its onset. Many authors subsequently tried to correlate interplanetary parameters with the K_p index of ground magnetic activity. This index responds to all sources of ground fluctuations since it is compiled from the data of mid-latitude stations, so it is not surprising that it correlates with virtually every bulk parameter of the solar wind; however, it <u>does</u> correlate positively with B_{south} (Schatten and Wilcox (1967), Wilcox et. al. (1967), Rostoker (1968), Hirshberg and Colburn (1969)). In addition, K_p is a 3 hourly index, so that 3-hourly solar-wind data was necessarily used by these authors. Since the substorm expansion lasts only about an hour K_p is again a far from ideal index to use. However, Hirshberg and Colburn had also shown that geomagnetic world-wide storms (comprising a sequence of substorms in rapid succession) occur only if the interplanetary field is southwards following an interplanetary shock (behind which large out of the ecliptic field components can occur). If it is northwards an s.i. (or s.s.c.) is the only result, the main phase starting only when B becomes large and southward. Arnoldy (1971) has recently clinched the matter by a correlation of interplanetary parameters with the hourly AE index, which specifically measures the strength of the DP-1 electrojet. He found that the only controlling parameter of AE was the sum of B_{south} for the <u>preceeding hour</u> (i.e. $\int_{t_1-1\text{ hour}}^{t_1} B_s\, dt$), which is a measure of the southward flux brought up to the magnetosphere by the solar wind ($v_{sw} \sim 400$ Km/sec). The positive

correlation here means that the larger the flux brought up, the larger the eventual substorm electrojet, an observation of relevance to theories of the expansive phase onset triggering mechanism.

The DP-1 equivalent current system (Fig. 2.5), the signature of the expansion phase, and shown to be correlated with periods of southward interplanetary field, does not correspond to the ionospheric current system expected from magnetospheric convection (Fig. 2.4(b)). However, Nishida (1968a,b;1971), discovered a new world-wide geomagnetic current system, prominent in polar cap records, which appears to be very closely controlled by the north-south component of the interplanetary field. This is called DP-2 and consists of two current vortices aligned approximately along the Earth-Sun line, with no auroral enhancement (the primary characteristic which distinguishes it from DP-1, apart from the different orientation of the vortices). An example is shown in Fig. 2.6, together with Imp 3 data of the interplanetary field. Nishida infers from this and other data that the DP-2 current system is coherent with respect to B_S, but there appears to be a time delay between the satellite and ground data of about 20 min, while we note that the solar wind transit time between the two is only about 5 min. The correspondence between these observations and those expected for convection should be clear, except that the magnetosphere appears to respond slowly (~ 20 min e-folding time) to the onset of a southward field. It would also seem that this component may have to exceed a minimum value of ~ 5 γ before DP-2 is set up, on one of Nishida's quiet days there existed a southward component for over 10 hours but its magnitude was only 3 γ.

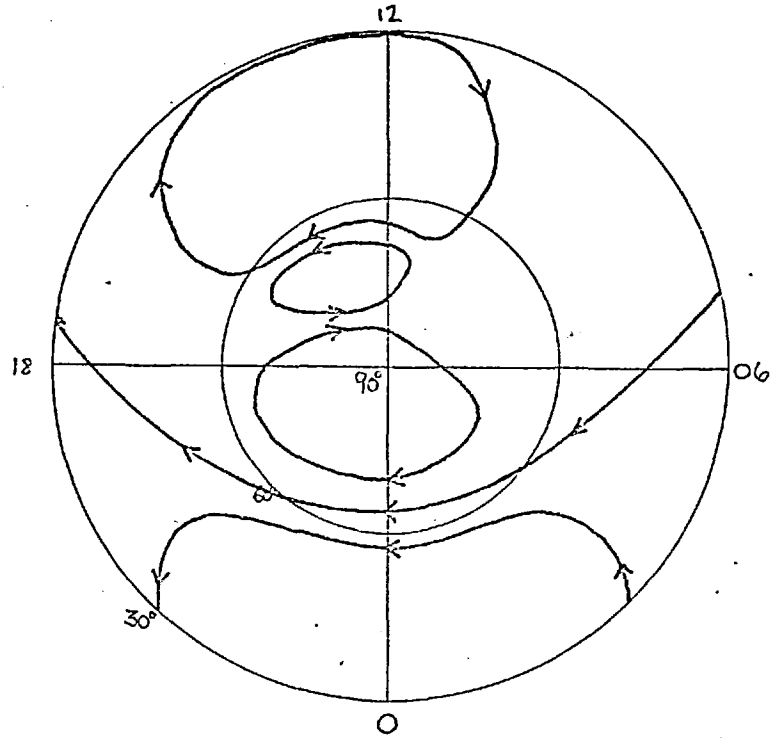

Figure 2.5: Typical DP-1 (electrojet) equivalent current system, the characteristic disturbance pattern of the substorm expansion phase (from Nishida (1971)).

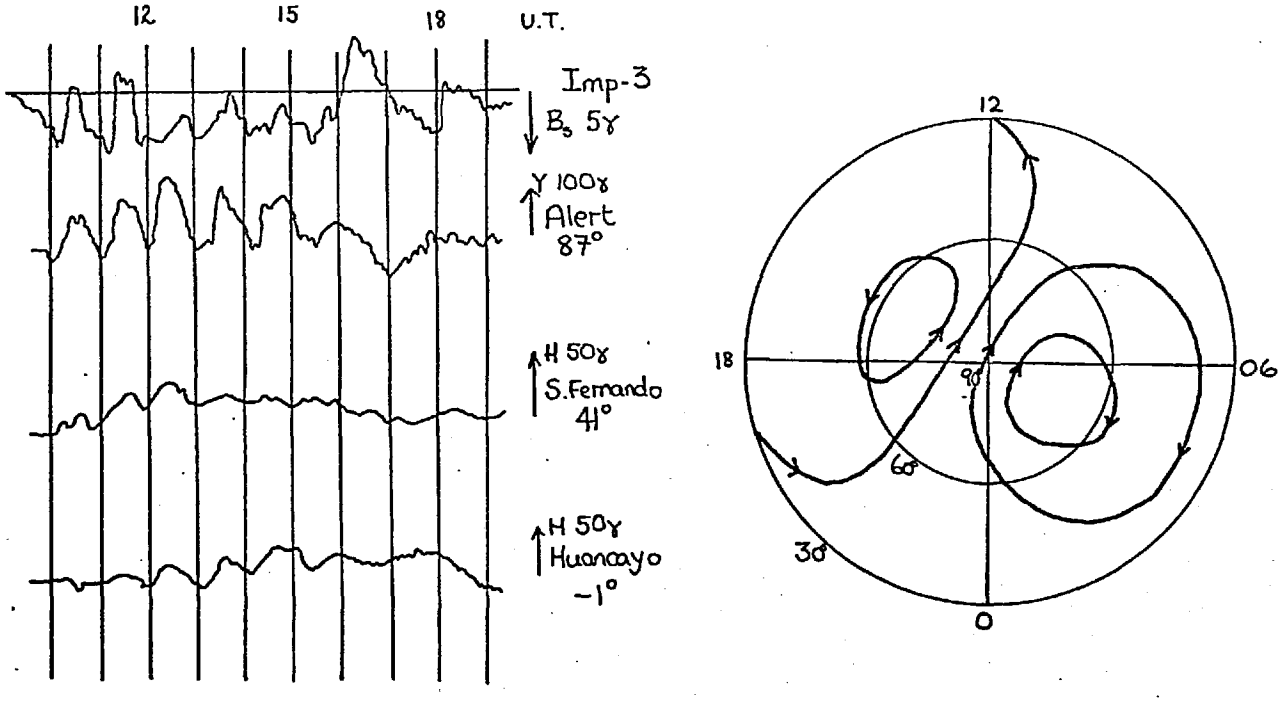

Figure 2.6: Simultaneous interplanetary and ground disturbance magnetic fields characteristic of DP-2, the signature of the growth phase (from Nishida (1971)).

(This may be a requirement on the θ angle of the field rather than its magnitude).

Thus convection is set up every time there exists a (significant?) southward field; a substorm expansion occurs after perhaps an hour of southward field, but is not otherwise related to any particular solar wind event. We note, in passing, that McPherron (1970), examining auroral zone magnetograms for an isolated substorm, noted 'fluctuations' for about an hour prior to breakup (presumably DP-2), and was the first to coin the phrase 'growth phase'.

The electric field direction across the polar cap required by the convective flow is shown in Fig. 2.4(b). In the dawn-dusk meridian it is from 'dawn to dusk' across the polar cap, reversing at lower latitude to become 'northward' in the evening and 'southward' in the morning. Recently, techniques have been developed which directly measure the magnetospheric electric field, usually near the Earth where it is strongest. These are the double probe technique (measuring the potential difference between two separated and insulated conductors in (hopefully) identical plasma conditions), either carried by a low altitude satellite or by balloon, and releases of barium ion clouds into the ionosphere where their motions can be observed (see review by Maynard (1971)). The first results of a rather crude experiment (double probe on Injun 5; Cauffman and Gurnett (1971)) detected the field reversal along the dawn-dusk meridian at latitudes between 70^{o} and 80^{o}, and occasionally the electric field across the entire polar cap was sufficiently large (even ~ 120 mV/m) for them to be able to detect it. Results of a more sophisticated experiment on

OGO-6 (Maynard (1972)) showed the continual presence of the expected electric field pattern, with general magnitude 10 to 40 mV/m, corresponding to flow speeds of 0.2 to 0.8 Km/sec or a north-south motion of 5 to 25° latitude per hour (Fig. 2.7). Polar cap barium releases (Heppner et. al. 1971) have supported these results, showing a day to night flow corresponding to electric fields of 20 to 40 mV/m. Balloon double-probe measurements of the electric field across the night-side auroral zone (60° to 80°) have shown that the expected westward field exists for about an hour prior to the sudden expansion (Mozer and Manka, (1971), Mozer (1971)). This field rises from a few mV/m to ~ 30 mV/m just prior to breakup. Except for these balloon measurements, none of the data have yet been correlated with interplanetary or other concurrent magnetospheric data, but may be said to generally support the reconnection picture of strong magnetospheric convective flow.

As we have said, the DP-2 current system (and hence the convection) takes 15 to 20 min to build up following the appearance of a southward component of the interplanetary field. If we assume that merging at the dayside magnetopause takes place whenever the field has such a component, then we must conclude that during the early growth phase, flux is removed from the dayside and added to the tail, without a balancing return flow from the tail restoring flux to the dayside, and this continues until a new equilibrium configuration is approached (i.e. strong convection equilibrium). These flux changes are observed experimentally as an inward motion of the magnetopause (the earth's field at the boundary must remain roughly constant, for pressure balance) and an increase in tail field strength.

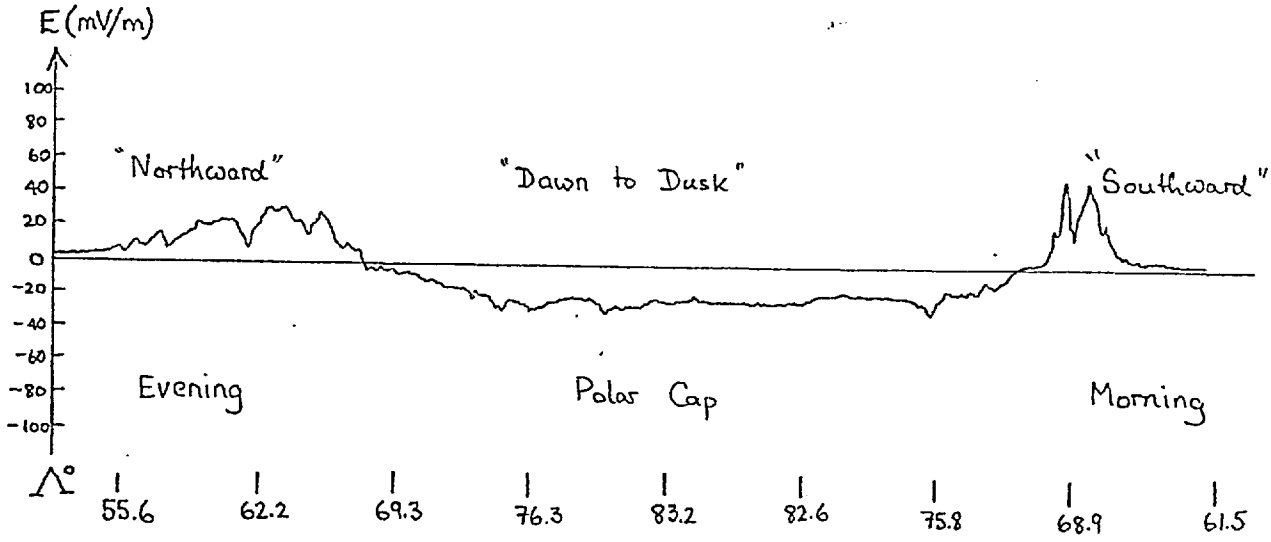

Figure 2.7: The component of horizontal electric field perpendicular to the Earth-sun line obtained by Maynard (1972) on OGO 6, after subtraction of $\underline{v} \wedge \underline{B}$. The satellite was very nearly in the dawn-dusk meridian, nearly passing over the north magnetic pole.

Meng (1970) showed on a statistical basis that large values of AE (hourly average) occur when the boundary is closer to earth than average. Typically $\langle R \rangle - R \simeq 1 \rightarrow 2\ R_E$ when AE ~ 200 → 400 γ, while for $R - \langle R \rangle \geq 0$ the AE index is small (≤ 10 to 100 γ). The first detailed observations of substorm-associated tail field changes were made by Camidge and Rostoker (1970) and Fairfield and Ness (1970), who showed that for one or two hours prior to the maximum of the AE index the field strength can approximately double in a roughly linear fashion, although motions of the plasma sheet can complicate the picture. During this time the field assumes a 'tail-like' configuration with very little (≤ 1 γ) north-south component, corresponding to an enhancement of the tail current system (see Fig. 2.8). However, simply adding flux to the tail does not increase the field strength if the magnetosheath pressure is constant. It was shown by Arnoldy (1971), Aubry et. al. (1970) and Aubry and McPherron (1971) that the increase in tail field was not due to changes in the thermal or dynamic pressures of the solar wind, so that the flaring angle of the tail must increase, if the field strength increases. In addition, the flux content of one of the quiet tail lobes at $X \simeq -20\ R_E$ is ~ 5×10^{16} maxwells (B ~ 20 γ), while if Meng's results of magnetopause motions are typical, the flux transferred from the dayside (~ 50 γ field at the boundary) is ~ 10^{16} maxwells. However, we may typically find field strengths of ~ 30 γ in the tail during the growth phase so that there is an indication that the tail radius decreases by a factor ~ 0.9 at least for $X \geq -20\ R_E$ (see Fig. 2.9(a))

These data have thus shown a strengthening and earth-

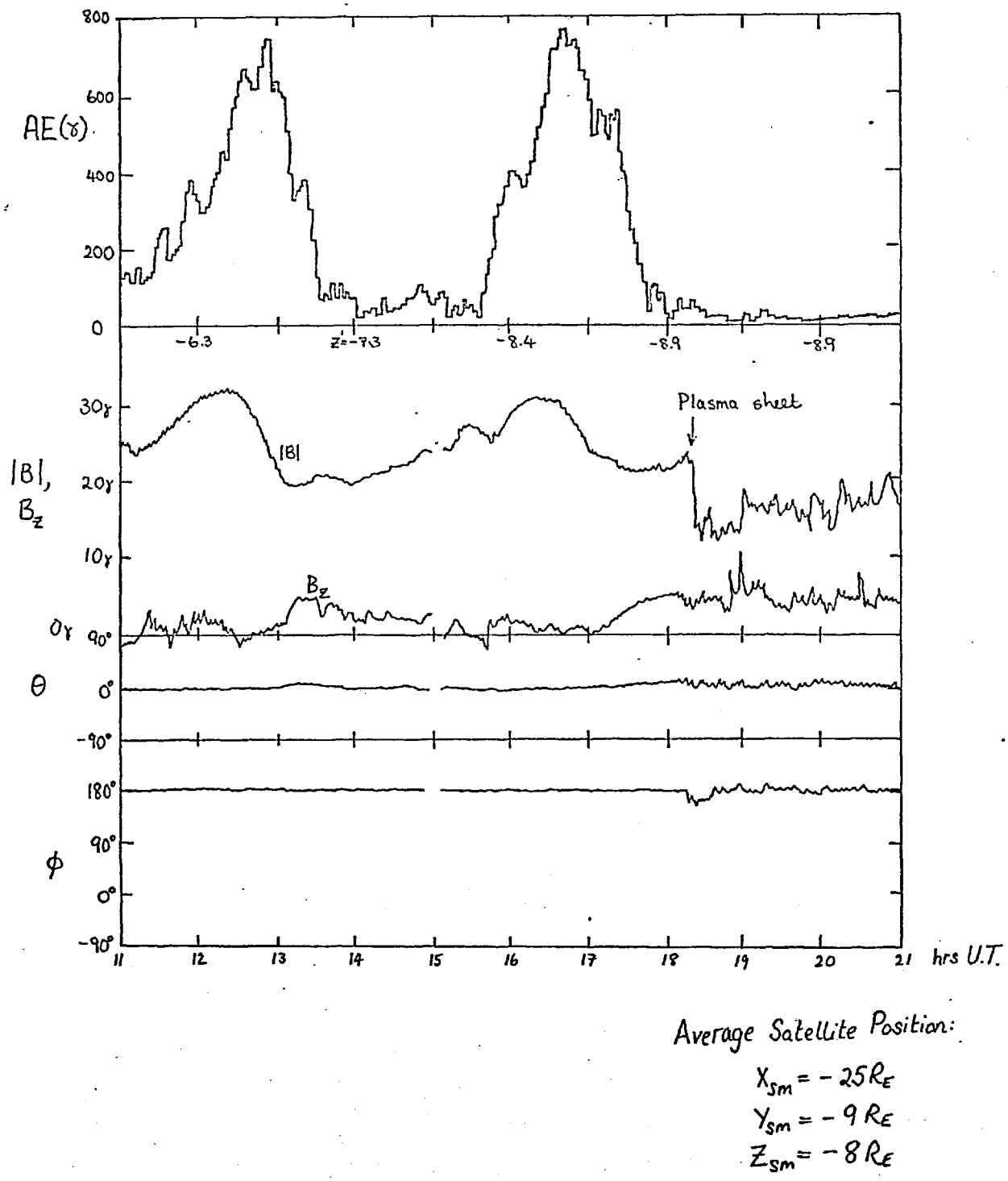

Average Satellite Position:

$X_{sm} = -25 R_E$

$Y_{sm} = -9 R_E$

$Z_{sm} = -8 R_E$

Figure 2.8: Behaviour of the tail field during isolated substorms when the spacecraft is far from the expected position of the neutral sheet (From Fairfield and Ness (1970)).

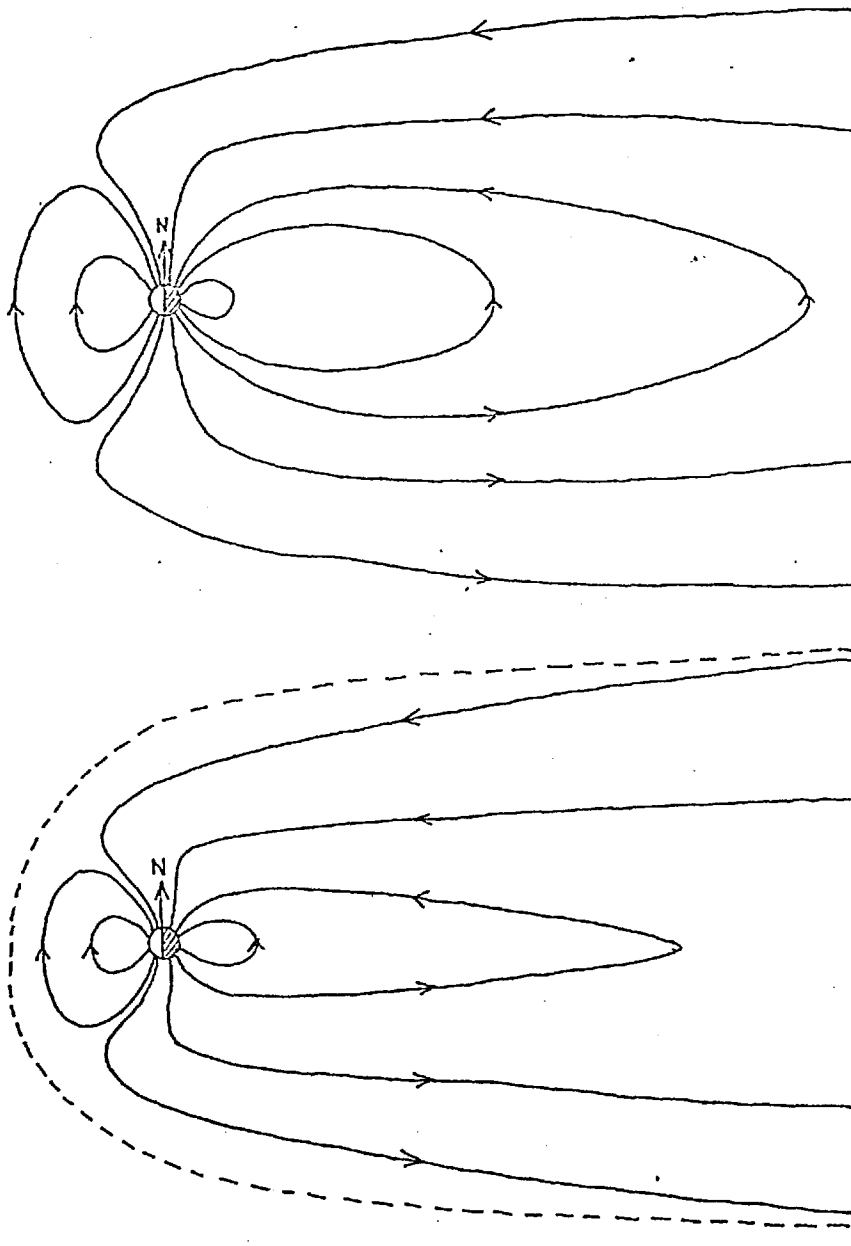

Figure 2.9(a): Schematic diagram of the change of field configuration between (i) quiet times, (ii) growth phase, prior to substorm onset. We have indicated the shrinkage of the nose of the magnetosphere, the increasing flaring angle of the tail, and the possible decrease of tail radius for the near-Earth section.

ward motion of the tail current system during the growth phase. Both these effects combine to make a large perturbation in the night-hours outer zone field (as observed on ATS-1 at 6.6 R_E by Cummings et. al. (1968)). Here, as expected, the growth phase is characterized by a decrease in field strength (the south to north field is the major component) on a time scale of an hour or two, by 20 to 60 γ (dipole field ~ 100 γ).

The most interesting data set so far obtained concerning this aspect of the growth phase has been presented by Aubry et. al. (1970) who used OGO-5 observations of the magnetopause motions with concurrent magnetic field data in the solar wind, magnetosheath and tail. They directly observed the inward motion of the magnetopause following the appearance of a southward component of the interplanetary field (the boundary oscillating about a ~ 2 R_E displacement after about 20 min. of such a field), and the increase in tail field (somewhat obscured by plasmasheet effects). A substorm expansion followed somewhat later. From this concurrent data set, the statistical result of Meng (1970), the observations of Cummings et. al. (1968) and Fairfield and Ness (1970) and the reconnection model of the magnetosphere are brought together to form a consistent picture of the evolution of the magnetosphere to a convection equilibrium.

The motion of the aurorae during the growth phase provide further coroborative evidence of the magnetospheric changes inferred here, although these effects are much less spectacular than the nightside breakup, bulge and surge phenomena during expansion. Aurorae of the dayside oval are produced

by ~ 150 eV electrons, associated with $\lesssim$ 1 keV proton precipitation (optical observations of Eather and Mende (1971)), and are discrete, rayed forms, which are very short-lived and fleeting, but nearly continuously present. The electron energy flux during quiet times was found to be ~ 0.1 erg/cm^2/sec throughout a region extended from ~ 77^o to 82^o near the noon meridian and was continuous in longitude from (at least) 09:00 to 15:00 L.T. This precipitating plasma forms a distinct 'soft-zone' of structured low-energy particle fluxes at high invariant latitudes on the day side. This was first detected unambiguously by Burch (1968) (75^o to 80^o at noon) and further investigated by Hoffman (1969) (75^o to 85^o at noon) from low altitude polar orbiting satellites. The first good energy spectra of these particles was obtained by Heikkila and Winningham (1971), and these showed considerable similarities to magnetosheath spectra, with energy fluxes of ~ 0.3 erg/cm^2/sec compared with ~ 0.5 erg/cm^2/sec in the sheath. That the dayside soft zone is magnetosheath in origin, having direct access via the polar cusp (i.e. dayside magnetopause neutral line or points) has recently been confirmed by Frank (1971) using particle measurements carried out by Imp 5 from the magnetosheath down to low altitudes. The identification of the soft-zone fluxes with dayside aurorae has recently been confirmed by Hoffman and Berko (1971). When the interplanetary field turns southward, the faint rayed structures of east-west elongation change to a more active and brighter band which moves equatorward (Kaneda (1971)). The brightening presumably corresponds to either neutral sheet acceleration during reconnection, or a different mode of access due to the

differing field configuration; the equatorward drift is expected since the loss of dayside flux during the early part of the growth phase means that the field lines connected to the magnetopause are to be found at lower latitudes. For an inward displacement of the magnetopause by 2 R_E at the equator, the shift in latitude is about 5^o. More recently Akasofu (1971) has also measured this equatorward shift and finds such a motion for an hour or two prior to breakup, with displacements of 5 to 7^o. For larger substorms larger shifts are seen, in confirmation of Arnoldy's (1971) result that the strength of the electrojet is proportional to the strength of the convection.

By contrast with the dayside, the aurorae of the night time oval take the form of simple arcs (one or more) of basically east-west elongation which may be stable in form for several hours. They are formed in the 100 → 200 km height range and extend for thousands of km along the oval, but are extremely thin (3 to 5 km). Their magnetospheric origin near the equator is indicated by the close conjugacy of the quiet arcs between north and south hemispheres observed by Belon et. al. (1969). This close conjugacy rapidly deteriorates during breakup events however. During quiet times these arcs are located near ~ 70^o at midnight, and are associated with ~ few keV electrons as measured by sounding rockets (see Hones et. al. (1971a) for a comprehensive reference list). The particles have not been measured by polar satellites because of the small latitudinal extent, and do not seem to be identifiable with magnetospheric particle distributions. Their most likely source seems to be neutral sheet acceleration on multiple

X-neutral lines in the near-Earth tail. During the growth phase the arcs drift equatorwards with the convection drift velocity (Kelley et. al. (1971)) of $3^{o} \rightarrow 7^{o}$/hr, ending up near $65^{o}\Lambda$ prior to breakup (corresponding to an equatorwards expansion of the auroral oval).

The occurrance of strong convection in the magnetosphere leads to very definite patterns of particle populations within it, and changes in the convection strength produces the temporal changes which occur. As has been previously stated, plasma flow within the region of closed field lines is basically towards the sun, i.e. particles are convected from the tail region, around the Earth to the dayside magnetopause. As they move from the weak magnetic fields of the tail region into the stronger fields near the Earth, preserving μ and J, they become energized (as may be seen from the conservation of $\mu = w_{\perp}/B$), the increasingly important velocity dependent magnetic drifts moving the particles across equipotentials. The motion of particles is thus highly dependent on their energy compared with the electric potential energy across the magnetosphere associated with the convection (~ 50 kV for strong convection). For particles starting with very low energies in the tail the electric drift dominates at all points on their drift path and their motion in the equatorial plane is simply along electric equipotential lines. They are hence rather easy to describe. With increasing energy in the tail the magnetic drifts become more important such that the particles near the Earth will have gained energies comparable with the electric potential energy (a few tens of kilovolts). Of course, energization is limited to the potential drop across

the magnetosphere, such that particles with too high an energy in the tail will drift to the magnetopause and be lost before they enter the region of strong magnetic fields near the Earth. However, any high energy particles (rather larger than the potential energy) which are produced near the Earth (not by convective energization) will drift around it on closed paths conserving μ and J, virtually ignoring the electric field. We thus expect, broadly speaking, to be able to describe the distribution of particles below a few tens of keV energies in terms of convective energization, while any particles of higher energy should have a different morphology owing to their different origins.

In the absence of convection, a radial (towards the Earth) electric field would exist, arising from the fact that the feet of the magnetospheric field lines are embedded in the conducting ionosphere, which corotates with the Earth. This electric field, which decreases with a $1/L^2$ dependence, produces circulation of the low-energy magnetospheric plasma around the Earth with a 24-hour period. If we simply add the corotation and convection electric fields together, the resulting equipotentials and low-energy particle path in the equatorial plane are shown in Fig. 2.9(b). We note that there exists a region near the Earth which does not take part in the convection, and that this constitutes a 'forbidden zone' for low-energy particles drifting in from the tail. If we consider a magnetic flux tube which is initially devoid of plasma and which is connected at either end to the ionosphere, a flow of plasma into the tube will start. This is initiated by ambipolar diffusion of the electrons setting up a parallel elec-

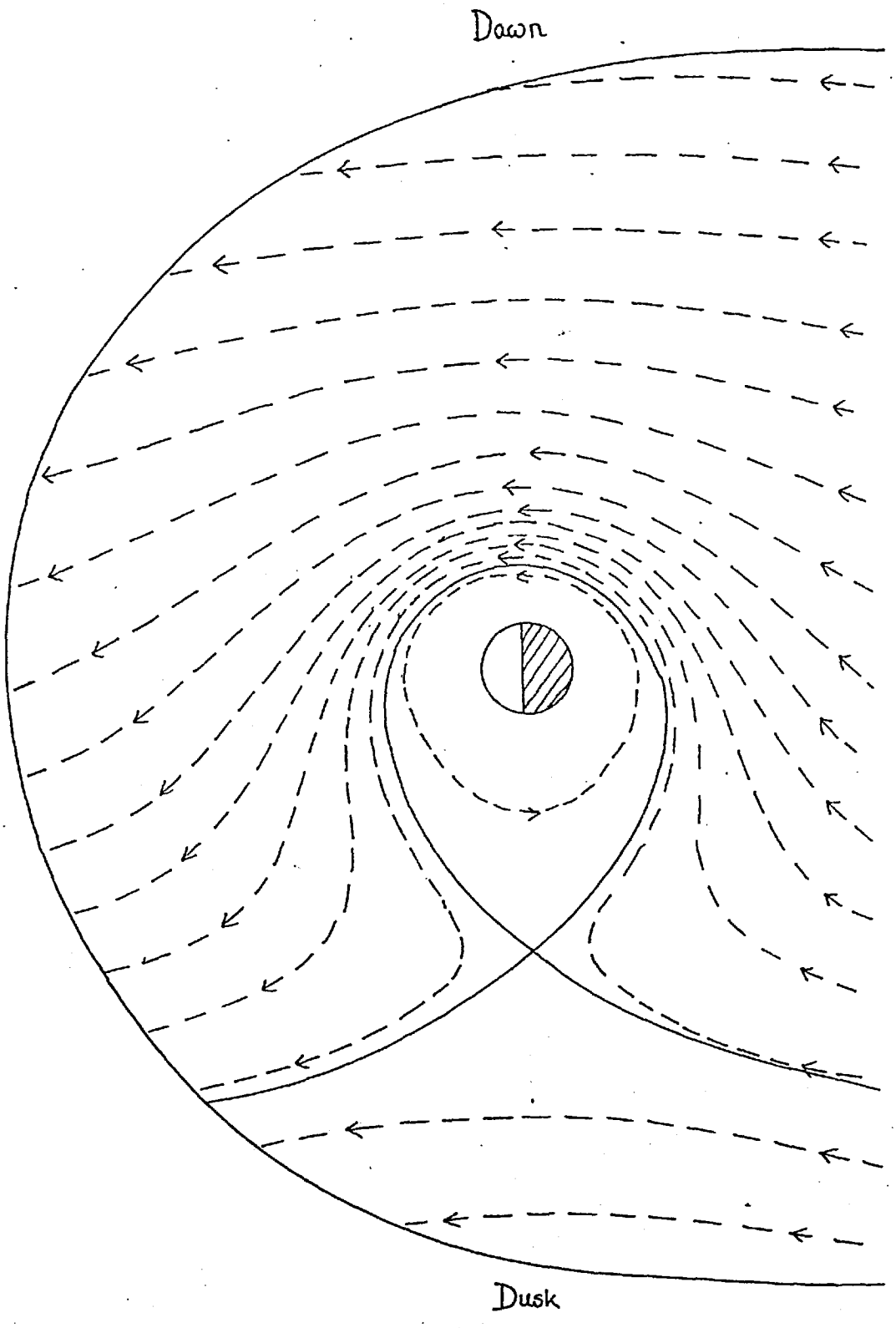

Figure 2.9(b): Electric equipotentials in the magnetic equatorial plane obtained by the addition of a radial corotation electric field to a uniform convection field from dawn to dusk across the magnetosphere. The total potential drop across the system is 40 keV. These lines are also the drift-paths for low energy plasma.

tric field, which pulls out the light ionospheric ions (mainly hydrogen), while the heavier ions (mainly oxygen) remain stationary. Banks and Holzer (1968) showed that such a flow of light-ion plasma would become supersonic above a few thousand km, with a flux out of the topside ionosphere of order 10^8 ions/cm^2/sec. The plasma streams from north and south hemispheres interact at the equator to produce shocks which propagate back into the ionosphere (taking several hours, Banks et. al. 1971) to terminate the supersonic flow. Subsonic flow then ensues for a period of a few days until an equilibrium distribution in the flux tube exists, with plasma densities comparable with topside ionospheric ion densities. Thus within the region of corotating field lines the low-energy plasma density should be high (~ 10^3 to 10^4 ions/cm^3) and this region is called the plasmasphere. Field lines taking part in the convective flow, however, periodically become 'open' allowing the escape of the thermal plasma and the setting up of supersonic flow from the ionosphere. This flow of plasma, mainly from the polar cap into the open tail field lines is termed the polar wind. When reconnection occurs in the tail, shocks are formed which, as above, propagate back to the ionosphere, but may not in fact reach it to terminate supersonic flow before the field line has moved towards the day side and become open again (the two time scales are comparable, Banks (1972)). Thus conditions for supersonic flow out of the ionosphere may exist at all latitudes above the plasmapause during extended periods of strong convection. The plasma density appropriate to the flow situation is very low compared to that of the plasmasphere, as

may be imagined from the fact that it takes several days for the equilibrium situation to be set up. For example, the polar wind density of the tail may be estimated from topside fluxes of order 10^7 to 10^8 ions/cm^2/sec as follows: Consider a tube of force of cross-sectional area A_I in the ionosphere, where the field magnitude is B_I, and of area A_T in the tail, with field strength B_T. Then we have

$$n_I v_I A_I = n_T v_T A_T \quad \text{and} \quad B_I A_I = B_T A_T$$

$$\text{or} \qquad n_T = \frac{(n_I v_I)}{v_T} \left(\frac{B_T}{B_I}\right) .$$

Since $B_T/B_I \simeq 10^3$ and $v_T \simeq 30$ to 40 km/sec (ε_p(bulk) ~ 10 eV) we find $n_T = 10^{-1}$ to 10^{-2}/cm^3 for topside fluxes (at 3000 km altitudes) of $(n_I v_I) \simeq 4 \times 10^7$ to 4×10^8 cm^2/sec. This, as far as is known, is the only continually present plasma component to exist on the open tail field lines, so that in our neutral sheet model of the magnetotail, we shall use plasma densities outside the current region of order 10^{-1} to 10^{-2}/cm^3 in numerical calculations.

Experimentally the plasmasphere and plasmapause were discovered by the study of the propagation of ducted whistler signals in the magnetosphere (Carpenter (1966)), but recently direct measurements have become possible. As expected, it is found that the plasmasphere is much larger during times of magnetic quiet (low convection electric field) than during disturbed times. Typically, the plasmapause moves in from $L \simeq 6$ for $K_p < 1$ (usually the boundary is not sharp during quiet times, because the outer regions are in the process of

being steadily filled), to $L \lesssim 3$ for $K_p \sim 4$ to 5. During such disturbed times the boundary is usually sharp with a drop of density from $\sim 10^3$ H^+ ions/cm^3 to ~ 0.1 cm^{-3} across it (Chappell et. al. (1970)). Simple theory (Fig. 2.9) suggests that the boundary should be rather local time dependent, being perhaps a factor two larger near dusk than near dawn, a trend noted by Carpenter, but not so far discussed in terms of the direct measurements. If the convection electric field increases (as during the growth phase) the region of closed drift paths becomes smaller, and the outer corotating field lines start to convect towards the day magnetopause, taking their high-density plasma with them. This leads to high-density plasma clouds becoming 'detached' from the plasmasphere, a process which establishes the new plasmapause position. Similarly, after a relaxation of the convection electric field, the region of closed drift-paths expands, and the newly corotating field lines start to fill with plasma. As this can take several days, a 'two-step' structure in the density profile is often observed, corresponding to the new and old plasmapause positions. (For examples of 'detached plasma' and 'two step profiles' see Harris et. al. (1970)).

Direct observations of plasma flow and associated topside density and ion composition changes above the plasmasphere latitude at 3000 km altitude have recently been obtained by Hoffman (1971). He observed fluxes of 3 to 5 x 10^8 ions/cm^2/sec from the winter pole and $\sim 5 \times 10^7$ ions/cm^2/sec from the summer, with speeds of $\sim$ 10 km/sec, thus confirming Banks and Holzer's results and our estimate of the tail number density.

Measurements in the tail of such low densities of very low energy (1 to 10 eV) particles is not at present possible, and until very recently only one report concerning the plasma of the high-latitude magnetotail had been published, presumably due to the background responses of most instruments, which are designed to detect higher fluxes of more energetic particles. Bame (1968) presented a sample spectrum obtained from a Vela satellite at a radial distance from Earth of 18 R_E. The calculated number densities for $E_e > 30$ eV, $E_p > 30$ eV were $n_e \leq 0.04\ cm^{-3}$ and $n_p \leq 0.2\ cm^{-3}$. Because of the poor statistics and unknown background counting rates (none were subtracted) these densities represent upper limits. In general it was stated that the indicated density (above 30 eV) was $\lesssim 0.1\ cm^{-3}$, with average energy < 100 eV for electrons and < 1 keV for protons. These particles, possibly of magnetosheath origin, have densities comparable with those expected from the low-energy polar wind, so that our original estimate of the density of particles in the open tail field lines is unaffected; their energies are low compared with the several tens of kilovolts expected across the tail and so may, to a first approximation, be treated as being 'cold', in the same way as the polar wind. It should be noted, however, that higher fluxes of more energetic plasma may exist at times in this region, as evidenced by the appearance of polar cap aurorae, although these, too, have received very little study. (Very recently Bame et. al. (1971) have reported the existance of a nearly monoenergetic stream of ions flowing outwards from the Earth in the high-latitude tail during magnetic storms. Typical energies lie in the range 300 eV to 3 keV, with ~ 10%

spread of energies about the mean, and fluxes are $\lesssim 10^5$ ions/cm^2/sec. Their density is thus typically less than 10^{-2} ions/cm^3. At the present time their detailed morphology and origins are unknown, and so will not be discussed further, except that it is interesting to note that mapping these fluxes back into the ionosphere gives fluxes of order 10^8 ions/cm^2/sec, similar to those of the polar wind).

While the high latitude magnetotail is thus a region of very low particle energy and density, a thick, hot slab of plasma (the plasma sheet), has been found to exist near the field minimum plane (Montgomery et. al. (1965)), over a wide range of distances from Earth $-10\ R_E \geq X \geq -60\ R_E$ (at least). Several authors have interpreted this as being due to the direct access of magnetosheath plasma near the B_{min} plane (Alfvén and Fälthammar (1971), Bird and Beard (1972), Atkinson (1972)), even though their spectra are rather different (though their mechanism of access may be energy dependent). However, it is also possible that the plasma sheet is produced in the small-angle wedge of the X-neutral field configuration by Speiser's acceleration mechanism acting on polar wind plasma (see Fig. 1.11), and such a model has been proposed by Holzer (1971). Since the particles constituting the radiation belts must come from the plasma sheet (convected inwards from the tail during substorms) this latter suggestion would imply that the whole of the magnetosphere's particle distribution is ionospheric in origin.

The majority of the information concerning the plasma sheet and its evolution during substorms has been obtained by the Los Alamos Vela series of satellites which have high

(60^{o}) inclination orbits with an almost constant radial distance of ~ 20 R_E. They thus cross the sheet basically in a north-south direction giving information on the density and energy profile with Z_{SM} at the given radial distance. Unfortunately they carry no magnetometers. During quiet times the particle population at $X \sim -20\ R_E$ at midnight is contained within ~ 8 R_E of the B_{min} plane (estimated from the formula of Russell and Brody (1967)) and has the following properties (Bame (1968)).

$$N \approx 0.5\ cm^{-3}\ (0.1 \text{ to } 3.0)\ ;\ \bar{\varepsilon}_e \approx 600\ eV\ (100\ eV \text{ to } 10\ keV)$$

$$\bar{\varepsilon}_p \approx 5\ keV\ (1 \text{ to } 20\ keV)$$

We note that the electron energy density is only 10% to 20% of that of the protons, although the electron distribution and its variations is most often used for plasma sheet studies. We also note that the typical energy densities of a few x 10^{-9} erg/cm^3, is equivalent to the pressure of a few x 10 γ magnetic field, so that a significant depression of the magnetic field (through the diamagnetic effect) is expected in the plasma sheet. This has been observed by Behannon (1970), Hruška and Hrušková (1970) and Fairfield and Ness (1970) in the radial distance range $x \sim -20\ R_E$ to $-40\ R_E$. Whether the plasma sheet represents the sole source of current-carrying plasma in the tail, in the sense that the magnetic field smoothly reverses over the 8 R_E thickness (as argued by Schindler (1971), Bird and Beard (1972)), or whether there is a region of strong current near the B_{min} plane causing a sharp reversal in the field, is presently being discussed.

Speiser and Ness (1967) reported the existence of such a current sheet at distances of - 16 to - 30 R_E, with thickness a few hundred to a few thousand km (< 1 R_E), while Mihalov et. al. (1970) interpret their data to show a current sheet of thickness a few tens to a few hundreds of km at $X \sim -60\ R_E$. Schindler and Ness (1971) claim, however, that these sharp changes in the magnetic field could be due to tearing mode noise near the B_{min} plane within a much thicker current sheet structure. It is interesting to note that Mihalov (1970), while finding the plasma sheet field depression in data obtained in the range $-20\ R_E \geq X_{SM} \geq -50\ R_E$, found none in samples obtained from $-50\ R_E \geq X_{SM} \geq -81\ R_E$. To date information does not exist on the radial gradients of the low energy plasma sheet particles; however, Meng (1971), using $E_e > 22$ keV and $E_e > 45$ keV electrons as plasma sheet markers (these form the high-energy (non-Maxwellian) tail of the plasmasheet distribution) found its existance over a broad region at $X \sim -60\ R_E$, although their fluxes were about a hundred times less than those at $X \sim -20\ R_E$ (i.e. peak fluxes ($\varepsilon_e > 45$ keV) of $\sim 2 \times 10^2$ $(cm^2\text{-sec-st})^{-1}$ at $X \simeq -60\ R_E$ compared with $\sim 10^4$ to 10^5 $(cm^2\text{-sec-st})^{-1}$ at $X \simeq -20\ R_E$ to $-30\ R_E$).

Early analyses of the observations of the plasma sheet behaviour associated with substorms at $X \sim -20\ R_E$, showed that the basic growth phase phenomenon was a 'plasma drop-out' i.e. a large decrease of particle density, coupled with a smaller decrease of particle average energy. Since the outer boundary of the plasma sheet is basically a density boundary this was interpreted as a 'thinning' (Hones et. al. (1967),

(1970)), a result which has been confirmed by simultaneous two-satellite studies (Hones et. al. (1971c)). (Fig. 2.10). No 'compression' effects are seen near the B_{min} plane (Fig. 2.11). Such changes must be related to the changing field configuration of the tail, and if Holzer's plasma sheet model is correct, it implies that either the angle of the closed-field wedge becomes smaller, or that the tail neutral line moves towards the Earth. Both effects would contribute to the large reduction of the northward field component across the tail lobes observed by Fairfield and Ness. From two-satellite studies the contraction speed is ~ 6 km/sec, and interpreted in terms of an $\underline{E} \wedge \underline{B}$ drift, gives ~ 50 kv across the tail. The process may continue for several tens of minutes after breakup, although the literature on this aspect is rather confused, due to difficulties in defining the onset time of substorm expansion with limited ground data.

The plasma sheet has a well-defined inner edge when observed in several hundred electronvolt electrons (the major constituent of the electron plasma sheet), which appears as a rapid drop in electron temperature (not in density) as one moves earthwards across the (presumably roughly field-line aligned) boundary. The first observations were presented by Vasyliunas (1968a,b), but the detailed energy spectral change were not available until the work of Schield and Frank (1970). According to the latter authors the boundary is approximately one R_E thick across which $\bar{\epsilon}_e$ changes from 2 to 5 keV in the plasma sheet to ~ 500 to 800 eV in the outer zone, with little change in particle density (~ 2 cm^{-3}). It is located between X ~ - 6 R_E to - 9 R_E in the noon-midnight meridian (local

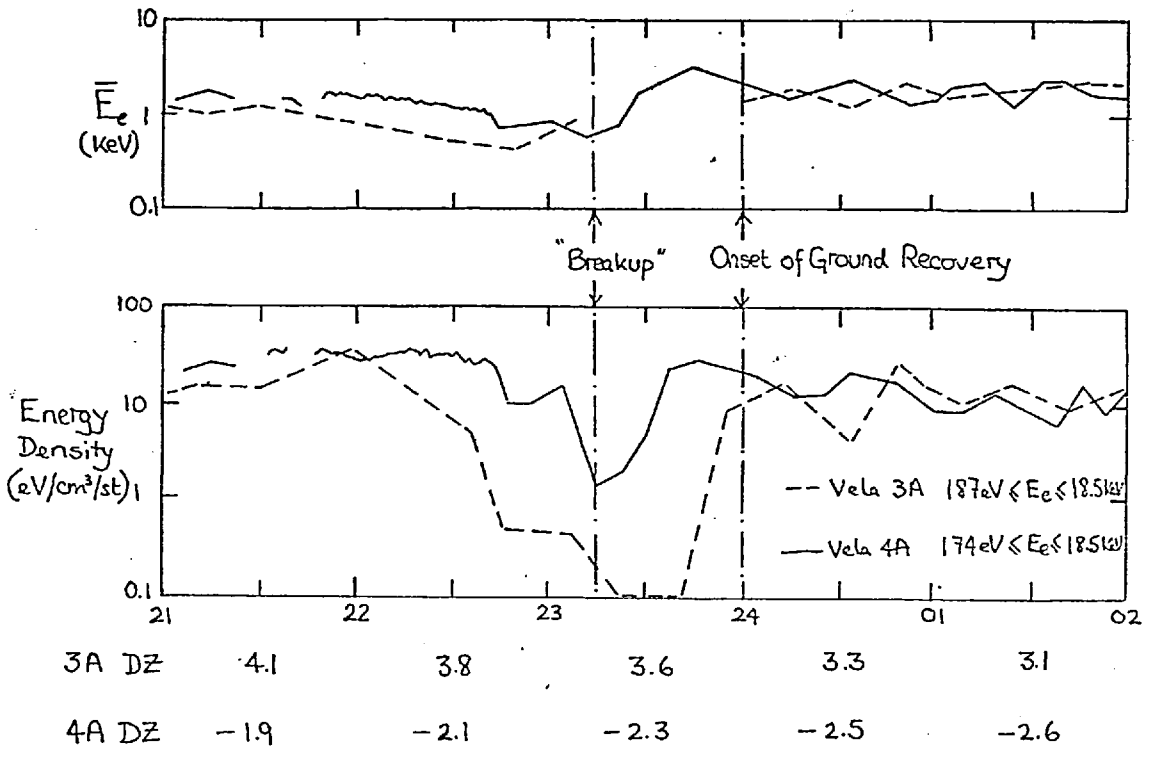

Figure 2.10: Ground magnetogram and concurrent plasma sheet electron data from a pair of Vela satellites (Hones et. al. (1971(b)). The plasma sheet 'drop-out', seen mainly as a decrease in plasma density, occurs for a period of about an hour prior to the expansion phase onset as shown in the magnetometer record. Note that the satellite furthest from the estimated position neutral sheet (as given by DZ) sees the longer-lasting and deeper 'drop out'. Plasma sheet recovery starts shortly after expansive phase onset.

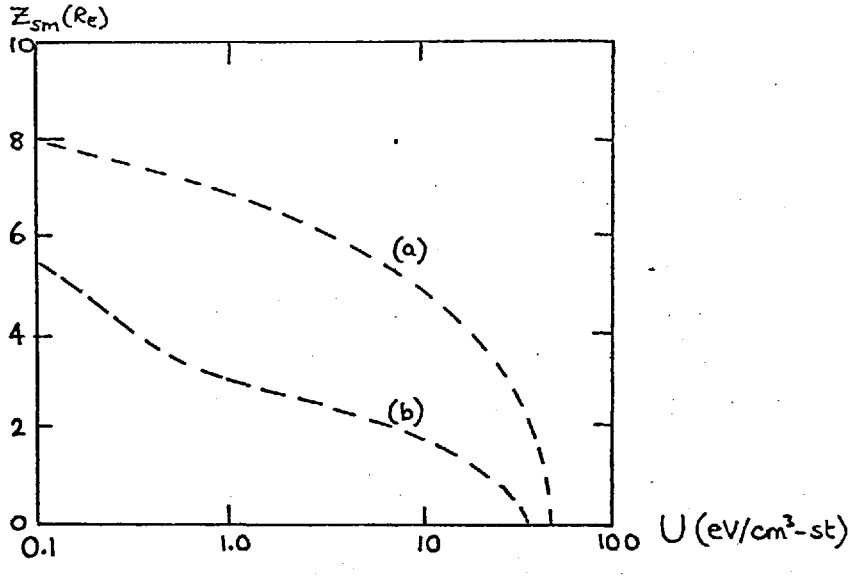

Figure 2.11: Plasma sheet electron energy density U(eV/cm^3-st) as a function of estimated distance from the neutral sheet, for (a) pre drop-out and recovery configurations, and (b) at the maximum epoch of thinning (Hones et. al. (1971c)).

time variations are shown in the work of Vasyliunas), separated by 1 to 3 R_E from the plasmapause. The region between the plasmasphere and the inner edge of the plasma sheet is termed the 'electron trough'. Note that the average plasma sheet electron energies at the inner edge are a factor ~ 5 times those observed at X ~ - 20 R_E, as may be expected from the increase in magnetic field strength and decrease of field-line length. Such observations can only be made as a 'snapshot' by a satellite in a highly eccentric orbit passing radially through the region. However, such 'snapshots' can only be made twice per orbit, and orbital periods are generally a couple of days. Thus inward motions of the boundary, as expected for enhanced convection, as a function of substorm phase are impossible to measure by such means. However, during substorm activity the inner edge is found much closer to the Earth, and also closer to the contracted plasmapause (L = 3 to 4), as reported by both Schield and Frank, and Vasyliunas.

The structure of the proton inner edge has not received such detailed study, but during quiet times it seems to be continuous from the plasmasheet, through the electron trough up to the plasmapause, inside which it decays away over a scale length of ~ 1 R_E. During periods of strong convection (e.g. world-wide magnetic storms) a similar situation is observed, but the inner edge lies just outside the plasmasphere (Russell and Thorne (1970) , using the proton data of Frank (1971) and plasmasphere data of Taylor et. al. (1968)).

These results can be interpreted in terms of convec-

tive particle drift from the tail (given a plasma sheet distribution at X ~ - 20 R_E), using the results obtained by Kavanagh et. al. (1968), Kennel (1969) and Wolfe (1970). In the same way as the plasmapause represents the boundary of a 'forbidden' zone for low energy particles convecting inwards from the tail (Fig. 2.9), 'forbidden zones' occur for higher energy particles drifting in from the tail with fixed μ and J. The results of Kavanagh et. al. (1968) show that these forbidden zones become larger with increase of particle tail energy, leading to rapid drops in plasma temperature as one moves earthwards, and the plasmasphere always lies within them, in agreement with the observations of Schield and Frank, and Russell and Thorne (for the strong convection case). The forbidden zone for protons of given tail energy generally lies closer to the Earth than that of the electrons of the same energy. Kennel (1969) considered the effect of precipitation of plasma sheet particles in the strong diffusion limit on inwardly convecting flux tubes, arguing that when the loss time for particles becomes equal to a scale time for the flow, then the tube rapidly becomes depleted of particles. The process is again energy dependent, high-energy particles precipitating first, such that the observed electron temperature boundary will be formed. With increasing convective speeds the particles penetrate further before becoming lost, such that the inner boundary moves towards the Earth. His results indicate that the inner plasma sheet edge for electrons is such a precipitation boundary, where particles of given energy become lost before their forbidden zone is reached, while protons of plasma sheet energies can move much further in, so that their inner edge may be a flow (forbidden-zone) boundary and consequently much closer to the plasmasphere.

Wolfe (1970), in addition to considering how magnetospheric flow is modified by the presence of a conducting ionosphere, suggested that the shape of the inner boundary of the electron plasma sheet observed by Vasyliunas could be accounted for by a combination of the forbidden zone and precipitation models, as shown in Fig. 2.12.

These models are not self-consistent, however, because the question of the space charge of convecting protons within the electron flow/precipitation boundary has not been considered. However, if Schield and Frank's electron trough is such a region, then it is clear that the proton space charge is neutralized, by ~ 100 eV electrons (see Fig. 2.13) presumably originating in the ionosphere. (Since we are outside the plasmasphere, the ambient density of thermal (ionospheric) particles is $\lesssim 0.1$ cm^{-3}, compared with observed electron trough densities (90 eV to 50 keV) of 1 to 2 cm^{-3}).

In addition to 'snapshots' of the radial profiles of particles, information has also been obtained at a fixed radial distance by satellites in circular orbits (mainly the geostationary distance 6.6 R_E). During the quiet times 6.6 R_E is generally located within, or near, the plasmapause, and hence outside the plasma sheet. With increasing convection electric fields, this boundary, which is energy dependent, moves across the spacecraft as the flow/precipitation boundaries contract towards the Earth. Such events occur in one to one correspondence with substorms (De Forest and McIlwain (1971)), but the latter authors claim that their results are consistent with an increase of fluxes starting at the substorm expansion phase. This is difficult to understand if strong

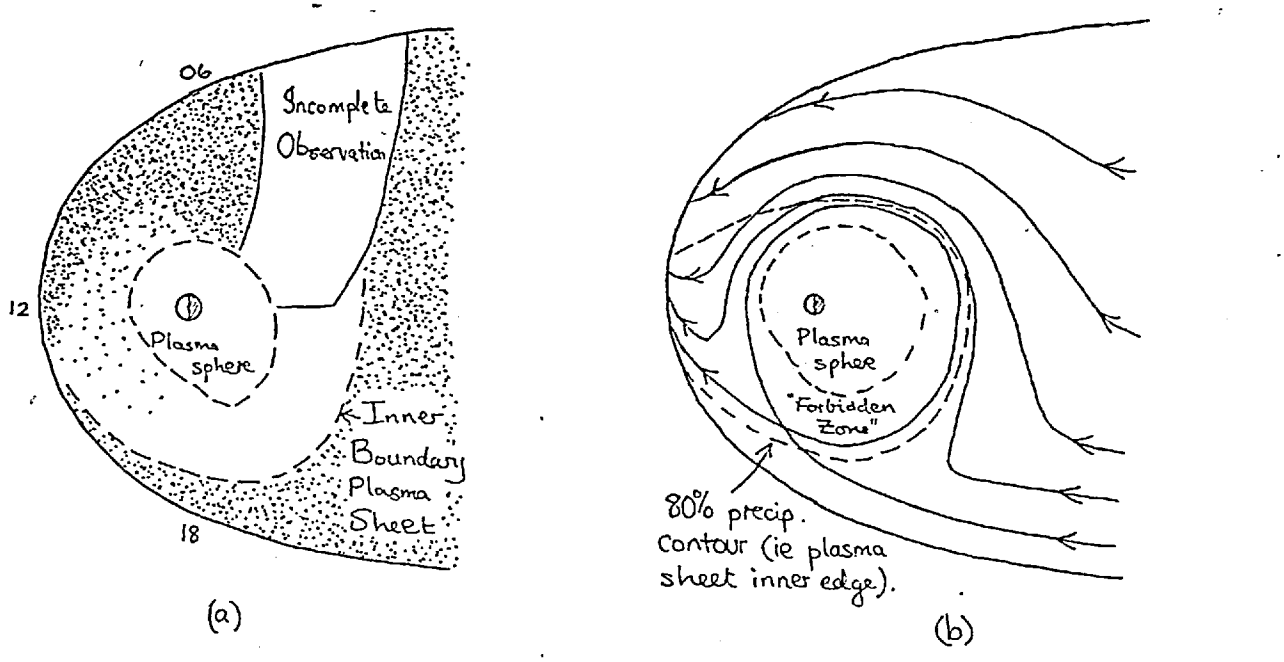

Figure 2.12: (a) The local-time dependence of the inner boundary of the plasma sheet electron fluxes (Vasyliunas (1968a,b)).

(b) Schematic drift-paths of plasma-sheet electrons in the magnetic equatorial plane, and the 80% precipitation contour (for strong pitch-angle scattering), showing how Vasyliunas' local-time dependence may be set up. (Simplified from the work of Wolfe (1970)).

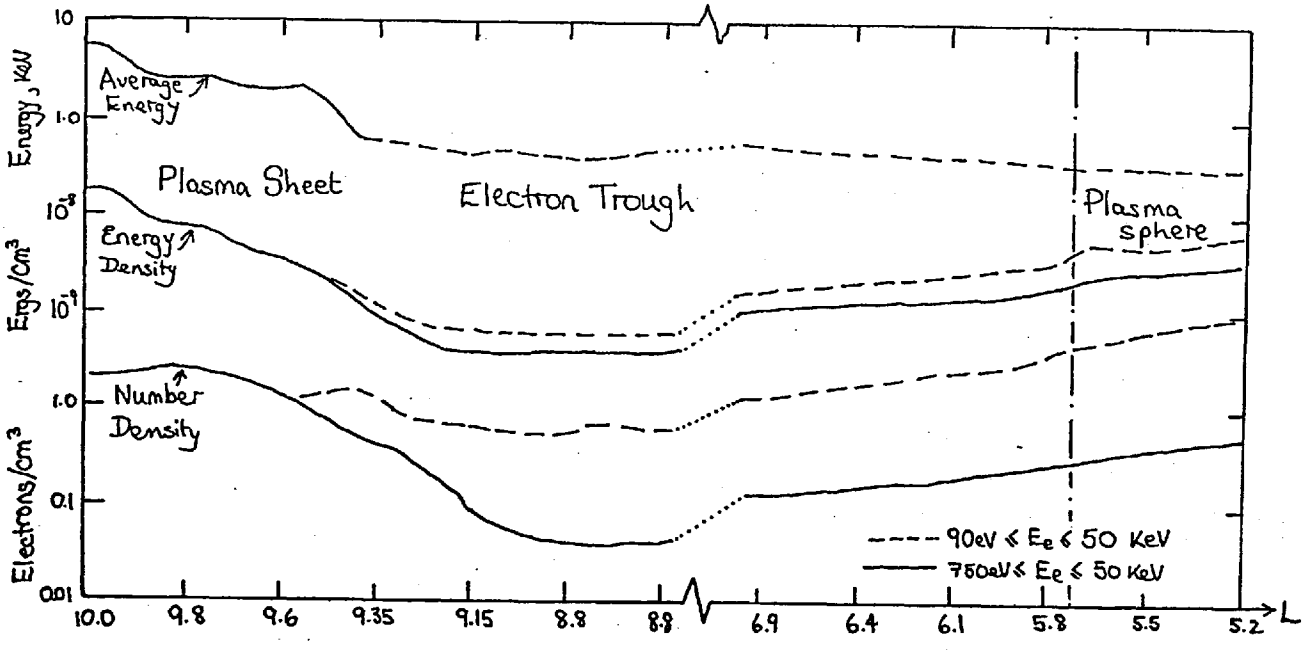

Figure 2.13: The variation in electron energy density and number density on a radial pass through the plasma sheet, electron trough and into the plasmasphere. (Schield and Frank (1970)). It can be seen that the 750 eV $\leq E_e \leq$ 50 keV number density falls rapidly at the plasma sheet inner boundary, but that charge neutrality is maintained by the 90 eV $\leq E_e \leq$ 700 eV particles.

convection takes place for ~ 1 hour preceding the expansion, but it may be noted that the Earthward convection speed at 6.6 R_E is ~ 1.5 R_E/hour such that the plasma sheet particles may only reach 6.6 R_E from their old location after an hour of strong convection. The lower energy particles, whose boundary is not far removed from the synchronous altitude according to Schield and Frank, should, however increase steadily during the growth phase. Such observations have not been noted by De Forest and McIlwain (1971), but have been reported by Shelley et. al. (1971) at the same altitude; measuring electrons (0.5 to 50 keV) they found that lower energy particle enhancements occurred before those of higher energy, the increases starting ~ 1 hour before a substorm expansion (i.e. during the growth phase).

Having reviewed the observations of magnetic field and particle populations and their temporal evolution into a strongly convecting state, we shall now consider briefly those effects associated with substorm expansion and recovery. To recapitulate, by the time expansion starts, the interplanetary field has been southwards for ~ 30 minutes to 1 hour (Arnoldy, (1971)), DP-2 currents are well-established (Nishida (1968a,b), Oguti (1969)), the tail current system is enhanced (Cummings et. al. (1968), Fairfield and Ness (1970)), the plasma sheet thinned (Hones et. al. (1971b,c)) and its inner boundary is being detected at ATS altitudes (i.e. 6.6 R_E) (Shelley et. al. (1971)), all processes qualitatively, and to some extent quantitatively understood in terms of the picture of strong convection set up by dayside merging. In the night-time auroral zone the quiet arcs have been drifting equatorwards

from $\Lambda \sim 70^{\circ}$ reaching $\Lambda \sim 65^{\circ}$ under the influence of a ~ 30 mV/m westward electric field (Kelley et. al. (1971), Mozer (1971)). Then, rather suddenly (over a minute or two) the arcs near the equatorward edge brighten and move rapidly northwards, varying in shape and intensity. The arcs become broken up, resulting in rapidly moving patches and irregularly folded pulsating bands moving eastwards. The area of activity expands westwards (as a surge along the quiet arcs) and eastwards (reaching past the dawn-dusk meridian after 10 or 20 minutes), as well as to the north; the general 'glow' becomes enhanced and active aurorae fill the whole sky in the nightside oval. The westward electrojet, producing negative bays in the H component, occurs over the region swept by the auroral bulge; the equivalent current system of an electrojet (DP-1) current system is shown in Fig. 2.5, indicating intense westward currents flowing in the nightside oval. After perhaps an hour the electrojet dies away, active aurorae fade and quiet arcs reform at high latitudes (see Hultqvist (1969), p. 145-146, for more details of ground observations and references).

Balloon-bourne electric field detectors in the auroral zone indicate that the ~ 30 mV/m westward electric field characterizing the growth phase remains during the expansion. Thus the northward motion of aurorae during the expansion does not imply $\underline{E} \wedge \underline{B}$ drift in an eastward electric field. However, the onset of the negative bay is coincident with the appearance of a large southward directed electric field of magnitude 20 to 100 mV/m (Mozer and Manka (1971), Mozer (1971)), which is consistent with the eastward motion of the broken up

arcs mentioned above (velocities ~ 500 to 1000 m/sec), (Kelley et. al. (1971)). Thus the westward electrojet is thought to represent the effect of the southward electric field in the Hall-conducting nightside oval.

In the magnetosphere, the tail current system declines in strength over a time scale of 30 min to 1 hour, if observed in the high-latitude magnetotail (uncontaminated with plasma sheet effects), and as a result the field in the tail and outer zone become more 'dipole like' (Fairfield and Ness (1970), Cummings et. al. (1968)). Specifically, the tail field magnitude drops, while the north-south component increases (Fig. 2.8). Nearer the B_{min} plane the field both rises more quickly during the growth phase and declines more quickly during recovery due to the contraction and subsequent expansion of the plasma sheet. Within the sheet B_x is much depressed, and the increased B_z is often the major field component. Multiple neutral sheet crossings (i.e. reversals of the minor B_x component) are often seen following sheet expansion (and during very quiet times), even as much as ~ 5 R_E from its estimated position. It is unlikely that any thin current layer exists at such times, a situation contrasting with that of the growth phase, when multiple crossings are not seen, usually only a single clear field reversal within the thinned plasma sheet. As expected, the field magnitude at 6.6 R_E in the outer zone increases, though these effects can sometimes be complicated by the current set up by the energized plasma sheet particles near the Earth (the ring current). The continuity of these signatures in the magnetic field has recently been shown by Russell et. al. (1971), who observed field changes due to four weak substorms while OGO-5

moved in from $X \simeq -18\ R_E$ to $X \simeq -6.5\ R_E$. They observed the 'tail' signature as close in as $\sim -9\ R_E$, where the field had been enhanced over that of a dipole during the growth phase. However, a 'recovery' observed 0.5 R_E closer to the Earth on the same pass, where the field had been depressed w.r.t. the dipolar field was accompanied by a field increase, as is the case at 6.6 R_E.

Observations of the plasma sheet recovery was initiated by Hones et. al. (1967), and continued by Hones et. al. (1970), (1971b,c). Briefly, the expansion starts (perhaps) some minutes after the breakup on the ground, and proceeds in the Z_{SM}direction with speeds in the range 5 to 20 km/sec (Hones et. al. (1971c). (See Fig. 2.10). Since the sheet expands by say $\sim 6\ R_E$, this takes some 30 min to 2 hours. Clearly, observations depend critically on distance from the B_{min} plane. Some information on the radial propagation of the expansion has been presented by Meng et. al. (1970) and Akasofu et. al. (1970), where examples include an expansion observed at Vela ($X_{SM} = -19\ R_E$, $Z_{SM} = -4.6\ R_E$) occurring half an hour after that at Imp 3 ($X_{SM} = -32 R_E$, $Z_{SM} = 0.2\ R_E$). Such results indicate that the expansion must start throughout the range $X_{SM} \simeq -20$ to $-30 R_E$ in a time short compared with 30 min.

It has been suggested in several of Hones' papers that the plasma sheet expansion is directly related to the northward expansion of the auroral bulge. He also showed (Hones et. al. (1971a)) that neither quiet nor post-breakup auroral particle spectra show any resemblance to plasma sheet spectra, the auroral particles having more flux at higher energies. Thus while the two may be related, individual

details should not be expected to correspond, although such a comparison has recently been carried out, with inconclusive results, by Akasofu et. al. (1971).

The northward expansion of the aurorae and the tail field changes are indicative of very rapid merging in the tail, but electric field and convection declines during the recovery phase by which time the period of southward interplanetary field is usually over. The particles which have been driven deep into the outer zone by strong convection thus find themselves within the new forbidden zones, and thus simply circulate about the Earth. Since the strong convection period lasts for only a fraction of the drift period around the Earth (for lowish energy particles), this results in a drifting plasma cloud which disperses as time goes on (the magnetic drifts are energy dependent), as has been shown by the results of De Forest and McIlwain (1971) from the ATS-5 satellite. Typical electron densities are 5 to 10 cm^{-3} during the substorm (50 eV to 50 keV), but this seems to decline fairly rapidly, down to 1 to 0.1 after several hours (reforming the electron trough). Proton densities are not so variable, indicating that charge neutrality is maintained by $\varepsilon_e < 50$ eV electrons. These protons, inside the (topological) plasma pause, form the 'quiet-time ring current', which has a decay time of a few days (Frank and Owens (1970)). The distribution seems to be 'mopped up' as the plasmapause move out (as it fills), on a time scale of days (Fig. 2.14), (Russell and Thorne (1970)). This accounts for the quiet time observations of a proton population ~ 1 R_E inside the plasmasphere.

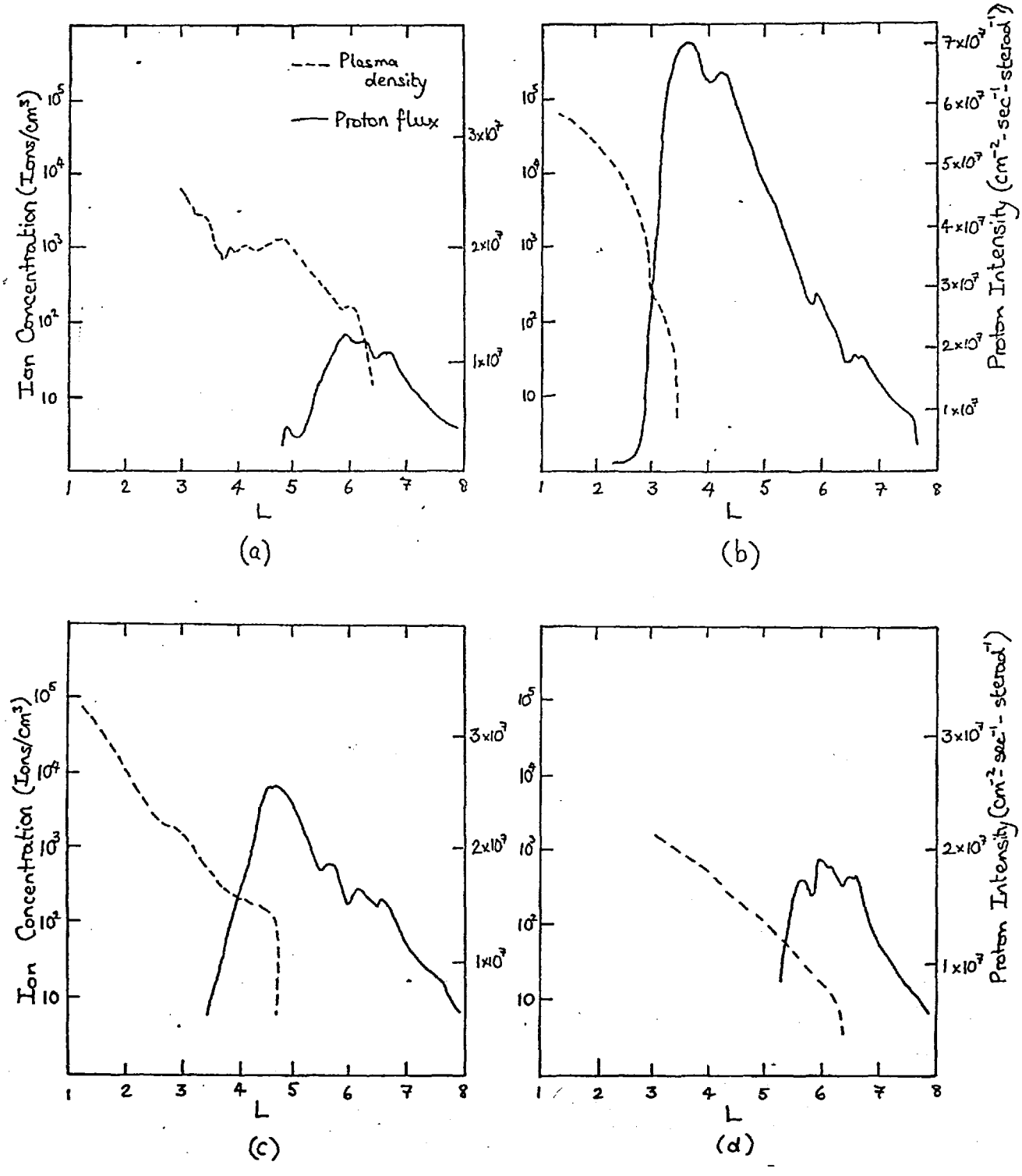

Figure 2.14: The relative distributions of thermal ion concentration (plasmasphere) and 31 keV $\leq E_p \leq$ 49 keV proton ring-current fluxes for (a) pre-storm, (b) world-wide storm main-phase (c) recovery phase, and (d) post-storm. It can be seen that the protons moved to low L-shells during periods of enhanced convection are depleted in step with the expanding (filling) plasmasphere. (Russel and Thorne (1970)).

It has been postulated by Cornwall et. al. (1971) that the energy of the proton distribution is dissipated by wave particle processes (cyclotron resonance) which operate only at sufficiently high ambient plasma density (i.e. when the plasmasphere has filled to a given n at a given L). The wave-energy is fed to the ionosphere by low energy electrons, and gives rise to the sub-auroral red (SAR) arcs. Though one might have expected some (small) discontinuity between the decaying quiet time ring current distribution with the plasmasphere and the protons forming the new flow inner boundary of the plasma sheet just outside the plasmasphere, none has been noted in the literature, and none is very evident in the published data.

As we commented at a very early stage, magnetospheric particles with energies above several tens of kilovolts cannot be produced by convective energization of ionospheric plasma, and so may be expected to show rather different behaviour from particles of lower energy, due to their different origins. Such electrons can conveniently be measured (as is usually done) by Geiger-Muller tubes sensitive to energies above ~ 45 keV. Significant fluxes of them can be found in the plasma sheet, where they represent the high-energy (non-Maxwellian) tail of the energy distribution, but it is found that their fluxes increase by several orders of magnitude (2 to 3) as one moves earthward across the electron inner boundary of the plasmasheet. (Frank (1967a), Schield and Frank (1970) (Fig. 2.15). The formation of the two features by strong diffusion of particles appears intimately related. After production, their motion will be dominated by magnetic drifts, and the magnetic field model of Fairfield (1968b) indicates that

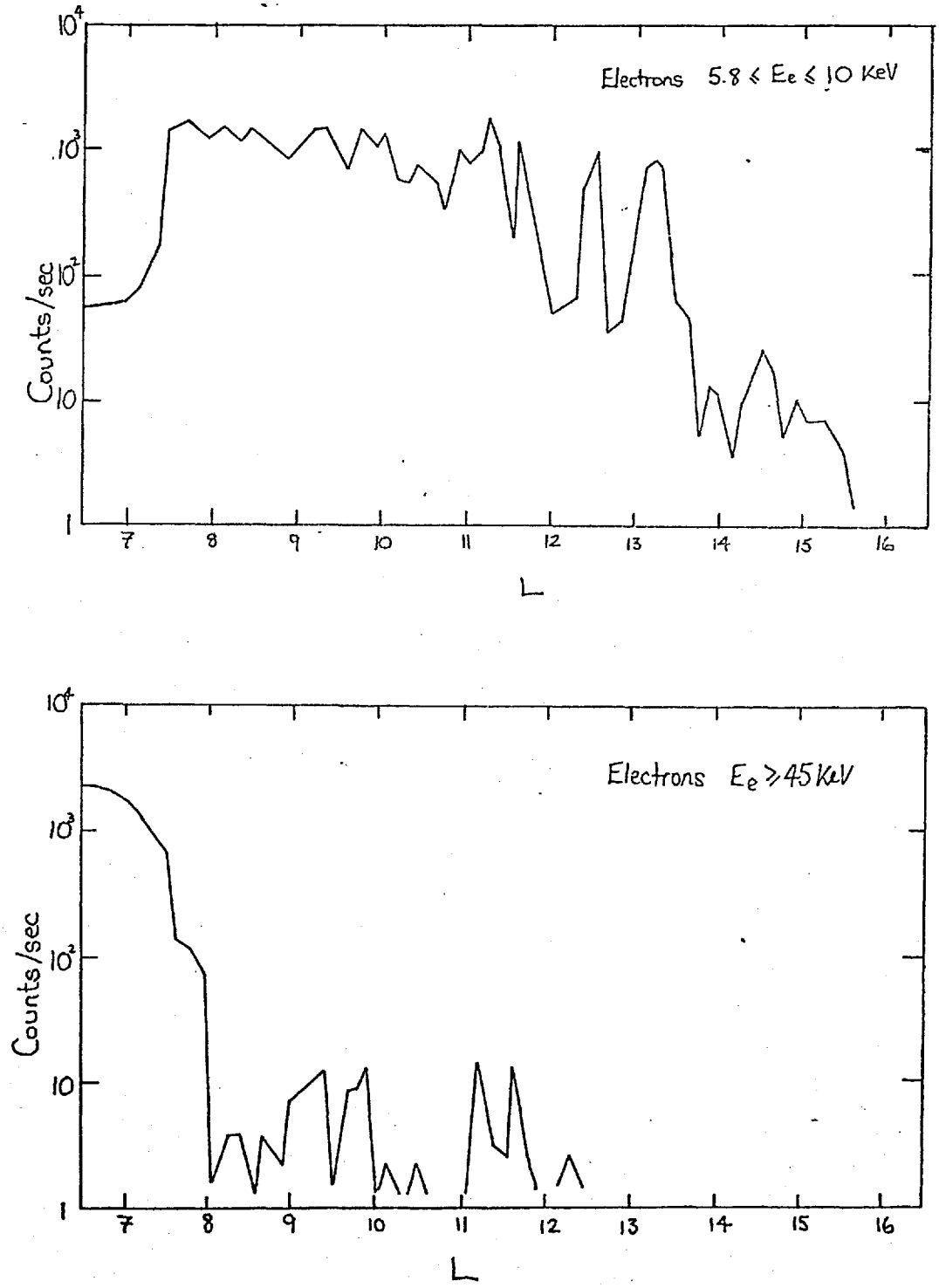

Figure 2.15: The inner edge of the electron plasma sheet as seen in 5.8 ≤ E_e ≤ 10 keV particles, correlates with the region where a three order-of-magnitude increase is seen in the fluxes of E_e > 45 keV electrons (Frank (1967(a))).

only those particles produced within $L \lesssim 7\ R_E$ near the midnight meridian will be able to execute a complete drift around the Earth without intersecting the magnetopause at dawn. During the strong convection periods associated with substorms we find, as expected, that these particles are produced in the region swept out by the inward moving inner plasma sheet boundary. It appears from the results of Pfitzer and Winckler (1969) that such particles are continuously generated in the region between (at least) 5 to 8 R_E from the Earth for about an hour during the substorm. Such generation occurs in one to one correspondence with substorms, and as with the low-energy particles, results in 'clouds' which drift around the Earth from the midnight sector, being observed at successively later times (from storm onset) at 6.6 R_E as the satellite moves from midnight through dawn to the dayside; the delay corresponding to the appropriate fraction of the drift period. These clouds can sometimes be seen on the second lap, but now dispersed and attenuated by precipitation (Arnoldy and Chan (1969), Lezniak and Winckler (1970)). This population of high-energy electrons is apparently much more stable than the low-energy particles, decaying away over a time period of several days (Owens and Frank (1968)) presumably by cyclotron scattering and radial diffusion; it clearly exists quite happily within the plasmasphere while the quiet time ring current protons are being depleted (Russell and Thorne (1970)).

We would now like briefly to relate this discussion of the particle morphology in the magnetosphere to the observation made by low-altitude polar orbiting satellites and

ground data obtained primarily during the night hours. At all local times two distinct electron precipitation zones occur at low altitudes, 'soft' and 'hard', the soft zone at higher latitudes, the latitude of the boundary between them being a function of local time (Burch (1968), Hoffman (1972)). Due to the crude nature of these particle experiments (two or three point energy spectra) this classification cannot be made more precise; high resolution spectra are not yet available. As has already been discussed, the dayside soft zone ($\Lambda \sim 75^{o}$ to 82^{o}) can be identified with magnetosheath plasma entering via the dayside polar cusp. The nightside soft zone at midnight is found between the latitudes of 68^{o} and 77^{o} (Hoffman (1972)). The photometric measurements of Eather and Mende (1971) have also detected this band of precipitation, and find it to be produced by an influx of 0.1 erg/cm^2-sec, consisting of ~ 500 eV electrons, with insignificant proton fluxes, between $\Lambda \sim 71^{o}$ to 79^{o} during quiet times. It is tempting to identify this region with the plasma sheet ($\bar{\varepsilon}_e \sim 600$ eV), and this identification is supported by the magnetic models of Fairfield and Ness (1970) who show the plasma sheet mapping into $\Lambda \simeq 70^{o}$ to 76^{o} during quiet times. Furthermore, an isotropic pitch-angle distribution of plasma sheet particles produces electron energy fluxes of ~ 0.3 erg/cm^2, and proton energy fluxes of ~ 0.2 erg/cm^2/sec. While the electron fluxes agree quite well with Eather and Mende's observations, the lack of observed protons indicates that these particles have a loss cone in their distribution. Thus noise within the plasma sheet may be sufficient to isotropize the electrons (strong diffusion) but not the protons

(weak diffusion).

Both day and night 'hard' zones (as identified by large fluxes of ~ 10 keV electrons) are then associated with the high energy electrons (10 keV to 10^3 keV) produced and injected into the outer radiation zone during substorms. The latitudinal extent given by Hoffman (1972) is 64° to 69° at midnight (L = 5 to 8) and 68° to 75° at noon. This precipitation is associated with a sub auroral-zone latitude, unstructured subvisual glow, known as the 'mantle aurorae'. In addition, because of the appreciable numbers of ε_e > 10 keV electrons present, there is appreciable penetration of the ionosphere down into the D-region. Following the injection of a cloud of such particles the ionization and absorption of that region is increased, whence riometers measuring galactic (or cosmic) radio noise see a decrease in signal strength. Such CNA (cosmic noise absorption) events can be used to study the progress of the energetic electron clouds of the hard zone as they move around from midnight on the morning side following substorms. The 'hard zone' boundaries are, however, easily detectable at low altitudes from ε_e > 40 keV GM-tube electron data. McDiarmid and Burrows (1968) found that the smooth flux profile at low latitudes suddenly begins to change rapidly in slope and intensity on moving to higher latitudes (the 'smooth' boundary, Λ_S ~ 65° at midnight), and then rapidly decreases by several orders of magnitude (the 'background' boundary, Λ_B ~ 70° at midnight) (Fig. 2.16). The interpretation in terms of Λ_B mapping into the inner edge of the electron plasma sheet is clear, with the 'smooth' boundary associated with the lowest latitude of substorm par-

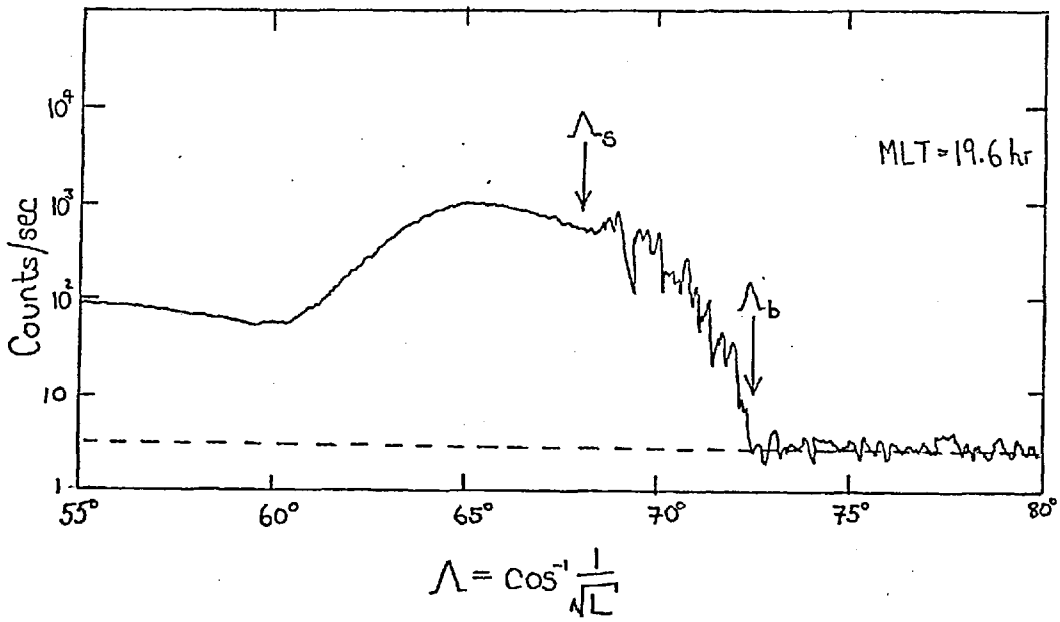

Figure 2.16: Typical latitudinal variation of fluxes of E_e > 35 keV electrons at low altitude, showing the 'smooth' (Λ_s) and 'background' boundaries (Λ_b). The background boundary should map into the ~ 10 keV inner boundary of the plasma sheet. (McDiarmid and Burrows (1968)).

ticles recently directly injected into the outer zone. The smoothly varying fluxes at lower L-shells are presumably the result of radial diffusion over many successive storms and substorms. Fritz (1968, 1970) has confirmed these results, using quiet-time data only, and also found that on the night and morning sides the region between the smooth and background boundaries is characterized by isotropic particle fluxes, though this only indicates that the loss-cone in space is isotropic (maybe produced by an ionospheric effect) not that the whole distribution is isotropic.

The motion of these boundaries during substorm activity has been studied by Rao (1969a,b). He found that the high-latitude boundary ($\Lambda \sim 68^{o}$) did not move during a substorm prior to recovery, but that (effectively) the region between the background and smooth boundaries widened to lower latitudes (down to $\sim 60^{o}$), and inside this region the flux levels were much enhanced (by 1 to 2 orders of magnitude). This is consistent with the magnetospheric measurements of the inward convecting plasma sheet producing such particles over a wide range of L (5 to 8, corresponding to $\Lambda \simeq 64^{o}$ to 69^{o}). During recovery the fluxes extend to higher latitudes. It would seem fairly easy to identify (roughly) the region of origin of the nightside quiet arcs by using optical data concurrent with low-altitude $E_e > 45$ keV electron measurements, used as a marker of the inner edge of the electron plasma sheet. McDiarmid and Burrows (1968) compared their Λ_B and Λ_S values as functions of local time with the average auroral zone of Feldstein (1966); this approach is unsatisfactory, however, because of the wide range of latitudes over which

the quiet arcs can be found, depending on the convection rate.

In this section we have reviewed in detail the interpretation of magnetospheric particle distributions and field configuration in terms of the reconnection model of the magnetosphere. Strong uniform convection occurs during the substorm growth phase, leading to the particle and field changes discussed. Indeed, the entire population of low-energy particles and their temporal behaviour can be (at least) qualitatively understood within the framework of the model. However, the substorm expansion phase cannot be explained in terms of uniform convection, and at present there exists no widely accepted interpretation. Strong convection must still be involved, but the detailed flow is different from that of the growth phase. Using the results of the next three chapters, a possible explanation will be attempted in Chapter 6.

(iv) Applicability of the Straight Field-Line Model of Alfvén

The discussion concerning this section centers on the importance of the component of the magnetic field normal to the current sheet in determining its physical properties. We recall from Chapter 1 that (from the results of Speiser, 1965, 1968) low energy particles drifting into the current sheet under the action of the convection electric field become trapped about the neutral line and accelerated along it. For no normal field (i.e. straight field lines) the particles are accelerated indefinitely along it, eventually being lost at the dusk and dawn boundaries of the tail, into the magnetosheath. Including a weak normal component of magnetic field now causes the particles to turn around in the sheet as they accelerate. Protons and electrons are turned towards the Earth if the field is directed

northwards, and they turn until moving perpendicular to the electric field and 'looking' straight down a field line emerging from the sheet. They then leave the field reversal region, moving out along the field line towards the Earth, with very small pitch angle (a few degrees) in the Earth's frame (Speiser, 1965). For our model to be valid, therefore, the perpendicular magnetic field must be small enough so that particles do not turn around and leave the sheet before they have travelled across the tail and have been lost from the sides. It was shown in Chapter 1, under the assumption of a uniform electric field E_o and polar wind flow velocity in the tail negligible compared with the convection velocity that the distance travelled across the tail in the current sheet is, for particles of mass m_j

$$Y_j = \frac{2\, m_j\, c^2\, E_o}{e\, B_\perp^2} ,$$

and that the electric field is given by

$$E_o = \frac{B_x^2}{4\pi N_o e (Y_p + Y_e)} \quad \text{for} \quad Y_p << d \quad \text{and} \quad Y_e << d$$

$$E_o = \frac{B_x^2}{4\pi N_o e d} \quad \text{for} \quad Y_p > d \quad \text{and} \quad Y_e > d.$$

In the latter case $Y_j = \frac{m_j c^2}{2\pi N_o e^2 d} \left(\frac{B_x}{B_z}\right)^2$

and for consistency $(Y_j > d)$ we require

$$B_z < \left(\frac{m_j c^2}{2\pi N_o e^2 d^2} \right)^{\frac{1}{2}} B_x .$$

The maximum values of B_z for the values of N_o typical of the high-latitude magnetotail (last section) are shown below. B_x has been given the nominal value of 10 γ, but we note that B_x varies from ~ 20 γ at quiet times up to ~ 40 γ during storm

times in the near-Earth tail.

	$N_o = 0.1$ cm^{-3}	$N_o = 0.01$ cm^{-3}
Electron	0.001 γ	0.003 γ
Proton	0.04 γ	0.12 γ

In the region of the tail where the particles are turned onto the field lines towards the Earth (within the small-angled wedge of the X-neutral field configuration), we form the plasma sheet, according to Holzer (1971). Thus the straight-field line model is not expected to throw any light on this aspect of the tail phenomena, and plasma sheet parameters are not appropriate for substitution into our numerical calculations. The plasma parameters to be considered should be those of the high-latitude magnetotail as have been used here, and discussed in the preceeding section.

Observationally, the perpendicular field component is usually northward pointing within the lunar distance ($X > -60\ R_E$, the region of extensive satellite mapping), but is highly variable at a fixed distance from Earth due to substorm effects previously discussed. During quiet times following substorms the northward field is the major component inside the expanded plasma sheet, and can be 5 γ to 10 γ in magnitude. 'Field reversals' in the minor B_X component then only correspond to a 'wobbling' of the field about the Z-axis, and lead to 'multiple sheet crossings', as defined by the ϕ_{SM} angle of the field. During such periods the models of Schindler (1971) and Bird and Beard (1972) may be of relevance (i.e. a thick

current sheet, with no enhancements near the B_{min} plane). During the growth phase and outside of the thinned plasma sheet the normal field is small, generally less than 1 γ, with almost equal positive and negative excursions (see Fig.2.17, taken from Fairfield and Ness (1970)), presumably due to 'wobbling' of the field about the X-axis. Inside the growth phase plasma sheet, B_X is the dominant component, with $B_Z \lesssim 1\ \gamma$ and generally northwards; there also exists a current enhancement near the B_{min} plane at such times (see the field reversal at ~ 06:21 hrs in Fig. 2.17), as must be the case if the tail current system is enhanced while the plasma sheet thins without compression. For such situations the model discussed by Eastwood (1971) may be valid, where the majority of the current is supplied in a thin sheet by the acceleration of polar wind plasma flowing into the tail (similar to the straight-field-line model). The above comments are relevant to the radial distance range X_{SM} ~ - 20 to - 40 R_E; at and beyond the lunar distance the incidence of southward directed fields at the B_{min} plane increases as expected for a reconnecting tail. Mihalov et. al. (1970) found that out of the 60 sheet clear crossings they analysed, 4 had $B_Z < -0.5\ \gamma$, 16 had $B_Z > 0.5\ \gamma$, but the majority were within one digitization window ($\pm$ 0.25 γ) of zero.

Thus, although our model will only be valid for extremely weak B_Z (< 0.001 γ, such that electrons can travel across the width of the tail in the current sheet and be lost from the sides), it appears possible, in view of the measured values of B_Z, that protons may be accelerated across the whole sheet width without turning out of the sheet as close in as

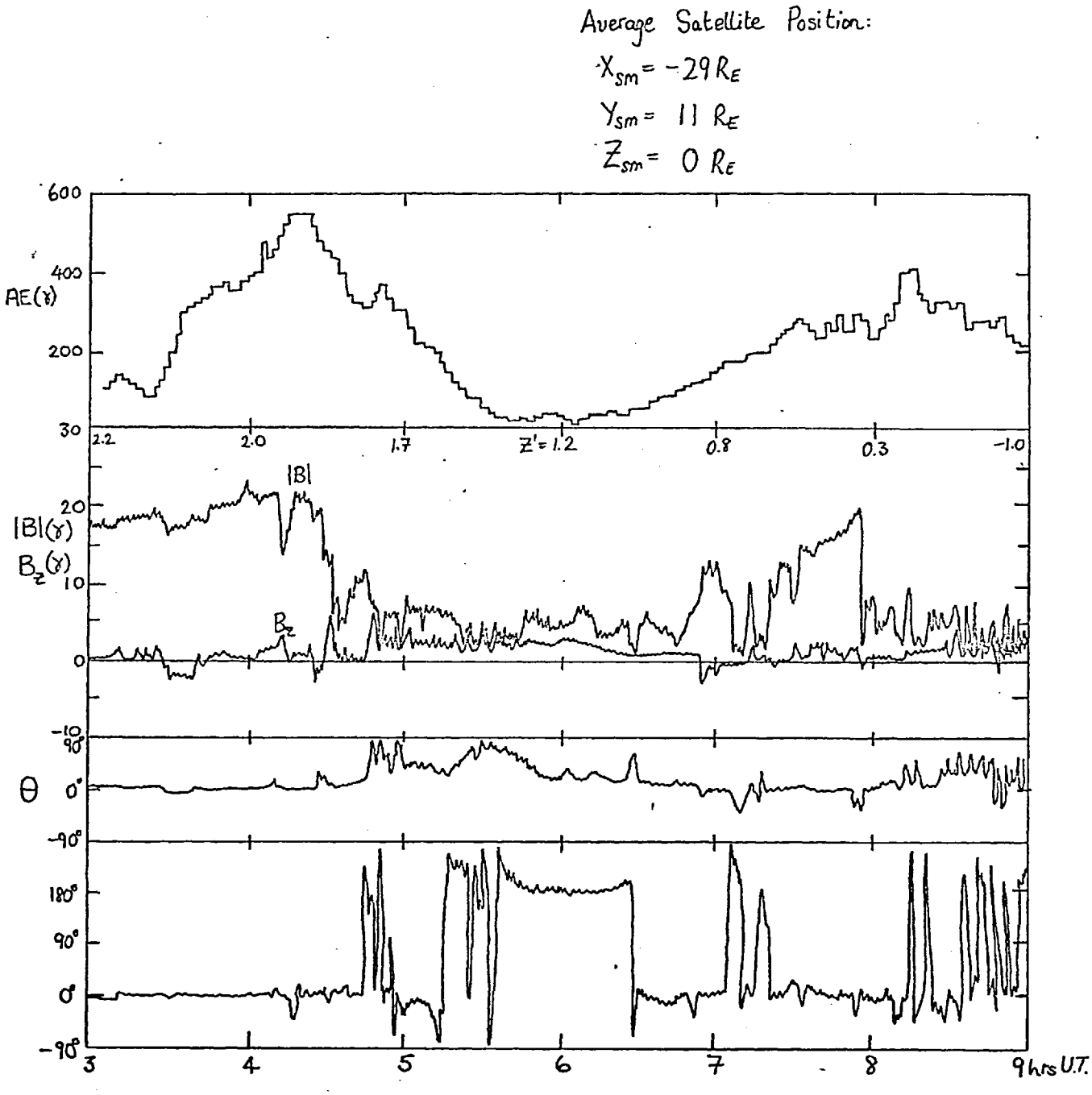

Figure 2.17: Behaviour of the tail field during isolated substorms seen by a satellite near the vicinity of the neutral sheet. Very rapid changes in field-strength are related to plasma-sheet motions. Note the single sharp field reversal at - 06:21 hours U.T. during the growth phase of the second substorm, as compared with the expansion-phase 'multiple field reversals'.

20 R_E during the storm growth phase. Clearly, future work should include generalizing the model to describe the situation in which protons are accelerated the whole way across the tail, while electrons are turned out of the sheet over distances less than the tail width.

References

Akasofu, S.-I. 1968. Polar and magnetospheric substorms. D. Reidel Publishing Co., Dordrecht-Holland.

Akasofu, S.-I. 1971. Midday auroras at the south pole during magnetospheric substorms. Preprint, Geophysical Institute of Alaska.

Akasofu, S.-I., Hones, E.W. Jr., and Meng, C.-I. 1970. Simultaneous observations of an energetic electron event in the magnetotail by the Vela 3A and Imp 3 satellites, 2. J. Geophys. Res., 75, 7296-7298.

Akasofu, S.-I., Hones, E.W. Jr., Montgomery, M.D., Bame, S.J. and Singer, S. 1971. Association of magnetotail phenomena with visible auroral features. J. Geophys. Res., 76, 5985-6003.

Alfvén, H. and Fälthammar, C.-G. 1971. A new approach to the theory of the magnetosphere. Cosmic Electrodyn., 2, 78-88.

Arnoldy, R.L. 1971. Signature in the interplanetary medium for substorms. J. Geophys. Res., 76, 5189-5201.

Arnoldy, R.L. and Chan, K.W. 1969. Particle substorms observed at the geostationary orbit. J. Geophys. Res., 74, 5019-5028.

Atkinson, G. 1972. Magnetospheric flows and substorms. In Magnetosphere-Ionosphere Interactions, University of Oslo Press, Oslo.

Aubry, M.P. and McPherron, R.L. 1971. Magnetotail changes in relation to the solar wind magnetic field and magnetospheric substorms. J. Geophys. Res., 76, 4381-4401.

Aubry, M.P., Russell, C.T. and Kivelson, M.G. 1970. Inward motion of the magnetopause before a substorm. J. Geophys. Res., 75, 7018-7031.

Axford, W.I. and Hines, C.O. 1961. A unifying theory of high latitude geophysical phenomena and geomagnetic storms. Can. J. Phys., 39, 1433-1464.

Bame, S.J. 1968. Plasma sheet and adjacent regions. Earth's Particles and Fields (Ed. McCormac), Reinhold Book Corporation, New York.

Bame, S.J., Hones, E.W. Jr., Akasofu, S.-I., Montgomery, M.D. and Asbridge, J.R. 1971. Geomagnetic storm particles in the high latitude magnetotail. J. Geophys. Res., 76, 7566-7583.

Banks, P.M. 1972. Dynamical behaviour of the polar topside ionosphere. In Magnetosphere-Ionosphere Interactions, University of Oslo Press, Oslo.

Banks, P.M. and Holzer, T.E. 1968. The polar wind. J. Geophys. Res., 73, 6846-6854.

Banks, P.M., Nagy, A.F. and Axford, W.I. 1971. Dynamical behaviour of thermal protons in the mid-latitude ionosphere and magnetosphere. Planetary and Space Sci., 19, 1053-1067.

Behannon, K.W. 1970. Geometry of the geomagnetic tail. J. Geophys. Res., 75, 743-753.

Behannon, K.W. and Fairfield, D.H. 1969. Spatial variations of the magnetosheath magnetic field. Planetary and Space Sci., 17, 1803-1816.

Belon, A.E., Maggs, J.E., Davis, T.N., Mather, K.B., Glass, N.W. and Hughes, G.F. 1969. Conjugacy of visual

auroras during magnetically quiet periods. J. Geophys. Res., 74, 1-28.

Bird, M. and Beard, D.B. 1972. The structure of the magnetotail, with a finite plasma sheet and northward component of the magnetic field. Preprint, University of Kansas.

Burch, J.L. 1968. Low energy electron fluxes at latitudes above the auroral zone. J. Geophys. Res., 73, 3585-3591.

Cahill, L.J. 1966. Inflation of the magnetosphere near 8 earth radii in the dark hemisphere. Space Res., 6, 662-678.

Camidge, F.P. and Rostoker, A. 1970. Magnetic field perturbations associated with polar magnetic substorms. Can. J. Phys., 48, 2002-2010.

Carpenter, D.L. 1966. Whistler studies of the plasmapause in the magnetosphere, 1, Temporal variations in the position of the knee and some evidence on plasma motions near the knee. J. Geophys. Res., 71, 693-709.

Cauffman, D.P. and Gurnett, D.A. 1971. Double probe measurements of dc electric fields with the Injun-5 satellite. J. Geophys. Res., 76, 6014-6027.

Chappell, C.R., Harris, K.K. and Sharp, G.W. 1971. A study of the influence of magnetic activity on the location of the plasmapause as measured by OGO 5. J. Geophys. Res., 75, 50-56.

Cornwall, J.M., Coroniti, F.V. and Thorne, R.M. 1971. Unified theory of SAR arc formation at the plasmapause. J. Geophys. Res., 76, 4428-4445.

Coroniti, F.V. and Kennel, C.F. 1971. Magnetospheric substorms. UCLA preprint, PPG-98. To be published (1972) in Proc. of Conf. on Cosmic Plasma Physics, ESRIN, Frascati, Italy.

Cummings, W.D., Barfield, J.N. and Coleman, P.J. Jr. 1968. Magnetospheric substorms observed at the synchronous orbit. J. Geophys. Res., 73, 6687-6698.

DeForest, S.E. and McIlwain, C.E. 1971. Plasma clouds in the magnetosphere. J. Geophys. Res., 76, 3587-3611.

Dungey, J.W. 1961. Interplanetary magnetic field and the auroral zones. Phys. Rev. Letters, 6, 47-48.

Dungey, J.W. 1968. Polar substorms: Theoretical review. Space Research, 8, (ed. A.P. Mitra, L.G. Jacchia, W.S. Newman), 1291-1298, Academic Press, New York.

Eastwood, J.W. 1971. Consistency of fields and particle motion in the 'Speiser' model of the current sheet. Imperial College Scientific Report, October 1971.

Eather, R.H. and Mende, S.B. 1971. Airborne observations of auroral precipitation patterns. J. Geophys. Res., 76, 1746-1755.

Fairfield, D.H. 1968a. Simultaneous measurements on three satellites and the observation of the geomagnetic tail at 1000 R_E. J. Geophys. Res., 73, 6179-6187.

Fairfield, D.H. 1968b. Average magnetic field configuration of the outer magnetosphere. J. Geophys. Res., 73, 7329-7338.

Fairfield, D.H. and Cahill, L.J. Jr. 1966. Transition region magnetic field and polar magnetic disturbances. J. Geophys. Res., 71, 155-169.

Fairfield, D.H. and Ness, N.F. 1970. Configuration of the geomagnetic tail during substorms. J. Geophys. Res., 75, 7032-7047.

Feldstein, Y.I. 1966. Peculiarities in the auroral distribution and magnetic disturbance distribution in high latitudes caused by the asymmetrical form of the magnetosphere. Planetary & Space Sci., 14, 121-130.

Frank, L.A. 1967a. Initial observations of low energy electrons in the earth's magnetosphere with OGO 3. J. Geophys. Res., 72, 185-196.

Frank, L.A. 1967b. On the extraterrestrial ring current during geomagnetic storms. J. Geophys. Res., 72, 3753-3768.

Frank, L.A. 1971. Plasma in the earth's polar magnetosphere. J. Geophys. Res., 76, 5202-5219.

Frank, L.A. and Owens, H.D. 1970. Omnidirectional intensity contours of low-energy protons ($0.5 \leq E \leq 50$ keV) in the earth's outer radiation zone at the magnetic equator. J. Geophys. Res., 75, 1269-1278.

Fritz, T.A. 1968. High-latitude outer-zone boundary region for $\geq$ 40-keV electrons during geomagnetically quiet periods. J. Geophys. Res., 73, 7245-7255.

Fritz, T.A. 1970. Study of the high-latitude, outer-zone boundary region for $\geq$ 40-keV electrons with satellite Injun 3. J. Geophys. Res., 75, 5387-5400.

Harris, K.K., Sharp, G.W. and Chappell, C.R. 1970. Observations of the plasmapause from OGO 5. J. Geophys. Res., 75, 219-224.

Heikkila, W.J. and Winningham, J.D. 1971. Penetration of magnetosheath plasma to low altitudes through the dayside magnetospheric cusps. J. Geophys. Res., 76, 883-891.

Heppner, J.P., Stolarik, J.D. and Wescott, E.M. 1971. Electric-field measurements and the identification of currents causing magnetic disturbances in the polar cap. J. Geophys. Res., 76, 6028-6053.

Hirshberg, J. and Colburn, D.S. 1969. The interplanetary field and geomagnetic variations - a unified view. Planetary and Space Sci., 17, 1183-1206.

Hoffman, J.H. 1971. Polar wind measurements (abstract). EOS Trans. Am. Geophys. Union, 4, 301.

Hoffman, R.A. 1969. Low-energy electron precipitation at high latitudes. J. Geophys. Res., 74, 2425-2432.

Hoffman, R.A. 1972 Properties of low energy particle impacts in the polar domain in the dawn and dayside hours. In Magnetosphere-Ionosphere Interactions, University of Oslo Press, Oslo.

Hoffman, R.A. and Berko, F.W. 1971. Primary electron influx to the dayside auroral oval. J. Geophys. Res., 76, 2967-2976.

Holzer, T.E. 1971. Formation of the plasma sheet (abstract) EOS Trans. Am. Geophys. Union, 52, 905.

Hones, E.W. Jr., Asbridge, J.R., Bame, S.J. and Strong, I.B. 1967. Outward flow of plasma in the magnetotail following geomagnetic bays. J. Geophys. Res., 72, 5879-5892.

Hones, E.W. Jr., Akasofu, S.-I., Perrault, P., Bame, S.J. and Singer, S. 1970. Poleward expansion of the auroral oval and associated phenomena in the magnetotail during

auroral substorms, 1. J. Geophys. Res., 75, 7060-7074.

Hones, E.W. Jr., Asbridge, J.R., Bame, S.J. and Singer, S. 1971a. Energy spectra and angular distributions of particles in the plasma sheet and their comparison with rocket measurements over the auroral zone. J. Geophys. Res., 76, 63-87.

Hones, E.W. Jr., Singer, S., Lanzerotti, L.J. Pierson, J.D. and Rosenberg, T.J. 1971b. Magnetospheric substorm of August 25-26, 1967. J. Geophys. Res., 76, 2977-3009.

Hones, E.W. Jr., Asbridge, J.R. and Bame, S.J. 1971c. Time variations of the magnetotail plasma sheet at 18 R_E determined from concurrent observations by a pair of Vela satellites. J. Geophys. Res., 76, 4402-4419.

Hruška, A. and Hrušková, J. 1970. Transverse structure of the Earth's magnetotail and fluctuations of the tail magnetic field. J. Geophys. Res., 75, 2449-2457.

Hultqvist, B. 1969. Auroras and polar substorms: Observations and theory. Rev. Geophys., 7, 129-177.

Kaneda, E. 1971. Precusory auroral activity before breakup (abstract) Programs and Abstracts XV IUGG, Moscow, 109.

Kavanagh, L.D. Jr., Freeman, J.W. Jr. and Chen, A.J. 1968. Plasma flow in the magnetosphere. J. Geophys. Res., 73, 5511-5519.

Kelley, M.C., Starr, J.A. and Mozer, F.S. 1971. Relationship between magnetospheric electric fields and the motion of auroral forms. J. Geophys. Res., 76, 5269-5277.

Kennel, C.F. 1969. Consequences of a magnetospheric plasma. Rev. Geophys., 7, 379-419.

Lezniak, T.W. and Winckler, J.R. 1970. Experimental study of magnetospheric motions and the acceleration of energetic electrons during substorms. J. Geophys. Res., 75, 7075-7098.

Mariani, F. and Ness, N.F. 1969. Observations of the geomagnetic tail at 500 earth radii by Pioneer 8. J. Geophys. Res., 74, 5633-5641.

Maynard, N.C. 1972. Electric fields in the ionosphere and magnetosphere. In Magnetosphere-Ionosphere Interactions University of Oslo Press, Oslo.

McDiarmid, I.B. and Burrows, J.R. 1968. Local time asymmetries in the high-latitude boundary of the outer radiation zone for different electron energies. Can. J. Phys., 46, 49-57.

McPherron, R.L. 1970. Growth phase of magnetospheric substorms J. Geophys. Res., 75, 5592-5599.

Meng, C.-I. 1970. Variation of the magnetopause position with substorm activity. J. Geophys. Res., 75, 3252-3254.

Meng, C.-I., Hones, E.W., and Akasofu, S.-I. 1970. Simultaneous observations of an energetic electron event in the magnetotail by the Vela 3A and Imp 3 satellites. J. J. Geophys. Res., 75, 7294-7295.

Meng, C.-I. 1971. Energetic electrons in the magnetotail at 60 R_E. J. Geophys. Res., 76, 862-872.

Mihalov, J.D. 1970. On geomagnetic tail structure near the null sheet. Planetary and Space Sci., 18, 1845-1847.

Mihalov, J.D., Sonett, C.P. and Colburn, D.S. 1970. Reconnection and noise in the geomagnetic tail. Cosmic Electrodyn., 1, 178-204.

Montgomery, M.D., Singer, S., Conner, J.P. and Stogsdill, E.E. 1965. Spatial distribution, energy spectra, time variations of energetic electrons (E > 50 keV) at 17.7 earth radii. Phys. Rev. Letters, 14, 209-213.

Montgomery, M.D. 1971. Thermal energy transport in the solar wind. Los Alamos Scientific Lab. preprint LA-DC-12485. To be published (1972) in Proc. of Conf. on Cosmic Plasma Physics, ESRIN, Frascati, Italy.

Mozer, F.S. and Manka, R.H. 1971. Magnetospheric electric field properties deduced from simultaneous balloon flights. J. Geophys. Res., 76, 1697-1712.

Mozer, F.S. 1971. Origin and effects of electric fields during isolated magnetospheric substorms. J. Geophys. Res., 76, 7595-7608.

Ness, N.F. 1965. The earth's magnetic tail. J. Geophys. Res., 70, 2989-3005.

Ness, N.F., Scearce, C.S. and Cantarano, S.C. 1967. Probable observation of the geomagnetic tail at 10^3 R_E by Pioneer 7. J. Geophys. Res., 72, 3769-3776.

Nishida, A. 1968a. Geomagnetic DP-2 fluctuations and associated magnetospheric phenomena. J. Geophys. Res., 73, 1795-1803.

Nishida, A. 1968b. Coherence of geomagnetic DP-2 fluctuations with interplanetary magnetic variations. J. Geophys. Res., 73, 5549-5559.

Nishida, A. 1971. DP-2 and polar substorm. Planetary and Space Sci., 19, 205-221.

Oguti, T. 1969. Poleward travel of electric current filament in the polar cap region. Rept. of Ionos. & Space Res. in Japan, 23, 175-184.

Owens, H.D. and Frank, L.A. 1968. Electron omnidirectional intensity contours in the Earth's outer radiation zone at the magnetic equator. J. Geophys. Res., 73, 199-208.

Pfitzer, K.A. and Winckler, J.R. 1969. Intensity correlations and substorm electron drift effects in the outer radiation belt measured with the OGO 3 and ATS 1 satellites. J. Geophys. Res., 74, 5005-5018.

Rao, C.S.R. 1969a. Some observations of energetic electrons in the outer radiation zone during magnetic bays. J. Geophys. Res., 74, 794-801.

Rao, C.S.R. 1969b. Some observations on energetic electrons in the outer Van Allen zone during auroral substorms in relation to open and closed field-lines. J. Geophys. Res., 74, 6513-6517.

Rostoker, G. 1968. Relationship between the onset of a geomagnetic bay and the configuration of the interplanetary magnetic field. J. Geophys. Res., 73, 4382-4387.

Russell, C.T. and Brody, K.I. 1967. Some remarks on the position and shape of the neutral sheet. J. Geophys. Res., 72, 6104-6106.

Russell, C.T. and Thorne, R.M. 1970. On the structure of the inner magnetosphere. Cosmic Electrodyn., 1, 67-89.

Russell, C.T., McPherron, R.L. and Coleman, P.J. Jr. 1971. Magnetic field variations in the near geomagnetic tail associated with weak substorm activity. J. Geophys. Res., 76, 1823-1829.

Schatten, K.H. and Wilcox, J.M. 1967. Response of the geomagnetic activity index K_p to the interplanetary magnetic field. J. Geophys. Res., 72, 5185-5192.

Schield, M.A. and Frank, L.A. 1970. Electron observations between the inner edge of the plasma sheet and the plasmasphere. J. Geophys. Res., 75, 5401-5414.

Schindler, K. 1971. A self-consistent theory of the tail of the magnetosphere. ESRIN preprint, Frascati, Italy. To be published.

Schindler, K. and Ness, N.F. 1971. Internal structure of the geomagnetic neutral sheet. ESRIN Internal Note 143, May 1971. To be published.

Shelley, E.G., Johnson, R.G. and Sharp, R.D. 1971. Plasma-sheet convection velocities inferred from electron flux measurements at synchronous altitude. Radio Sci., 6, 305-313.

Slutz, R.J. and Winkelman, J.R. 1964. Shape of the magnetospheric boundary under solar wind pressure. J. Geophys. Res., 69, 4933-4948.

Speiser, T.W. 1965. Particle trajectories in model current sheets, 1. Analytical solutions. J. Geophys. Res., 70, 4219-4226.

Speiser, T.W. 1968. On the uncoupling of parallel and perpendicular motion in a neutral sheet. J. Geophys. Res., 73, 1112-1113.

Speiser, T.W. and Ness, N.F. 1967. The neutral sheet in the geomagnetic tail: Its motion, equivalent currents, and field line connection through it. J. Geophys. Res., 72, 131-141.

Taylor, H.A. Jr., Brinton, H.C. and Pharo, M.W. III. 1968. Contraction of the plasmasphere during geomagnetically disturbed periods. J. Geophys. Res., 73, 961-968.

Vasyliunas, V.M. 1968a. A survey of low-energy electrons in the evening sector of the magnetosphere with OGO 1 and OGO 3. J. Geophys. Res., 73, 2839-2884.

Vasyliunas, V.M. 1968b. Low-energy electrons on the day side of the magnetosphere. J. Geophys. Res., 73, 7519-7523.

Wilcox, J.M., Schatten, K.H. and Ness, N.F. 1967. Influence of interplanetary magnetic field and plasma on geomagnetic activity during quiet-sun conditions. J. Geophys. Res., 72, 19-26.

Wolfe, R.A. 1970. Effects of ionospheric conductivity on convective flow of plasma in the magnetosphere. J. Geophys. Res., 75, 4677-4698.

CHAPTER 3

THE ADIABATIC FLOW MODEL OF A NEUTRAL SHEET

(i) Particle Motions in Simple Neutral Sheet Fields and the Self-Consistent Magnetic Field Structure.

This first analysis of the properties of Alfvén's neutral sheet will be based on a study of particle motions in simple electromagnetic fields which was initiated by Speiser (1965).

Near the neutral sheet Speiser assumed that the field could be approximated by the simplest possible structure

$$\underline{E} = (0, E_o, 0) \qquad \underline{B} = (B_x(z), 0, 0) \tag{3.1}$$

where $B_x(z) = B_o\frac{z}{a}$, and $B_o > 0$, $E_o > 0$. If B_o is taken as the value of the magnetic field outside the field reversal region, then 'a' is the half-thickness of the current sheet. The particle equations of motion in these fields are

$$\frac{m}{q}\frac{dv_z}{dt} = -\frac{v_y B_x}{c} \qquad \frac{m}{q}\frac{dv_y}{dt} = (E_o + \frac{v_z B_x}{c}) \qquad \frac{m}{q}\frac{dv_x}{dt} = 0 \tag{3.2}$$

or

$$\frac{m}{q}\frac{dv_z}{dt} = -\frac{v_y B_o}{ac}\, z \qquad \frac{m}{q}\frac{dv_y}{dt} = (E_o + \frac{B_o v_z z}{ac}) \tag{3.3a,b}$$

Clearly, if $qv_y > 0$ then oscillatory solutions of (3.3a) occur and the particle moves in a trapped orbit about the neutral line. From (3.3b)

$$\frac{d}{dt}\left(\frac{mv_y}{q} - \frac{B_o z^2}{2ac}\right) = E_o .$$

$$\text{or} \quad v_y = v_{yo} + \frac{q\,B_o}{2amc}\,(z^2 - z_o^2) + \frac{qE_o}{m}\,(t-t_o) \qquad (3.4)$$

Thus, if the amplitude of the oscillation is small, the particle may be considered to be uniformly accelerating along the neutral sheet in the electric field in which case we would have $q\,v_y > 0$. Speiser also noted that sufficiently far from any zeros of v_y these oscillating and accelerating particle trajectories would be approximated by the WKB solution to (3.3a). In general terms the differential equation

$$\ddot{z}(t) + g(t)\,z(t) = 0 \qquad (3.5)$$

has an approximate (WKB) solution

$$Z(t) \approx \frac{C}{g^{1/4}} \cos\left(\int_{t_o}^{t} g^{1/2}(t')\,dt' + \phi\right) \qquad (3.6)$$

where C and ϕ are arbitrary constants. This solution is valid far away from the zeros of g (at $t = t_o$) provided that g(t) is 'slowly varying' (i.e. only a 'small' change in one period of the oscillation). Thus, from (3.3a)

$$Z(t) \approx \frac{C}{\left\{\frac{q B_o v_y(t)}{mac}\right\}^{1/4}} \cos\left(\int_{t_o}^{t} \left\{\frac{q B_o v_y(t')}{mac}\right\}^{1/2} dt' + \phi\right) \qquad (3.7)$$

The amplitude constant C is dependent on the initial conditions. Speiser showed that particles drifting into the field reversal region become trapped in these orbits and accelerated along the neutral line. In order to determine C for such circumstances we must therefore investigate the particle motion as the plasma drifts into the sheet from the exterior region.

In the presence of non-uniform crossed electric and

magnetic fields, where $\underline{B}$ has zero curvature, the motion of cold particles (zero magnetic moment) in the steady state can be written in the series form (Northrop, 1963)

$$\underline{v}_D = \underline{v}_E + \frac{mc}{q}\frac{\underline{B}}{B^2} \wedge (\underline{v}_E \cdot \underline{\nabla})\, \underline{v}_E + \ldots = \underline{v}^{(0)} + \underline{v}^{(1)} + \ldots \quad (3.8)$$

where $\underline{v}_E = c\underline{E} \wedge \underline{B}/B^2$.

This expansion is valid (i.e. $v^{(0)} >> v^{(1)}$ etc.) provided that the scale lengths for changes in the electromagnetic field is much larger than the distance travelled by a particle at the velocity $\underline{v}_E$ during $\frac{1}{2\pi}$ of a gyroperiod. This length we call the gyrolength, $g = v_E/\Omega$. The first term in the expansion is the adiabatic approximation, where the inertial terms are entirely neglected in the equation of motion and represents particle drift along equipotentials. The second term has, in general, components parallel and perpendicular to the electric field, the parallel component being just such as to account for the changes in kinetic energy associated with changes in $\underline{v}_E$, i.e.

$$\frac{d}{dt}\left(\frac{mv_E^2}{2}\right) = q\,\underline{E} \cdot \underline{v}^{(1)} \quad (3.9)$$

The zero-order drift provides no current, since it is independent of mass or charge, however, there exists current due to first order terms which satisfies

$$\rho_o \frac{d\underline{v}_E}{dt} = \frac{\underline{j}^{(1)} \wedge \underline{B}}{c} \quad (3.10)$$

where $\underline{j}^{(1)} = N_o e\,(\underline{v}_p^{(1)} - \underline{v}_e^{(1)})$ and $\rho_o = N_o(m_p + m_e)$.

However, the scale length for changes in the magnetic field

associated with $\underline{j}^{(1)}$ is given by

$$L = \frac{B_o}{|\nabla \wedge \underline{B}|} = \frac{B_o c}{4\pi N_o e |\underline{v}_p^{(0)} - \underline{v}_e^{(0)}|} = \frac{K v_E}{v^{(0)}} d \qquad (3.11)$$

where we have used $|E| = kB_o^2/4\pi N_o ed$ from Alfvén's equation for ϕ, the total potential across the system. Thus if $k \sim \mathcal{O}(1)$ then $L >> d$ in the region where the adiabatic approximation to the flow is valid. We thus expect the current sheet, where large currents flow, to be the region where the adiabatic assumption breaks down, so that the scale lengths of this region must be approaching the gyrolength of the incoming particles. In following Speiser's analysis of the particle motions with a uniform electric field and a varying magnetic field we are thus making the assumption that the breakdown of the drift equations, and the consequent growth of current, is set up by the inhomogeneity in the magnetic field. However, the variation in the magnetic field is produced by the currents, so that a self-consistent description must be sought. With a uniform electric field the drift expansion (3.8) breaks down ($v^{(0)} \approx v^{(1)}$) when

$$\frac{B_x(z)}{(\frac{dB_x}{dz})} = \frac{mc^2 E_o}{e B_x^2} .$$

We see that this is equivalent to the statement

$$L = \frac{v_E}{\Omega}$$

where L is the scale length of the magnetic field. For a magnetic field $B_x = B_o z/a$ we thus have

$$\left(\frac{z_B}{a}\right) = \left(\frac{mc^2E_o}{ae\ B_o^2}\right)^{1/3} = \frac{1}{R^{1/3}} \tag{3.12}$$

where z_B is the distance from the neutral plane where the drift expansion breaks down and R is the ratio of the sheet half-thickness (a) to the incoming particle gyrolength ($mc^2E_o/eB_o^2 = v_E/\Omega$). Up to the position z_B the particle accelerates towards the sheet as the magnetic field decreases

$$\underline{v}_E = -\frac{cE_o}{B_o}\left(\frac{a}{z}\right)\hat{\underline{z}} \ .$$

However, as was noted above, the inertial terms become important at the breakdown of the drift equations and the particle ceases to accelerate towards the sheet. Thus the particle moves towards the sheet with a velocity

$$v_z \simeq -\frac{cE_o}{B_o}\ R^{1/3}$$

and reaches it at a time $t \simeq \frac{aB_o}{cE_o}\ \frac{1}{R^{2/3}}$ after the breakdown of the drift equation. While this description is seen from Fig. 3.1 to be rather rough, it gives a surprisingly good account of the particle velocity at the neutral sheet.

It is to be noted that while the adiabatic approximation is valid the electric and magnetic forces balance in the equation of motion parallel to the sheet (3.3b); or with reference to equation (3.4)

$$\frac{B_o^2}{2ac}\ (z_o^2 - z^2) = E_o(t - t_o)$$

for any (z_o, t_o) so that

$$v_y = v_{yo} = 0.$$

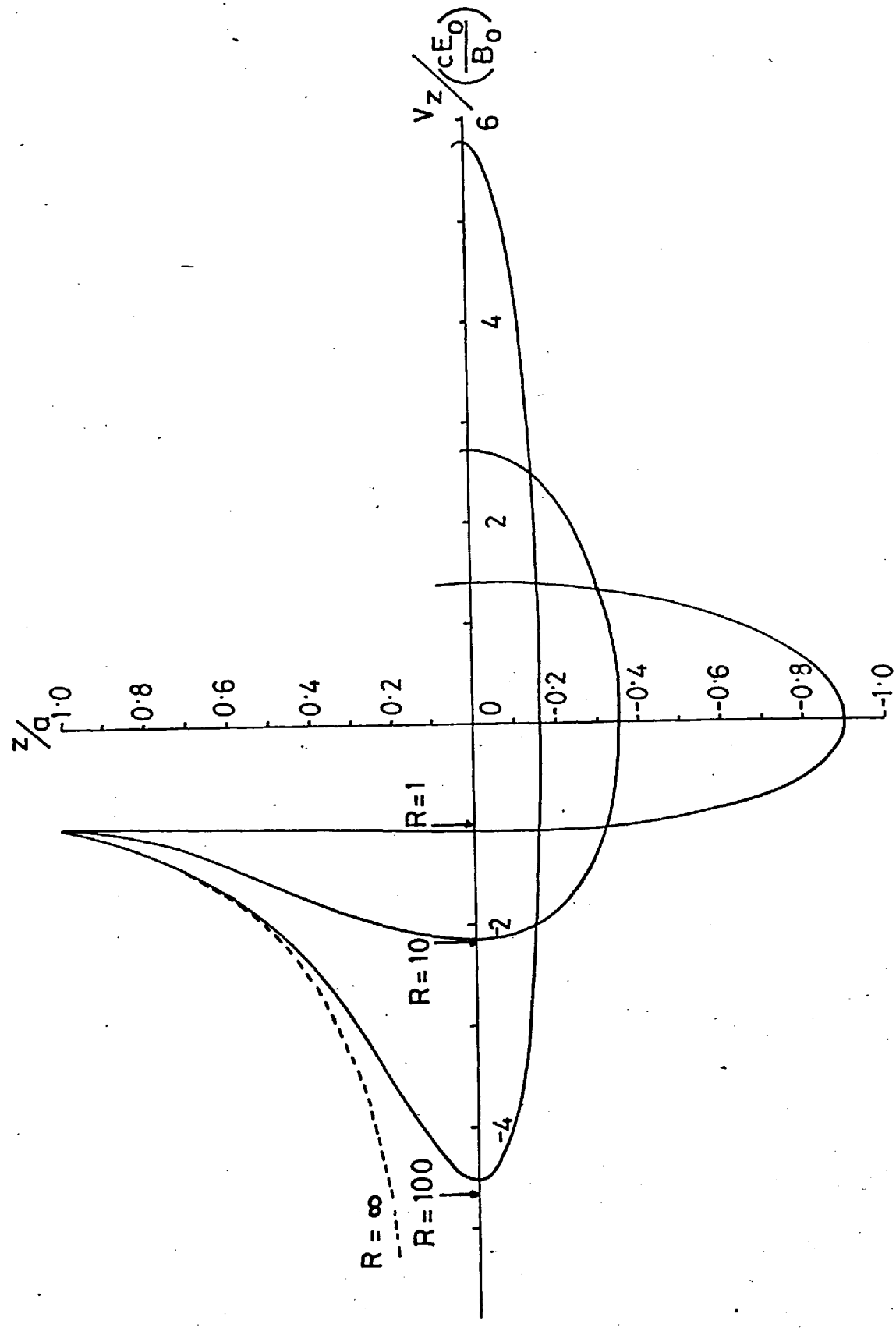
$v_z/\left(\frac{cE_0}{B_0}\right)$
6
4
2
-2
-4
z/a
1·0
0·8
0·6
0·4
0·2
0
-0·2
-0·4
-0·6
-0·8
-1·0
R=1
R=10
R=100
R=∞

Figure 3.1

Figure 3.1: z/a versus $\frac{v_z}{(\frac{cE_o}{B_o})}$ for computed proton trajectories in fields given by $B_x = B_o\, z/a$, $E_y = E_o$; for various values of R, the ratio of sheet half-thickness a over the incoming gyrolength $g_o = \frac{cE_o}{B_o\Omega_o}$. Particles were started at $z=a$ with $v_z = -cE_o/B_o$. The trajectory of a zero-mass particle (i.e. truely adiabatic, $R=\infty$) is indicated by the dotted line. Arrowed are the values of $v_z/(\frac{cE_o}{eB_o})$ at the neutral sheet expected from the simple theory ($v_z = -R^{1/3}\, cE_o/B_o$), for the R values corresponding to the computed particles. Good agreement is obtained over the two-order-of-magnitude range of R.

After the breakdown of the adiabatic approximation the electric force becomes stronger than the magnetic force (since v_z is smaller than the adiabatic approximation) and the particle starts to be accelerated by the electric field. Thus taking $t_o = 0$ and $z_o = z_B$ (the breakdown of the adiabatic condition), we have from (3.4)

$$v_y \simeq \frac{q}{m}\left(\frac{B_o}{ac}(z^2 - z_B^2) + E_o t\right)$$

or

$$\mathrm{sgn}(q) v_y \simeq \frac{cE_o}{B_o}\left\{\frac{B_o e t}{c} + \frac{1}{2}\left(R\left(\frac{z}{a}\right)^2 - R^{1/3}\right)\right\}$$

At the first crossing of the neutral sheet $\left(t \simeq \frac{aB_o}{cE_o} - \frac{1}{R^{2/3}}\right)$ we thus have

$$\mathrm{sgn}(q) v_y \simeq \frac{cE_o}{B_o}\left\{R^{1/3} - \frac{1}{2}R^{1/3}\right\}$$

so that we see that the magnetic term in (3.4) is already half the electric term. If the amplitude of the oscillations then remains at $z \sim a/R^{1/3}$ (as will be shown from the WKB solution) after one or two oscillations the magnetic term may be entirely neglected, and the particle accelerated uniformly in the electric field to a very good approximation. Thus, with increasing accuracy as time goes on $\mathrm{sgn}(q)\, v_y\,(t) \simeq \frac{e}{m} E_o t$, where time is measured from the breakdown of the adiabatic approximation.

Returning now to the WKB solution for the oscillations, equation (3.5), we have

$$g(t) \simeq \frac{e^2 B_o E_o t}{m^2 ac} .$$

Thus the amplitude of the oscillations is

$$\hat{Z}(t) \simeq \frac{C}{\left\{\frac{e^2 B_o E_o t}{m^2 a c}\right\}^{1/4}}$$

and we also have the velocity amplitude

$$\hat{V}_z(t) \simeq C\left\{\frac{e^2 B_o E_o t}{m^2 a c}\right\}^{1/4}$$

where C is to be determined. We have, from the above discussion that

$$v_z \simeq -\frac{cE_o}{B_o} R^{1/3}$$

for times of order $\frac{aB_o}{cE_o} \frac{1}{R^{2/3}}$

and hence we put

$$\hat{V}_z(t) \simeq \frac{cE_o}{B_o} R^{1/3}\left\{\frac{R^{2/3} t}{(aB_o/cE_o)}\right\}^{1/4}$$

Thus $C = \frac{cE_o}{B_o} R^{1/3} \frac{1}{(eB_o/mcR^{1/3})^{1/2}}$

and hence

$$\hat{Z}(t) = \frac{\left\{\frac{cE_o}{B_o}\frac{mc}{eB_o}\right\}R^{2/3}}{\left(\frac{R^{2/3}t}{(aB_o/cE_o)}\right)^{1/4}} = \frac{a}{R^{1/3}}\left(\frac{R^{2/3}t}{(aB_o/cE_o)}\right)^{-1/4}$$

Thus the initial amplitude of the oscillations is approximately the distance away from the sheet at which the drift expansion breaks down, thus vindicating the statement concerning the negligibility of the magnetic term in the equation for motion parallel to the sheet in the above discussion. The validity of this theory was checked against the initial oscillation amplitude of computed particle trajectories and the results are

shown in Fig. 3.2. The magnetic field chosen for these computations was

$$B_x(z) = B_o \tanh\left(\frac{z}{a}\right)$$

so that for $\frac{z}{a}$ small $B_x(z) \simeq B_o \frac{z}{a}$. The above theory is expected to hold for $R < 1$ when using this magnetic field structure, and good agreement is found. For $R > 1$ we may approximate the neutral sheet by a step in the magnetic field and the initial amplitude of the resulting cycloidal motion is given by

$$\frac{\hat{z}}{a} = (\sqrt{3} - \pi/3)/R \simeq \frac{0.685}{R}$$

The computed points are seen to make a smooth transition between the curves representing these extreme approximations to the $\tanh(\frac{z}{a})$ field.

As we previously stated, the magnetic structure must be made consistent with the particle orbits. If we make the sheet width consistent with the proton orbits then the oscillation amplitude must be the same as the sheet thickness. Thus approximately

$$\frac{\hat{z}}{a} \simeq \frac{1}{R_p^{1/3}} \simeq 1$$

for consistency, or

$$a \simeq \frac{cE_o}{B_o} \frac{m_p c}{eB_o}$$

as we might have expected. Then the drift expansion breaks down due to the magnetic gradient immediately the particles enter the sheet and the electric current extends over the whole sheet width.

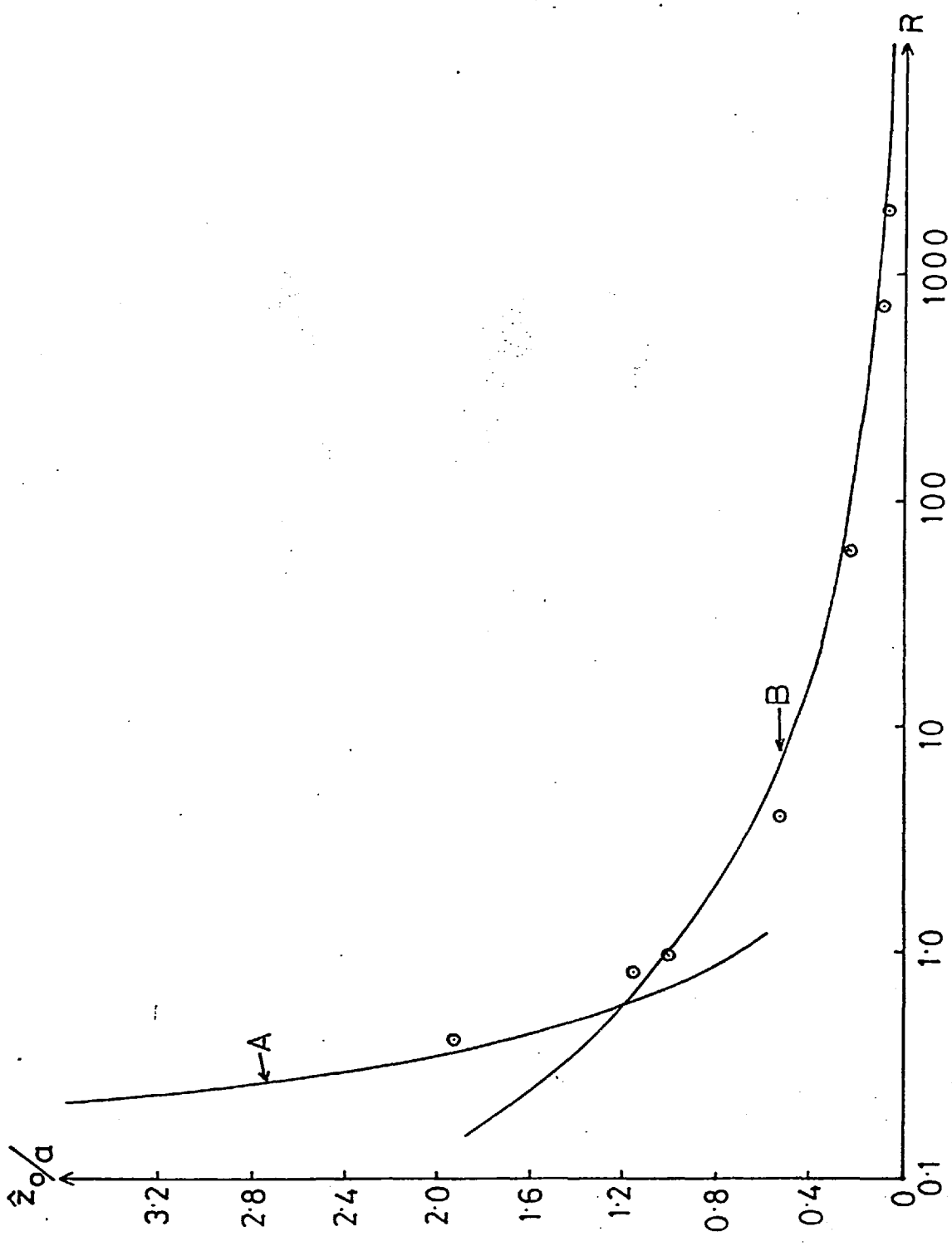

Figure 3.2

Figure 3.2: Initial amplitude of oscillation $\hat{z}_o$ of computed particle trajectories (in units of 'a', the sheet half-thickness) in fields given by $B_x = B_o \tanh (z/a)$, $E_y = E_o$) for various values of $R = a/g_o$. Particles were started at large distances from the neutral sheet $[(z/a) \geq 5]$ with the adiabatic velocity. Curve A represents the behaviour of a particle incident on a step in the magnetic field, a valid approximation to the given field if $g_o > a$ (i.e. $R < 1$). Curve B represents the expected behaviour for a particle in a field of uniform gradient ($B_x = B_o z/a$), a valid approximation for $g_o < a$ (i.e. $R > 1$). A smooth transition of agreement between the two approximations is seen at $R=1$. In addition if $\hat{z}_o/a \approx 1$ is required for cocsistency between the field and current then $R \approx 1$ or $a \approx g_o$.

Thus the proton orbits are approximated by

$$v_y \simeq \frac{q}{m} E_o t \qquad \hat{v}_z(t) \simeq \frac{cE_o}{B_o} \left\{ \frac{t}{(aB_o/cE_o)} \right\}^{1/4}$$

$$\hat{z}(t) \simeq \frac{a}{\left\{ \frac{t}{(aB_o/cE_o)} \right\}^{1/4}}$$

A comparison of these results with the results of a computed particle trajectory for R = 1 is shown in Figs. 3.3a and 3.3b and again, good agreement is obtained. The complete particle orbit is shown in Fig. 3.4a. The WKB solution becomes a better approximation as time increases; if we could determine C and ϕ at a later time, the accuracy would be improved when compared with the computed orbit. In Figs. 3.4b and 3.4c, C and ϕ were determined from the computed orbit at $t = 20\ aB_o/cE_o$ and the WKB solution then gives an excellent account of the motion almost from the first crossing of the neutral sheet.

We noted in the first chapter that significant charge densities may exist in the neutral sheet, set up by the accelerating particles and these will be examined quantitatively later in this chapter. Within the framework of the WKB theory we may include electric fields of the form $E_z = E_1 \frac{z}{a}$ into the z-equation of motion, and we may take such a field as a first representation of the electric field of the charge. The equation of motion perpendicular to the sheet then becomes

$$\frac{m}{q} \frac{dv_z}{dt} = (E_1 - \frac{v_y B_o}{c}) \frac{z}{a}$$

which is of WKB form. However, if the particles are adiabatic outside the sheet we have

$$v_y = \frac{cE_1}{B_o}$$

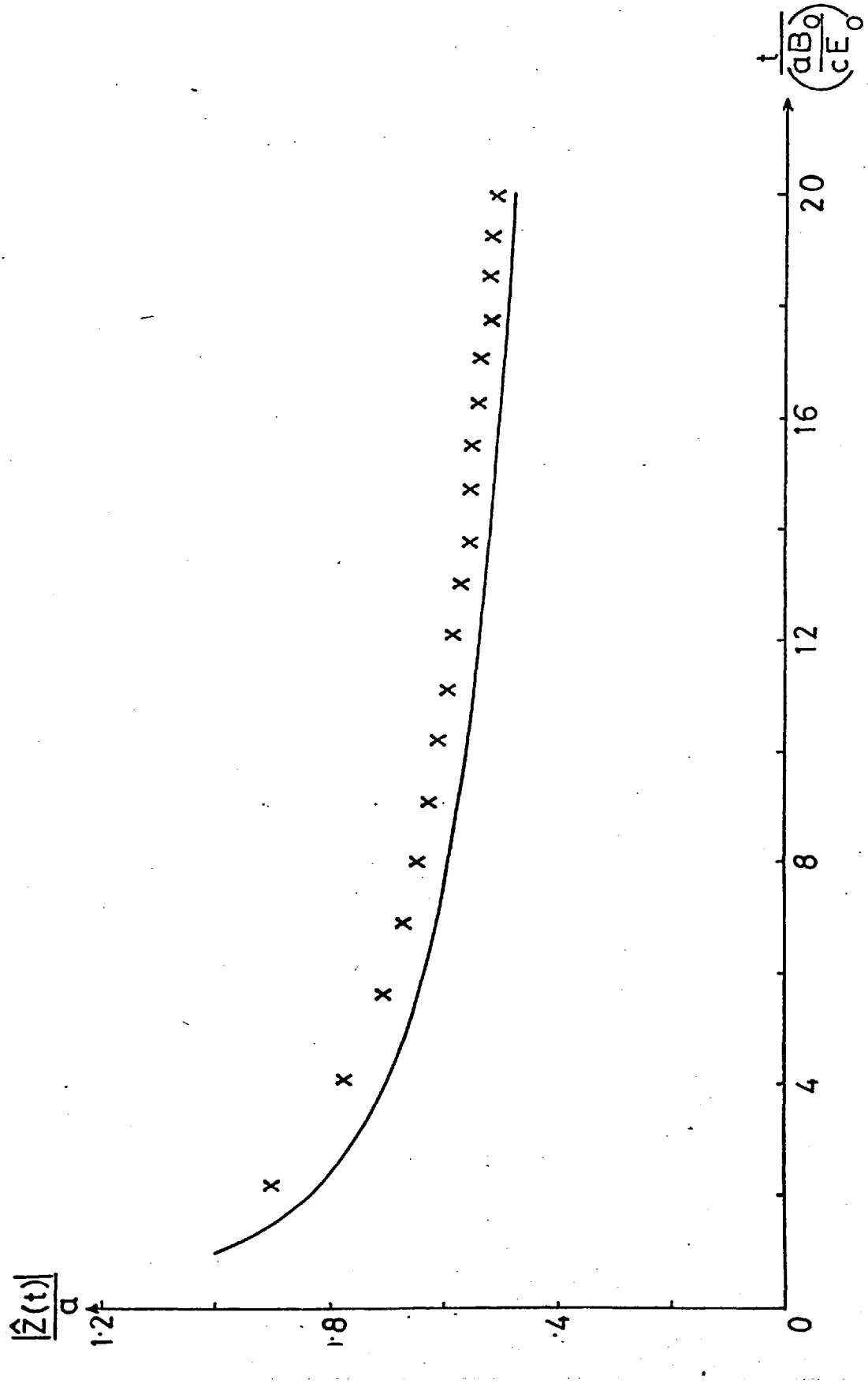

Figure 3.3(a)

Figure 3.3(a): Amplitude of oscillation $\hat{z}(t)/a$ for a computed proton trajectory in fields given by

$$B_x = B_o \frac{z}{a} \qquad E_y = E_o \qquad \frac{a}{g_o} = R = 1.$$

The particle was started at $z/a = 1$ with $\frac{v_z}{(\frac{cE_o}{B_o})} = -1$ at time t=o, and the values of $|\frac{z}{a}|$ at the extreme of the oscillatory motion are marked with crosses. The solid line represents the expected values from the WKB theory,

i.e. $\frac{\hat{z}}{a} = \left(\frac{aB_o}{cE_o t}\right)^{\frac{1}{4}}$

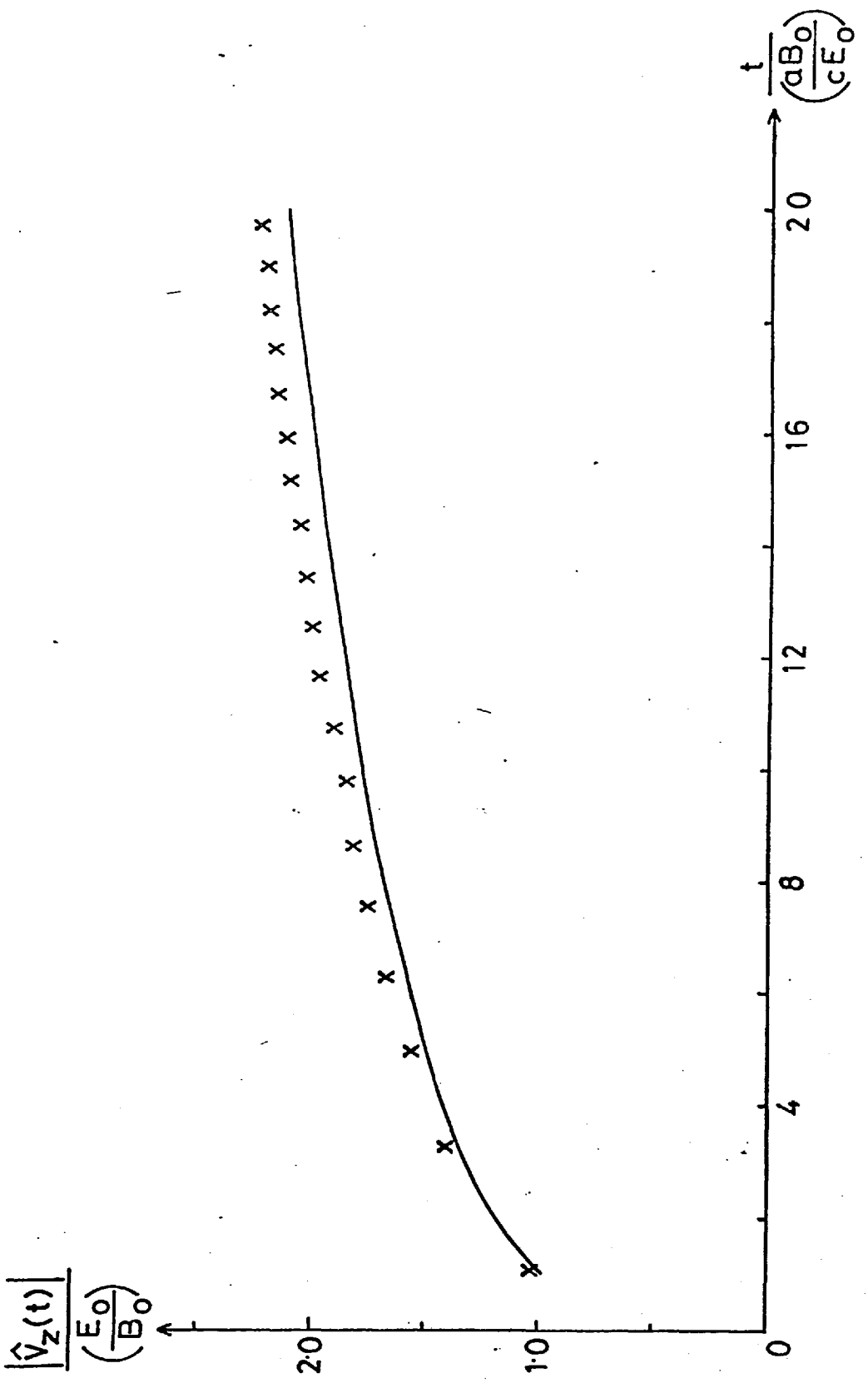

Figure 3.3(b)

Figure 3.3(b): Velocity amplitude $v_z(t)/(\frac{cE_o}{B_o})$ for the computed proton trajectory of Fig. 3.3(b). The values of the velocity amplitude at the neutral sheet crossings are indicated by crosses. The solid line represents the expected values from WKB theory,

i.e. $$\frac{\hat{v}_z(t)}{(\frac{cE_o}{B_o})} \simeq \left(\frac{t}{(\frac{aB_o}{cE_o})}\right)^{\frac{1}{4}}$$

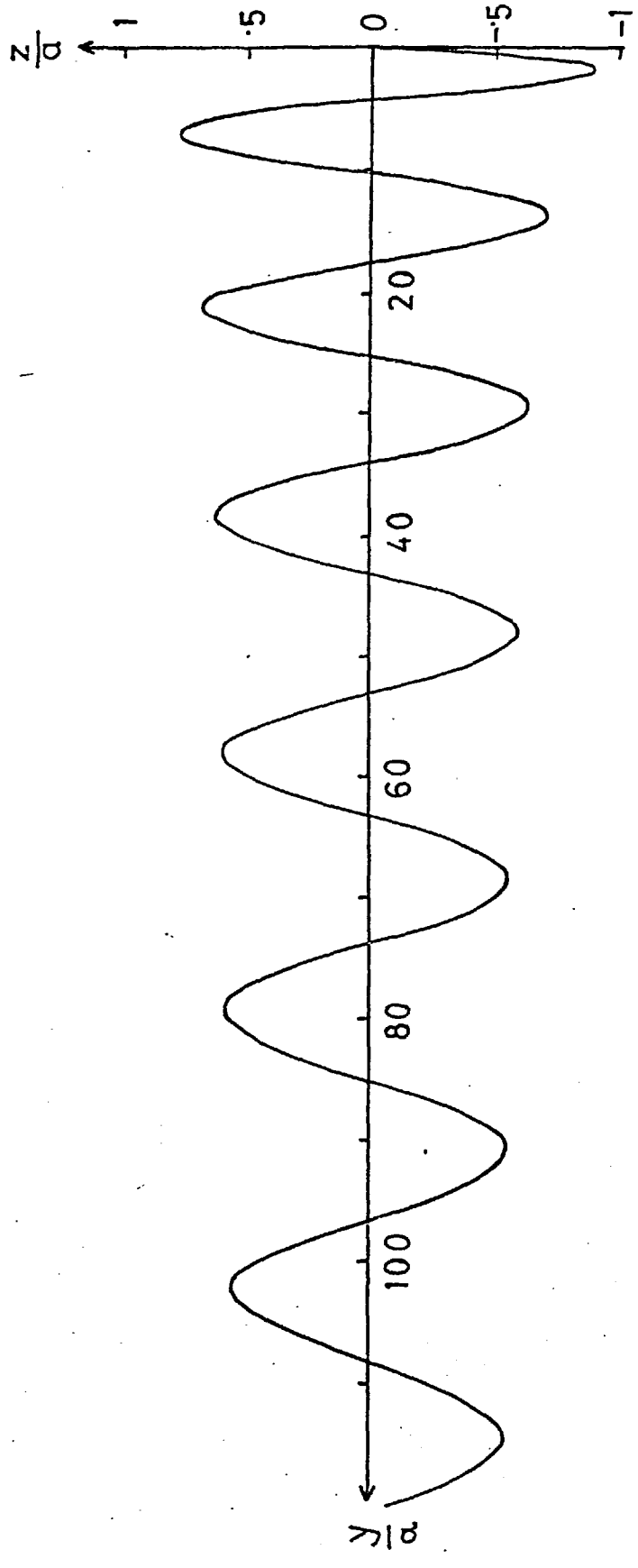

Figure 3.4(a): Computed proton trajectory (z versus y) in the fields of Figs. 3.3(a), 3.3(b).

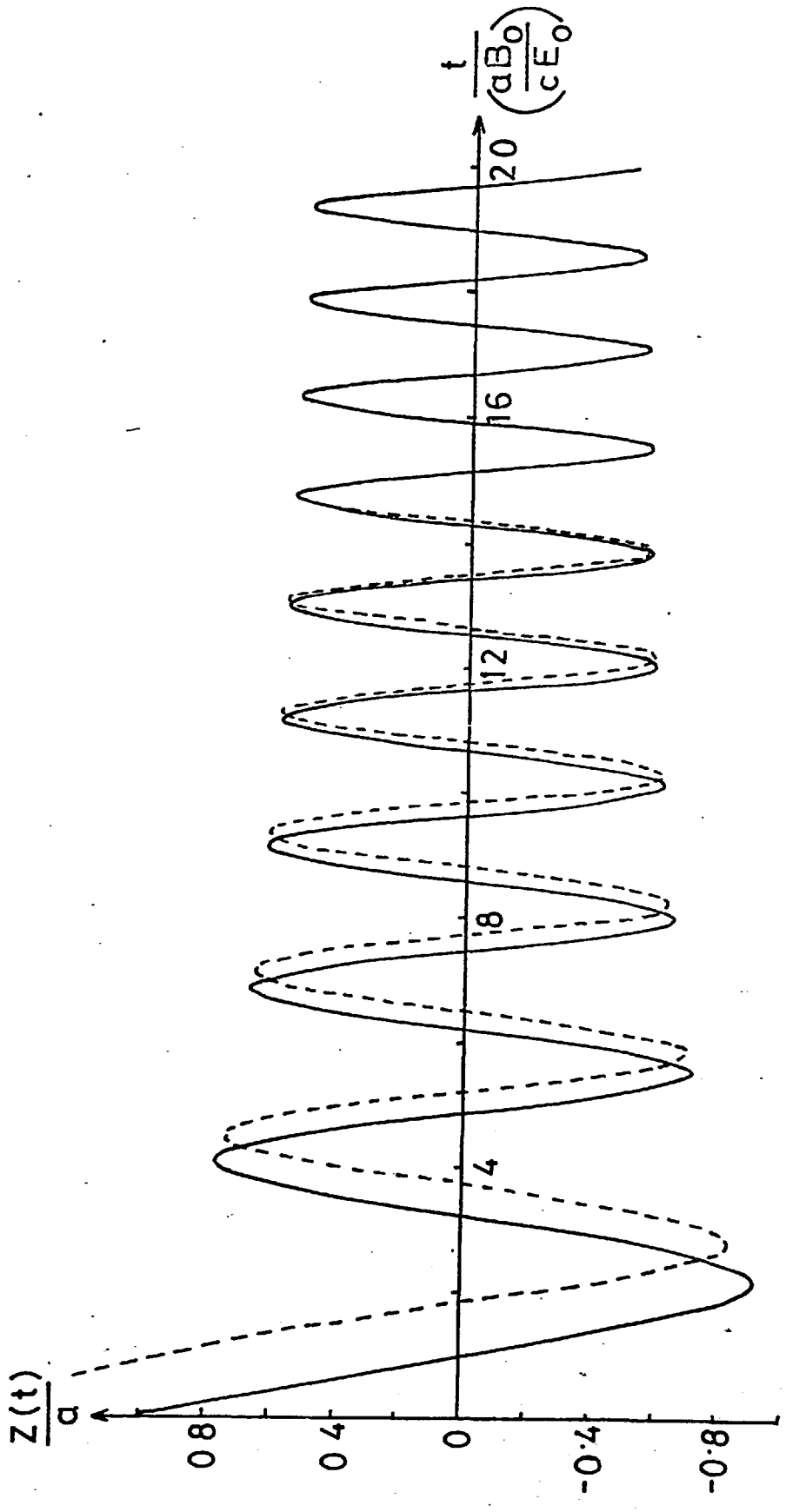

Figure 3.4(b): $z(t)/a$ for the computed proton trajectory in the fields of Fig. 3.3(a), compared with the WKB solution (dotted), where the WKB constants C and ϕ were fitted to the trajectory at $\frac{t}{(\frac{aB_o}{cE_o})} = 20$

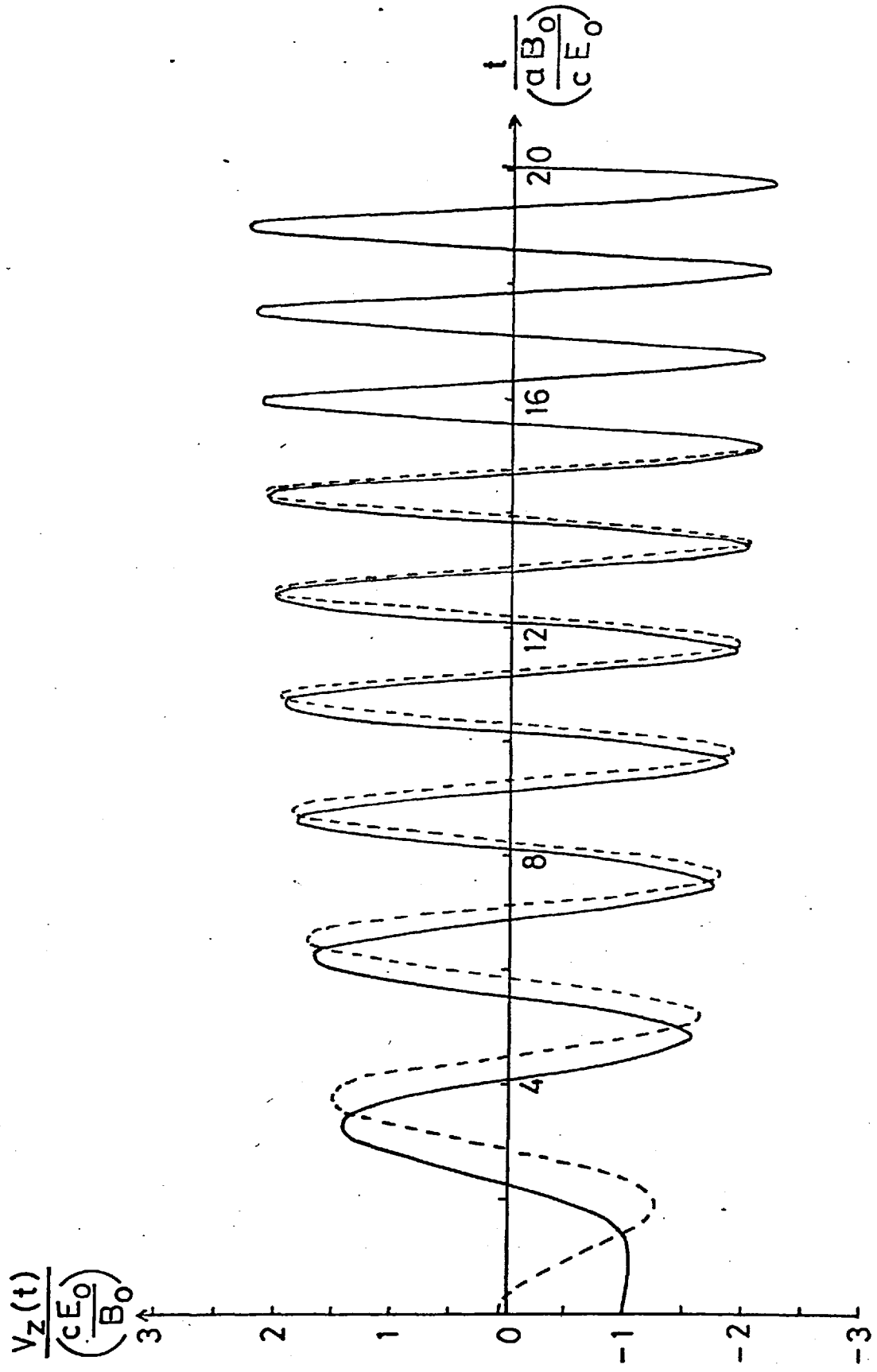

Figure 3.4(c): $v_z(t) \Big/ \left(\frac{cE_o}{B_o}\right)$ for the computed proton trajectory in the fields of Fig. 3.3(a) compared with the WKB solution (dotted), where the WKB constants C and ϕ were fitted to the trajectory at $\frac{t}{\left(\frac{aB_o}{cE_o}\right)} = 20$

on entry into the field reversal region. As the particles accelerate

$$v_y \approx \frac{cE_1}{B_o} + \frac{q}{m} E_o t$$

and hence $\frac{m}{q}\frac{dv_z}{dt} = -(\frac{qE_oB_ot}{mc})^{z}/_{a}$ as before.

We can thus remove such an electric field by a frame transformation along the sheet with velocity $cE_{\perp}/B_o$ and in this frame the trajectories are as given above.

In the most general WKB form we have

$$g(t) \approx \frac{q}{m}\left(\frac{B_o(t)v_y(t)}{a_1(t)\ c} - \frac{E_1(t)}{a_2(t)}\right)$$

but for the present purposes we can take $B_o(t) = B_o$, a constant, and $a_1(t) = a_2(t)$ so that

$$g(t) \approx \frac{q}{ma(t)}\left(\frac{v_y(t)B_o}{c} - E_1(t)\right) \qquad (3.14)$$

hence $$\hat{Z}(t) = \frac{C}{\left\{\frac{q}{ma(t)}\left(\frac{V_y(t)B_o}{c} - E_\perp(t)\right)\right\}^{1/4}} \qquad (3.15a)$$

$$\hat{V}_z(t) = C\left\{\frac{q}{ma(t)}\left(\frac{V_y(t)B_o}{c} - E_\perp(t)\right)\right\}^{1/4} \qquad (3.15b)$$

Following the less general analysis above, we consider the case $R(t=o) \approx 1$, where $t=o$ is the time the particle enters the sheet. Then for $t \approx \frac{a(o)B_o}{c\ E_y(o)}$ we have $\hat{v}_z \approx \frac{c\ E_y(o)}{B_o}$ and since for $t \to o$ $v_y(t) \approx \frac{q}{m} E_y(o)t + \frac{cE_1(o)}{B_o}$ we have at this

time

$$v_y \simeq \frac{q B_o}{mc} a(o) + \frac{cE_\perp(o)}{B_o} \quad .$$

Thus from (3.15b) $\quad C \simeq \frac{cE_y(o)}{B_o} \cdot \frac{1}{(\frac{eB_o}{mc})^{\frac{1}{2}}}$

and hence for the general case

$$\hat{V}_z(t) \approx \hat{V}_z(o) \left\{ \frac{sgn(q)\left(V_y(t) - cE_\perp(t)/B_o\right)}{(a(t)eB_o/mc)} \right\}^{1/4} \tag{3.16a}$$

$$\hat{Z}(t) \approx a(o) \left\{ \frac{sgn(q)\left(V_y(t) - cE_\perp(t)/B_o\right)}{(a(t)eB_o/mc)} \right\}^{1/4} \tag{3.16b}$$

In the present chapter we shall assume that the flow energies in the adiabatic motion above the sheet are very small compared with the potential energy across the system. This is equivalent to the assumption that the adiabatic approximation of the flow outside the sheet, i.e. $\underline{v} = c\underline{E} \wedge \underline{B}/B^2$ is a good approximation, since with the above assumption, the particles need only drift a small way from their 'parent' equipotential in order to make the energy change indicated by the change in $\underline{v}_E$. The condition for small flow energies is

$$\frac{mc^2E^2}{2B_o^2} \ll e\Phi \tag{3.17}$$

while the condition for the validity of the adiabatic approximation is

$$\frac{g}{L} \ll 1 \quad \text{or} \quad \frac{mc^2E}{eB_o^2L} \ll 1 \tag{3.18}$$

where L is the scale length of the electric field (the magnetic

field is very nearly constant in this region as shown above). However, since the total potential across the system is fixed we have

$$EL \simeq \Phi .$$

Thus equation (3.18) becomes

$$\frac{mc^2E^2}{B_o^2} << e\Phi$$

and hence the two approximations are equivalent. Thus if the adiabatic flow approximation is valid outside the field reversal region the incoming particle energies are much smaller than the energies gained by acceleration along the neutral sheet and may be neglected in equations (3.16a) and (3.16b). We now consider the ratio of the energy in the oscillatory motion of the particles compared with the kinetic energy along the sheet. From equation (3.16a) we have

$$\left(\frac{\hat{V}_z}{V_y}\right)^2 \simeq \frac{c^2E_y^2(o)}{B_o^2V_y^2(t)}\left\{\frac{sgn(q)\,V_y(t)}{a(t)eB_o/mc}\right\}^{1/2} \qquad (3.19)$$

or, writing $a(t) = k(t)\,\frac{cE_y(o)}{B_o}.\frac{mc}{eB_o}$ we obtain

$$\left(\frac{\hat{V}_z}{V_y}\right)^2 \simeq \left(\frac{cE_y(o)}{B_oV_y(t)}\right)^{3/2}\frac{1}{\sqrt{k(t)}} \qquad (3.20)$$

Thus as the particle accelerates along the sheet and $v_y(t) >> cE_o(o)/B_o$ the importance of the energy in the oscillations rapidly diminishes, and may very quickly be approximated by a particle linearly accelerated along the neutral line, i.e.

$$\frac{mv_y^2}{2} \simeq q\,(\phi_o - \phi) \qquad (3.21)$$

where ϕ_o is the potential at which the particle entered the sheet. This is shown from the computed particle trajectory for the case where k(t)=1 and the electric field uniform (see Fig. 3.5). After acceleration through a potential of order Φ the amplitude of the oscillation is, from (3.16b)

$$\frac{\hat{z}}{a(o)} \simeq \left\{ \frac{k^2(t)\, mc^2 E_y^2(o)/B_o^2}{e\Phi} \right\}^{1/8} \qquad (3.22)$$

and even if the potential energy exceeds the flow energies by several orders of magnitude, the oscillation amplitude of the particles does not change very much during the acceleration, due to the ⅛ power law. Thus we expect $k(t) \simeq 1$ for consistency at all positions along the sheet.

However, since the electrons carry a significant contribution to the current and their oscillation amplitude is much smaller than the protons, the magnetic field structure cannot be as simple as this. For example, if we have an assumed field structure $B_x(z) = B_o z/a$ and $a = m_p c^2 E_o/eB_o^2$ so that $R = 1$ for protons, then the electrons have an initial amplitude from equation (3.13) of $\simeq (\frac{m_e}{m_p})^{1/3} a \sim 0.1a$ (see Fig. 3.2). This results from the fact that the electron mass is much smaller than the proton mass and hence they remain adiabatic (negligible inertial terms) up to much smaller distances from the sheet. We may thus expect two scale lengths in the magnetic field at the neutral sheet, one consistent with the proton sheet and one consistent with the electron sheet.

At a potential ϕ in the sheet the ratio of the current

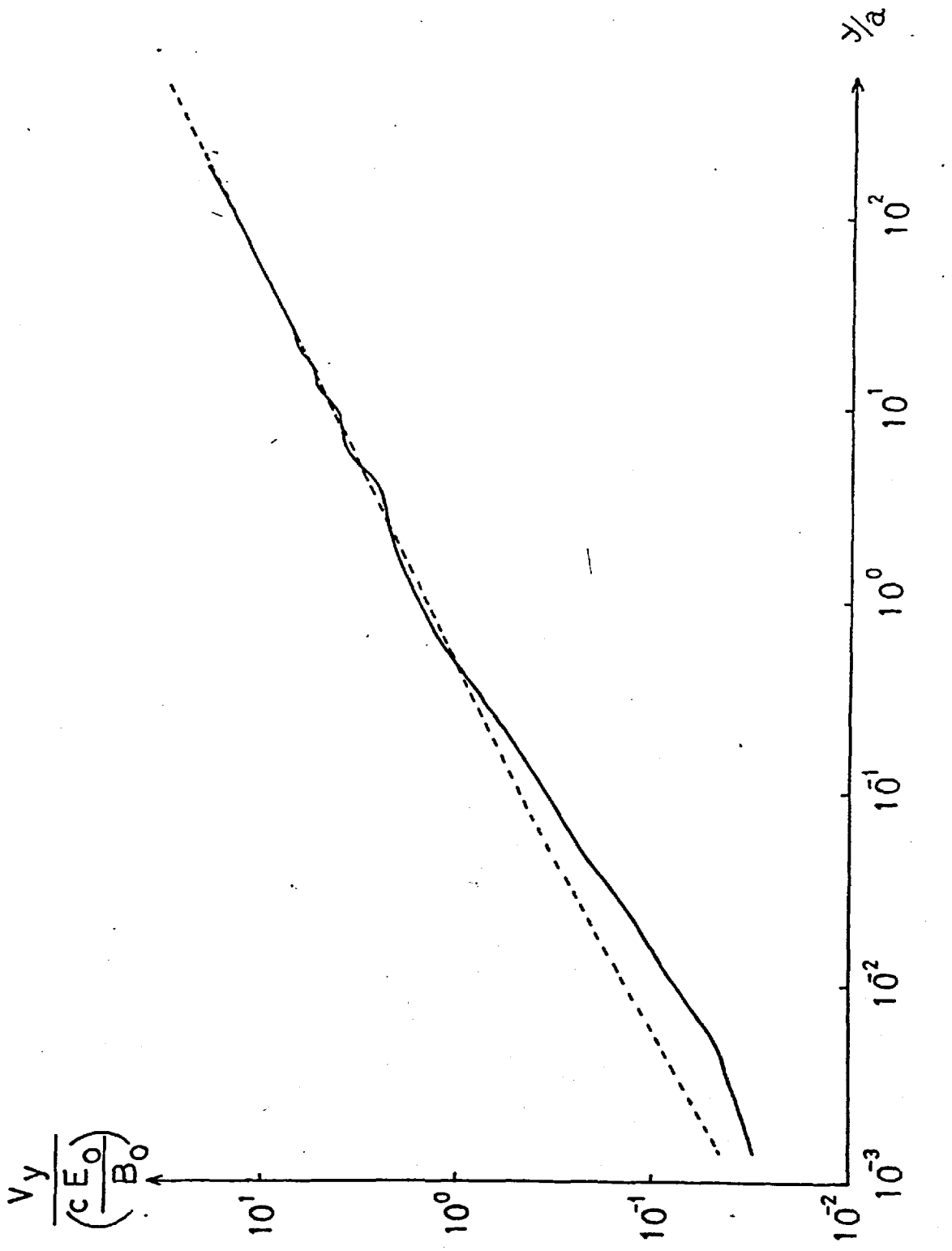

Figure 3.5: $v_y/(\frac{cE_o}{B_o})$ against y/a for a computed particle trajectory in the fields of Fig. 3.3(a) (R=1); compared with a particle uniformly accelerating along the neutral line in the electric field (dotted). The latter is given by

$$\frac{m_p v_y^2}{2} = E_o y \quad \text{or} \quad \frac{v_y}{(\frac{cE_o}{B_o})} = (\frac{2y}{a})^{\frac{1}{2}} \quad \text{for R=1} .$$

carried by protons to that carried by electrons is

$$\frac{I_p}{I_e} = \frac{(1 - \frac{\phi}{\Phi})}{(\phi/\Phi)} \tag{3.23}$$

and for simplicity we assume that the current is distributed uniformly across both the proton and electron sheets. The half-widths of these current sheets are respectively a_p and a_e such that at potential ϕ

$$B_x(z) = B_o\left(1 - \frac{\phi}{\Phi}\right) \begin{cases} z/a_p & \text{for } |z| \leq a_p \\ 1 & \text{for } |z| > a_p \end{cases}$$

$$+ B_o \frac{\phi}{\Phi} \begin{cases} z/a_e & \text{for } |z| \leq a_e \\ 1 & \text{for } |z| > a_e \end{cases}$$

For consistency the particles must become non-adiabatic near the current sheet boundaries so that

$$\frac{B}{(\frac{dB}{dz})} \simeq \frac{mc^2 E_o}{eB^2}$$

At the boundary of the electron sheet $B = B_o(1 - \frac{\phi}{\Phi}) \frac{a_e}{a_p} + B_o \frac{\phi}{\Phi}$ where we have assumed $a_e < a_p$, and

$$\frac{dB}{dz} = B_o(1 - \frac{\phi}{\Phi}) \frac{1}{a_p} + B_o \frac{\phi}{\Phi} \frac{1}{a_e} = \frac{B}{a_e}$$

Thus the consistency condition becomes

$$a_e \simeq \frac{m_e c^2 E_o}{e\left\{B_o\left(1 - \frac{\phi}{\Phi}\right)\frac{a_e}{a_p} + B_o \frac{\phi}{\Phi}\right\}^2} \tag{3.24}$$

which is a cubic equation for a_e. At the boundary of the proton sheet we have $B = B_o$ and

$$\frac{dB}{dz} = B_o\left(1 - \frac{\phi}{\Phi}\right)\frac{1}{a_p}$$

so that

$$a_p \simeq \left(1 - \frac{\phi}{\Phi}\right)\frac{m_p c^2 E_o}{eB_o^2} \tag{3.25}$$

For $\phi \simeq 0$ the electron sheet is given by $a_e \simeq \left(\frac{m_e c^2 E_o}{eB_o^2}\right)^{1/3}$ in agreement with the previous discussion, while for $\phi > 0$ we have $a_e << a_p$ due to the mass factor and

$$a_e \simeq \frac{m_e c^2 E_o}{eB_o^2} \cdot \frac{1}{(\phi/\Phi)^2} \tag{3.26}$$

Thus although we cannot apply the results of the WKB treatment of the particle motions exactly, there is no reason to suppose that the qualitative results are in serious error.

We have thus developed an internally consistent series of approximations which describe a model neutral sheet structure based on Speiser's trajectory analysis and the assumption of adiabatic particle flow external to the sheet. In this model the current is very small outside of the region where the particles oscillate about the neutral sheet. Adiabatic theory breaks down in the field reversal region due to the small scale length of the magnetic field. The sheet width is then given by $a \simeq v_p/\Omega$. Adiabatic theory is valid if the incoming particle energies are very small compared with the potential energy and the motion of the particles constituting the current in the sheet can be well approximated by uniform acceleration by the electric field along the neutral line.

The assumption of adiabatic flow leads to a very simple description of the region external to the sheet. Because the drift velocity is independent of the mass or charge of the particles there is no significant currents flowing in this region and also no charge densities. The magnetic structure then depends simply on the current flowing in the neutral sheet and on the bounding equipotential surfaces, and the electric field on the charge in the neutral sheet and external boundary conditions.

The total current in the neutral sheet must be uniform across the system since each incoming stream of neutral plasma charge-separates at the sheet to produce equal fluxes of positive particles moving towards $\phi = 0$ and negative particles towards $\phi = \Phi$. Thus, with appropriate boundary currents the magnetic field may be taken as uniform in the external region. By particle flux conservation N/B is a constant along a trajectory for adiabatic flow, so that the particle density may also be taken to be constant in this region.

We now turn to consider charge in the neutral sheet on the basis of this model. If the electric field produced by the charge is so strong that $mc^2E^2/B^2 \sim \mathcal{O}(e\Phi)$ then the model breaks down. In this case the non-adiabatic condition for the growth of the current depends on the electric field scale lengths rather than the magnetic field scale lengths as is implied by the discussion of the particle trajectories above. The flow structure for such a situation will be discussed in the next two chapters.

(ii) Charge in the Neutral Sheet and the Self-Consistent Electric Field.

Charge in the neutral sheet certainly warrants consideration since, as we stated in the preceding section, incoming neutral plasma charge-separates at the neutral sheet to provide a positively charged beam moving towards $\phi = 0$ and a negative beam moving towards $\phi = \Phi$. We thus expect the sheet to become positively charged near $\phi = 0$ and negatively charged near $\phi = \Phi$. If we consider a closed volume into, and out of which equal fluxes of protons and electrons flow, the charge content of the volume in the steady state is proportional to the difference in time a proton and an electron remains within the volume

$$\text{i.e.} \quad Q = eF\,(\tau_p - \tau_e) \tag{3.27}$$

where F is the total flux (particles/sec) of positive or negative particles entering or leaving the closed volume. Considering a unit length (along the magnetic field) of the field reversal region as the closed volume, eF is the total current flowing, i.e.

$$eF = I = \frac{cB_o}{2\pi} \tag{3.28}$$

The time a particle spends accelerating along the sheet is given by

$$t = \left(\frac{2my}{E_o}\right)^{\frac{1}{2}}$$

where y is the distance travelled in the sheet. Writing $y = d/2$ for definiteness (d is the width of the sheet) we then have

$$\tau_p \simeq \left(\frac{m_p d}{e E_o}\right)^{1/2} \simeq \frac{d}{V_A} \qquad \tau_e \simeq \left(\frac{m_e}{m_p}\right)^{1/2} \frac{d}{V_A} \tag{3.29}$$

where we have used Alfvén's formula for the electric field and V_A is the Alfvén velocity in the region external to the sheet. (We previously noted that a particle accelerated through potential $\Phi/2$ reaches a velocity V_A). In addition the electron spends a time

$$\tau \simeq \frac{aB_o}{cE_o}$$

moving adiabatically towards the neutral sheet in the field reversal region before it becomes non-adiabatic. If $a \simeq m_p c^2 E_o / eB_o^2$ then

$$\tau \simeq \frac{m_p c}{eB_o} .$$

The condition $\tau_e >> \tau$ is $\left(\frac{\lambda\!\!\!^{-}_p}{d}\right) << \left(\frac{m_e}{m_p}\right)^{\frac{1}{2}}$ where $\lambda\!\!\!^{-}_p$ is the proton plasma wavelength

$$\lambda\!\!\!^{-}_p = \frac{c}{\left(\frac{4\pi N_o e^2}{m_p}\right)^{\frac{1}{2}}} \tag{3.30}$$

However, for the adiabatic assumption to be valid we require at the very least

$$\frac{m_p c^2 E_o^2}{2B_o^2} << e\Phi$$

which may be rewritten $\left(\frac{\lambda\!\!\!^{-}_p}{d}\right)^2 << 2$. Thus if this condition is well satisfied we have $\tau_e >> \tau$, and we need consider only the acceleration phase. Hence the total charge content of the neutral sheet (per unit length along the magnetic field) is expected to be

$$Q \simeq \frac{Id}{V_A}\{1 - (\frac{m_e}{m_p})^{\frac{1}{2}}\}. \qquad (3.31)$$

From this discussion we expect the sheet to be, on the whole, positively charged, the electron charge being of order $(m_e/m_p)^{\frac{1}{2}} \sim 1/40$ compared with the proton charge. If we divide Q by d we obtain a typical 'surface charge density' σ (i.e. charge per unit area of the sheet), and the electric field produced by such a sheet is $E_z \simeq 2\pi\sigma$, thus

$$E_z \simeq \frac{2\pi I}{V_A}$$

This is to be compared with the uniform Alfvén field $E_o = \Phi/d$ where $e\Phi = m_p V_A^2$ from Alfvén's formula for Φ. The ratio between these two fields is

$$\frac{E_z}{E_o} \simeq \frac{2\pi e I d}{m_p V_A^3} = \frac{ced}{m_p B_o^2}(4\pi N_o m_p)^{3/2} \qquad (3.32)$$

In order to obtain internal consistency with this model we require

$$\frac{m_p c^2 E^2}{2B_o^2} \ll e\Phi$$

where E is given by equation (3.32) for $E >> E_o$. Rearranging, this becomes

$$(\frac{B_o^2}{4\pi})^2 >> \frac{(N_o m_p c^2)^2}{2} \qquad (3.33)$$

i.e. the magnetic energy density must be somewhat larger than the mass-energy density of the particles. In such a case

and we investigate the relationship between points (1) and (2) in the stream. Point (1) is in the adiabatic flow and point (2) is in the field reversal region. By conservation of flux we have

$$F_1 = N_o v_1 dL_1 = N_o v_{z_1} d_{y1} = n_2 v_2 dL_2 \tag{3.34}$$

We also have $\frac{v_{z2}}{v_{y2}} = \frac{dz_2}{d_{y2}} = \tan\theta$ (see Fig. 3.7)

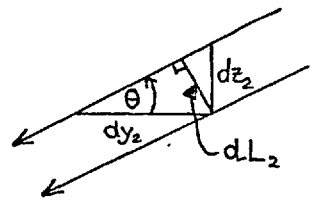

Figure 3.7

Thus we have $\cos\theta = \frac{dL_2}{dz_2} = \frac{v_{y2}}{v_2}$.

Then the surface charge density contributed by the stream is

$$d\sigma = n_2\, dz_2 = \frac{F_1 dz_2}{v_2 dL_2} = \frac{F_1}{v_{y2}} \tag{3.35}$$

and the current along the sheet is, of course

$$dI_{11} = q\, n_2\, v_{y2}\, dz_2 = q\, F_1 \frac{v_{y2}\, dz_2}{v_2\, dL_2} = q\, F_1$$

Since the point (1) is in the adiabatic flow region

$$F_1 = \frac{cN_o E_y}{B_o} dy_1 = -\frac{cN_o}{B_o}\left(\frac{\partial\phi}{\partial y}\right)_{y_1} dy_1 \tag{3.36}$$

and from the analysis of the particle orbits (equation (3.21))

$$v_{y2} \simeq v_2 = \left(\frac{2q}{m}\right)^{\frac{1}{2}} \left(\phi(y_1) - \phi(y_2)\right)^{\frac{1}{2}} \operatorname{sgn}(q) \tag{3.37}$$

where $\phi(y_1)$ and $\phi(y_2)$ are the electrostatic potential in the sheet at points (1) and (2)

Thus

$$d\sigma(\phi(y)) = -\frac{2ecN_o}{B_o}\left(\frac{\partial\phi}{\partial y}\right)_{y_1} dy_1 \Big/ \left(\frac{2q}{m}\right)^{\frac{1}{2}} \left(\phi(y_1) - \phi(y_2)\right)^{\frac{1}{2}}$$

where we have multiplied by two to account for particle inflow from both sides of the sheet. From their direction of travel the protons which contribute to the charge density at $\phi(y_2)$ enter the sheet with $\phi(y_2) \le \phi(y_1) \le \Phi$, while electrons contributing at (y_2) enter with $0 \le \phi(y_1) \le \phi(y_2)$.

Thus

$$\sigma_p(\phi) = \frac{2ecN_o}{B_o}\left(\frac{m_p}{2e}\right)^{\frac{1}{2}} \int_{\phi}^{\Phi} \frac{d\phi'}{(\phi' - \phi)^{\frac{1}{2}}}$$

hence $$\sigma_p(\phi) = \left(\frac{4ecN_o}{B_o}\right)\left(\frac{m_p}{2e}\right)^{\frac{1}{2}} \left\{\Phi - \phi\right\}^{\frac{1}{2}} \tag{3.38}$$

and $$\sigma_e(\phi) = -\frac{2ecN_o}{B_o}\left(\frac{m_e}{2e}\right)^{\frac{1}{2}} \int_{0}^{\phi} \frac{d\phi'}{(\phi - \phi')^{\frac{1}{2}}}$$

hence $$\sigma_e(\phi) = -\frac{4ecN_o}{B_o}\left(\frac{m_e}{2e}\right)^{\frac{1}{2}} \phi^{\frac{1}{2}} \tag{3.39}$$

(We do not expect there to be large potential differences across the sheet thickness at a given y-position for this model). Thus the total surface charge in the sheet at potential ϕ due to the oscillating particles is

$$\sigma(\phi) = \frac{4ecN_o}{B_o}\left(\frac{m_p}{2e}\right)^{1/2}\left\{(\Phi-\phi)^{1/2} - \left(\frac{m_e}{m_p}\phi\right)^{1/2}\right\} \qquad (3.40)$$

As we anticipated, the sheet is mainly positively charged, and this is largest near $\phi = 0$; the negative charge is largest near $\phi = \Phi$. Examination shows that for $\phi = \Phi/2$ equation (3.40) is identical to Q/d from equation (3.31) which was derived earlier from the more qualitative time-of-flight argument.

Since we now have the charge as a function of the potential and the potential may be derived from the charge (with boundary conditions) by Coulomb's equation, we can now write down an integral equation for $\phi(y)$ in the neutral sheet. We assume that the charge is uniformly distributed over a constant thickness a, giving a charge density $\rho(\phi) = \sigma(\phi)/a$ for $|z| \leq a$. Although we could use the value of 'a' discussed in this chapter, the results do not depend on its assumed value, provided $d/a >> 1$. For convenience $d/a = 100$ was used here in the numerical work. Then Coulomb's equation for a slab of charge of thickness 'a' gives

$$\phi(y) = \phi_o\left(\frac{1}{2} - \frac{y}{d}\right) + \int_{-d/2}^{d/2} dy_1 \int_{-a/2}^{a/2} dz_1 \int_{-\infty}^{\infty} dx_1 \, \frac{\sigma(\phi(y_1))}{a} \times$$

$$\times \left\{ \frac{1}{\left(z_1^2 + x_1^2 + (y-y_1)^2\right)^{1/2}} - \frac{1}{\left(z_1^2 + x_1^2 + (d/2 - y_1)^2\right)^{1/2}} \right\} \qquad (3.41)$$

where the last term in the curly bracket produces a constant contribution to $\phi(y)$ which ensures $\phi(y = d/2) = 0$. The first term which varies linearly with y is used to set the boundary condition $\phi(y = -d/2) = \Phi$ by adjustment of ϕ_o (see Fig. 3.8).

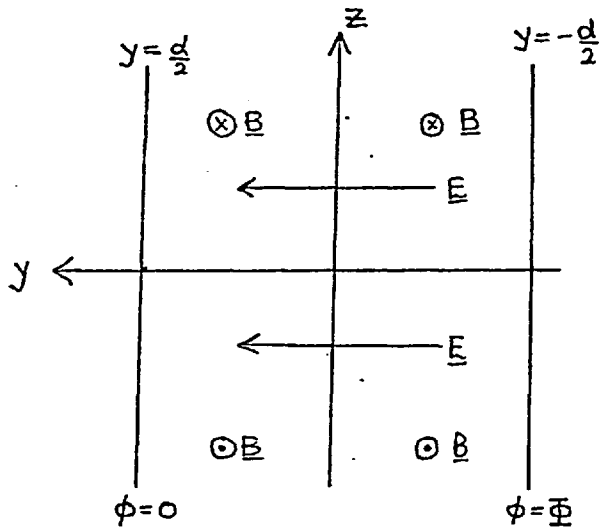

Figure 3.8

Performing the above integrals over z_1 and x_1 we find

$$\phi(y) = \phi_0\left(\frac{1}{2} - \frac{y}{d}\right) + \int_{-d/2}^{d/2} dy_1 \, \frac{\sigma(\phi(y_1))}{a} \, f(y,y_1) \tag{3.42}$$

where the Coulomb geometric factor $f(y,y_1)$ is given by

$$f(y,y_1) = a \log\left\{\frac{\left(\frac{d}{2}-y_1\right)^2 + \left(\frac{a}{2}\right)^2}{(y-y_1)^2 + \left(\frac{a}{2}\right)^2}\right\} + \tag{3.43}$$

$$+ 4\left\{\left(\frac{d}{2}-y_1\right)\tan^{-1}\left(\frac{a}{2\left(\frac{d}{2}-y_1\right)}\right) - (y-y_1)\tan^{-1}\left(\frac{a}{2(y-y_1)}\right)\right\}$$

Since $\phi(y = d/2) = \Phi$ we thus have

$$\phi_0 = \Phi - \int_{-d/2}^{d/2} dy_1 \, \frac{\sigma(\phi(y_1))}{a} \, f\left(-\frac{d}{2}, y_1\right)$$

so that, finally

$$\phi(y) = \Phi\left(\frac{1}{2} - \frac{y}{d}\right) + \int_{-d/2}^{d/2} dy_1 \, \frac{\sigma(\phi(y_1))}{a}\left(f(y,y_1) - \left(\frac{1}{2} - \frac{y}{d}\right) f\left(-\frac{d}{2}, y_1\right)\right) \tag{3.44}$$

where the integral term now represents the whole effect of the charges.

We now dedimensionalize by writing $y' = Y/d$ and $\phi' = \phi/\Phi$ to obtain for $-\frac{1}{2} \le y' \le \frac{1}{2}$

$$\phi'(y') = \left(\tfrac{1}{2} - y'\right) + A \int_{-1/2}^{1/2} dy_1' \, \sigma'(\phi'(y_1')) \left\{ f'(y', y_1') - \left(\tfrac{1}{2} - y'\right) f'\left(-\tfrac{1}{2}, y_1'\right) \right\} \tag{3.45}$$

where $$\sigma'(\phi'(y_1')) = \left(1 - \phi'(y_1')\right)^{1/2} - \left(\frac{m_e}{m_p}\right)^{1/2} \phi'^{1/2}(y_1')$$

$$f'(y', y_1') = \log \left\{ \frac{\left(\frac{1}{2} - y_1'\right)^2 + \left(\frac{a'}{2}\right)^2}{(y' - y_1')^2 + \left(\frac{a'}{2}\right)^2} \right\}$$

$$+ \frac{4}{a'} \left\{ \left(\tfrac{1}{2} - y_1'\right) \tan^{-1}\left(\frac{a'}{2\left(\frac{1}{2} - y_1'\right)}\right) - (y' - y_1') \tan^{-1}\left(\frac{a'}{2(y' - y_1')}\right) \right\}$$

and $$A = 4(2\pi m_p)^{1/2} \left(\frac{ceN_o{}^{3/2}d}{B_o{}^2}\right) .$$

The value of the integral is of order unity, and so the value of parameter A determines the importance of the charges in the sheet. In fact

$$A = \frac{1}{\sqrt{2}\,\pi} \left(\frac{E_z}{E_o}\right) \tag{3.46}$$

from equation (3.32). For $A \ll 1$ the potential is distributed linearly across the sheet.

Solutions of (3.42) were obtained by successive substitutions of $\phi'(y')$ for $A = 0.46$, 2.40 and 5.16, taking a linear variation as the first approximation to $\phi'(y')$ for $A = 0.46$. The consistent solution for this value of A was then used as the first approximation for the next highest value

of A. As the value of A becomes larger than one, such that the integral term in (3.45) becomes more important that the linear term, the convergence became very poor, but the results for the above values are sufficient to indicate the trends. (There exists no standard technique for the solution of such non-linear integral equations as (3.45) for the case $A > 1$). The results obtained, of $\phi'(y')$ and $\sigma'(y')$ are shown in Fig. 3.9a,b. We see that the effect of the positive charge in the sheet is to localize the Alfvén potential drop over a short distance near the $\phi = 0$ boundary, as we might have expected from the direction of the electric field produced by the charge. This decreases the time the average proton remains in the field reversal region, by both increasing the accelerating electric field and reducing the distance travelled, i.e.

$$t_p = \left(\frac{2m_p y}{eE}\right)^{\frac{1}{2}}$$

and putting $E_y = \Phi/2$, we have

$$t_p = \frac{1}{E}\left(\frac{m_p \Phi}{e}\right)^{\frac{1}{2}} \qquad (3.47)$$

Thus t_p decreases as $1/E$ for a given potential drop $k\Phi$, and hence the total charge is reduced.

From equation (3.46), and writing $E_z L \approx \Phi$ where L is approximately the length over which the potential drop is localized in the sheet, we have

$$\frac{L}{d} \approx \frac{1}{\sqrt{2}\,\pi\, A}$$

Thus for $A = 0.46, 2.40, 5.16$, we expect $L/d \approx 0.49, 0.094, 0.044$, in good agreement with the results of Fig. 3.9a. The

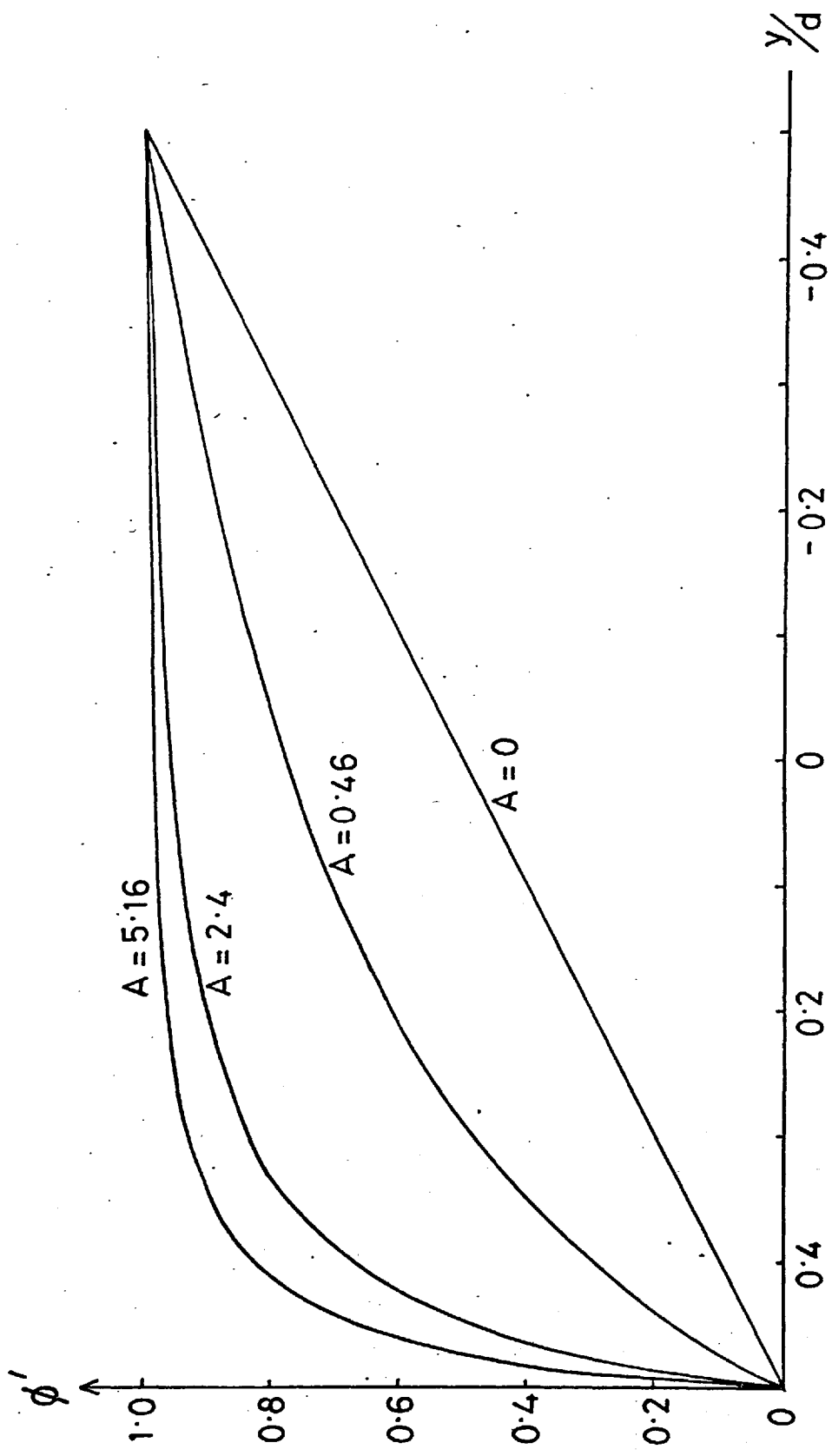

Figure 3.9(a): ϕ' versus Y/d along the neutral line.

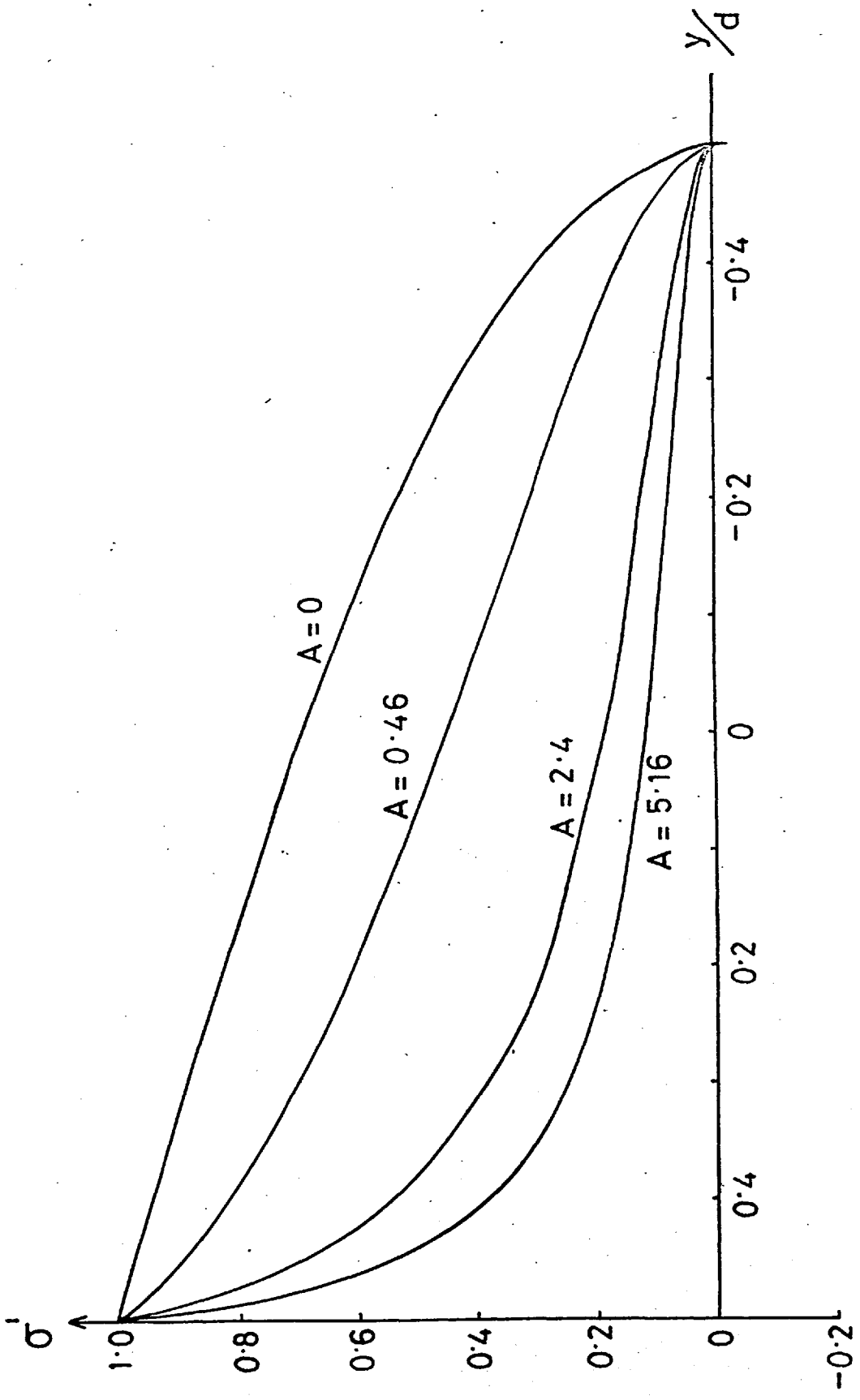

Figure 3.9(b): σ' versus y/d along the neutral line.

flow of plasma into the neutral sheet can then be obtained by solving Laplace's equation in the external region using $\phi'(y')$ as one of the boundary conditions. For the presentation of the resulting flow systems (plasma flows along the equipotentials) in Fig. 3.10 a,b,c we have taken the $\phi'=0$ equipotential to be given by the line $y'=\frac{1}{2}$ and $\phi'=\Phi$ is given by $y'=-\frac{1}{2}$. (i.e. flow between parallel boundaries). The method used to obtain solutions of Laplace's equation with such boundary conditions will be given in the next chapter. As can be seen, most of the plasma inflow occurs near $\phi=0$ for $A>1$, where the electric field E_y is large. The electric fields just outside the current sheet, E_y, E_z and $|E|$, normalized to the uniform Alfvén field E_o, are shown in Figs. 3.11 (a, b and c). A logarithmic plot of E_y/E_o versus ϕ/Φ is shown in Fig. 3.12, where it can be seen that, due to the increasing electron charge near $\phi=\Phi$, E_y tends to rise near this boundary. The system would be symmetrical about $y=0$ for equal mass particles. Finally, E_y, E_z and $|E|$ are plotted against ϕ in Figs 3.13 a,b,c.

(iii) Summary and Discussion

We have shown that the simple model of adiabatic drift towards the neutral sheet followed by Speiser-like acceleration along the neutral line is not valid for the geomagnetic tail due to the presence of the charge density of accelerating particles in the sheet. This charge creates such an electric field as to dominate the structure of the system, and the Alfvén-Speiser picture is only valid if (equation (3.33))

$$\frac{B_o^2}{4\pi} > \frac{N_o m_p c^2}{\sqrt{2}} .$$

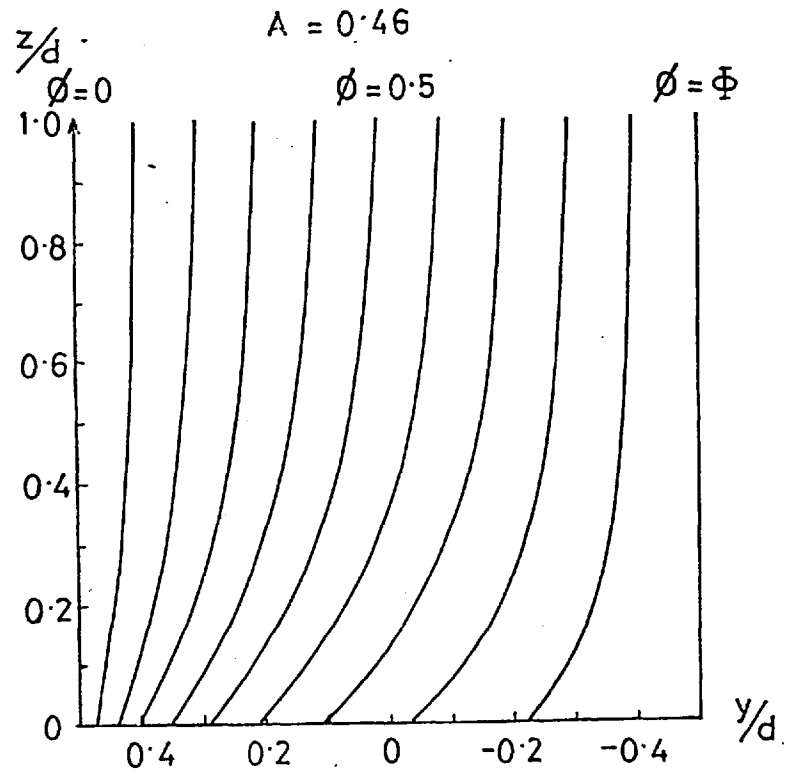

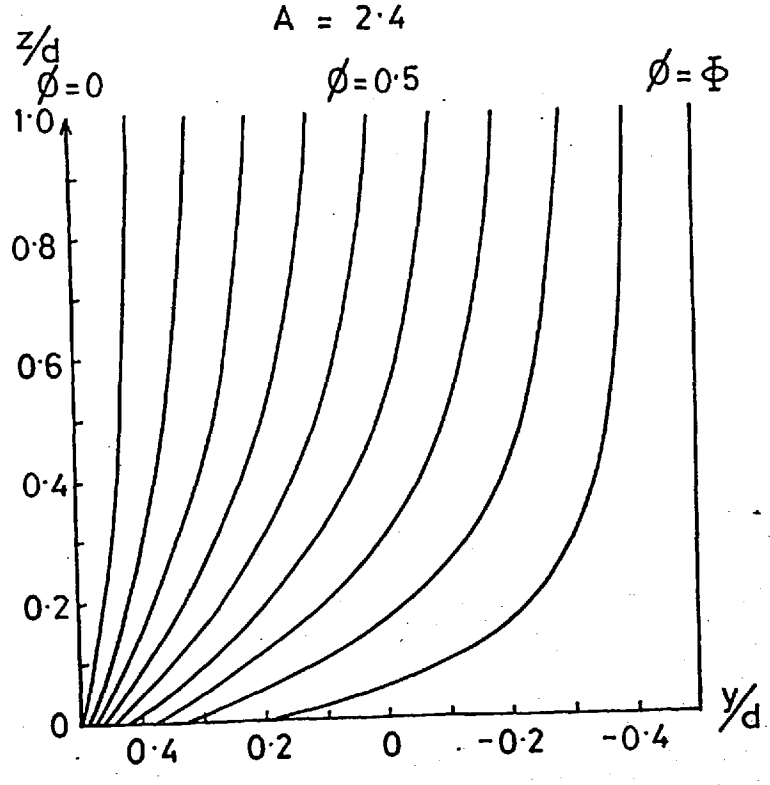

Figure 3.10(a,b)

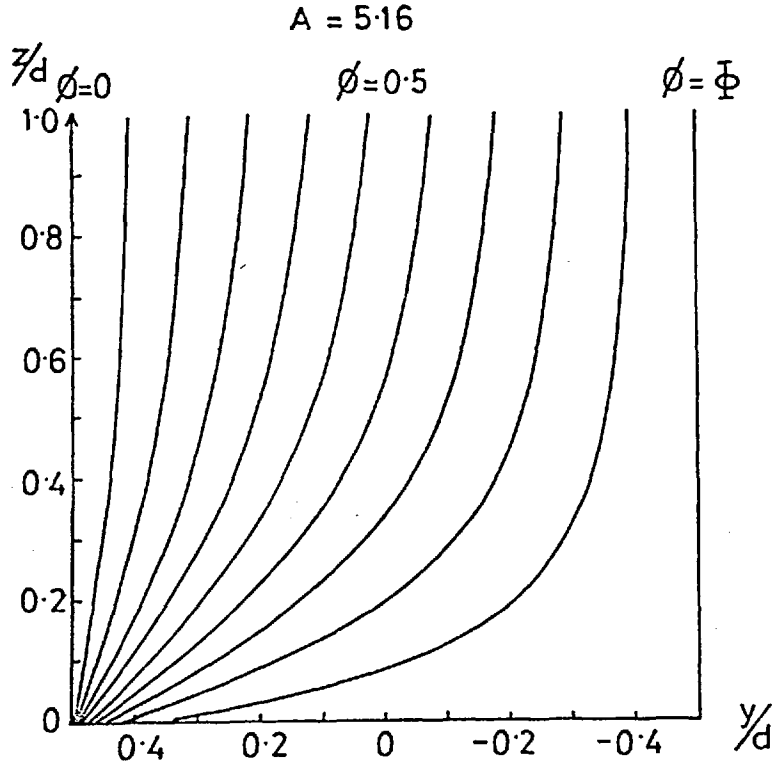

Figure 3.10 (a,b,c): Flow lines of plasma into the neutral sheet (i.e. equipotentials) for A = 0.46, 2.4, 5.16; obtained by solving Laplace's equation in a rectangular half-space using the results of Fig. 3.9(a) as boundary conditions along $z/_d = 0$.

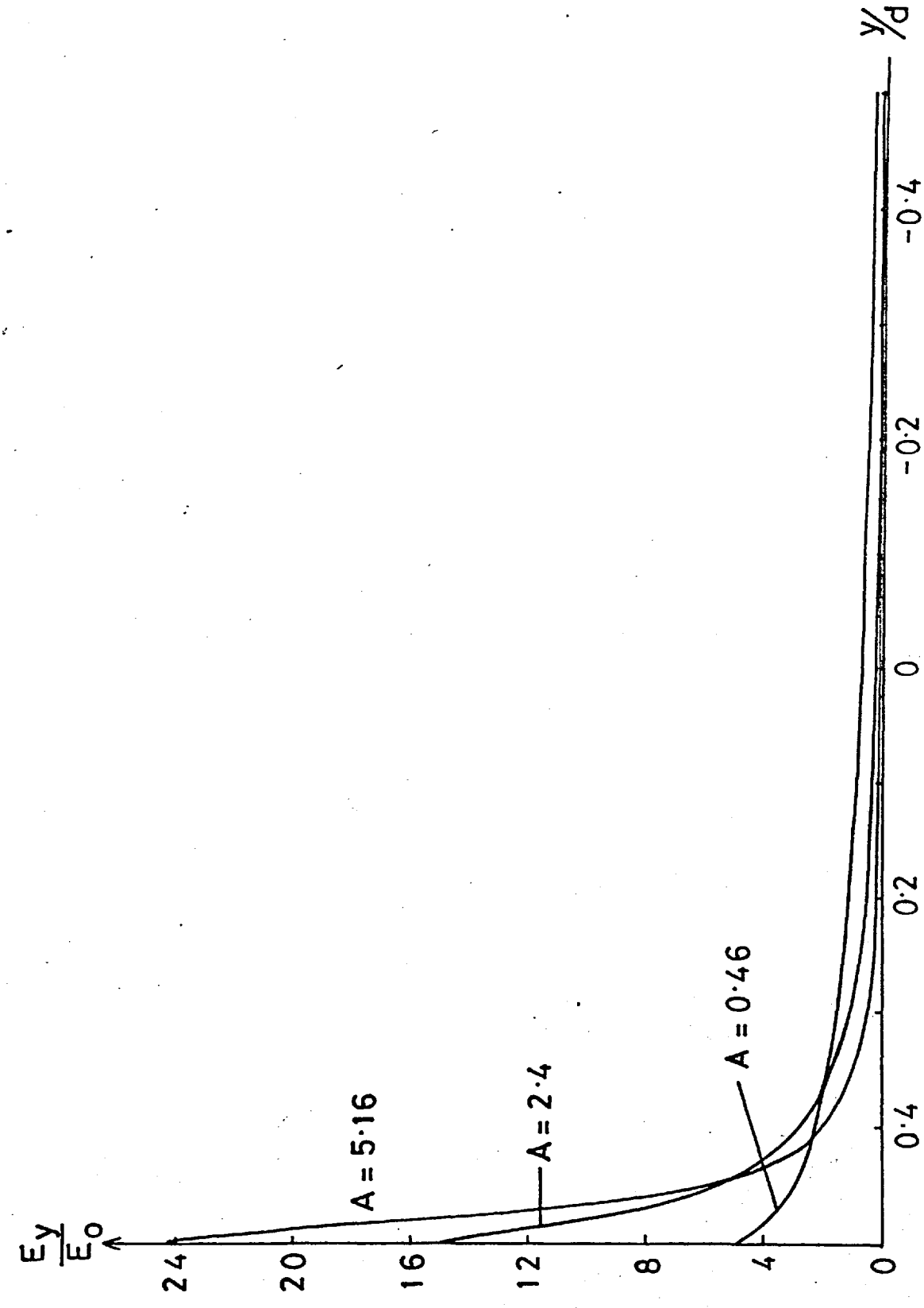

Figure 3.11(a): E_y along the neutral line, plotted against $Y/_d$ and normalized to the Alfvén electric field $E_o = \frac{\Phi}{d}$.

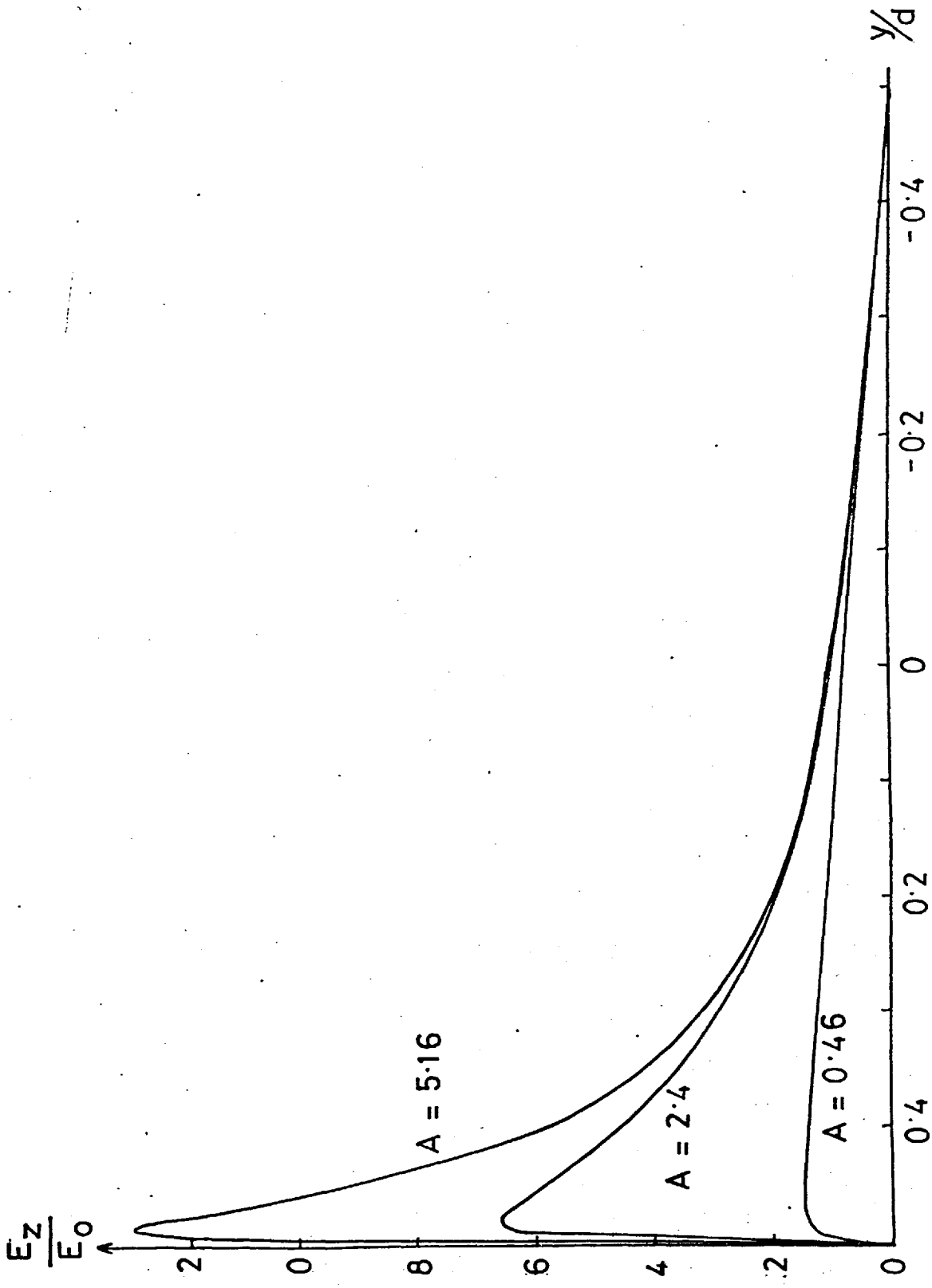

Figure 3.11(b): E_z just outside the current sheet, plotted against Y/d, and normalized to the Alfvén electric field $E_o = \Phi/d$.

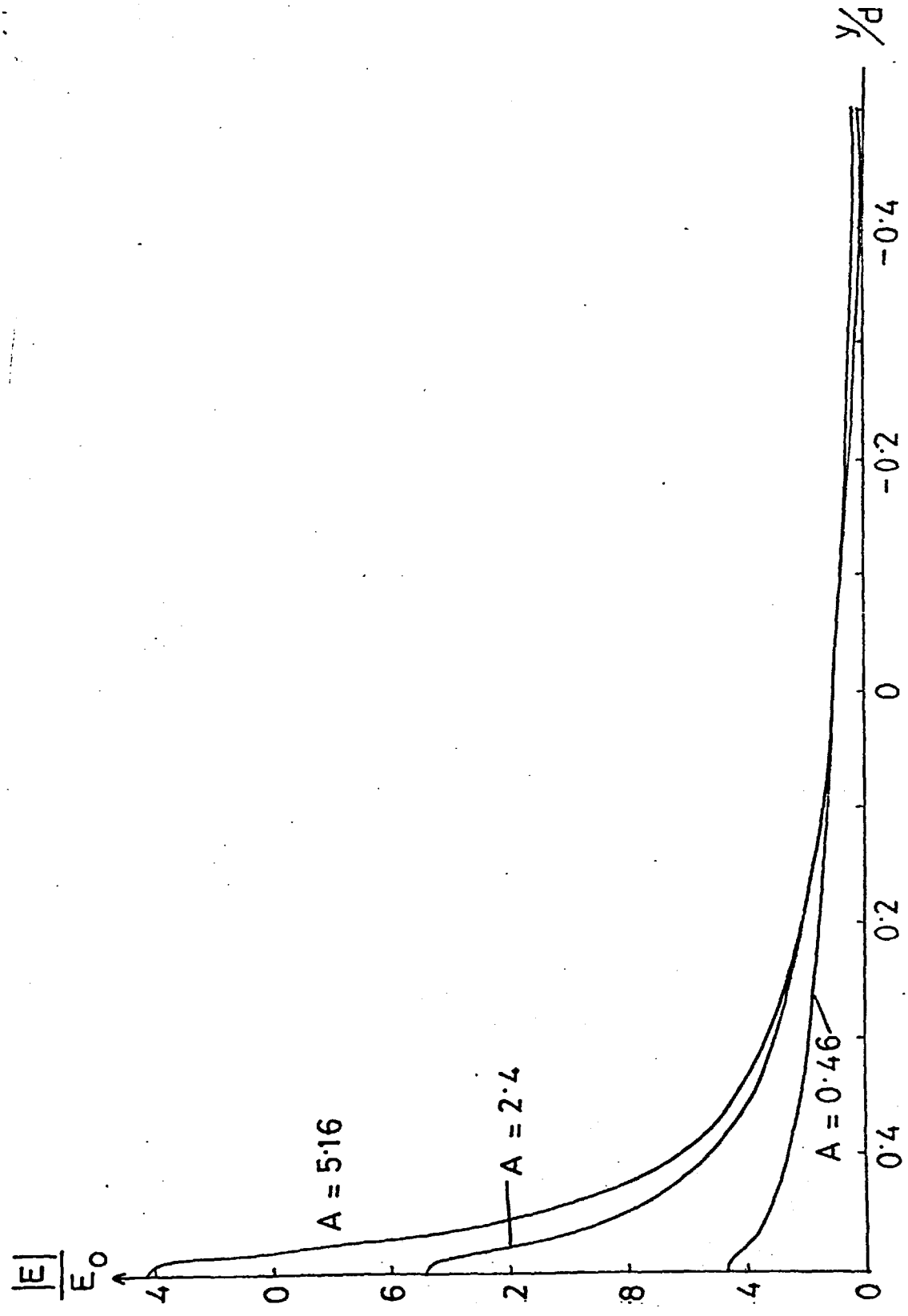

Figure 3.11(c): $|E| = (E_z^2 + E_y^2)^{\frac{1}{2}}$ just outside the current sheet plotted against Y/d and normalized to the Alfvén electric field $E_o = \Phi/d$.

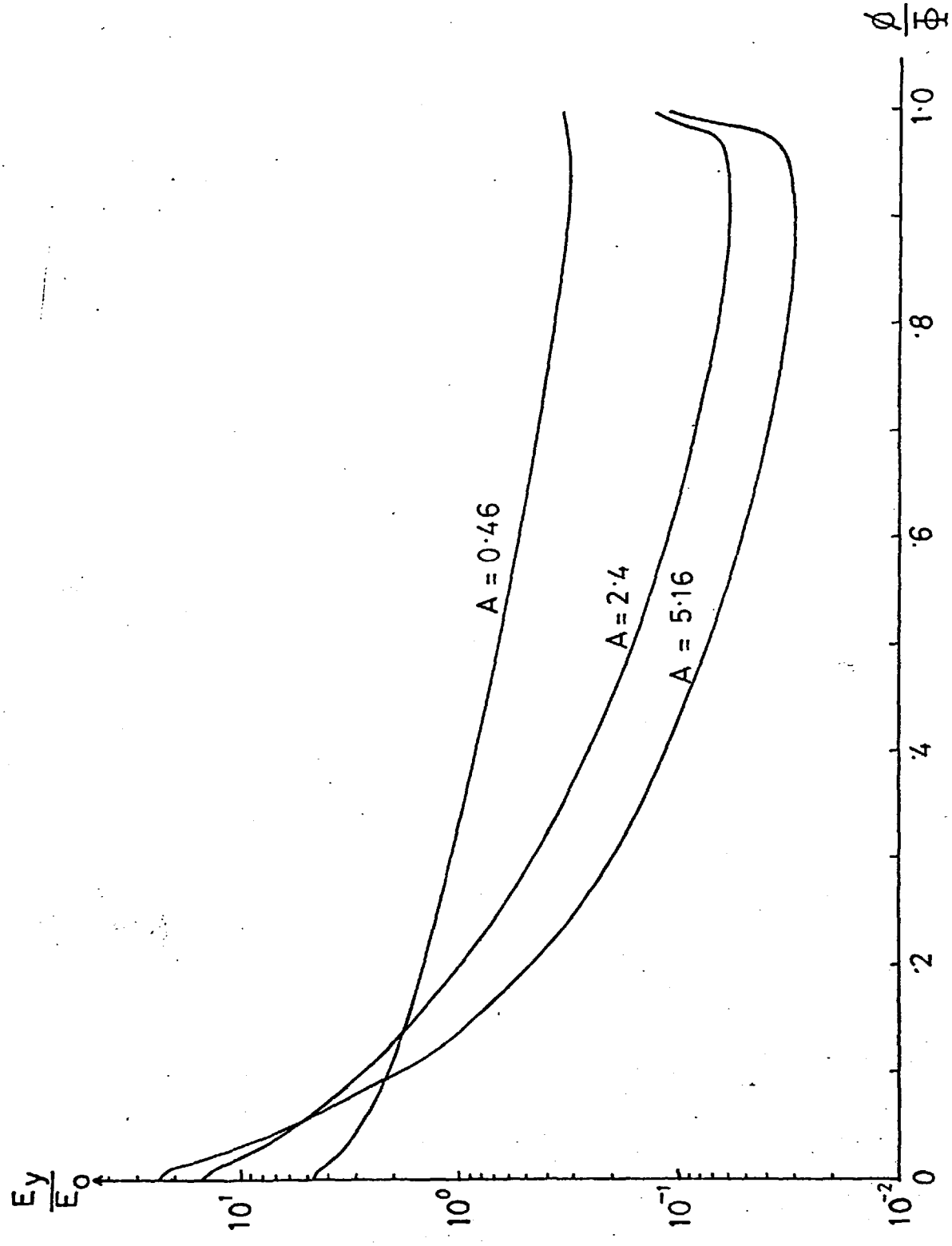

Figure 3.12: Logarithmic plot of E_y/E_o along the neutral line against ϕ/Φ .

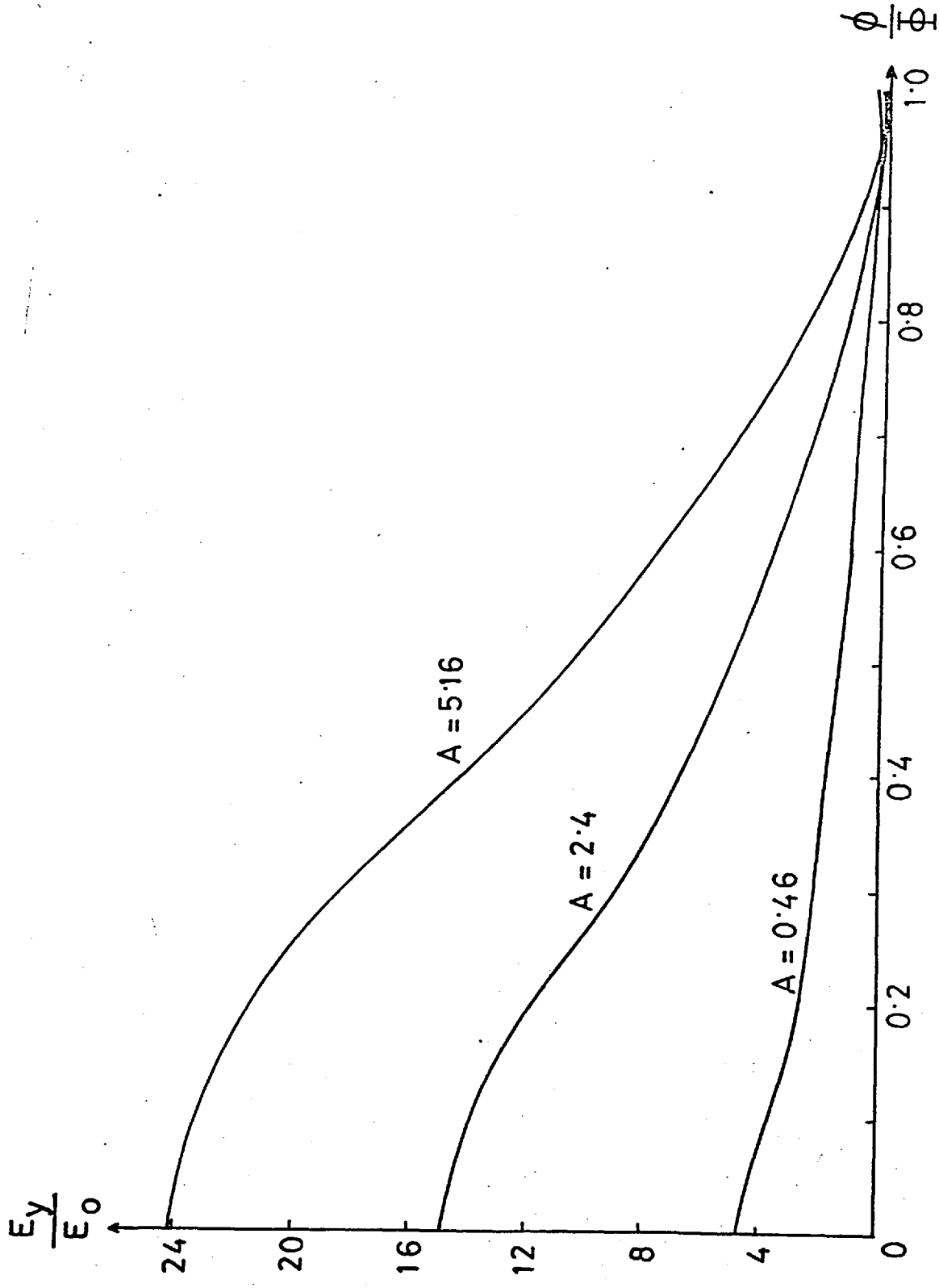

Figure 3.13(a): $\frac{E_y}{E_0}$ along the neutral line, plotted against ϕ/ϕ

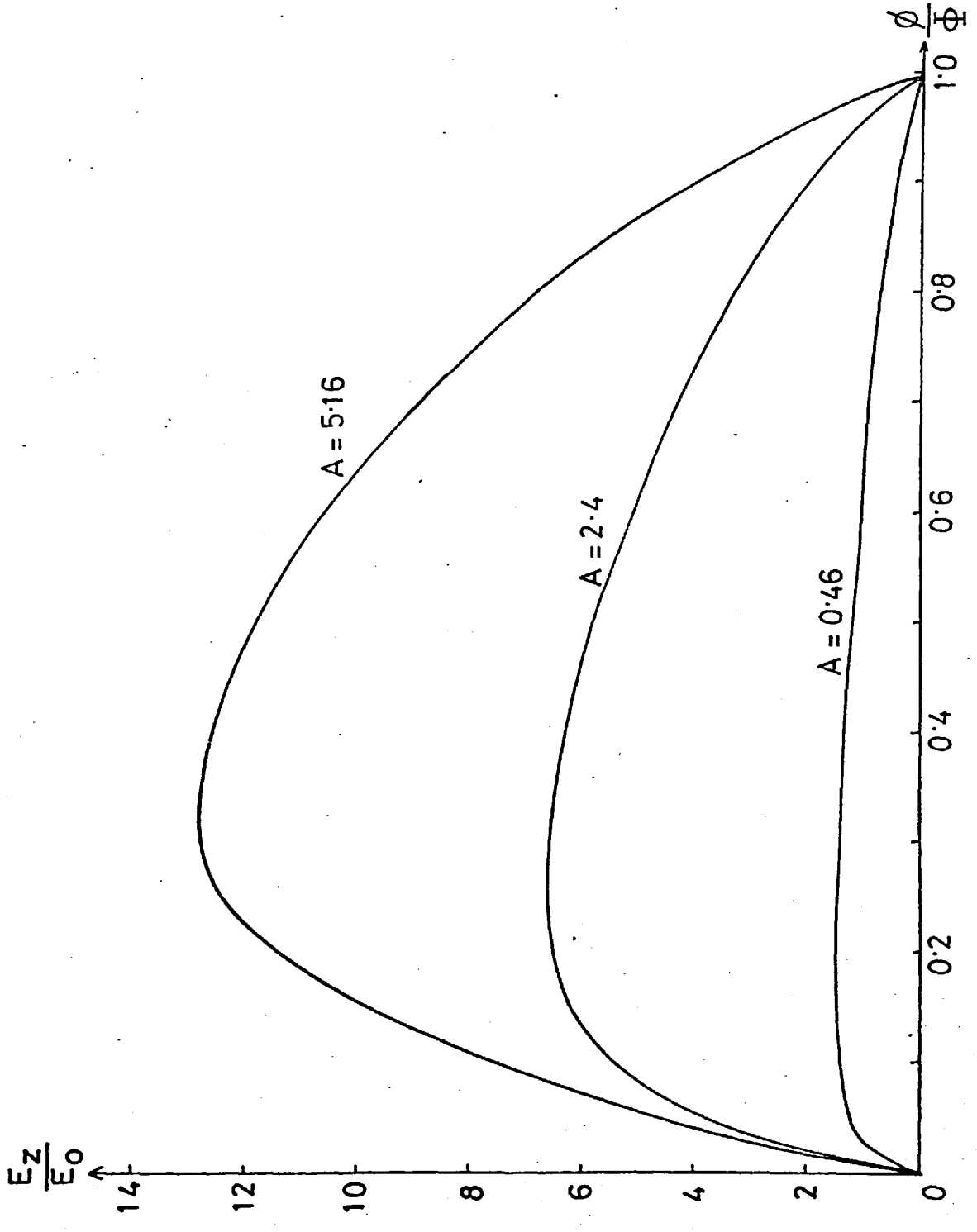

Figure 3.13(b): $\frac{E_z}{E_o}$ just outside the current sheet, plotted against ϕ/Φ .

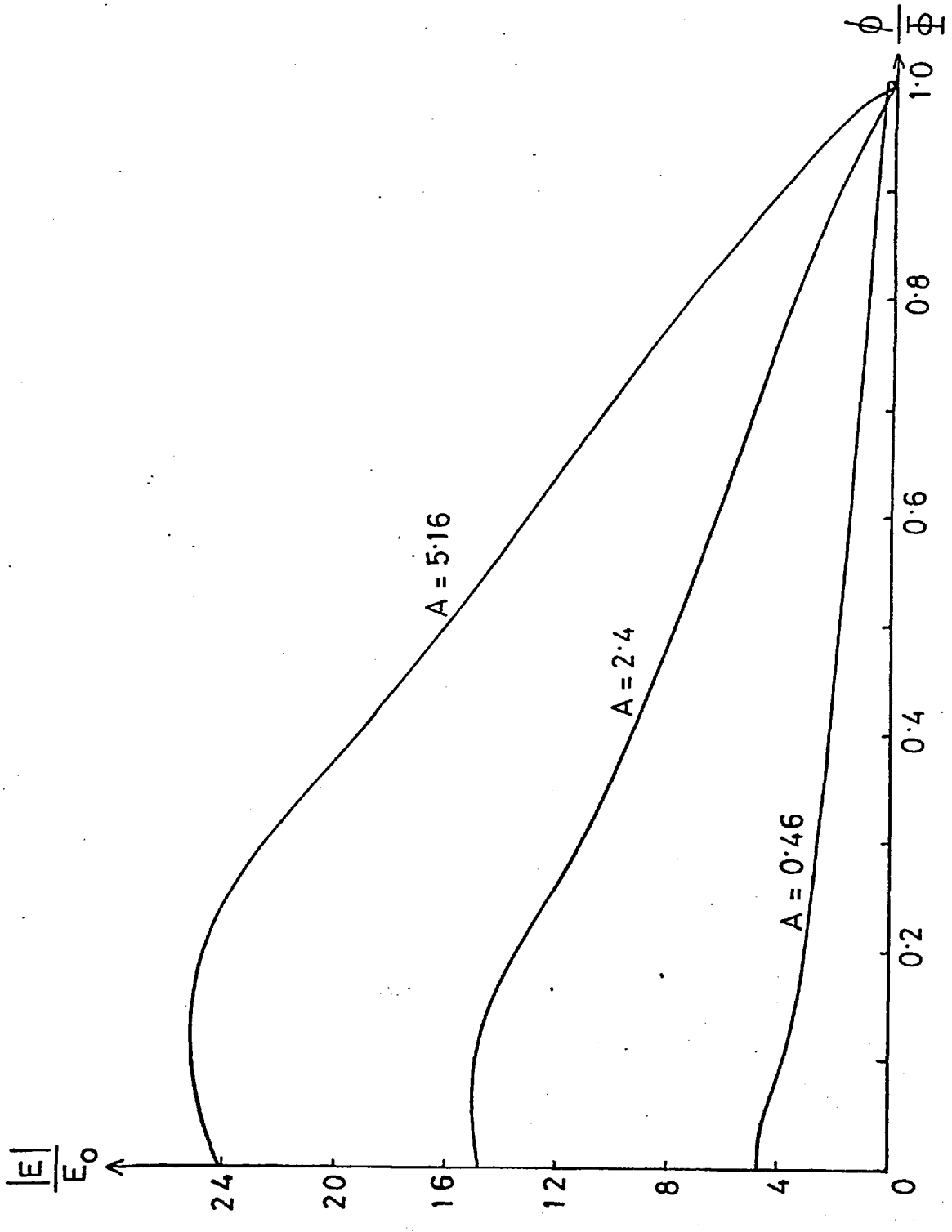

Figure 3.13(c): $\frac{|E|}{E_0}$ just outside the current sheet, plotted against ϕ/Φ .

It should, however, be emphasized that Alfvén's result for the total potential across the system is still valid for 'non-adiabatic flow' models, since this only depends on the assumption that all incoming particles contribute to the current.

For the tail field value of $B_o \simeq 10\gamma$ the above condition for the validity of the adiabatic flow model becomes $N_o < 10^{-5}$ cm^{-3}. For reasonable values of the density ($N_o \sim 0.1$ cm^{-3}) the electric field that would be produced by the charges greatly exceeds the Alfvén field, leading to breakdown of adiabatic assumptions. Such a situation corresponds to $A >> 1$ and we would expect approximate charge neutrality to hold in this case (i.e. $(\sigma_p - \sigma_e)/\sigma_p << 1$). From equation (3.40) this would be

$$\phi \simeq \frac{\Phi}{(1 + m_e/m_p)}$$

in the sheet, with very large electric fields near $\phi = 0$. Thus for such situations we need to consider the properties of cold plasma drift flow where the energies in the flow become of the same order as the potential across the system, and also the condition for charge neutrality in the sheet. If the flow velocities are much larger than $v_o \sim cE_o/B_o$ we might expect a much thicker field reversal region than we have given here. The negative charge contribution of electrons adiabatically drifting towards the neutral sheet then needs reconsideration as a source of neutralization for the accelerating protons.

In the next chapter the general theory of cold plasma drift-flow is presented, while in Chapter 5 further consideration is given to the structure of the field reversal region.

References

Alfvén, H. 1968. Some properties of magnetospheric neutral surfaces. J. Geophys. Res. 73, 4379-4381.

Cowley, S.W.H. 1971a. The Adiabatic Flow model of a neutral sheet. Cosmic Electrodynamics 2, 90-104.

Northrop, T.G. 1963. The Adiabatic Motion of Charged Particles. Interscience Publishers, New York.

Speiser, T.W. 1965. Particle trajectories in model current sheets, 1: Analytical Solutions. J. Geophys. Res. 70, 4219-4226.

CHAPTER 4

THE DRIFT-FLOW OF COLD PLASMA

(i) Introduction

In this chapter we shall derive the equations which govern the flow of cold plasma in crossed electric and magnetic fields for the case where the particle energies in the flow are not negligible compared with the potential energy across the system. We shall only consider two-dimensional flow in a plane, where the electric field is in the plane of the flow and the magnetic field perpendicular to it. Specifically, we will treat the problem where the flow is uniform at infinity but not necessarily of constant density. The assumption is made that the scale lengths characteristic of the flow are large compared with particle gyroradii.

In the simplest approximation used in the last chapter the inertia of the plasma is entirely neglected, the equation of motion then becomes

$$\underline{E} + \frac{\underline{v} \wedge \underline{B}}{c} = \underline{0} \qquad \text{or} \qquad \underline{v} = \frac{c\,\underline{E} \wedge \underline{B}}{B^2} \tag{4.1}$$

since by assumption $\underline{E} \cdot \underline{B} = 0$. Plasma streams perpendicular to the electric field, or in other words, along equipotentials. The velocity in equation (4.1) is independent of particle charge or mass so that all constituents of the plasma have the same velocity at all points. Thus there are no charge or current densities in the flow if the plasma at infinity is charge neutral. The electromagnetic field is then determined solely by the system boundary conditions, i.e. the field

sources.

However, of course, if the electromagnetic field imposed by the boundary conditions is non-uniform then the velocity along the equipotentials of the plasma changes. This implies that the particles change kinetic energy and must therefore slowly drift across equipotentials. The drift across equipotentials is obviously dependent on the particle mass and charge, the effect being more severe the larger is the mass. Such drifts obviously give rise to current densities in the flow leading to perturbations in the magnetic field; the charge neutrality of the plasma also needs investigation. We here derive the equations which determine the electromagnetic field and flow of the cold plasma when boundary conditions impose non-uniformities.

The equation of motion of a particle in the steady state can be written in Eulerian form, since by assumption the plasma is cold, having no 'thermal' motions. The velocity is then regarded as a function of position, so that

$$m\,(\underline{v}.\underline{\nabla})\underline{v} = q\left(\underline{E} + \frac{\underline{v}\wedge\underline{B}}{c}\right) \tag{4.2}$$

By using the vector identity

$$(\underline{v}.\underline{\nabla})\underline{v} = \underline{\nabla}\left(\frac{v^2}{2}\right) - \underline{v}\wedge(\underline{\nabla}\wedge\underline{v})$$

and since $\underline{E} = -\underline{\nabla}\phi$ in the steady state equation (4.2) becomes

$$\underline{\nabla}\left(q\phi + \frac{mv^2}{2}\right) = m\,\underline{v}\wedge(\underline{\nabla}\wedge\underline{v}) + \frac{q}{c}\underline{v}\wedge\underline{B} \tag{4.3}$$

The right hand side of equation (4.3) is a vector perpendicular to $\underline{v}$, so that $\underline{\nabla}(q\phi + \frac{mv^2}{2})$ is also perpendicular to $\underline{v}$. Thus the flow lines are lines of constant total energy, a very reasonable result! Hence we may in general write, for some λ

$$\underline{v} = \left(\frac{c\lambda}{qB}\right) \frac{\underline{B}}{B} \wedge \underline{\nabla}\left(q\phi + \frac{mv^2}{2}\right) \tag{4.4}$$

or equivalently

$$m\,\underline{v} \wedge (\underline{\nabla} \wedge \underline{v}) = (1-\lambda)\underline{\nabla}\left(q\phi + \frac{mv^2}{2}\right) \tag{4.5}$$

(ii) <u>The Velocity Expansion</u>

Now according to the well-known drift-theory of particle motions in an electromagnetic field (see for example, Northrop, 1963), the velocity of a particle at a point in the flow may be expressed in terms of the electromagnetic field values (and their derivatives) at that point, so long as the scale lengths L for changes in the field are much greater than the particle gyroradius (e.g. equation (4.1) for example). If the particles are cold (zero magnetic moment) the gyroradius is zero, and is replaced in the theory by the distance the particle travels, moving with the local drift velocity in $(\frac{1}{2\pi})$ of a gyroperiod. This distance we call the gyrolength g and is given by

$$g = \frac{v_D}{\Omega} \tag{4.6}$$

where $\Omega = \frac{eB}{me}$ is the local gyrofrequency.

For cold particles $\underline{v}_D$, the drift velocity, is the total

velocity of the particle and is determined as a series in $g/_L$ from the equation of motion (4.1), which we now write as

$$\underline{v} = \frac{c\underline{E}\wedge\underline{B}}{B^2} + \frac{mc}{q}\frac{\underline{B}}{B^2}\wedge(\underline{v}.\underline{\nabla})\underline{v} \qquad (4.7)$$

The series is generated as follows. As a first approximation we take

$$\underline{v}^{(o)} = \frac{c\underline{E}\wedge\underline{B}}{B^2} \qquad (4.8)$$

(i.e. neglect the inertial term as in equation (4.1)), and then substitute $\underline{v}^{(0)}$ into the inertial term to obtain $\underline{v}^{(1)}$ i.e.

$$\underline{v}^{(1)} = \frac{mc}{q}\frac{\underline{B}}{B^2}\wedge(\underline{v}^{(o)}.\underline{\nabla})\underline{v}^{(o)} \qquad (4.9)$$

These two terms are the same as those given by Northrop (1963). To obtain the general term we write

$$(\underline{v}^{(o)}+\underline{v}^{(1)}+\underline{v}^{(2)}+\cdots) = \frac{c\underline{E}\wedge\underline{B}}{B^2} + \frac{mc}{q}\frac{\underline{B}}{B^2}\wedge\left[(\underline{v}^{(o)}+\underline{v}^{(1)}+\cdots).\underline{\nabla}\right](\underline{v}^{(o)}+\underline{v}^{(1)}+\cdots)$$

to obtain

$$\underline{v}^{(j)} = \frac{mc}{q}\frac{\underline{B}}{B^2}\wedge\sum_{K=0}^{j-1}(\underline{v}^{(K)}.\underline{\nabla})\underline{v}^{(j-K-1)} \quad \text{for } j\geq 1 \qquad (4.10)$$

Thus we obtain $\underline{v}^{(j)}$ in terms of all lower-order velocities $\underline{v}^{(0)}$ to $\underline{v}^{(j-1)}$, each one of which is ultimately related to $\underline{v}^{(0)}$, i.e. to the local values of the fields $\underline{E}$ and $\underline{B}$. Taking a typical term in the series for $\underline{v}^{(j)}$ we have

$$|\underline{v}^{(j)}| \sim \mathcal{O}\left(\frac{mc}{q}v^{(j-1)}|\nabla\underline{v}^{(o)}|\right) \sim \mathcal{O}\left(\frac{g}{L}v^{(j-1)}\right)$$

It is clear therefore that we have generated a series, valid when the gyrolength is smaller than the field scale length, which relates the velocity of a particle at a point to the local field values. This velocity expansion must satisfy equations (4.4) and (4.5) and hence determines λ as a power series in g/L in the region where the drift theory is valid. In order to do this we first define an ordering of the energy $\varepsilon = q\phi + mv^2/2$ of the particle, consistent with the velocity ordering:

$$\varepsilon^{(0)} = q\phi \qquad \varepsilon^{(j)} = \frac{m}{2}\sum_{K=0}^{j-1} \underline{v}^{(K)} \cdot \underline{v}^{(j-K-1)} \quad \text{for } j \geq 1$$

such that $\varepsilon^{(1)} = \frac{m v^{2(0)}}{2}$ $\varepsilon^{(2)} = m\underline{v}^{(0)} \cdot \underline{v}^{(1)}$ etc.

From equation (4.4) we should then find

$$\underline{v}^{(j)} = \frac{c}{q}\frac{\underline{B}}{B^2} \wedge \sum_{K=0}^{j} \lambda^{(K)} \underline{\nabla} \varepsilon^{(j-K)}$$

For $j=0$ we have $\underline{v}^{(0)} = \frac{c}{q}\frac{\underline{B}}{B^2} \wedge (\lambda^{(0)}\, \underline{\nabla} q\phi)$. Comparing with equation (4.8) shows $\lambda^{(0)} = 1$. Similarly, for j=1 we have

$$\underline{v}^{(1)} = \frac{c}{q}\frac{\underline{B}}{B^2} \wedge \left(\lambda^{(0)} \underline{\nabla} \varepsilon^{(1)} + \lambda^{(1)} \underline{\nabla} \varepsilon^{(0)}\right) \tag{4.11}$$

From equation (4.9) we have

$$\underline{v}^{(1)} = \frac{mc}{q}\frac{\underline{B}}{B^2} \wedge (\underline{v}^{(0)} \cdot \underline{\nabla})\underline{v}^{(0)} = \frac{mc}{q}\frac{\underline{B}}{B^2} \wedge \left(\underline{\nabla}\left(\frac{v^{(0)2}}{2}\right) - \underline{v}^{(0)} \wedge (\underline{\nabla} \wedge \underline{v}^{(0)})\right)$$

In general from equation (4.10)

$$\underline{v}^{(j)} = \frac{c}{q}\frac{\underline{B}}{B} \wedge \underline{F}^{(j)} \qquad \text{where} \qquad \underline{F}^{(0)} = \frac{\underline{\nabla}(q\phi)}{B}$$

$$\text{and } \underline{F}^{(j)} = \frac{m\sum_{K=0}^{j-1}(\underline{v}^{(K)}\cdot\underline{\nabla})\underline{v}^{(j-K-1)}}{B} \qquad (4.12)$$

so that

$$\underline{v}^{(m)}\wedge(\underline{\nabla}\wedge\underline{v}^{(n)}) = \left(\frac{c}{q}\right)^2\left(\frac{\underline{B}}{B}\wedge\underline{F}^{(m)}\right)\wedge\left(\underline{\nabla}\wedge\left(\frac{\underline{B}}{B}\wedge\underline{F}^{(n)}\right)\right)$$

$$= \left(\frac{c}{q}\right)^2 \operatorname{div}\left(\underline{F}^{(n)}\right)\underline{F}^{(m)} \qquad (4.13)$$

Thus $\underline{v}^{(0)}\wedge(\underline{\nabla}\wedge\underline{v}^{(0)}) = \left(\frac{c}{q}\right)^2 \operatorname{div}\left(\frac{\underline{\nabla}(q\phi)}{B}\right)\frac{\underline{\nabla}(q\phi)}{B} = -\frac{c}{qB}\operatorname{div}\left(\frac{c\underline{E}}{B}\right)\underline{\nabla}(q\phi)$

and hence

$$\underline{v}^{(1)} = \frac{c}{q}\frac{\underline{B}}{B^2}\wedge\left(\underline{\nabla}\left(\frac{mv^2_{(0)}}{2}\right) + \left(\frac{mc}{qB}\right)\operatorname{div}\left(\frac{c\underline{E}}{B}\right)\underline{\nabla}(q\phi)\right).$$

Comparing with (4.11) shows that $\lambda^{(0)} = 1$ and $\lambda^{(1)} = \frac{mc}{qB}\operatorname{div}\left(\frac{c\underline{E}}{B}\right)$.

Again, for j=2 we have

$$\underline{v}^{(2)} = \frac{c}{q}\frac{\underline{B}}{B^2}\wedge\left(\lambda^{(0)}\underline{\nabla}\mathcal{E}^{(2)} + \lambda^{(1)}\underline{\nabla}\mathcal{E}^{(1)} + \lambda^{(2)}\underline{\nabla}\mathcal{E}^{(0)}\right) \qquad (4.14)$$

while from equation (4.10) we have

$$\underline{v}^{(2)} = \frac{mc}{q}\frac{\underline{B}}{B^2}\wedge\left\{(\underline{v}^{(1)}\cdot\underline{\nabla})\underline{v}^{(0)} + (\underline{v}^{(0)}\cdot\underline{\nabla})\underline{v}^{(1)}\right\}$$

$$= \frac{mc}{q}\frac{\underline{B}}{B^2}\wedge\left\{\underline{\nabla}(\underline{v}^{(0)}\cdot\underline{v}^{(1)}) - \underline{v}^{(1)}\wedge(\underline{\nabla}\wedge\underline{v}^{(0)}) - \underline{v}^{(0)}\wedge(\underline{\nabla}\wedge\underline{v}^{(1)})\right\}$$

From (4.13) we have

$$\underline{v}^{(0)}\wedge(\underline{\nabla}\wedge\underline{v}^{(1)}) = \left(\frac{c}{q}\right)^2 \operatorname{div}\left(\frac{m(\underline{v}^{(0)}\cdot\underline{\nabla})\underline{v}^{(0)}}{B}\right)\frac{\underline{\nabla}(q\phi)}{B}$$

and

$$\underline{v}^{(1)} \wedge \left(\underline{\nabla} \wedge \underline{v}^{(0)}\right) = \left(\frac{c}{q}\right)^2 \operatorname{div}\left(\frac{\underline{\nabla}(q\phi)}{B}\right) \frac{m\,(\underline{v}^{(0)} \cdot \underline{\nabla})\underline{v}^{(0)}}{B}$$

$$= -\left(\frac{mc}{qB}\right) \operatorname{div}\left(\frac{c\underline{E}}{B}\right)\left\{\underline{\nabla}\,\frac{v_{(0)}^2}{2} - \underline{v}^{(0)} \wedge \left(\underline{\nabla} \wedge \underline{v}^{(0)}\right)\right\}$$

$$= -\left(\frac{mc}{qB}\right) \operatorname{div}\left(\frac{c\underline{E}}{B}\right)\left\{\underline{\nabla}\,\frac{v_{(0)}^2}{2} + \frac{c}{qB} \operatorname{div}\left(\frac{c\underline{E}}{B}\right)\underline{\nabla}(q\phi)\right\}$$

Thus

$$\underline{v}^{(2)} = \frac{c}{q}\frac{\underline{B}}{B^2} \wedge \left\{\underline{\nabla}\left(m\underline{v}^{(0)} \cdot \underline{v}^{(1)}\right) + \frac{mc}{qB} \operatorname{div}\left(\frac{c\underline{E}}{B}\right)\underline{\nabla}\left(\frac{mv_{(0)}^2}{2}\right)\right.$$

$$\left. + \left(\frac{mc}{qB}\right)^2\left\{\left(\operatorname{div}\left(\frac{c\underline{E}}{B}\right)\right)^2 - B \operatorname{div}\left(\frac{(\underline{v}^{(0)} \cdot \underline{\nabla})\underline{v}^{(0)}}{B}\right)\right\}\underline{\nabla}(q\phi)\right\}$$

Comparing with (4.14) we thus find

$$\lambda^{(0)} = 1 \qquad \lambda^{(1)} = \left(\frac{mc}{qB}\right) \operatorname{div}\left(\frac{c\underline{E}}{B}\right)$$

$$\lambda^{(2)} = \left(\frac{mc}{qB}\right)^2\left\{\left(\operatorname{div}\left(\frac{c\underline{E}}{B}\right)\right)^2 - B \operatorname{div}\left(\frac{(\underline{v}^{(0)} \cdot \underline{\nabla})\underline{v}^{(0)}}{B}\right)\right\} \tag{4.15}$$

It is clear that $\lambda^{(1)} \sim \dfrac{(cE/B)}{\Omega L} \sim {}^{g}/_{L}$

and $\lambda^{(2)} \sim \left(\dfrac{cE/B}{\Omega L}\right)^2 \sim \left(\dfrac{g}{L}\right)^2$

Thus we have determined λ as a series with ${}^{g}/_{L}$ as the smallness parameter. The value of $\lambda^{(j)}$ may be found in a similar manner to that given above, though, of course, succeeding terms become ever more complex.

We have thus shown that equation (4.4) is satisfied

by the adiabatic drift expansion and we have evaluated the first three terms of the series for λ in this case.

It is worthwhile to point out at this stage that since the velocity and hence kinetic energy of the particles is known at each point in the flow, the total energy is also known, and has a unique value at each position. The particles move on a locus of constant energy, and so particle orbits of a single species never cross each other.

(iii) Current Densities in the Flow and Magnetic Perturbations

We now investigate the particle density N, in the flow via the continuity equation

$$\text{div}\,(N\underline{v}) = 0$$

Using the particle velocity in the drift-flow as given by equation (4.4) we have

$$\text{div}\left(\frac{N\lambda}{B}\frac{\underline{B}}{B}\wedge\underline{\nabla}\left(q\phi+\frac{mv^2}{2}\right)\right) = -\frac{\underline{B}}{B}\cdot\text{curl}\left(\frac{N\lambda}{B}\underline{\nabla}\left(q\phi+\frac{mv^2}{2}\right)\right)=0$$

where we have used the fact that $\underline{B}/B$ is a constant vector in two-dimensional flows. Also, since the curl of any vector in the plane of the flow is perpendicular to that plane and hence parallel to $\underline{B}/B$ this implies that

$$\text{curl}\left(\frac{N\lambda}{B}\underline{\nabla}\left(q\phi+\frac{mv^2}{2}\right)\right)=\underline{0}$$

Expanding this we have

$$\underline{\nabla}\left(\frac{N\lambda}{B}\right)\wedge\underline{\nabla}\left(q\phi+\frac{mv^2}{2}\right)=\underline{0} \qquad (4.16)$$

or using (4.4) again

$$\underline{v} \cdot \underline{\nabla} \left(\frac{N\lambda}{B}\right) = 0 \qquad (4.17)$$

Thus $N\lambda/B$ is a constant along a streamline. To zero order ($\lambda \simeq \lambda^{(0)} = 1$) we have N/B a constant along a streamline, thus recovering the well-known result for the zeroth order flow along equipotentials described by equations (4.1) and (4.8). (See, for example, Chandrasekhar, 1960, p.75). However, if the density at infinity is non-uniform, $N\lambda/B$ is not constant across streamlines. Cold particles produce no diamagnetic effect so that differing densities at infinity do not perturb the magnetic field, which we assume to be uniform. For definiteness we consider flow between parallel boundaries which have an electrostatic potential difference between them Φ. If the plasma at infinity is exactly charge-neutral the electric field is also constant across the system irrespective of density gradients. Thus with constant $\underline{E}$ and $\underline{B}$ the flow velocity between the boundaries is constant across the system and given by equation (4.1). For the incoming flow at large distances the density can thus be written as a function of the potential across the system. For species j we thus write

$$N_{oj}(\phi_i) = N_o f_j(\phi_i) \qquad (4.18)$$

where ϕ_i is the 'initial potential' of the streamline. For a two-component plasma (protons and electrons) the charge neutrality condition is

$$N_{op}(\phi_i) = N_{oe}(\phi_i).$$

Non-uniformities in the flow are then imposed by a boundary condition which, say, defines a non-uniform potential drop across the system at some position. In our case this boundary condition is set by the properties of the magnetic field reversal region where the conditions for the validity of the drift equations are no longer satisfied (See Fig. 4.1).

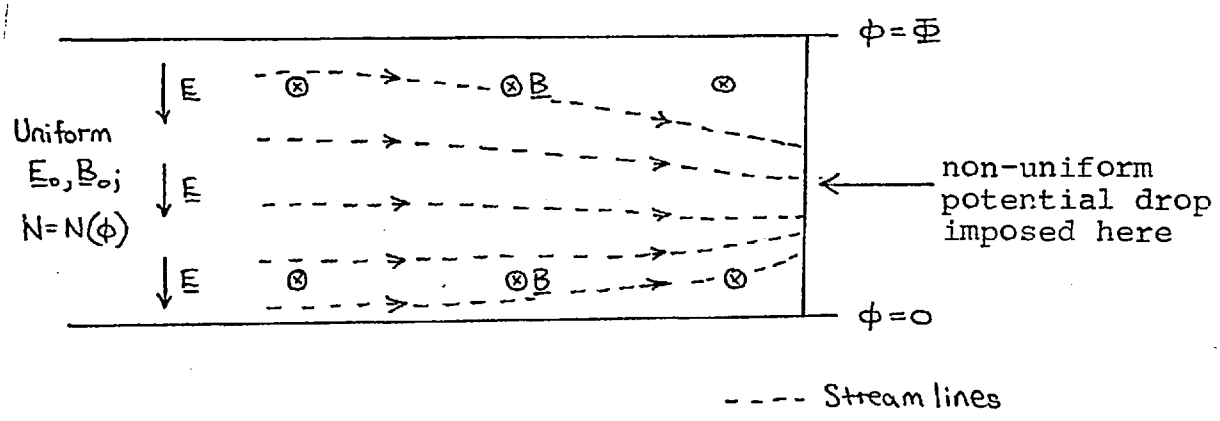

Figure 4.1

Since $N\lambda/B$ is constant along a streamline and energy is conserved, the density of particles of species j in the flow where the potential ϕ and the flow velocity v_j is given by (from (4.18))

$$N_j = \frac{N_o B}{\lambda_j B_o} f_j\left(\phi_i = \phi + \frac{m_j(v_j^2 - v_\infty^2)}{2q_j}\right) \qquad (4.19)$$

We shall first consider the magnetic field changes which are consistent with a given electric field perturbation. These are given by Maxwell's equation

$$\text{curl } \underline{B} = \underline{\nabla} B \wedge \frac{\underline{B}}{B} = \frac{4\pi}{c} \sum_j N_j q_j \underline{v}_j \qquad (4.20)$$

Using equation (4.4) for $\underline{v}_j$ and (4.19) for N_j we have

$$N_j q_j \underline{v}_j = \frac{c q_j N_o}{B_o} f_j\left(\phi_i = \phi + \frac{m_j(v_j^2 - v_\infty^2)}{2q_j}\right) \frac{\underline{B}}{B} \wedge \underline{\nabla}\left(\phi + \frac{m_j v_j^2}{2q_j}\right)$$

$$= c q_j \frac{N_o}{B_o} \frac{\underline{B}}{B} \wedge \underline{\nabla}\left\{\int f_j\left(\phi + \frac{m_j(v_j^2 - v_\infty^2)}{2q_j}\right) d\left(\phi + \frac{m_j(v_j^2 - v_\infty^2)}{2q_j}\right)\right\}$$

Thus, on integrating equation (4.20) we obtain

$$B + \frac{4\pi N_o}{B_o} \sum_j q_j \int f_j\left(\phi + \frac{m_j(v_j^2 - v_\infty^2)}{2q_j}\right) d\left(\phi + \frac{m_j(v_j^2 - v_\infty^2)}{2q_j}\right)$$

$$= \text{constant} \qquad (4.21)$$

or, in terms of $\phi_i = \phi + m_j(v_j^2 - v_\infty^2)/2q_j$ at any point this is

$$B + \frac{4\pi N_o}{B_o} \sum_j q_j \int f_j(\phi_i)\, d\phi_i = \text{Constant.}$$

The indefinite integral may be replaced by the definite integral

$$\int f_j(\phi_i)\, d\phi_i = \int_{\phi_i = \phi_{i_o}}^{\phi_i = \phi + m_j(v_j^2 - v_\infty^2)/2q_j} f_j(\phi_i')\, d\phi_i'$$

where ϕ_{io} is arbitrary. The lower limit represents the arbitrary constant, which contributes a constant term on either side of equation (4.21), and which may be cancelled. Far away from the sheet $v_j = v_\infty$ for all species, and $B = B_o$ so that equation (4.21) can be written

$$B + \frac{4\pi N_o}{B_o} \sum_j q_j \int_{\phi_{io}}^{\phi_i} f_j(\phi_i')\, d\phi_i' = B_o + \frac{4\pi N_o}{B_o} \sum_j q_j \int_{\phi_{io}}^{\phi_i = \phi_R} f_j(\phi_i')\, d\phi_i'$$

where ϕ_R on the right hand side can take any value and is

not necessarily the same as the ϕ_i on the left hand side. However, by the charge neutrality assumption

$$\sum_j q_j \int_{\phi_{i0}}^{\phi_R} f_j(\phi_i')\, d\phi_i' = 0$$

for all ϕ_R. So if we let $\phi_R = \phi$ we obtain

$$(B_0 - B) = \frac{4\pi N_0}{B_0} \sum_j q_j \int_{\phi}^{\phi_i = \phi + m_j(v_j^2 - v_\infty^2)/2q_j} f_j(\phi_i')\, d\phi_i' \qquad (4.22)$$

The interpretation of this equation becomes clear if we consider the flux of particles crossing an equipotential ϕ along which the flow velocity varies, while energy is conserved in the flow. If the flow velocity for species j is $\underline{v}_j$ at potential ϕ at any point the flow, the change in kinetic energy undergone by the particles is $m_j(v_j^2 - v_\infty^2)/2$, this implying that particles with initial potentials between ϕ and $\phi + m_j(v_j^2 - v_\infty^2)/2q_j$ have crossed equipotential ϕ. The particle flux at infinity is

$$F_j = N_0 v_\infty f_j(\phi_i) = \frac{c N_0 E_0}{B_0} f_j(\phi_i)$$

and the number of particles per second crossing an element dL perpendicular to the flow is FdL. Writing $E_0 dL = d\phi_i$, the number per second crossing the potential $d\phi_i$ is

$$\frac{F\, d\phi_i}{E_0} = \frac{c N_0}{B_0} f_j(\phi_i)\, d\phi_i$$

Thus the total flux of particles moving across the equipotential ϕ is given by

$$\frac{cN_o}{B_o}\int_{\phi}^{\phi+m_j(v_j^2-v_\infty^2)/2q_j} f_j(\phi_i')\,d\phi_i'$$

The current in the direction of the electric field is thus

$$I = \frac{cN_o}{B_o}\sum_j q_j \int_{\phi}^{\phi+m_j(v_j^2-v_\infty^2)/2q_j} f_j(\phi_i')\,d\phi_i'$$

which gives, via Maxwell's equation

$$(B_o - B) = \frac{4\pi N_o}{B_o}\sum_j q_j \int_{\phi}^{\phi+m_j(v_j^2-v_\infty^2)/2q_j} f_j(\phi_i')\,d\phi_i'$$

For illustration we consider the simple case of a linear variation of N across the system, with N_o the average density (at the centre of the system) and the density at the boundaries $N_o(1\pm\psi/2)$. Then

$$N_o(\phi_i) = N_o\left(1+\psi\left(\frac{\phi_i}{\Phi}-\frac{1}{2}\right)\right)$$

with $|\psi| \le 2$, and Φ the total potential across the system. Thus

$$f(\phi_i) = \left(1+\psi\left(\frac{\phi_i}{\Phi}-\frac{1}{2}\right)\right) \qquad (4.23)$$

and $$\int f(\phi_i)\,d\phi_i = \phi_i\left(1-\frac{\psi}{2}\left(1-\frac{\phi_i}{\Phi}\right)\right)$$

With this simple form for $f(\phi_i)$ equation (4.22) becomes

$$(B_o - B) = \frac{4\pi N_o}{B_o}\sum_j q_j\left\{\left(\phi+\frac{m_j(v_j^2-v_\infty^2)}{2q_j}\right)\left(1-\frac{\psi}{2}\left(1-\frac{\phi}{\Phi}-\frac{m_j(v_j^2-v_\infty^2)}{2q_j\Phi}\right)\right)\right.$$
$$\left.-\phi\left(1-\frac{\psi}{2}\left(1-\frac{\phi}{\Phi}\right)\right)\right\}$$

or

$$(B_o - B) = \frac{2\pi N_o}{B_o} \sum_j m_j (v_j^2 - v_\infty^2) \left(1 - \frac{\psi}{2}\left(1 - \frac{2\phi}{\Phi} - \frac{m_j(v_j^2 - v_\infty^2)}{2q_j\Phi}\right)\right) \quad (4.24)$$

For the special case $\psi = 0$ (uniform flow) this reduces to

$$(B_o - B) = \frac{2\pi N_o}{B_o} \sum_j m_j (v_j^2 - v_\infty^2) \quad (4.24a)$$

For an electron-proton plasma, we see that due to the mass factor $m_p/m_e \sim 2000$ and the fact that $v_p \approx v_e$ in the drift flow only the term due to protons need be included. Perturbations in the electromagnetic field which considerably affect protons leave electrons flowing very nearly along equipotentials.

Then (4.24) simplifies to

$$(B_o - B) = \frac{2\pi N_o}{B_o} m_p (v_p^2 - v_\infty^2) \left(1 - \frac{\psi}{2}\left(1 - \frac{2\phi}{\Phi} - \frac{m_p(v_p^2 - v_\infty^2)}{2e\Phi}\right)\right) \quad (4.25)$$

At a potential ϕ the maximum possible value of $m_p(v_p^2 - v_\infty^2)/2e$ is $(\Phi - \phi)$ so that again neglecting the electron contribution, the minimum value of B from equation (4.22) is given by

$$(B_o - B) = \frac{4\pi N_o e}{B_o} \int_\phi^\Phi f_j(\phi_i')\, d\phi_i'$$

At $\phi = 0$ we expect all the current to be carried by protons (the above neglect of electrons then being immaterial) and the minimum value of B must be zero for self-consistency between the magnetic field and the current. If, in the above expression N_o is the average incoming particle density then

$$\int_0^\Phi f_j(\phi_i')\, d\phi_i' = \Phi$$

Thus, for self-consistency ($B_{min} = 0$ at $\phi = 0$) the total potential across the system is given by

$$\Phi = \frac{B_o^2}{4\pi N_o e} \tag{4.26}$$

where N_o is the average density.

This equation is the same as that derived by Alfvén (1968) under the assumption that all incoming particles contribute to the current. This assumption is equivalent to ours that protons carry all the current at $\phi = 0$; (electrons carry all the current at $\phi = \Phi$). Accepting this value of Φ (4.25) becomes, for the linear density variation

$$\frac{B}{B_o} = 1 - \frac{(m_p(v_p^2 - v_\infty^2)/2)}{e\Phi}\left(1 - \frac{\psi}{2}\left(1 - \frac{2\phi}{\Phi} - \frac{m_p(v_p^2 - v_\infty^2)}{2e\Phi}\right)\right) \tag{4.27}$$

and from the above discussion

$$\left(\frac{B}{B_o}\right)_{min} = \frac{\phi}{\Phi}\left(1 - \frac{\psi}{2}\left(1 - \frac{\phi}{\Phi}\right)\right) \tag{4.28}$$

Writing $m_p(v_p^2 - v_\infty^2)/2 = e(\phi_i - \phi)$ equation (4.27) becomes

$$\frac{B}{B_o} = 1 - \frac{(\phi_i - \phi)}{\Phi}\left(1 - \frac{\psi}{2}\left(1 - (\phi + \phi_i)\right)\right)$$

We have plotted in Fig. 4.2 B/B_o vs ϕ_i for given ϕ values. The effects of increasing the incoming flux near $\phi = \Phi$ ($\psi > 0$) and increasing it near $\phi = 0$ ($\psi < 0$) are apparent.

Now since in the drift-flow region the velocity can be expressed as a function of the local electromagnetic field and its derivatives, equation (4.22) is, in fact a relationship between the local electric and magnetic fields as a

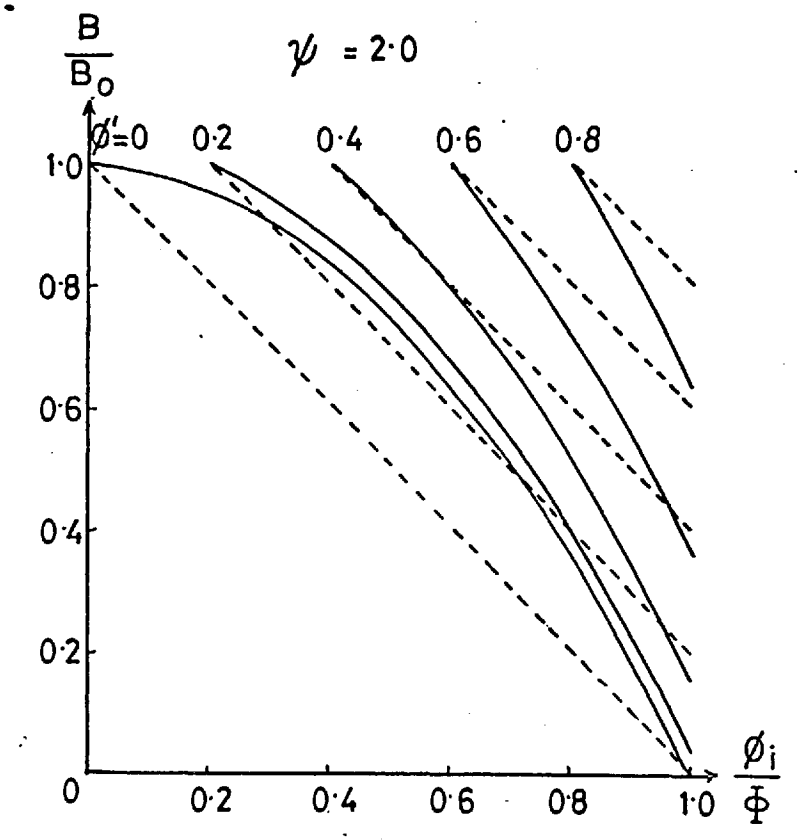
B/B0
ψ = 2·0
Ø'=0
0·2
0·4
0·6
0·8
1·0
0·8
0·6
0·4
0·2
0
0·2
0·4
0·6
0·8
1·0
Øi/Φ

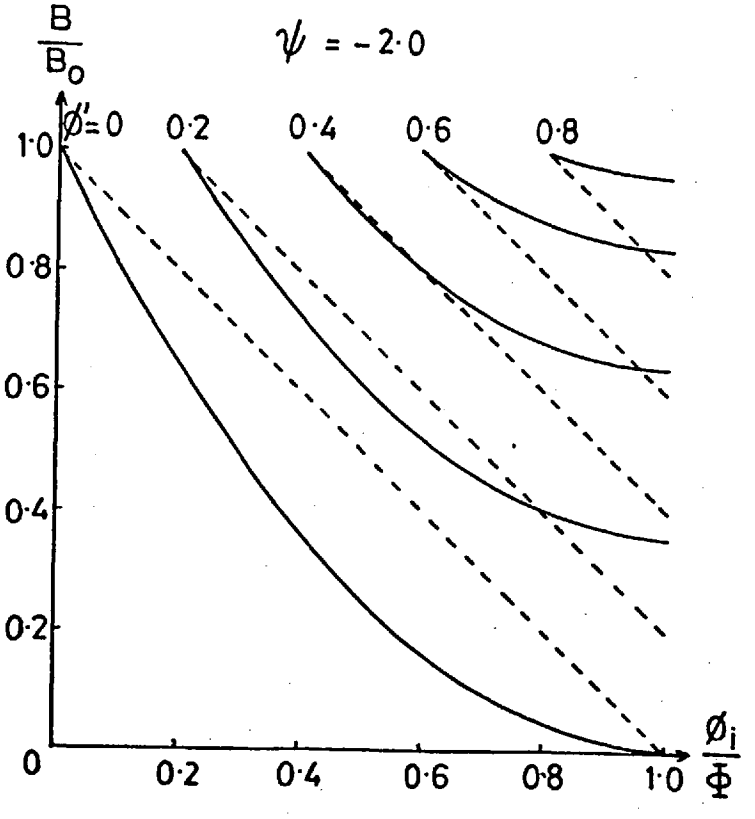
B/B0
ψ = -2·0
Ø'=0
0·2
0·4
0·6
0·8
1·0
0·8
0·6
0·4
0·2
0
0·2
0·4
0·6
0·8
1·0
Øi/Φ

Figure 4.2(a,b)

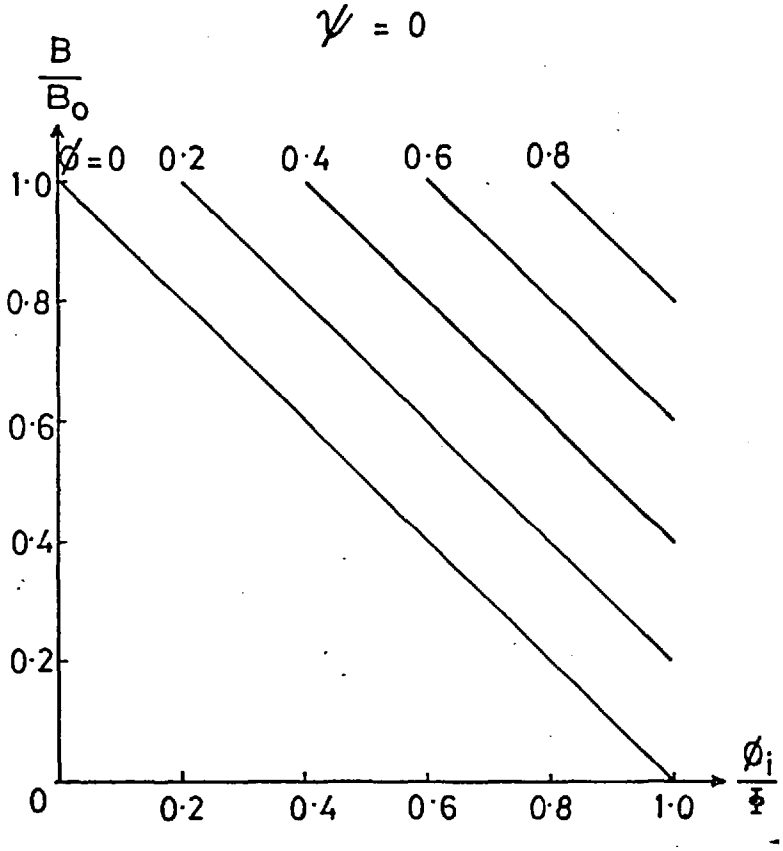

Figure 4.2 (a,b,c): The value of B/B_O versus $\phi_i/\Phi = \{\frac{\phi}{\Phi} + \frac{m_p(v_p^2 - v_\infty^2)}{2e\Phi}\}$ for various values of ϕ/Φ. As $\phi_i (\geq \phi)$ at a given ϕ increases, the cross-equipotential proton fluxes increases and B/B_O decreases; for $\phi_i = \phi$ there are no fluxes and $B/B_O = 1$. The variations shown for non-uniform inflow are in accord with expectations for

(a) larger densities near $\phi = \Phi$ ($\psi > 0$) i.e. smaller changes of B/B_O at $\phi = 0$ for a given ϕ_i, than for the uniform density case (dotted)

(b) larger densities near $\phi = 0$ ($\psi < 0$) i.e. larger changes of B/B_O at $\phi = 0$ for a given ϕ_i, than for the uniform density case (dotted)

(c) uniform incoming profile, ($\psi = 0$) a linear variation of B/B_O at a given ϕ as ϕ_i ($\geq \phi$) increases.

function of the potential. To lowest order we have $v_p \approx cE/B$, and (4.22) and (4.27) are in this approximation a direct relationship between E and B in the flow.

The ratio of the incoming kinetic energy to the particle potential energy (at $\phi = \Phi$) is

$$\left(\frac{m_p V_\infty^2}{2e\Phi}\right) = \frac{1}{2}\frac{\left(\frac{m_p N_o V_\infty^2}{2}\right)}{\left(\frac{B_o^2}{8\pi}\right)}$$

i.e. half the ratio between the incoming particle kinetic energy density and the magnetic field energy density. We shall be interested in systems where this ratio is very small (e.g. the geomagnetic tail fed by polar wind plasma). Thus if we wish to consider $m_p v_p^2/2 \sim \mathcal{O}(e\Phi)$ such that significant magnetic field perturbations occur, then the incoming flow energy may be neglected in (4.27) to obtain

$$\frac{\Psi}{2}\left(\frac{B_o}{B}\right)^2\left\{\left(\frac{m_p V_\infty^2}{2e\Phi}\right)\left(\frac{E}{E_o}\right)^2\right\}^2 + \left(1-\frac{\Psi}{2}\left(1-\frac{2\phi}{\Phi}\right)\right)\left\{\left(\frac{m_p V_\infty^2}{2e\Phi}\right)\left(\frac{E}{E_o}\right)^2\right\}$$

$$= \left(\frac{B}{B_o}\right)^2\left(1-\frac{B}{B_o}\right) \qquad (4.29)$$

i.e. a biquadratic equation for $\left(\frac{E}{E_o}\right)$ in terms of $\left(B/B_o\right)$ with solution

$$\left(\frac{E}{E_o}\right) = \frac{B}{B_o}\left(\frac{2e\Phi}{m_p V_\infty^2}\right)^{1/2}\left\{\frac{1}{\Psi}\left(\sqrt{\left(1+\frac{\Psi}{2}\left(\frac{2\phi}{\Phi}-1\right)\right)^2+2\Psi\left(1-\frac{B}{B_o}\right)}-\left(1+\frac{\Psi}{2}\left(\frac{2\phi}{\Phi}-1\right)\right)\right)\right\}^{1/2} \qquad (4.30)$$

and

$$\frac{V_p}{V_\infty} = \left(\frac{2e\Phi}{m_p V_\infty^2}\right)^{1/2}\left\{\frac{1}{\Psi}\left(\sqrt{\left(1+\frac{\Psi}{2}\left(\frac{2\phi}{\Phi}-1\right)\right)^2+2\Psi\left(1-\frac{B}{B_o}\right)}-\left(1+\frac{\Psi}{2}\left(\frac{2\phi}{\Phi}-1\right)\right)\right)\right\}^{1/2} \qquad (4.31)$$

It is to be remembered, from (4.28) that $\frac{\phi}{\Phi}(1-\frac{\psi}{2}(1-\frac{\phi}{\Phi})) \leq \frac{B}{B_o} \leq 1$. For uniform inflow ($\psi = 0$) the above reduces to

$$\left(\frac{E}{E_o}\right) = \left(\frac{2e\Phi}{m_p V_\infty^2}\right)^{1/2}\left(\frac{B}{B_o}\right)\left(\left(1+\left(\frac{m_p V_\infty^2}{2e\Phi}\right)\right) - \frac{B}{B_o}\right)^{1/2} \qquad (4.32)$$

and

$$\left(\frac{V_p}{V_\infty}\right) = \left(\frac{2e\Phi}{m_p V_\infty^2}\right)^{1/2}\left(\left(1+\left(\frac{m_p V_\infty^2}{2e\Phi}\right)\right) - \frac{B}{B_o}\right)^{1/2} \qquad (4.33)$$

the latter two results without the approximation $v_\infty << v_p$. The general form of equations (4.30) and (4.31) may be found by considering the simpler equations for $\psi = 0$, (4.32) and (4.33). From equation (4.32) we see that (E/E_o) is zero at $B_o = 0$ and at $B/B_o = 1 + (\frac{m_p v_\infty^2}{2e\Phi}) \approx 1$ (these are the maximum and minimum values of B in the system). Between these values (E/E_o) has a maximum value of

$$\left(\frac{E}{E_o}\right)_{max} \simeq \frac{2}{3\sqrt{3}}\left(\frac{2e\Phi}{m_p V_\infty^2}\right)^{1/2} \quad \text{at} \quad \frac{B}{B_o} \simeq \frac{2}{3}$$

For these values $(\frac{v_p}{v_\infty}) \simeq (\frac{2e\Phi}{m_p v_\infty^2})^{\frac{1}{2}} \frac{1}{\sqrt{3}}$. The maximum value of v_p is given by $(\frac{v_p}{v_\infty})_{max} \simeq (\frac{2e\Phi}{mv_\infty^2})^{\frac{1}{2}}$ at $B = 0$ and v_p is monotonically decreasing as B/B_o increases. Thus v_p has its maximum value at the minimum B rather than the maximum of E. Graphs of (E/E_o) and (v_p/v_∞) as functions of B/B_o for various ϕ and ψ can be seen in Fig. 4.3.

In summary, therefore, we have seen how the variation in drift-flow velocity along an equipotential sets up current densities and perturbs the magnetic field. This effect is produced by particles drifting across equipotentials (as described by non zeroth-order terms in the drift velocity

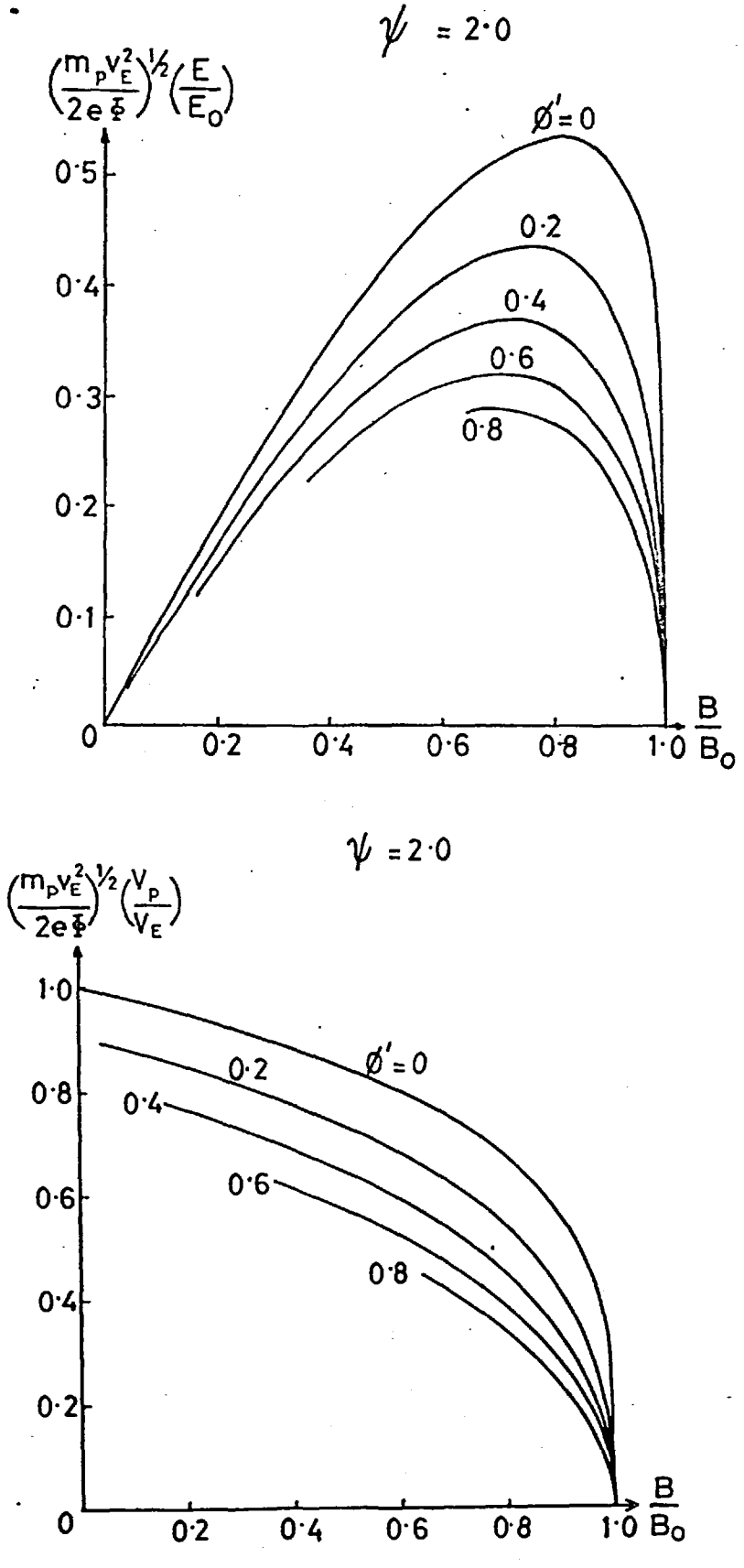

Figure 4.3(a): Variation of E and v_p as functions of B/B_0 at given potentials for $\psi = 2.0$ from eqns. (4.30) and (4.31). If v_p is known at a given potential then E and B can be separately determined to 1st order.

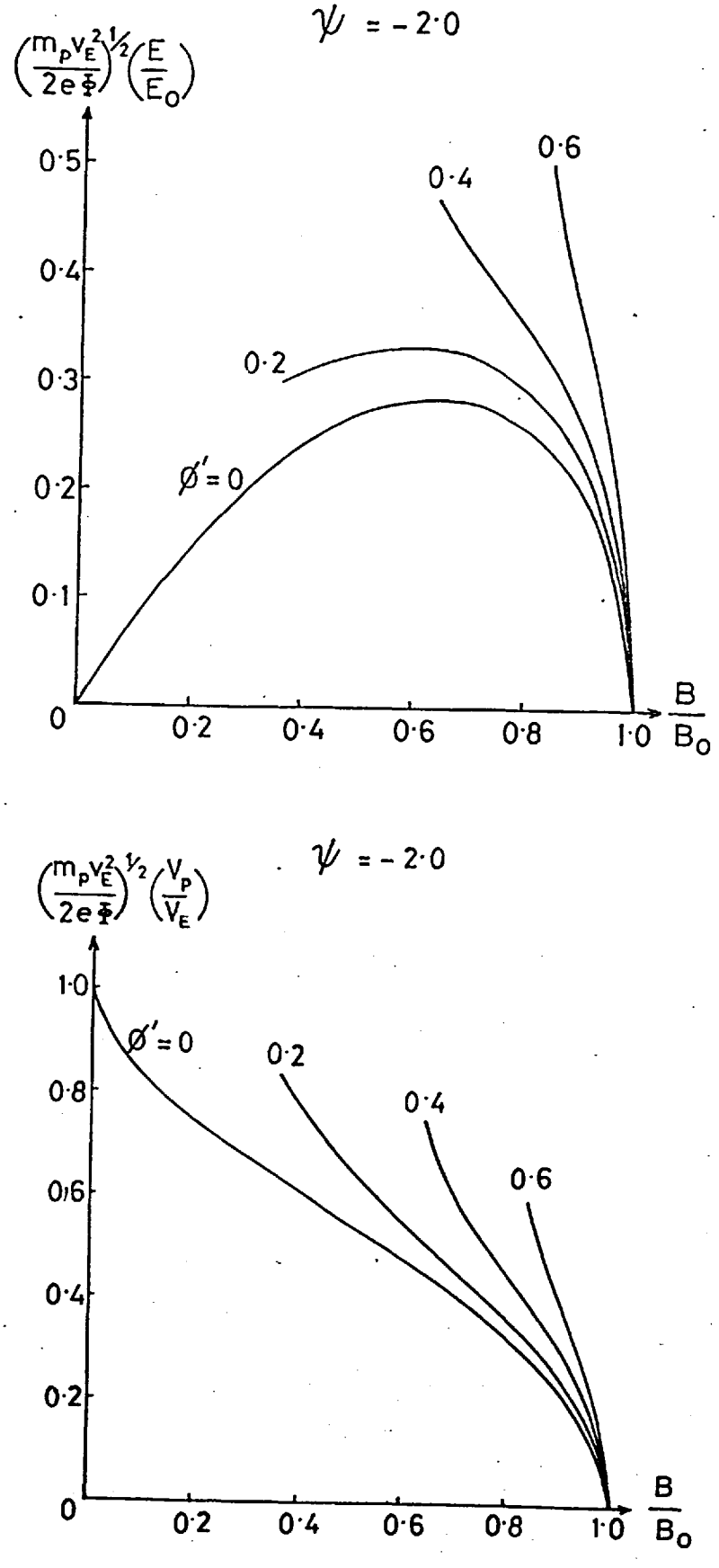

Figure 4.3(b): Variation of E and v_p as functions of B/E_0 at given potentials for $\psi = -2.0$, from eqns. (4.30) & (4.31).

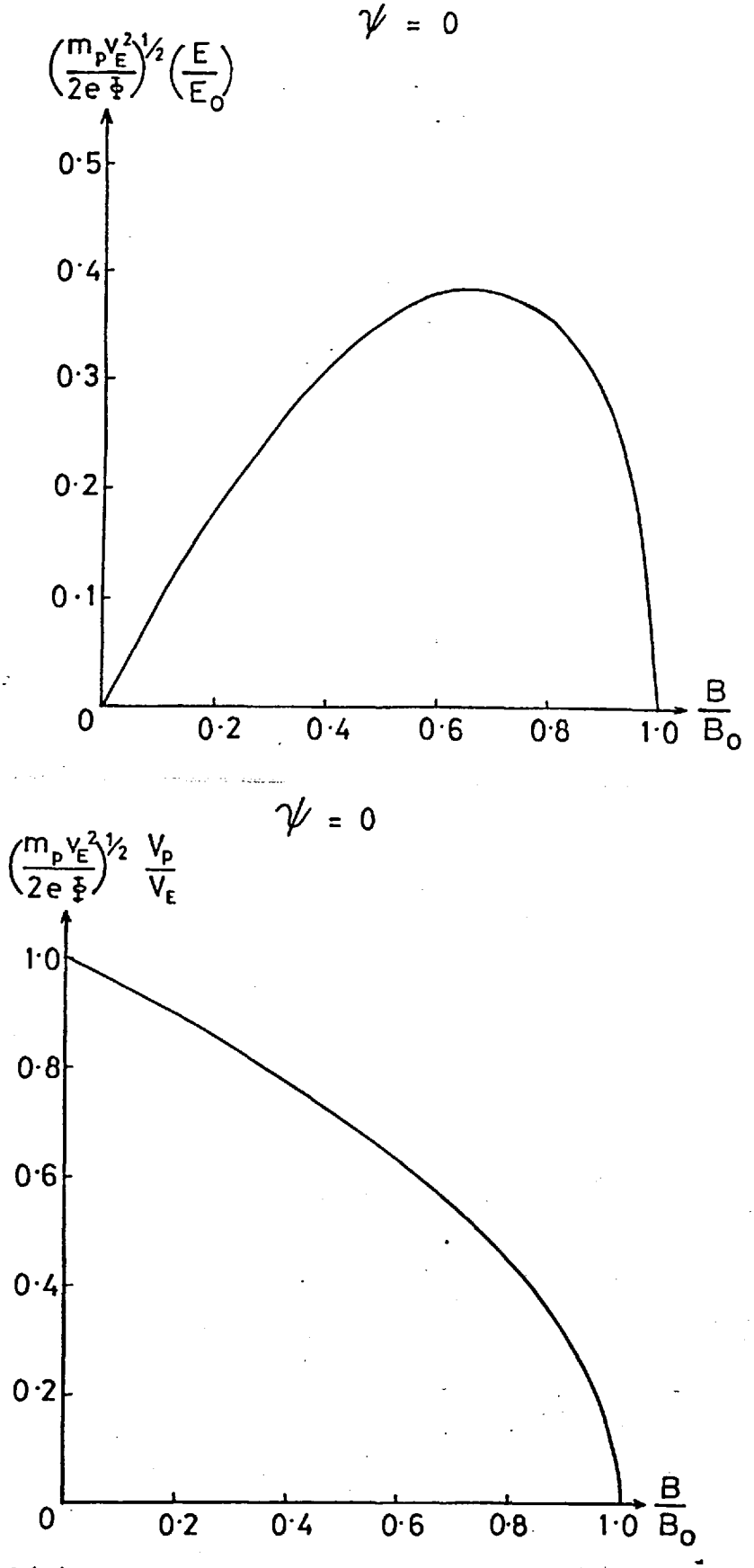

Figure 4.3(c): Variation of E and v_p as functions of B/B_0 for uniform inflow, from equations (4.32) and (4.33). The results are now independent of the potential, except that at a potential ϕ, $(B/B_0)_{min} = 1 - \frac{m_p(v_p^2 - v_\infty^2)_{max}}{e\Phi} = \frac{\phi}{\Phi}$.

expansion) and so conserving energy. We hence obtain a relationship between v_j and B/B_o, and using as a first approximation $v_j = cE/B$ we obtain a relationship between E and B in the flow (in the general case as a function of $\dot{\phi}/\phi$). We have also found that, for self-consistency between the available current source (the incoming particle flux) and the magnetic field at large distances, a total potential Φ must exist across the system, given by equation (4.26), which is in agreement with Alfvén's result.

A given value of v_p however, implies a given value of E, and for $m_p v_p^2/2 \sim \mathcal{O}(e\Phi)$ we have found that

$$\left(\frac{E}{E_o}\right) \sim \mathcal{O}\left(\frac{2e\Phi}{m_p V_\infty^2}\right)^{1/2} \gg 1$$

for the systems of interest here. Since the total potential across the system is fixed, however, such electric fields can exist only over small regions of the system. This implies that for a given value of E scale lengths L exist such that

$$(E - E_o)\, L \sim \mathcal{O}(\Phi).$$

We thus write

$$L = \frac{K\Phi}{(E - E_o)} \qquad \text{where } K \geq 1. \tag{4.34}$$

Hence $$\vartheta_{p/L} \simeq \frac{V_p}{\Omega L} \simeq \frac{m_p V_p^2}{Ke\Phi} \tag{4.35}$$

Thus the drift-expansion will only be valid in the region where the flow energies are rather less than the potential energies. In order to estimate the likely importance of high-order terms in the drift-expansion of such quantities

as v_j and λ we consider the properties of the series

$$S_\infty = \sum_{n=0}^{\infty} \left(\frac{g}{L}\right)^n = \frac{1}{(1-g/L)} \qquad \text{for } g/L < 1$$

A graph of S_∞ versus (g/L) is shown in Fig. 4.4 together with the first two approximations $1 + (g/L)$ and $1 + (g/L) + (g/L)^2$. If we approximate the series by the first m terms, then the error is

$$\mathcal{E}_m = S_\infty - S_m = \frac{(g/L)^m}{(1-g/L)} \qquad \text{and} \qquad \frac{\mathcal{E}_m}{S_\infty} = \left(\frac{g}{L}\right)^m$$

Thus for a maximum fractional error of $f = \mathcal{E}_m/S_\infty$ we must have

$$\left(\frac{g}{L}\right) \leq \sqrt[m]{f} \tag{4.36}$$

For example, if we choose $f = 0.1$ (a 10% error) as the maximum error allowable in say, v_j and λ, then by using only the first two terms ($\underline{v}_j \simeq \underline{v}^{(0)} + \underline{v}^{(1)}$ and $\lambda \simeq \lambda^{(0)} + \lambda^{(1)}$) we must restrict ourselves to $g/L \leq 0.3$ or, from equation (4.35)

$$\frac{m_p V_p^2}{2e\Phi} \simeq \frac{1}{2}\frac{g}{L} \lesssim 0.16$$

On the other hand, if three terms were taken, then for $f \leq 0.1$ we require $g/L \leq 0.46$ or

$$\frac{m_p V_p^2}{2e\Phi} \lesssim 0.23$$

The above considerations give us a quantitative estimate of the error involved in any quantitative calculations based on

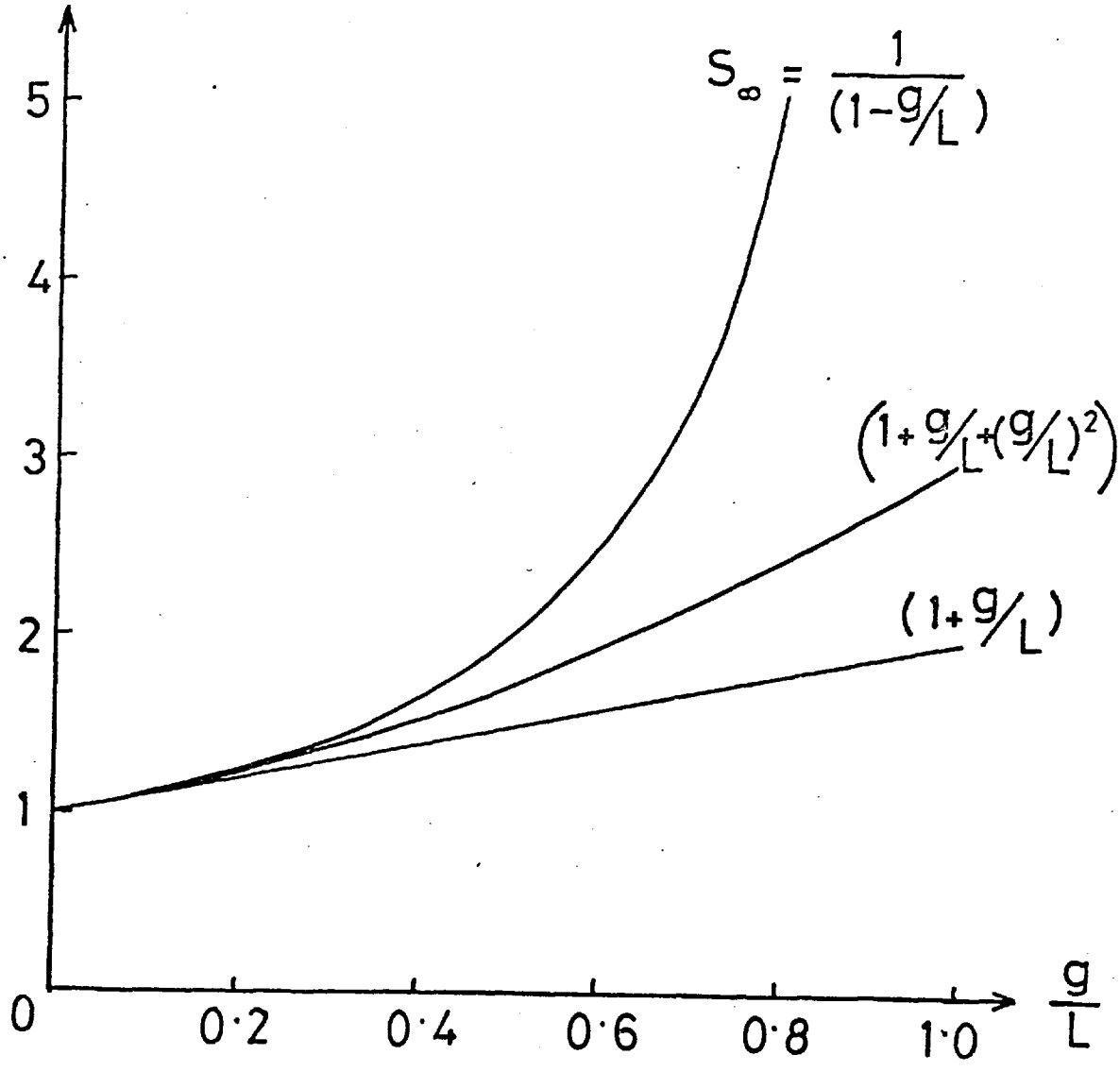

Figure 4.4: The function $\frac{1}{(1-g/L)}$ versus g/L together with the first two approximations $1+g/L$ and $(1+g/L+(g/L)^2)$.

the drift theory, and also some idea of its limits of validity.

(iv) Charge Densities and Poisson's Equation for the Drift-Flow.

We now investigate charge neutrality in the flow and derive the form for Poisson's equation which, when integrated with given boundary conditions finds the electric field (and equipotential structure) in the region where drift-flow theory is valid.

If the potential at a point is ϕ and the flow velocity for species j is v_j (given in terms of the local field values), then since $N\lambda/B$ is constant along a trajectory, we have

$$N_j = \frac{BN_o}{\lambda_j B_o} f_j\left(\phi_i = \phi + m_j (V_j^2 - V_\infty^2)/2q_j\right)$$

as before. Thus for the proton-electron plasma, the charge density is given by

$$(N_p - N_e) = \frac{BN_o}{B_o}\left\{\frac{f(\phi_i = \phi + m_p(V_p^2 - V_\infty^2)/2e)}{\lambda_p} - \frac{f(\phi_i = \phi - m_e(V_e^2 - V_\infty^2)/2e)}{\lambda_e}\right\} \tag{4.37}$$

Rewriting (4.37) we have

$$(N_p - N_e) = \frac{N_o B}{\lambda_p B_o}\left\{f(\phi)\left(\frac{\lambda_e - \lambda_p}{\lambda_e}\right) + \left(f\left(\phi + \frac{m_p(V_p^2 - V_\infty^2)}{2e}\right) - f(\phi)\right)\times\right.$$

$$\left.\times\left(1 - \frac{\lambda_p}{\lambda_e}\frac{\left(f(\phi\ \ m_e(V_e^2 - V_\infty^2)/2e) - f(\phi)\right)}{\left(f(\phi + m_p(V_p^2 - V_\infty^2)/2e) - f(\phi)\right)}\right)\right\} \tag{4.38}$$

This equation may be simplified first of all by noting that since $m_e/m_p \sim \mathcal{O}(10^{-3})$ we may take $\lambda_e = 1$ for our first-order theory. For instance, if $g_p/L \approx 0.1$, then

$g_e/_L \sim 10^{-4}$ and $\lambda_e \simeq 1 + \mathcal{O}((\frac{g_p}{L})^4)$ while $\lambda_p \simeq 1 + \mathcal{O}(g_p/_L)$. Secondly, again because of the mass ratio, and the fact that $v_p \simeq v_e$ we see that

$$\frac{f(\phi - m_e(v_e^2 - V_\infty^2)/2e) - f(\phi)}{f(\phi + m_p(v_p^2 - V_\infty^2)/2e) - f(\phi)} \simeq \mathcal{O}\left(\frac{m_e}{m_p}\right) \tag{4.39}$$

unless the function f varies very pathologically. These simplifications amount to the neglect of the electron inertia, considering them simply to flow down equipotentials with the velocity given by equations (4.1) and (4.8). Thus we simplify (4.38) to

$$N_p - N_e \simeq \frac{N_0 B}{\lambda_p B_0}\left\{f(\phi)(1-\lambda_p) + \left(f(\phi + m_p(v_p^2 - V_\infty^2)/2e) - f(\phi)\right)\right\} \tag{4.40}$$

From equation (4.15) we have

$$(\lambda_p - 1) = \frac{m_p c}{eB}\,\mathrm{div}\left(\frac{c\underline{E}}{B}\right) + \mathcal{O}\left(\left(\frac{g_p}{L}\right)^2\right)$$

$$\simeq \frac{m_p c^2}{eB^2}\left(\mathrm{div}\,\underline{E} - \frac{\underline{E}\cdot\nabla B}{B}\right).$$

Substituting into equation (4.40) we finally have, to first order,

$$N_p - N_e \simeq \frac{m_p c^2 N_0}{\lambda_p e B B_0}\left\{f(\phi)\left(\frac{\underline{E}\cdot\nabla B}{B} - \mathrm{div}\,\underline{E}\right) + \frac{eB^2}{m_p c^2}\left(f\left(\phi + \frac{m_p(v_p^2 - V_\infty^2)}{2e}\right) - f(\phi)\right)\right\} \tag{4.41}$$

For the case of the uniform gradient in the incoming density (equation (4.23)), equation (4.38) is

$$N_p - N_e = \frac{B N_0}{\lambda_p B_0}\left\{\left(1 + \psi\left(\frac{\phi}{\Phi} - \frac{1}{2}\right)\right)\left(\frac{\lambda_e - \lambda_p}{\lambda_e}\right) + \frac{\psi m_p(v_p^2 - V_\infty^2)}{2e\Phi}\left[1 - \frac{m_e}{m_p}\frac{\lambda_p}{\lambda_e} \times \left(\frac{v_e^2 - V_\infty^2}{v_p^2 - V_\infty^2}\right)\right]\right\} \tag{4.42}$$

and, noting that (4.39) is satisfied the equation may be

simplified to the form of (4.41)

$$N_p - N_e \simeq \frac{m_p c^2 N_o}{\lambda_p e B B_o}\left\{-\left(\operatorname{div}\underline{E} - \frac{\underline{E}\cdot\nabla B}{B}\right)\left(1+\psi\left(\frac{\phi}{\Phi}-\frac{1}{2}\right)\right)+\frac{\psi B^2}{2\Phi}\frac{(v_p^2-v_\infty^2)}{c^2}\right\} \quad (4.43)$$

The first term on the right-hand side of equations (4.40), (4.41) and (4.43) is the charge density set up by the variation of λ_p along the trajectories, while the second term is only present for a non-uniform initial density across the system and is simply set up by cross-equipotential flow of protons while electrons remain tied to equipotentials. If the initial particle density is higher at higher potentials ($\psi > 0$), increasing proton velocities ($v_p > v_\infty$) causes them to drift to lower potentials and hence a positive charge density results. Similarly, a negative charge density results when $\psi < 0$ and $v_p > v_\infty$.

We now note that $(\lambda_p - 1) \sim \mathcal{O}(g_p/L) \sim \mathcal{O}\left(\frac{m_p v_p^2}{2e\phi}\right)$ from (4.35), and that

$$f\left(\phi + m_p(v_p^2 - v_\infty^2)/2e\right) - f(\phi) \simeq \frac{m_p(v_p^2 - v_\infty^2)}{2e\Phi}\left(\frac{\partial f}{\partial(\phi/\Phi)}\right)_\phi$$

Thus, if $f(\phi)$ and $\left(\partial f/\partial(\phi/\phi)\right) \sim \mathcal{O}(1)$ the first and second terms in equation (4.40) are of the same order and we can look for the condition for charge neutrality.

To this end it is now usual to invoke the 'plasma approximation', that is in this case

$$\frac{N_p - N_e}{N_o} = \varepsilon \ll 1$$

and hence equate to zero the right-hand side of equations (4.40) or (4.41). However, to justify this step we first

look at the consequences of having $N_p \neq N_e$. Firstly, from Maxwell's equation

$$\text{div } \underline{E} = 4\pi e(N_p - N_e)$$

and, very crudely, $\text{div } \underline{E} \sim E/L$ where L is the scale length of the electric field produced by the charge imbalance. Again using the argument contained in (4.34) we have

$$\frac{E^2}{K\Phi} \sim 4\pi e(N_p - N_e) .$$

Now according to the previous discussion $\left(\frac{E}{E_o}\right)^2_{max} \sim \left(\frac{e\Phi}{m_p v_\infty^2}\right)$, for higher electric fields the drift-flow theory breaks down. Thus

$$(N_p - N_e)_{max} \sim \left(\frac{E^2}{4\pi e K \Phi}\right)_{max} \sim \frac{B_o^2 N_o e}{4\pi K m_p c^2}$$

or

$$\left(\frac{N_p - N_e}{N_o}\right)_{max} \sim \frac{e\Phi}{K m_p c^2} \qquad (4.44)$$

Now $m_p c^2 \simeq 10^6$ KeV while the typical $e\Phi$ values we shall be considering are in the range $1 \to 10^2$ KeV. Thus

$$\left(\frac{N_p - N_e}{N_o}\right) \lesssim 10^{-4} \to 10^{-6}$$

in the drift-flow region. We thus write

$$\text{div } \underline{E} = 4\pi e N_o \varepsilon \qquad (4.45)$$

where $\varepsilon \lesssim 10^{-4} \to 10^{-6}$ produces significant perturbations of the electric field in the flow. However, from (4.41) we have

$$\left\{\frac{eB^2}{m_pc^2}\left(f\left(\phi+\frac{m_p(v_p^2-v_\infty^2)}{2e}\right)-f(\phi)\right)-f(\phi)\left(\operatorname{div}\underline{E}-\frac{\underline{E}.\underline{\underline{\nabla}}\underline{B}}{B^2}\right)\right\}\Big/4\pi N_o e$$

$$\simeq \frac{\lambda_p e B B_o}{m_p c^2}\epsilon = \frac{\lambda_p B}{B_o}\left(\frac{e\Phi}{m_p c^2}\right)\epsilon \qquad (4.46)$$

But we have seen from (4.44) that $\epsilon \lesssim \left(\frac{e\Phi}{m_p c^2}\right)$ in the drift-flow region, so that with $\lambda_p \simeq 1$ and $B/B_o \lesssim 1$

$$\frac{\lambda_p B}{B_o}\left(\frac{e\Phi}{m_p c^2}\right)\epsilon \sim \mathcal{O}(\epsilon^2)$$

Thus, comparing equations (4.45) and (4.46) we see that while each term on the left-hand side of (4.46) is of order ϵ, the combination shown is of order (or thereabouts) of ϵ^2. We have therefore justified the use of the plasma approximation in the drift-flow region, i.e. equating the right-hand side of (4.41) to zero to obtain

$$\operatorname{div}\underline{E} \simeq \frac{\underline{E}.\underline{\underline{\nabla}}\underline{B}}{B} + \frac{eB^2}{m_pc^2}\left\{f\left(\phi+\frac{m_p(v_p^2-v_\infty^2)}{2e}\right)-f(\phi)\right\}\Big/f(\phi) \qquad (4.47)$$

For the uniform gradient example this becomes

$$\operatorname{div}\underline{E} \simeq \frac{\underline{E}.\underline{\underline{\nabla}}\underline{B}}{B} + \frac{\psi B^2}{2\Phi}\left(\frac{v_p^2-v_\infty^2}{c^2}\right)\Big/\left(1+\psi\left(\frac{\phi}{\Phi}-\frac{1}{2}\right)\right) \qquad (4.48)$$

On putting to zeroth order $v_p \simeq cE/B$ we have finally

$$\operatorname{div}\underline{E} \simeq \frac{\underline{E}.\underline{\underline{\nabla}}\underline{B}}{B} + \frac{\psi}{2\Phi}\,\frac{\left(E^2-E_o^2\left(\frac{B}{B_o}\right)^2\right)}{\left(1+\psi\left(\frac{\phi}{\Phi}-\frac{1}{2}\right)\right)} \qquad (4.49)$$

which is Poisson's equation for the drift-flow.

Since, from equation (4.30) we have B/B_o as a function of E/E_o in the drift-flow region, equations (4.47) and (4.49)

determine the structure of the flow. These equations are equivalent to Laplace's equation $\nabla^2\phi = 0$ (or div $\underline{E} = 0$) for ϕ in a vacuum, which may be integrated is some region for the potential field when the boundary conditions are given. In the simpler case $\psi = 0$ (uniform inflow), we have from equation (4.40) that $\lambda_p = 1$ is the governing equation; or to first order from (4.49) that

$$\text{div } \underline{E} \simeq \frac{\underline{E} \cdot \underline{\nabla} B}{B} \qquad (4.50)$$

From equation (4.5) we note that this implies that $\underline{\nabla} \wedge \underline{v}_p = \underline{0}$, the flow is, in hydromagnetic terms, irrotational.

(v) Numerical Results of Drift-Flows Obtained from Poisson's Equation

In this section we shall present some results of numerical solutions of equation (4.49) i.e. the flow for uniform incoming density gradients. The method used will be discussed in some detail, since it was found to be highly satisfactory in dealing with problems of this type when used in conjunction with high-speed computers.

The method chosen is a relaxation method, known as the cyclic Chebyshev modification of the successive over-relaxation by points (SOR) process (see, for example, Hockney (1970)). The potential $\phi_{i,j}$ is defined on an $n \times n$ mesh covering the region of interest, the length of a mesh spacing being h, and $1 \leq i, j \leq n$. Using the usual five-point difference expression for the Laplacian operator, Poisson's equation in difference form is

$$\phi_{(i+1),j} + \phi_{(i-1),j} + \phi_{i,(j+1)} + \phi_{i,(j-1)} - 4\phi_{i,j} = -4\pi\rho_{i,j}h^2 = -q_{i,j} \qquad (4.51)$$

In order to shorten such expressions we define

$$4\phi^{off}_{i,j} = \phi_{(i+1),j} + \phi_{(i-1),j} + \phi_{i,(j+1)} + \phi_{i,(j-1)} \qquad (4.52)$$

The mesh is 'swept' in some manner and the potential at each point (except the boundary points) is recalculated according to the following procedure. First the residual R is calculated

$$R = 4\left[\phi^{off}_{i,j} - \phi_{i,j} + \frac{q_{i,j}}{4}\right]$$

and we then replace $\phi^{new}_{i,j} = \phi^{old}_{i,j} + (\frac{W}{4})R$. W is the "over-relaxation factor" which may be adjusted to improve overall convergence.

Equivalently, we can calculate a $\phi'_{i,j}$ from (4.51)

$$\phi'_{i,j} = \phi^{off}_{i,j} + \frac{q_{i,j}}{4}$$

and then take $\phi^{new}_{i,j} = (1-W)\,\phi^{old}_{i,j} + W\,\phi'_{i,j}$. (4.53)

In the straight SOR procedure W is fixed, and it has been shown for model problems that best convergence results when

$$W = W_b = 2/(1 + (1-\mu^2)^{\frac{1}{2}})$$

where $\mu = \cos(\pi/n)$. Note that for n large $W_b \simeq 2$, so that from (4.53) we are 'over-relaxing' the solution. The guaranteed asymptotic (after $\sim n/2$ iterations) decay of the error at each point is then $(W_b - 1)$ per iteration. For n large we have

$$W_b \simeq 2\left(1 - \left(\frac{\pi}{n}\right)\right)$$

so that the error reduction factor is $(1 - \frac{2\pi}{n})$ per iteration. As can be seen, the convergence is very slow for very large numbers of mesh points. In the model problem the 'sweep' is first carried out over the odd mesh points (those for which $i + j$ is odd), then over the even mesh points ($i + j$ even), the 'new' values of potential immediately replacing the 'old' values on the mesh and being used in all succeeding recalculations. This method has been used in the calculations presented here.

In the cyclic Chebyshev modification, the over-relaxation factor W is changed for each of these 'half-iterations', according to

$$W^{(0)} = 1 \quad ; \quad W^{(\frac{1}{2})} = 1/(1-\frac{\mu^2}{2}) \; ; \; W^{(t+\frac{1}{2})} = 1/\left(1-\frac{\mu^2 W^{(t)}}{4}\right)$$

$$t = \tfrac{1}{2}, 1, \tfrac{3}{2}, \cdots$$

This leads to a much improved initial error decay, although for large t $W \to W_b$ so that the asymptotic error decay is the same as for the straight SOR process. Of course, the absolute error after n iterations depends principally on the errors in the initial 'guessed' solution. In the calculations performed here for flow between parallel boundaries we have used the solution to Laplace's equation with the given boundary conditions as the initial 'good guess'. This solution will be derived below.

Although the convergence of these relaxation methods are rather poor for large meshes, and the procedures relatively inefficient when compared with the 'direct' methods their great advantage is that they are very easy to program for a

computer. For instance, Hockney's Fast Fourier Analysis/ Synthesis procedure calculates in 'one shot' the exact solution to the difference equations in the time required to perform 5 or 6 SOR iterations. However, the large amount of code required to do this is to be compared with the SOR which, to carry out a sweep of the mesh, correct the potential, including the odd/even logic reduces to just six Fortran statements.

```
      DØ  10  I = 2,M
      K = (I - (I/2)*2) + 2
      IF ((IT/2)*2.NE.IT) K = (I/2)*2-I+3
      DØ  20   J = K,M,2
   20 PH(I,J)=(1.-W)*PH(I,J)+W*(PH(I+1,J)+PH(I-1,J)+PH(I,J+1)
     1 + PH(I,J-1) + Q(I,J))
   10 CØNTINUE
```

where M is n-1, PH(I,J) is $\phi_{i,j}$ and IT is the number of the iteration (IT = 1,2,3, etc). We correct the odd mesh when IT is odd and the even mesh when IT is even. In the present problem, however, the $q_{i,j}$ are not fixed, but are functions of the local field values derivable from the potential. In this case we simply allow $q_{i,j}$ to relax with the solution.

As has been stated we use the solution of Laplace's equation with the given boundary conditions on the potential as our initial 'good guess' solution. We first dedimensionalize as follows:

$$\phi' = \frac{\phi}{\Phi} \qquad \text{and} \qquad x', z' = \frac{x}{d}, \frac{z}{d} .$$

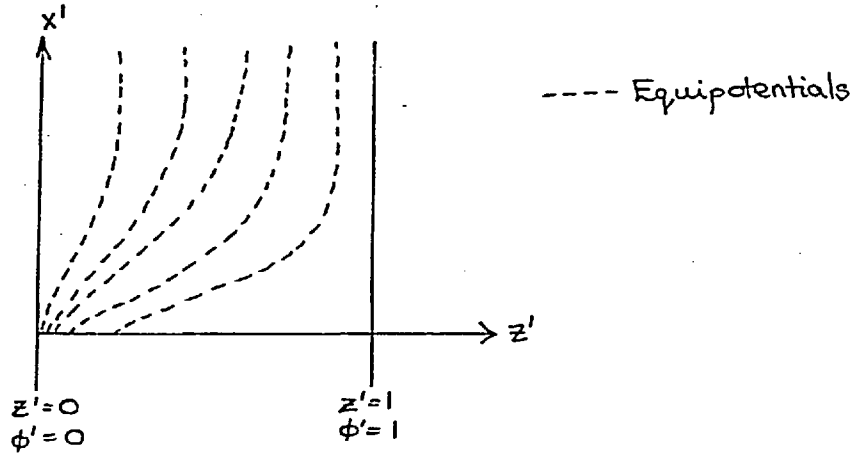

Figure 4.5

where x', z' are as shown in Fig. 4.5. The boundary conditions on $\phi'(x',z')$ are: $\phi'(x',0) = 0$, $\phi'(x',1) = 1$ and $\phi'(0,z') = f(z')$, where $f(0) = 0$ and $f(1) = 1$. If we first consider the problem with $\phi'(x',1) = 0$, the solution of our problem with $\phi'(x',1) = 1$ is given simply by adding z' to the former solution (i.e. a uniform electric field). This is possible because of the linearity of Laplace's equation. We look for a separable solution of the form $\phi'(x',z') = X(x')Z(z')$, and using separation constant k^2 obtain

$$Z(z') = A \cos kz' + B \sin kz'$$

$$X(x') = C\, e^{kx'} + D\, e^{-kx'} .$$

Applying the boundary conditions $\phi'(x',0) = 0$; $\phi'(x',1) = 0$ and $\phi(x',z') \to 0$ as $x' \to \infty$ (the solution to be valid for $x' \geq 0$) we obtain $A = 0$, $C = 0$ and $k = n\pi$, $n = 1,2,3,\ldots$ Thus the general solution

$$\phi'(x',z') = \sum_{n=1}^{\infty} A_n \sin(n\pi z')\, e^{-n\pi x'}$$

or, for boundary conditions $\phi'(x',1) = 1$ we obtain

$$\phi'(x',z') = z' + \sum_{n=1}^{\infty} A_n \sin(n\pi z')\, e^{-n\pi x'} \qquad (4.54)$$

Clearly, the A_n are the coefficients of the Fourier series of the boundary condition $\phi'(0,z') = f(z')$, and hence are obtained from

$$A_n = 2\int_0^1 \left(f(z') - z'\right) \sin(n\pi z')\, dz' \tag{4.55}$$

As can be seen, the shorter the wavelength of the Fourier mode, the faster is its exponential decay away from the $x' = 0$ boundary. We are interested in problems where the electric field becomes much larger than the value in the incoming flow, and so we choose the $x' = 0$ boundary condition such that the potential drop occurs across a small region near $z' = 0$. In order to obtain a simple form for the A_n we choose (see Fig. 4.6)

$$f(z') = \begin{cases} \sin pz' & 0 \le z' \le \pi/2p \\ 1 & \pi/2p \le z' \le 1 \end{cases} \tag{4.56}$$

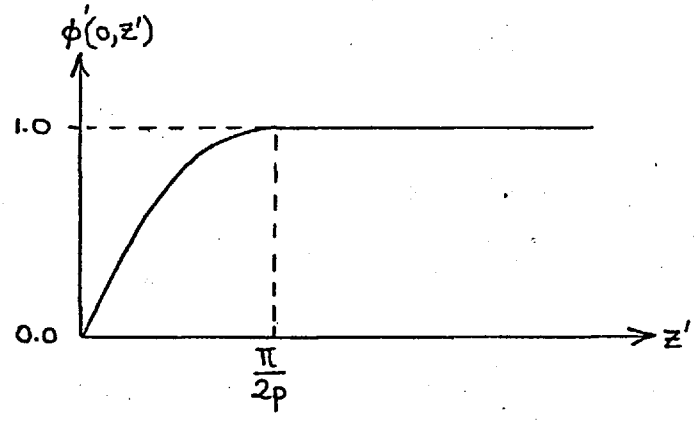

Figure 4.6

Then substituting (4.56) into (4.55) for the Fourier coefficients we have

$$A_n = \frac{2p^2}{n\pi\left(p^2 - (n\pi)^2\right)} \cdot \cos\left(\frac{\pi n^2}{2p}\right) \tag{4.57}$$

Clearly, in order to obtain a good representation of the boundary potential we must not terminate the series until $n >> p/\pi$. For $x' > 0$ the short-wavelength modes rapidly die away and far fewer terms need to be considered.

We choose p such that the maximum flow velocities in the system are a significant fraction of the total potential energy for the range of system parameters of interest. The maximum value of E occurs at $x' = z' = 0$ and is given by

$$\left(\frac{E}{E_o}\right)_{max} = p \ .$$

Let us thus write $\frac{m_p c^2 E^2}{B^2} = Ke\Phi$ where K is the 'significant fraction'. Then

$$\left(\frac{E}{E_o}\right) = \frac{ed\mathcal{B}}{c B_o}\left(\frac{4\pi K N_o}{m_p}\right)^{1/2}$$

For the geomagnetic tail we have $d \simeq 3 \times 10^{10}$ cm and $N_o = 0.1 \rightarrow .01$ cm^{-3}. Taking $N_o = 0.05$ for definiteness and $\mathcal{B}/B_o \simeq 1$ (for $\psi = 0$ we have $\mathcal{B}/B_o = 1-K$ from (4.33)) we find

$$\left(\frac{E}{E_o}\right)_{max} \simeq 300\ K^{\frac{1}{2}}$$

Then putting $K = 0.1$ we have $\left(\frac{E}{E_o}\right)_{max} = p = 100$. We thus choose $p = 100$ as being representative of the order of the electric field enhancement we are likely to obtain in the systems of interest. As indicated above, we must therefore not terminate the Fourier series until $n >> 30$. Using (4.57) and (4.54) the potential in the region $x' \geq 0$ and $0 \leq z' \leq 1$ was then evaluated using a maximum of 200 series terms ($\lesssim 0.2\%$ error in ϕ), but successively less terms being used as the short wave-length modes exponentially decay with

increasing x'. The equipotential lines from this calculation are shown in Fig. 4.7.

The most significant perturbations from a uniform electric field occurs in the region where the electric field is considerably enhanced, i.e. near $x' = 0$, $z' = 0$. The approximate solution to Laplace's equation in this region for these boundary conditions is (see Fig. 4.8)

$$\phi(\theta) = \frac{2\Phi}{\pi}\theta$$

for $\frac{\pi d}{2p} \lesssim r << d$, where $\theta = \tan^{-1}(\frac{z}{x})$ and $r = (x^2+z^2)^{\frac{1}{2}}$.

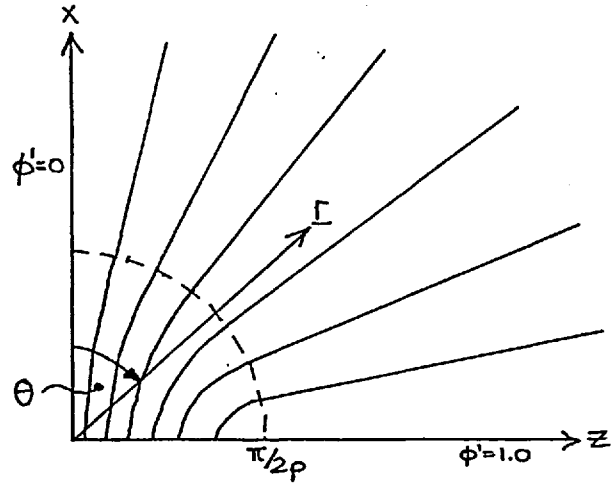

Figure 4.8

We then have $\underline{E} = E_\theta \hat{\underline{\theta}}$ and $E_\theta = -2\Phi/\pi r$. Putting $E_o = \Phi/d$ we obtain

$$\frac{|E_\theta|}{E_o} = \frac{2}{\pi}\left(\frac{d}{r}\right)$$

If again K is the ratio between the kinetic energy of the flow and the total potential across the system we can find K as a function of the radial distance from $x' = z' = 0$.

$$K = \frac{m_p v_p^2}{2e\Phi} \simeq \frac{m_p c^2 E_\theta^2}{2e B^2 \Phi} \simeq \frac{m_p c^2}{2d^2 e^2 N_o \pi^3}\left(\frac{B_o}{B}\right)^2\left(\frac{d}{r}\right)^2$$

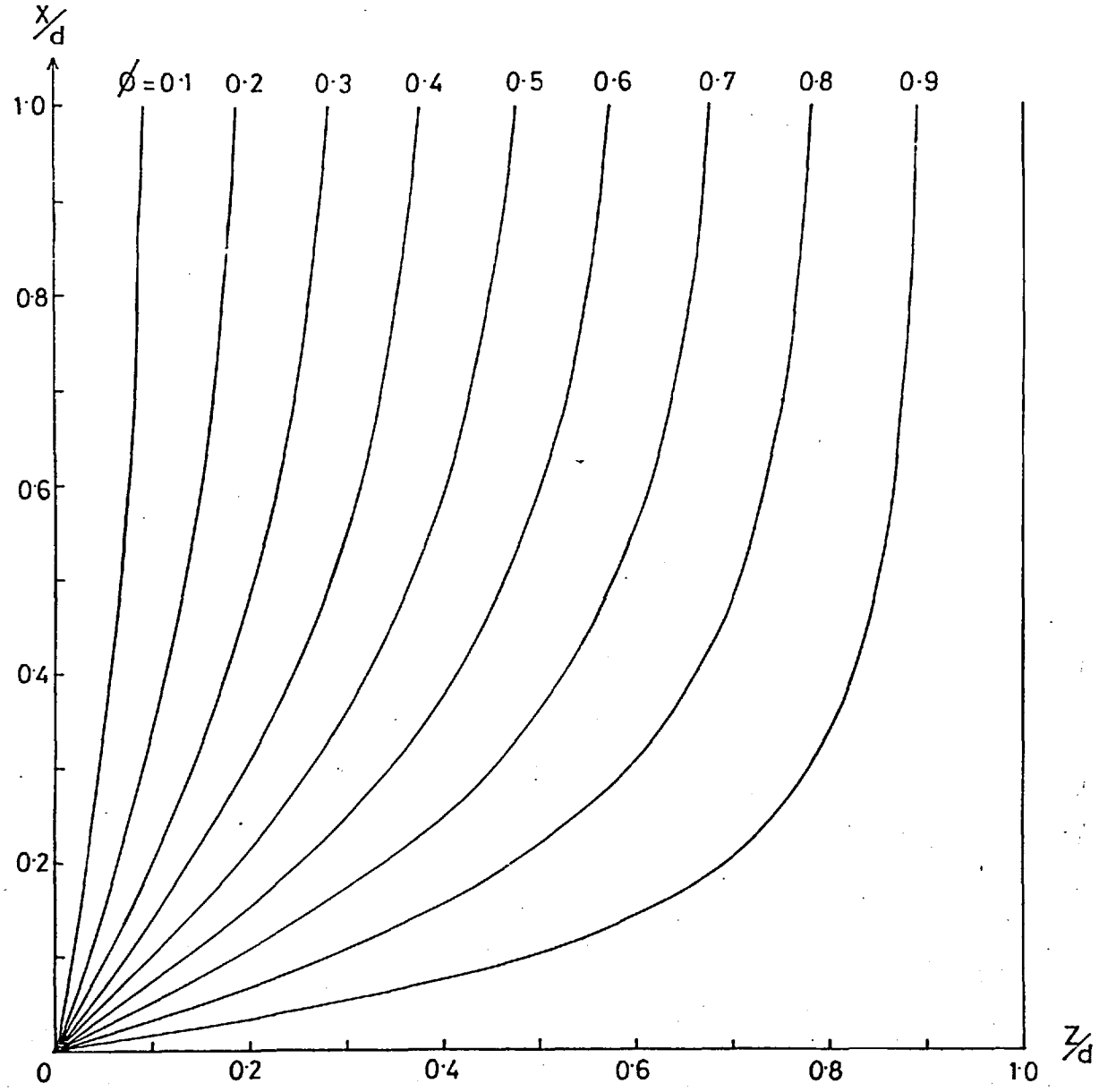

Figure 4.7: Equipotentials of the solution of Laplace's equation in a rectangular space using the boundary condition (4.56) along the line x'=0, with $\phi'(z'=0) = 0$ and $\phi'(z'=1) = 1$. Obtained by Fourier analysis of the x'=0 boundary potential variation.

or for geomagnetic tail parameters $K \simeq \frac{10^{-7}}{N_o} \left(\frac{d}{r}\right)^2$ (where $B/B_o \simeq 1-K$ and $K << 1$). Thus $K << 1$ for $\left(\frac{r}{d}\right) > \left(\frac{10^{-7}}{N_o}\right)^{\frac{1}{2}}$ or, for $N_o = 0.1 \rightarrow 0.01$ cm^{-3} for $\left(\frac{r}{d}\right) > 10^{-3}$.

Since the number of mesh points to be corrected per iteration increases as $(n-2)^2$ and the guaranteed asymptotic error decay decreases as n increases as described above, we should use a minimum number of mesh points compatible with the detail of information required from the calculation. The region of interest is near $x' = 0$, $z' = 0$, and in view of the above consideration we choose to restrict our calculation to a region given by $0 \leq x', z' \leq 5 \times 10^{-2}$, such that K on the boundary has a maximum value of $\sim 4 \times 10^{-5}/N_o$. From the above we also have $|E_\theta|/E_o \simeq 10$ on the boundary, so that for $\psi \neq 0$ from (4.49) div $\underline{E}$ is likely to be significant on the boundary, although much less than in the interior region. We have chosen to cover the region with a 51 x 51 mesh which gives a sufficiently detailed description of the potential distribution in the region. The potential on the boundaries of the region was taken for all calculations to be the values given by the analytic solution to Laplace's equation.

In order to test the iteration scheme, Laplace's equation was first solved on the mesh with the above boundary conditions but starting with $\phi_{i,j} = 0$ on the interior points (i.e. a 'bad initial guess'). After 100 steps (50 full sweeps of the mesh), the values of potential were changing by $\lesssim 1\%$ in 5 full sweeps and were in agreement with the analytic solution to the differential equation (rather than the difference equation being solved here) to within about 1%. Such satisfactory agreement gives us a high degree of confidence

in the quality of the solutions of Poisson's equation for the drift-flow (equation (4.49)) obtained by this iteration scheme, and now to be discussed.

We first dedimensionalize according to

$$\underline{\nabla}' = d\underline{\nabla} \quad ; \quad \phi' = \phi/\Phi \quad ; \quad B' = B/B_O \quad ; \quad \underline{E}' = \underline{E}/E_O \ .$$

These preserve the relationship $\underline{E}' = -\underline{\nabla}'\phi'$.

The first case to be considered is $\psi = 0$, so that Poisson's equation becomes

$$\underline{\nabla}'.\underline{E}' = \frac{\underline{E}'.\underline{\nabla}'B'}{B'} \qquad \text{or} \qquad \nabla'^2\phi' = \frac{\underline{\nabla}\phi'.\underline{\nabla}'B'}{B'} \tag{4.58}$$

In difference form this is

$$4\left(\phi'^{off}_{i,j} - \phi'_{i,j}\right) = \left((\phi_{i,(j+1)} - \phi_{i,(j-1)})(B_{i,(j+1)} - B_{i,(j-1)}\right.$$
$$\left. + (\phi_{(i+1),j} - \phi_{(i-1),j})(B_{(i+1),j} - B_{(i-1),j})\right)/(4B_{i,j})$$

so that the correction step in the iteration scheme becomes

$$\phi'^{new}_{i,j} = (1-W)\phi^{old}_{i,j} + W\left\{\phi'^{off}_{i,j} - \frac{1}{16B_{i,j}}\left((\phi_{i,(j+1)} - \phi_{i,(j-1)})(B_{i,(j+1)} - B_{i,(j-1)})\right.\right.$$
$$\left.\left. + (\phi_{(i+1),j} - \phi_{(i-1),j})(B_{(i+1),j} - B_{(i-1),j})\right)\right\}$$

We calculate $B = B(E)$ from equation (4.32)

$$E' = \alpha^{\frac{1}{2}} B' \left((1 + 1/\alpha) - B'\right)^{\frac{1}{2}}$$

where we choose $\alpha = \frac{2e\Phi}{m_p V_\infty^2}$ such that the maximum electric field perturbation ($E' \simeq 100$) results in the maximum magnetic

field perturbation. From Fig. 4.3 we see that the maximum electric field in the drift-flow is given by

$$\left(\frac{E'}{\alpha^{1/2}}\right)_{max} \simeq 0.4$$

which results in $B' \simeq 0.7$. For $E'_{max} \simeq 100$ we thus find $\alpha \simeq 6 \times 10^4$. For higher values of α, $E' \simeq 100$ does not produce such large magnetic field perturbations. We have chosen to use $\alpha = 9 \times 10^4$ such that $(E'/\alpha^{1/2})_{max} \simeq 0.33$ and the minimum value of B' on the mesh is thus $\simeq 0.85$. Since we also have

$$\alpha = \frac{8\pi e^2 d^2 N_o}{m_p c^2}$$

for tail parameters, $\alpha = 9 \times 10^4$ corresponds to $N_o \sim 0.03$ cm^{-3}, which is within the range of interest ($0.1 \rightarrow 0.01$ cm^{-3}). The results of the calculation after 40 full sweeps of the mesh are shown in Fig. 4.9, where the solid line represents the equipotentials of the solution and the dotted line the solution of Laplace's equation. The small ($\lesssim 1\%$) changes in the potential on the mesh are due to the facts that, first, $\underline{\nabla}B$ is small, and secondly that since approximately $\phi \simeq \phi(\theta)$ so that $\underline{E} \simeq E_\theta(r)\hat{\underline{\theta}}$ and hence $\underline{\nabla}B = |\underline{\nabla}B|\hat{\underline{r}}$, we have $\underline{E} \cdot \underline{\nabla}B \simeq 0$ in the region of interest.

The perturbations of the equipotentials when $\psi \neq 0$, are more pronounced. In dimensionless form the equation for which we require a solution is

$$\nabla'^2\phi' = \frac{\underline{\nabla}'\phi' \cdot \underline{\nabla}'B'}{B'} - \frac{\psi}{2}\frac{(E'^2 - B'^2)}{(1+\psi(\phi' - \frac{1}{2}))} \qquad (4.59)$$

Since we have already found that the perturbations due to the

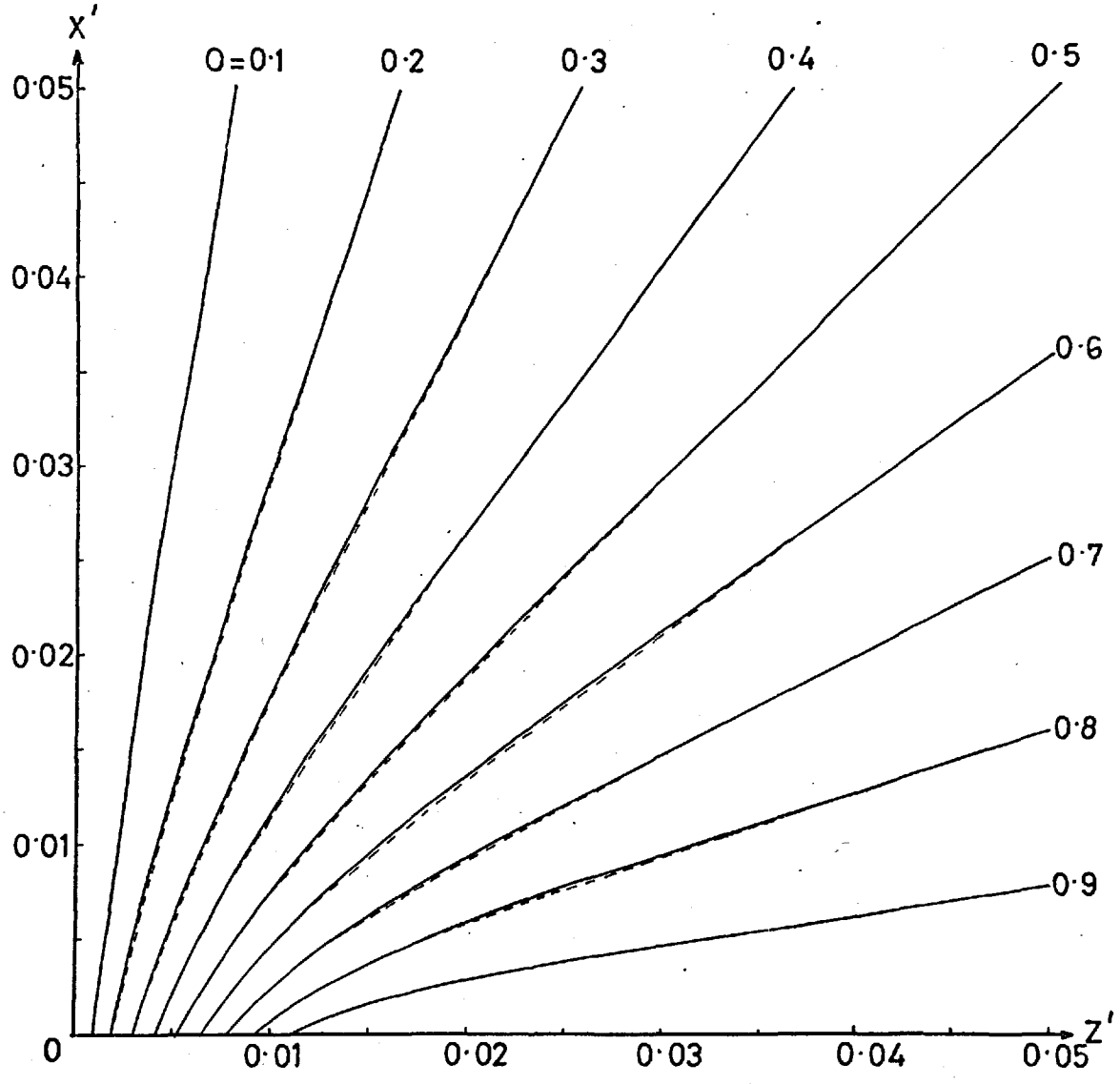

Figure 4.9: Equipotentials of the solution of Poisson's equation for cold plasma drift-flow, for incoming plasma of uniform density (ψ=0) (solid line). The boundary potentials used for the computed region $0 \leq x', z' \leq 0.05$, are those from the solution of Laplace's equation (Fig. 4.7). The equipotentials of the solution of Laplace's equation with these boundary conditions are shown dotted; only very minor variations are noted.

first term on the right-hand side are small, we neglect it. Also, since $E'^2 >> B'^2$ in the region of interest, we finally simplify equation (4.59) to

$$\nabla'^2\phi' \simeq -\frac{\psi}{2}\frac{(\nabla'\phi')^2}{(1+\psi(\phi'-\frac{1}{2}))} \tag{4.60}$$

Then Poisson's equation in difference form becomes

$$4\left\{\phi'^{\,off}_{i,j} - \phi'_{i,j}\right\} = \frac{\psi}{8}\frac{\left\{(\phi'_{(i+1),j}-\phi'_{(i-1),j})^2 + (\phi_{i,(j+1)}-\phi_{i,(j-1)})^2\right\}}{(1+\psi(\phi'_{i,j}-\frac{1}{2}))}$$

and the correction step in the cyclic Chebyshev iteration scheme is

$$\phi^{new}_{i,j} = (1-W)\phi^{old}_{i,j} + \frac{W}{2}\left\{\phi^{old}_{i,j} + \frac{\psi}{8}\frac{\left\{(\phi_{(i+1),j}-\phi_{(i-1),j})^2 + (\phi_{i,(j+1)}-\phi_{i,(j-1)})^2\right\}}{(1+\psi(\phi_{i,j}-\frac{1}{2}))}\right\}$$

The results for various values of ψ ($|\psi| < 2$) are shown in the form of equipotential lines in Fig. 4.10. These results were obtained after 50 full sweeps of the mesh, at which stage the solutions were changing by < 1% in 10 full sweeps. It is clear from the figures that significant perturbations of the Laplace potential will exist outside of the region computed, that the equipotentials all converge to the same points on the boundary is just a consequence of maintaining fixed boundary potentials (as must be done in such numerical calculations). We first note that the equipotential systems obtained, while significantly perturbed from the Laplace solution, do not represent an enormous change in the qualitative nature of the fields. For $\psi > 0$ it can be seen that the

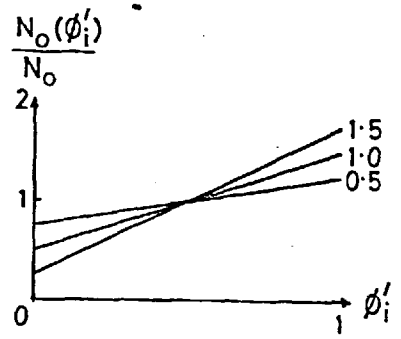

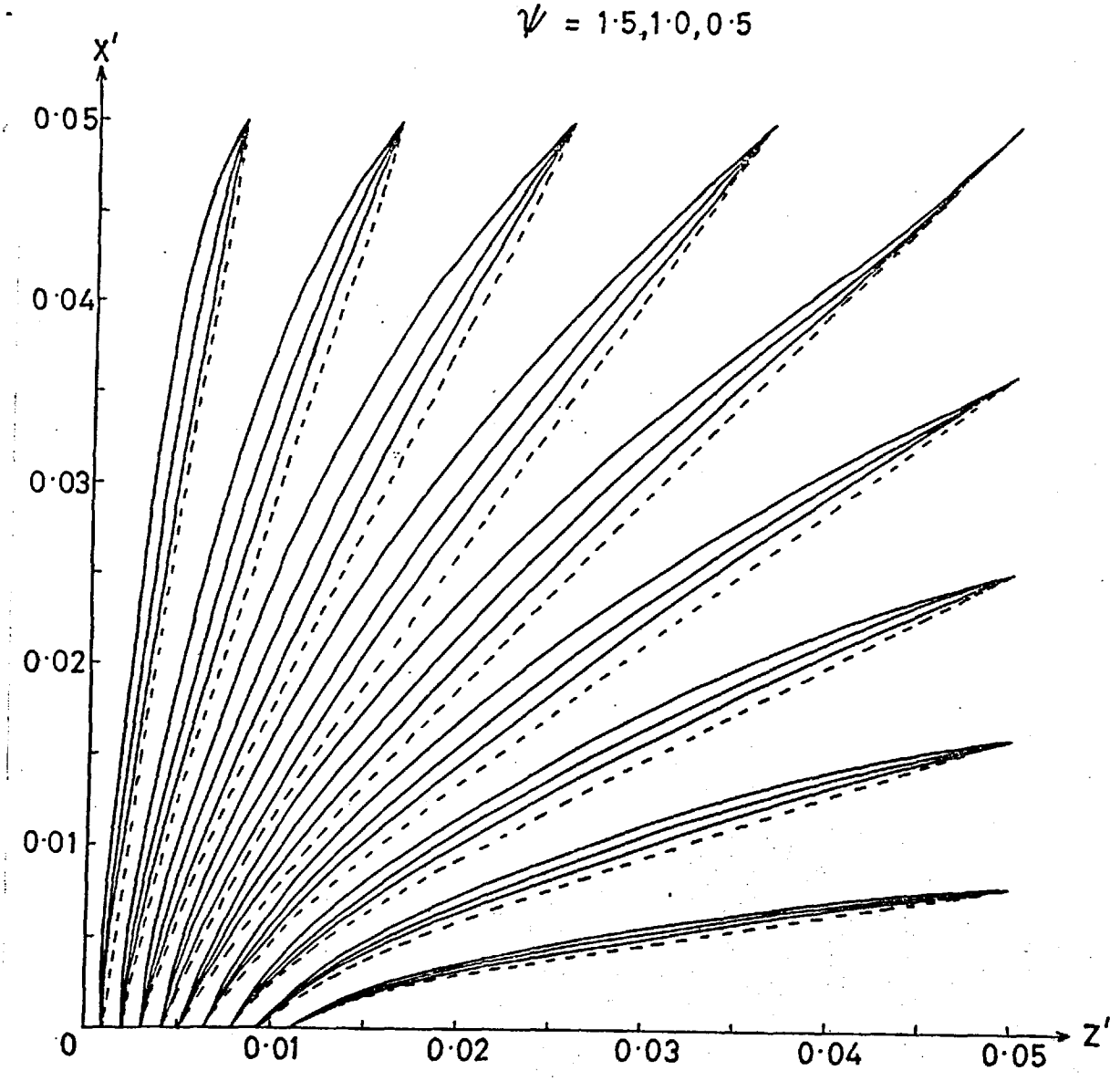

Figure 4.10(a): Equipotentials of the solution of Poisson's equation for the drift flow for ψ = 0.5, 1.0, 1.5 (solid lines). The boundary potentials used for the computed region $0 \leq x'$, $z' \leq 0.05$ are those from the solution of Laplace's equation (fig. 4.7). The equipotentials of the solution of Laplace's equation with these boundary conditions is shown dotted; the variations shown are those expected for a positive charge density in the region.

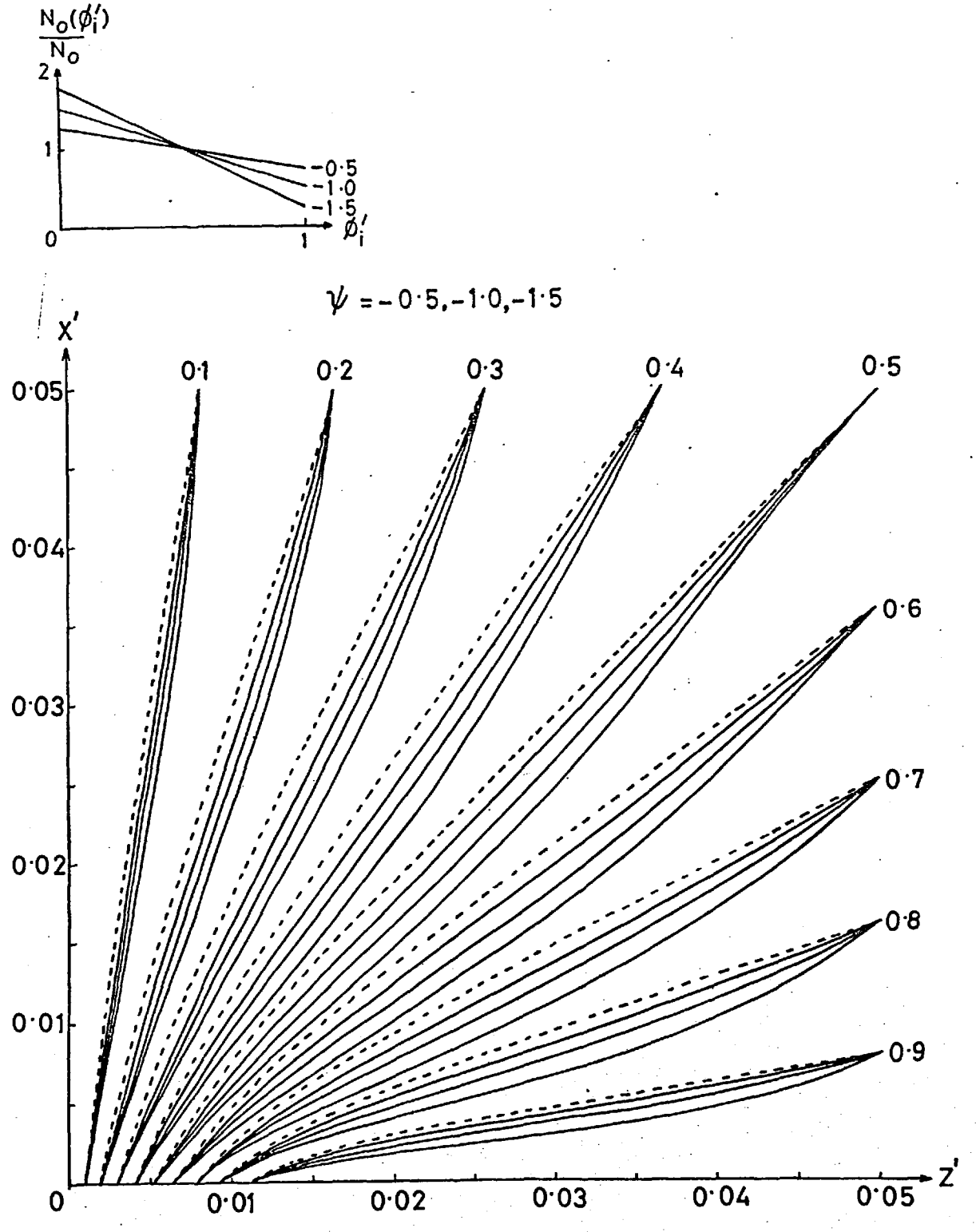

Figure 4.10(b): As for Fig. 4.10(a) except ψ = -0.5, -1.0, -1.5 (solid lines). The variations shown are those expected for a negative charge density in the region.

high electric field region near $z' = 0$ is extended to higher x' values, i.e. the equipotentials are relaxing back to a uniform electric field configuration more slowly than the Laplace solution. Indeed, for large enough ψ the maximum in the electric field occurs for $x' > 0$ rather than on the boundary $x' = 0$. These results are not surprising when one considers the direction of the electric field set up by a region of positive space charge (which is present when $\psi > 0$ and $v_p > V_\infty$); it enhances $|E_z|$ for small values of z' and diminishes it for larger values. Similarly the negative space-charge present when $\psi < 0$ has the opposite effect, and, as can be seen, this results in the equipotential structure relaxing back to the uniform electric field configuration over a shorter distance in x'. These differences are more clearly displayed in contours of $|E|$ for various ψ values shown in Fig. 4.11.

Summary

In this chapter we have developed the equations which govern the drift-flow of cold plasma in crossed electric and magnetic fields. The magnetic field is consistent with current densities in the flow and the electric field is given by the boundary conditions together with charge densities in the flow. The resulting equations are a relationship between B and E, and a Poisson's equation for the equipotential structure respectively. A method of obtaining solutions of Poisson's equation for the drift flow which has been found highly successful has been described and some sample results presented.

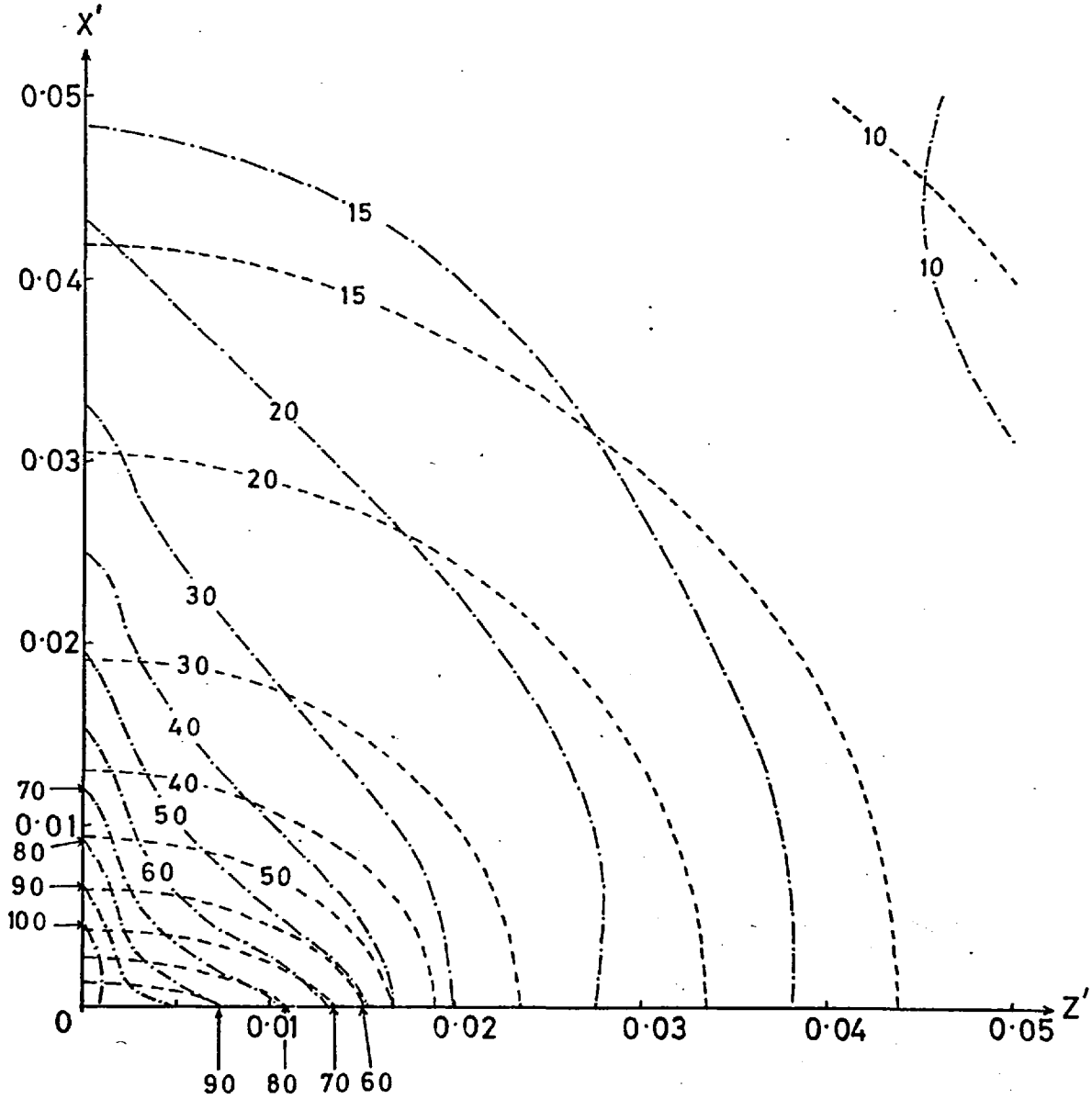

Figure 4.11(a): Contours of $\frac{|E|}{E_o}$ for $\psi = 1.5$ (dot-dash) and for $\psi = 0.0$ (dotted), showing the enhancement of the electric field near $z' = 0$ due to the positive charge.

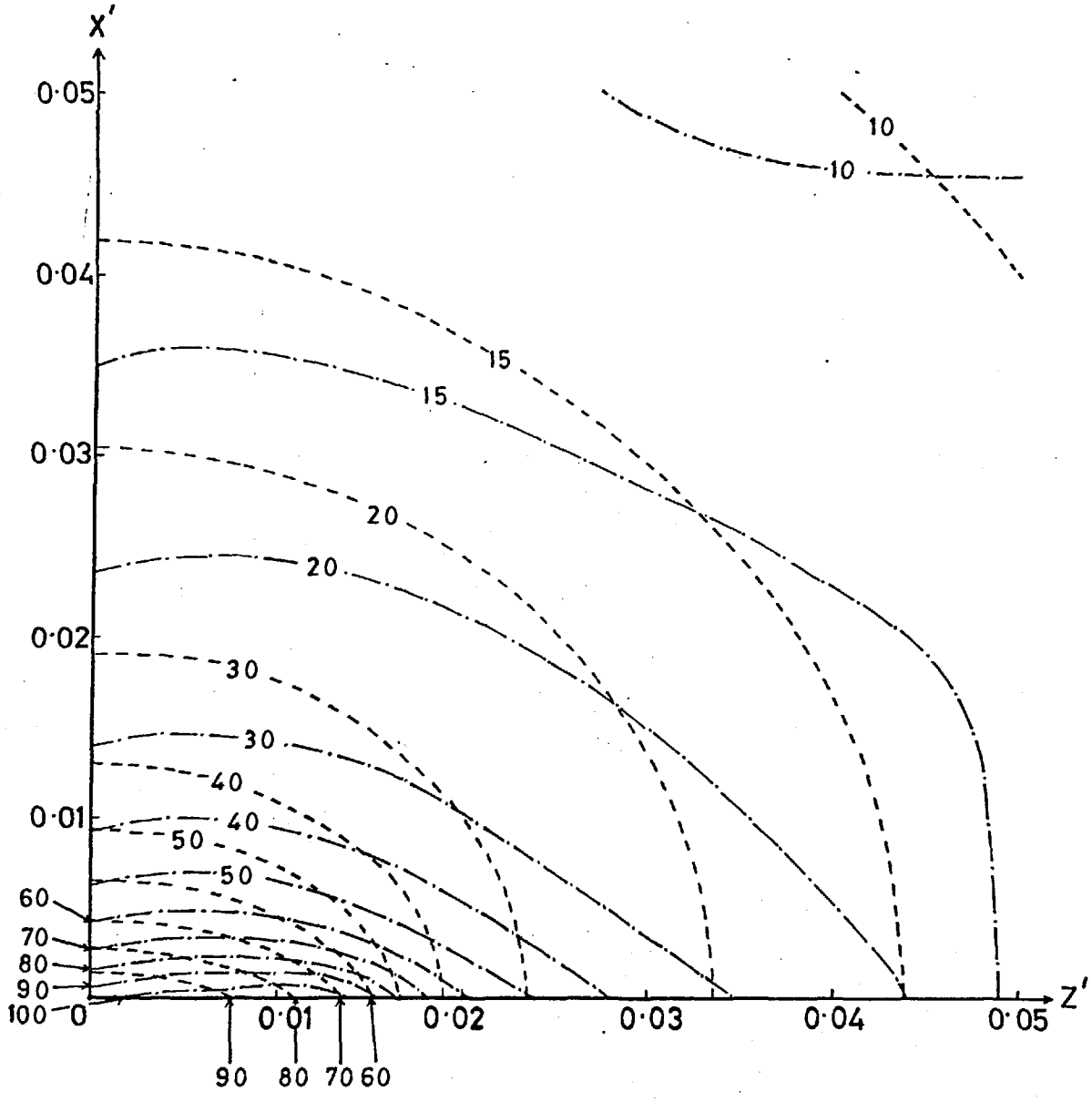

Figure 4.11(b): Contours of $|E|/E_o$ for ψ = -1.5 (dot-dash) and for ψ = 0.0 (dotted), showing the enhancement of the electric field along z'=0, and its reduction along x'=0, expected for a negative charge in the region.

References

Alfvén, H. 1968. Some properties of magnetospheric neutral surfaces. J. Geophys. Res. 73, 4379-4381.

Chandrasekhar, S. 1960. Plasma Physics (notes compiled by S.K. Trehan), Chicago and London, University of Chicago Press.

Hockney, R.W. 1970. The potential calculation and some applications. Methods in Computational Physics (Ed. Alder), Academic Press, New York, 135-212.

Northrop, T.G. 1963. The Adiabatic Motion of Charged Particles, Interscience Publishers, New York.

CHAPTER 5

A SELF-CONSISTENT DESCRIPTION OF THE PROPERTIES OF A MAGNETIC NEUTRAL SHEET SURROUNDED BY COLD PLASMA

(i) General Discussion

We have previously shown that the simple assumptions about the structure of the electromagnetic field in a neutral sheet system made by Alfvén and Speiser (i.e. nearly uniform electric field and adiabatic particle flow) are only valid if

$$\frac{B_o^2}{4\pi N_o} >> m_p c^2 .$$

This condition ensures that the kinetic energy of the flow into the field reversal region is much less than the electrostatic potential energies across the system when account is taken of the electric field produced by the charge of trapped, accelerating particles. Systems in which this condition is not satisfied (e.g. the geomagnetic tail) should thus be controlled by the structure of the electric field, which must be extremely non-uniform. We also saw that the effect of the positive charge in the sheet was to localize the Alfvén potential drop near the $\phi = 0$ boundary. Thus we may infer that the electric field scale length involved in the breakdown of adiabatic flow is related to the distance over which the Alfvén potential falls near this boundary. For the breakdown of the adiabatic approximation we require

$$\frac{v_p}{\Omega L} = \frac{m_p c^2 E}{eB^2 L} \simeq 1 \qquad (5.1)$$

and with the above interpretation of L we may write

$$EL \simeq \Phi \,. \tag{5.2}$$

Eliminating L from (5.1) and (5.2) gives

$$\frac{m_p c^2 E}{B^2} \simeq e\Phi$$

i.e. the flow energies in this region are comparable to the potential energy, indicating that particles drifting across equipotentials provide significant currents, together with any particles oscillating about the sheet. This further implies that a significant fraction of the protons reach the $\phi = 0$ boundary without crossing the neutral sheet and oscillating about it.

If we eliminate E from (5.1) and (5.2) we then determine L, i.e.

$$L \simeq \frac{c}{(\frac{4\pi N_o e^2}{m_p})^{\frac{1}{2}}} = \frac{c}{\omega_{pi}} = \lambda_p \tag{5.3}$$

We thus expect the potential drop to occur over a distance comparable with the proton plasma wavelength.

In Chapter 3 we found that

$$(\frac{\lambda_p}{d}) = (\frac{m_p v_o^2}{e\Phi})^{\frac{1}{2}} \qquad \text{where} \qquad v_o = \frac{c\Phi}{B_o d}$$

and so, if $m_p v_o^2 << e\Phi$ then $L << d$. Numerically equation (5.3) is

$$L \simeq \frac{2 \times 10^2}{N_o^{\frac{1}{2}}} \text{ Km}$$

or $L \simeq 600$ Km when $N_o = 0.1$ cm^{-3}, and $L \simeq 2000$ Km when

$N_o \simeq 0.01$ cm^{-3}. This may be compared with $d \simeq 3 \times 10^5$ Km for the geomagnetic tail.

However, it should be noted that even with such non-uniform electric fields the electrons remain adiabatic since if

$$g_{p/L} \simeq \frac{m_p c^2 E}{eBL} \simeq 1 \quad \text{then} \quad g_{e/L} \simeq \frac{m_e}{m_p} << 1 .$$

The electrons thus remain adiabatic until they are very close to the neutral sheet when adiabatic theory breaks down due to the magnetic field scale length. (We assume that there are no electric fields so large that $m_e c^2 E^2/B^2 \sim e\Phi$).

From the previous discussions it should be clear that the plasma approximation

$$\frac{n_p - n_e}{n_p} << 1$$

must be valid for such a neutral sheet system, and we may again consider charge neutrality by the time-of-flight argument used in Chapter 3. We first apply it to the region of length L in which proton currents are important. The time electrons and protons spend in this region being accelerated by the electric field is

$$t_p \simeq \left(\frac{L\, m_p}{eE}\right)^{\frac{1}{2}} \qquad t_e \simeq \left(\frac{L\, m_e}{eE}\right)^{\frac{1}{2}} \qquad (5.4a,b)$$

and clearly $t_p >> t_e$. However, as we noted above, electrons remain adiabatic (i.e. moving along equipotentials) until they are very close to the sheet, and hence spend a time

$$t_e' \simeq \frac{a}{v_e} \qquad (5.5)$$

drifting through the proton current region towards the neutral sheet. Here 'a' is the thickness of the proton current sheet. Equating t_p and t_e to find 'a', and using $v_p \simeq v_e \simeq (e\Phi/m_p)^{\frac{1}{2}}$ we thus find

$$a \simeq \frac{v_p}{\Omega} \simeq L \qquad (5.6)$$

which is a reasonable result. We thus see that the proton charge density must be balanced by electrons adiabatically drifting towards the field reversal region. Since $n_e \simeq N_o B/B_o$ the density in the proton current sheet $n_p \lesssim N_o$. In the Speiser picture protons and electrons spend approximately equal times reaching the neutral sheet, but the largest time is spent oscillating and accelerating along the neutral sheet. It can now be seen that the system responds to the charge density produced by such motions such that a significant fraction of protons no longer have this oscillation phase. Those particles which do enter the neutral sheet (with $\phi \sim \Phi$) will only perform a few oscillations since the length of the proton current sheet L is of the order of the incoming particle gyrolengths. Thus while Speiser's description of the particle orbits holds good for electrons, the behaviour of protons is rather different, significant currents being produced in the 'drift-flow' as well as in the 'current sheet' (there being no strict dividing line between the two regions); see Fig. 5.1. Since we expect the potential ϕ to fall across a region of dimension L near $\phi = 0$ and $L \ll d$, over most of the sheet we expect the current to be carried by electrons moving in a thin current layer, where the electric field parallel to the layer is very small indeed. Considerations of

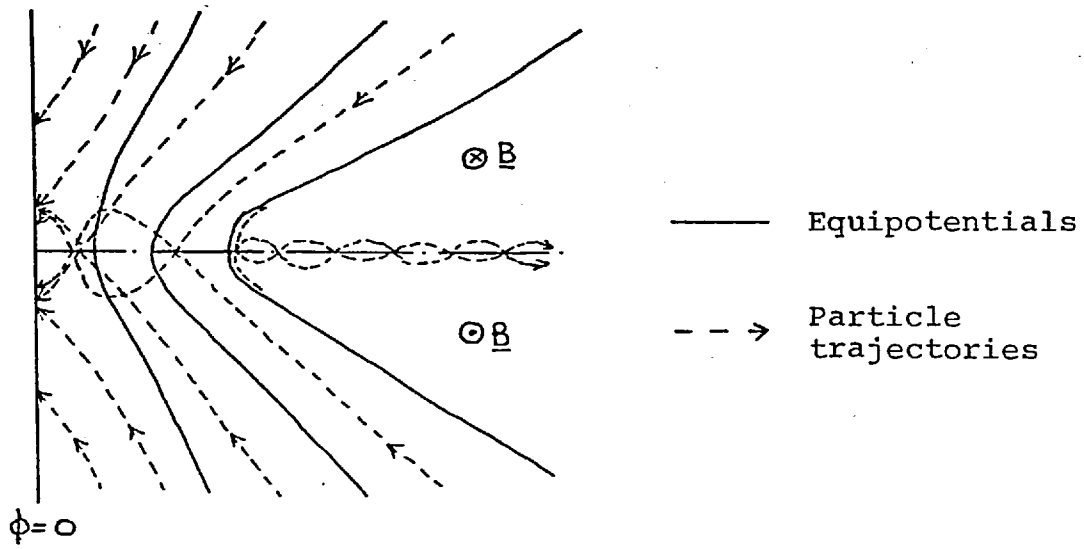

Figure 5.1

the structure of this layer is given in a later section of this chapter, but we shall now investigate in detail the structure of the small proton current region of length L.

(ii) Charge Neutrality & Momentum Conservation in the Current Sheet.

We shall first consider what can be learned from the charge neutrality condition. Since the charge density of electrons adiabatically flowing towards the neutral sheet has been shown to be important we need to be able to calculate their contribution to the charge content of the region at a given potential ϕ. We have already calculated the charge content at ϕ due to accelerating particles in the sheet in Chapter 3.

The adiabatic contribution may be calculated from the relation B/N = constant for adiabatic flow, but we require a model for the magnetic field. The current carried across equipotential line ϕ comprises an electron and proton contribution given by

$$I_e = \frac{\phi}{\Phi} I_o \qquad I_p = (1 - \frac{\phi}{\Phi}) I_o \tag{5.7}$$

where I_o, the total current, is $I_o = c/4\pi B_o$. Since electrons are expected to remain adiabatic until very close to the sheet we assume that the electron current is carried in a very thin layer near the neutral sheet. For simplicity we assume that the proton current is uniform over a region of half-thickness a. The magnetic field structure at potential ϕ is then assumed to be given by

$$B_x(z) \simeq B_o \{\frac{\phi}{\Phi} \operatorname{sgn}(z) + (1 - \frac{\phi}{\Phi}) \frac{z}{a}\} \tag{5.8}$$

for $|z| \leq a$ and outside of the thin electron current layer. Note that we have made no distinction between the regions where the proton current is carried by particles in the 'drift flow' and where it is carried by particles oscillating about the neutral sheet. This appears to be justified because the current densities in the two regions must be nearly the same, so that the nature of the magnetic field does not change across the boundary of the region of oscillating particles.

Using the model structure (5.8) the adiabatic electron surface charge density is given by

$$\sigma_{ae}(\phi) = -2e \int_o^a N_e(z,\phi)dz = \frac{-2eN_o}{B_o} \int_o^a B(z,\phi)dz$$

so that $$\sigma_{ae} \simeq - e N_o a (1 + \frac{\phi}{\Phi}) . \tag{5.9}$$

Since the protons are essentially being accelerated across equipotentials from small velocities by the electric field in this region, both in the drift-flow and in the oscillatory

motion about the neutral sheet, we expect the expressions derived in Chapter 3 for the surface density of accelerating particles to be valid (equation (3.40))

$$\text{i.e.} \quad \sigma(\phi) \simeq \frac{4ecN_o}{B_o}\left(\frac{m_p}{2e}\right)^{\frac{1}{2}}\left\{(\Phi-\phi)^{\frac{1}{2}} - \left(\frac{m_e}{m_p}\right)^{\frac{1}{2}}\phi^{\frac{1}{2}}\right\}$$

Thus writing $\sigma(\phi) + \sigma_{ae} \simeq 0$ for charge neutrality gives the sheet half-thickness 'a' as a function of ϕ

$$a \simeq \frac{4\lambda_p}{\sqrt{2}}\left\{\frac{(1-\phi/\Phi)^{\frac{1}{2}} - \left(\frac{m_e}{m_p}\right)^{\frac{1}{2}}\left(\frac{\phi}{\Phi}\right)^2}{(1+\phi/\Phi)}\right\} \qquad (5.10)$$

which, apart from numerical factors, agrees with the time-of-flight argument used above which gave $a \simeq \lambda_p$. The value of 'a' versus ϕ from this calculation is shown in Fig. 5.2 for $N_o = 0.1\ \text{cm}^{-3}$ and $N_o = 0.01\ \text{cm}^{-3}$. An estimate of the thickness of the electron current layer may be obtained if it is assumed that the breakdown of the adiabatic condition for these particles is consistent with the scale lengths of the magnetic field. This gives

$$a_e \simeq \frac{v_e}{\Omega_e}$$

where $v_e = cE/B$ and $m_p\left(\frac{cE}{B}\right)^2 \simeq e\Phi$.

Thus $a_e \simeq \left(\frac{m_e}{m_p}\right)\lambda_p$, and since $a_p \simeq \lambda_p$, our approximation that the electron current layer provides a 'step' in the magnetic field appears to be justified.

As an independent check on these results for the thickness of the proton current sheet we now turn to consider conservation of momentum for the system. Clearly a problem exists for the component of the momentum flux parallel to the

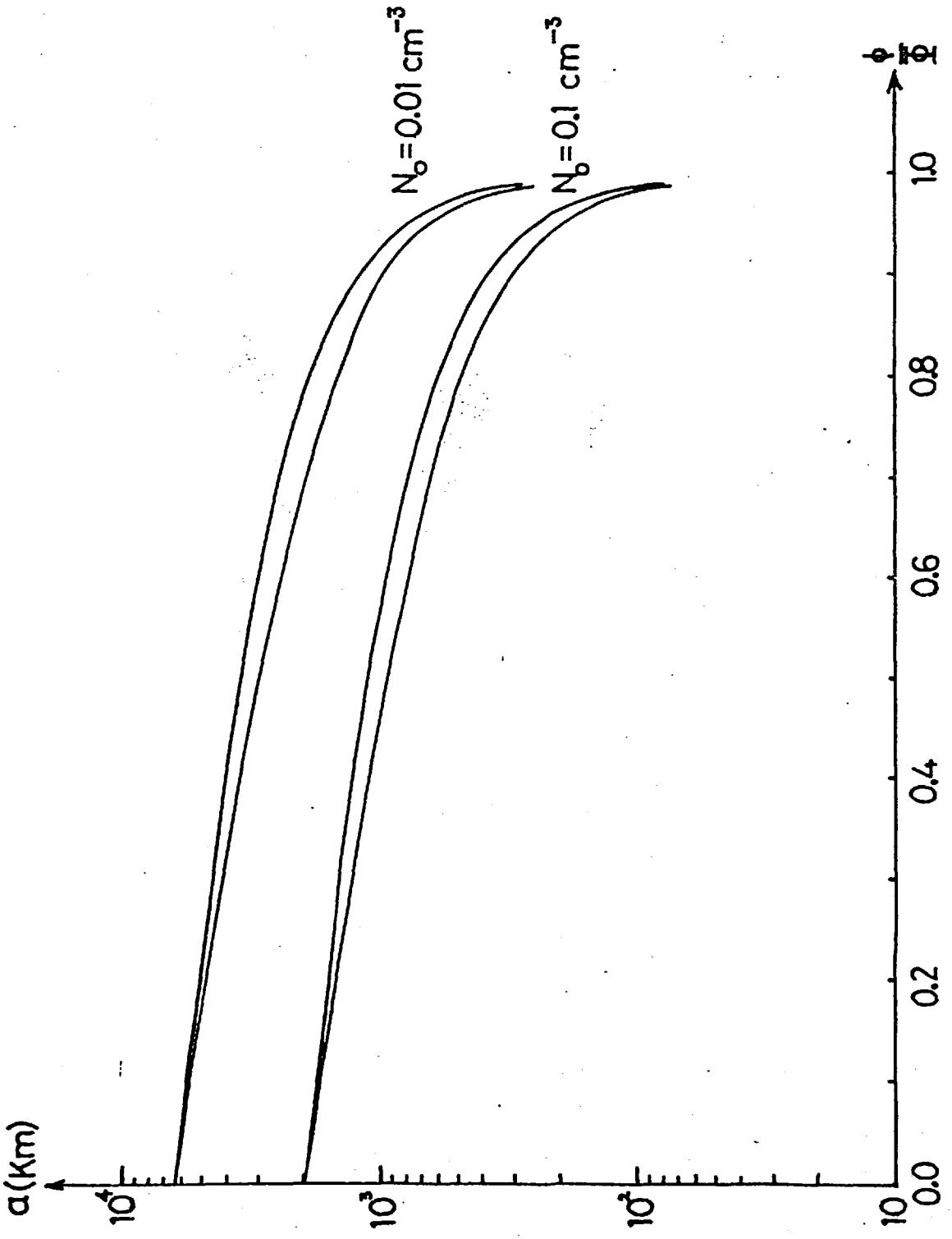

Figure 5.2: The values of the half thickness 'a' of the proton current sheet for geomagnetic tail parameters N_o = 0.1, 0.01 cm^{-3} plotted against ϕ/ϕ. The upper curve for a given density was calculated for conservation of momentum (eqn. 5.20), while the lower curve is that for charge neutrality between the adiabatic electrons and accelerating protons (equation 5.10).

neutral sheet (and perpendicular to $\underline{B}$) since we have protons emerging from one boundary with the same energy spectrum as electrons from the other, but carrying a factor $(m_p/m_e)^{\frac{1}{2}}$ times more momentum.

We first calculate the momentum flux of particles in the direction parallel to the sheet carried across equipotential ϕ by protons and electrons. The maximum momentum flux in this direction occurs if the particles are moving very nearly parallel to the sheet with small perpendicular velocities. This is the situation we expect in the electron and proton current layers where the particles are being accelerated across equipotentials by the electric field parallel to the sheet.

The proton momentum flux crossing equipotential ϕ consists of those particles flowing into the system with initial potential energies ϕ_i in the range $\phi \leq \phi_i \leq \Phi$. The flux of protons entering the system between equipotentials ϕ_i to $\phi_i + d\phi_i$ is

$$dF = \frac{2cN_o d\phi_i}{B_o} \tag{5.11}$$

and this flux is preserved as the particles are accelerated in the current layer across potential ϕ. Assuming, as above, that these particles are moving very nearly parallel to the sheet, by conservation of energy their parallel velocity at potential ϕ is

$$v_y \simeq \left\{\frac{2e}{m_p}(\phi_i - \phi)\right\}^{\frac{1}{2}} \tag{5.12}$$

where we have neglected the small kinetic energy of the inflow far away from the sheet. Thus the momentum per unit length

of the system (along $\underline{B}$) per second carried across potential ϕ by these particles is

$$dM_p = \frac{2cN_o}{B_o} (2em_p)^{\frac{1}{2}} (\phi_i - \phi)^{\frac{1}{2}} d\phi_i \qquad (5.13)$$

and integrating ϕ_i from ϕ to Φ to account for all incoming protons crossing equipotential ϕ we have

$$M_p(\phi) = \frac{2cN_o}{B_o} (2em_p)^{\frac{1}{2}} \int_{\phi}^{\Phi} d\phi_i \, (\phi_i - \phi)^{\frac{1}{2}}$$

$$= \frac{4}{3} (2em_p)^{\frac{1}{2}} \frac{cN_o}{B_o} (\Phi - \phi)^{3/2} \qquad (5.14)$$

Similarly for electrons (travelling in the opposite direction)

$$M_e(\phi) = \frac{4}{3} (2em_e)^{\frac{1}{2}} \frac{cN_o}{B_o} \phi^{3/2} \qquad (5.15)$$

As expected, we find $M_p(\phi=o) = (\frac{m_p}{m_e})^{\frac{1}{2}} M_e(\Phi)$. We note that any motion of particles perpendicular to the neutral sheet on crossing equipotential ϕ will reduce the above values, but as discussed above, we expect this to be a small effect for particles accelerating in the current layers.

It is clear from the above expressions that due to the mass factor we have a net particle momentum flux towards $\phi = 0$ carried by the protons. This must be balanced by the electromagnetic momentum, as expressed by the second (momentum) moment of the steady-state collisionless Boltzmann equation.

$$\text{div} \left(\sum_j m_j \int_{-\infty}^{\infty} d^3v \, f_j \, \underline{v} \, \underline{v} - \underline{\underline{T}} \right) = \underline{0} \qquad (5.16)$$

In equation (5.16) f_j is the particle distribution function in $(\underline{v},\underline{x})$ space of particle species j, and $\underline{\underline{T}}$ is the Maxwell

stress tensor, given by

$$\underline{\underline{T}} = \frac{1}{4\pi} (\underline{E}\,\underline{E} + \underline{B}\,\underline{B} - \tfrac{1}{2} (E^2 + B^2)\, \underline{\underline{1}}).$$

Quadratic terms in E will be of order $(v/c)^2$ compared with those in B, where v is the particle flow velocity ($v \approx cE/B$), and are hence neglected. Since $\underline{B} = B_x(y,z)\, \hat{\underline{x}}$ we have $\underline{\underline{T}}$ diagonal with

$$T_{xx} = - T_{yy} = - T_{zz} = B_x^2/8\pi$$

Performing a volume integral on equation (5.16) and using the divergence theorem we have

$$\oint \underline{dS} \cdot (\sum_j m_j \int_{-\infty}^{\infty} d^3v\, f_j\, \underline{v}\,\underline{v} - \underline{\underline{T}}) = \underline{0} \qquad (5.17)$$

which is just a statement that the net momentum in any direction flowing through a closed surface is zero in the steady state. The volume we shall consider will consist of a unit-length slab of the system (along the magnetic field), bounded by the ϕ and Φ equipotentials. It is closed at a large distance from the sheet where the momentum flux is small and directed towards the sheet (see Fig. 5.3). There is no momentum flow in the $\hat{\underline{x}}$ direction, and that in the $\hat{\underline{z}}$ direction cancels to zero if the incoming streams are symmetrical. We are left with the momentum flux parallel to the sheet across the equipotentials ϕ and Φ. The appropriate component of equation (5.17) then reads

$$\int_{\phi} dz\, (M_{yy} + \frac{P^2}{8\pi}) = \int_{\Phi} dz\, (M_{yy} + \frac{B^2}{8\pi}) \qquad (5.18)$$

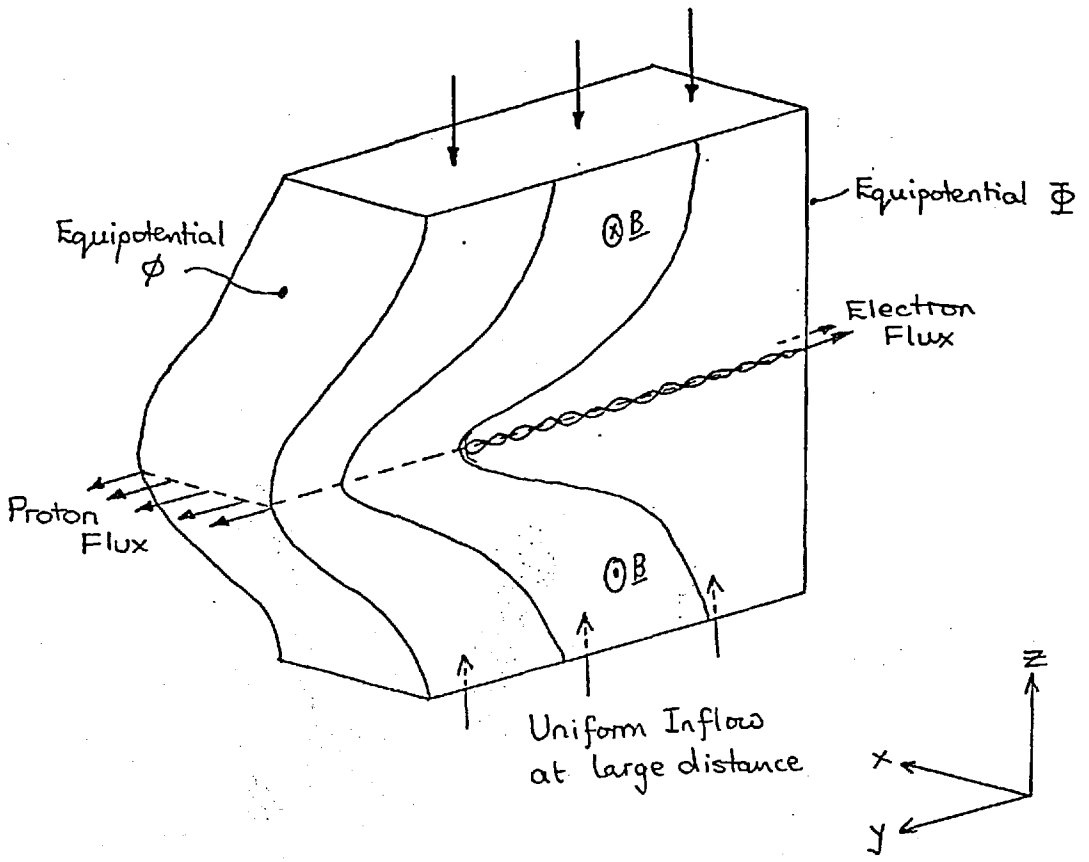

Figure 5.3

where $M_{yy} = \sum_j m_j \int_{-\infty}^{\infty} d^3v\, f_j\, v_y^2$ is the particle momentum flux in the y-direction. The integrals of these latter quantities along the equipotentials has already been found in equations (5.14) and (5.15), i.e.

$$\int_{\phi} dz\, M_{yy} \simeq \frac{4}{3}(2em_p)^{\frac{1}{2}} \frac{cN_o}{B_o} \{(\Phi-\phi)^{3/2} + (\frac{m_e}{m_p})^{\frac{1}{2}} \phi^{3/2}\}$$

$$\int_{\Phi} dz\, M_{yy} \simeq \frac{4}{3}(2em_p)^{\frac{1}{2}} \frac{cN_o}{B_o} (\frac{m_e}{m_p})^{\frac{1}{2}} \Phi^{3/2}$$

Thus using (5.18) we have

$$\int_{\Phi} dz \frac{B_x^2}{8\pi} - \int_{\phi} dz \frac{B_x^2}{8\pi} = \frac{4}{3}(2em_p)^{\frac{1}{2}} \frac{cN_o}{B_o} \{(\Phi-\phi)^{3/2} - (\frac{m_e}{m_p})^{\frac{1}{2}} (\Phi^{3/2} - \phi^{3/2})\} \qquad (5.19)$$

Neglecting the small electron term on the right hand side, the integral of $B^2/8\pi$ along an equipotential is monotonically decreasing with decreasing potential in the sheet. We interpret this as simply a change in the thickness of the field reversal region, it being thickest near $\phi = 0$. This result is in qualitative agreement with the result obtained by considering charge neutrality. However, by again using the model magnetic field structure, equation (5.8) which contains the arbitrary thickness parameter 'a', we can use equation (5.19) to determine 'a' as a function of ϕ/Φ for momentum conservation. This then can be compared with the 'a' required for charge neutrality.

Using the model field

$$\int_{\Phi} B^2\, dz - \int_{\phi} B^2\, dz = \frac{2}{3} B_o{}^2 a \left(2 + \frac{\phi}{\Phi}\right)\left(1 - \frac{\phi}{\Phi}\right)$$

and hence from equation (5.19) we find

$$a_m \simeq \frac{4\,\lambda_p}{\sqrt{2}} \left\{ \frac{(1 - \phi/\Phi)^{3/2} - \left(\frac{m_e}{m_p}\right)^{\frac{1}{2}} \left(1 - (\phi/\Phi)^{3/2}\right)}{(1 - \phi/\Phi)(1 + \phi/2\Phi)} \right\} \qquad (5.20)$$

The similarity to equation (5.10) is remarkable, and we have plotted a_m vs ϕ/Φ in Fig. 5.2 to facilitate an easy comparison with the charge-neutrality calculation of a. Thus while both calculations may be considered rather rough, using a model magnetic field, the agreement we have found here indicates that the model must bear fairly close resemblance to the truth. Since the electron charge density is related to the magnetic field through $N/B \simeq$ constant, and hence to the current, the problems of magnetic and electric field structure

are closely coupled. The above calculation then shows that the sheet thicknesses expected to be produced by the proton currents are entirely consistent with those required for charge neutrality.

(iii) Trajectory Studies in Model Fields

In order to obtain a clearer picture of the field configuration and the particle orbits which we are envisaging here, we have computed some proton trajectories in a model field configuration which resembles the structure to be expected. This has been chosen so that the flow energies are comparable with the potential energies, and resembles the solution to Laplace's equation at large distances (see Fig. 4.8 and discussion).

For simplicity we have taken a uniform magnetic field which reverses as a step across the neutral sheet. The changes in drift-flow energy are then only associated with changes in the electric field strength along the equipotentials. In order to set up the electric field structure we look for separable solutions of curl $\underline{E} = 0$ in polar coordinates defined in Fig. 5.3(a)

From this we obtain

$$E_r = f(r)\, g(\theta) \qquad E_\theta = \frac{1}{r} \int_0^r f(r')\, dr' \, \frac{dg}{d\theta}$$

where we impose the constraints

$$g(0) = 1 \qquad g(\tfrac{\pi}{2}) = 0 \qquad \frac{dg}{d\theta}(0) = 0 .$$

The function $f(r)$ may be obtained by requiring, say,

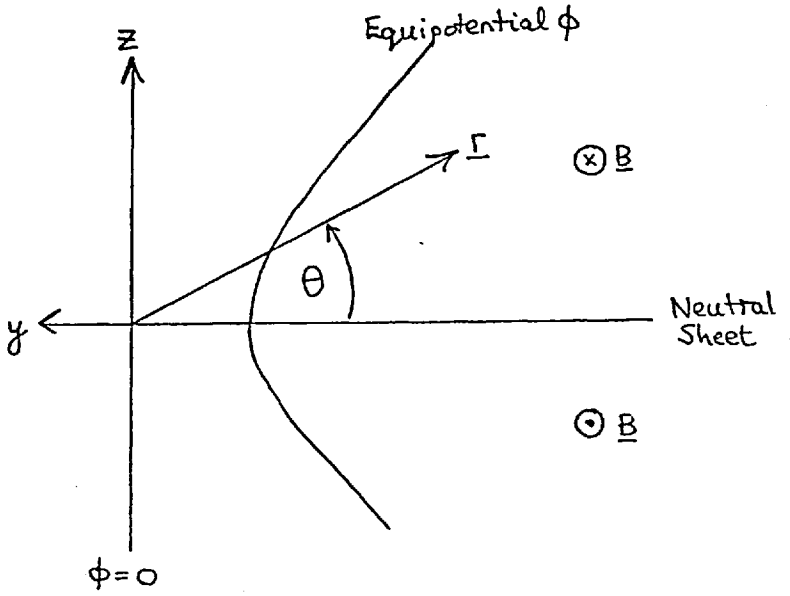

Figure 5.3(a)

$\frac{E_r}{E_o} = h\,(\phi/\Phi)$ along $\theta = 0$ (the neutral sheet).

For simplicity we take $E_r/E_o = (1 - \phi/\Phi)$ such that $E_o = E_r(r=0)$, and $E_o < 0$. From this we obtain

$$\phi(r, \theta=0) = \Phi(1 - e^{-r/L})$$

where $L = \Phi/|E_o|$, and hence

$$f(r) = -|E_o|\, e^{-r/L}$$

The function $g(\theta)$ satisfying the above constraints was chosen to be $g(\theta) = \cos\theta$. We thus arrive at the model fields

$$\phi(r, \theta) = \Phi(1 - e^{-r/L}) \cos\theta$$

$$E_r = -|E_o|\, e^{-r/L} \cos\theta \qquad E_\theta = \frac{|E_o|}{(r/L)}(1 - e^{-r/L}) \sin\theta$$

In Fig. 5.4 we show the equipotential lines and the contours

of E/E_o, where the length scales are in units of L. The drift flow-lines to first order are the contours of ϕ_i/Φ where

$$\frac{\phi_i}{\Phi} = \frac{\phi}{\Phi} + \frac{m_p c^2 E_o^2}{2 B_o^2 e\Phi} \left(\frac{E}{E_o}\right)^2 .$$

The maximum flow energy occurs at $r = 0$ where E takes its maximum value E_o. If we thus write

$$\frac{m_p c^2 E_o^2}{2B_o^2} = K e \Phi$$

then those particles with initial potential energies in the range $0 \leq \phi_i/\Phi \leq K$ will drift out of the system (across the $\phi = 0$ equipotential) before reaching the neutral sheet. For the results shown here we have chosen $K = 0.4$, so that the drift-lines are given by

$$\phi/\Phi + 0.4 \left(\frac{E}{E_o}\right)^2 = \frac{\phi_i}{\Phi} = \text{constant}.$$

These are plotted in Fig. 5.4. In Fig. 5.5 we show ϕ/Φ, E/E_o and ϕ_i/Φ as functions of r/L along the neutral line.

The results of the trajectory integration in these fields are shown in Fig. 5.6. The particles were started on the lines where $\phi_i = 0.1, \ldots 0.9$ at large distances from the origin ($r/L \geq 5$), with the adiabatic velocity. The computed orbits follow the lines of ϕ_i = constant as expected; those particles with $\phi_i/\Phi \lesssim 0.4$ do not reach the neutral sheet. Particles with $\phi_i/\Phi \gtrsim 0.4$ reach the neutral sheet and then oscillate about it in Speiser-type orbits, being accelerated towards the $\phi = 0$ boundary. The initial amplitude

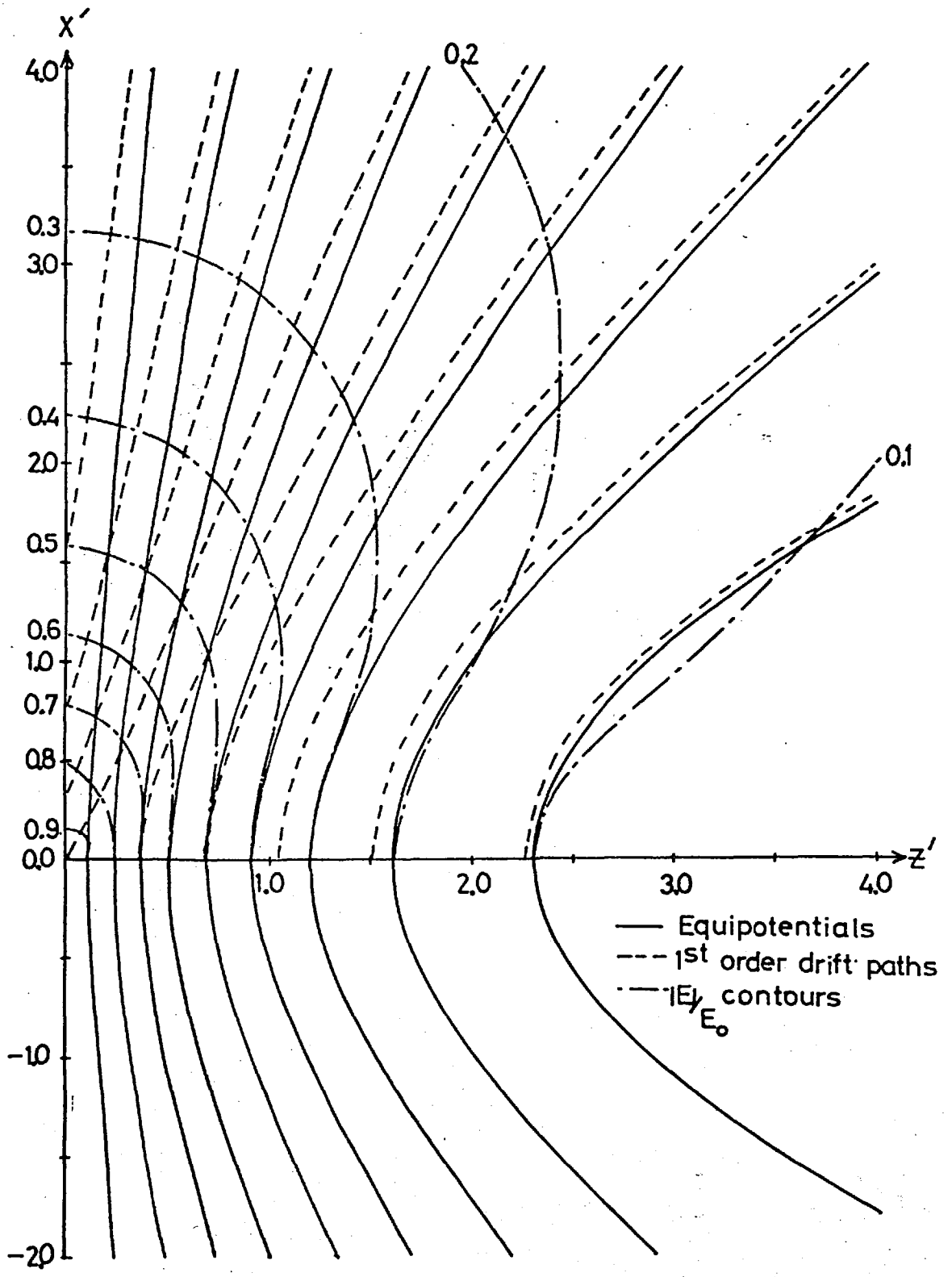

Figure 5.4: Properties of the model field structure used in the trajectory studies of section (5-iii). Shown (solid) are the equipotential lines, the first order particle trajectories (dashed) and the contours of the electric field normalised to the value of E_z at $z' = x' = 0$. The length scales are in units of L (see text). The magnetic field is taken to be uniform with a step across the neutral sheet for simplicity.

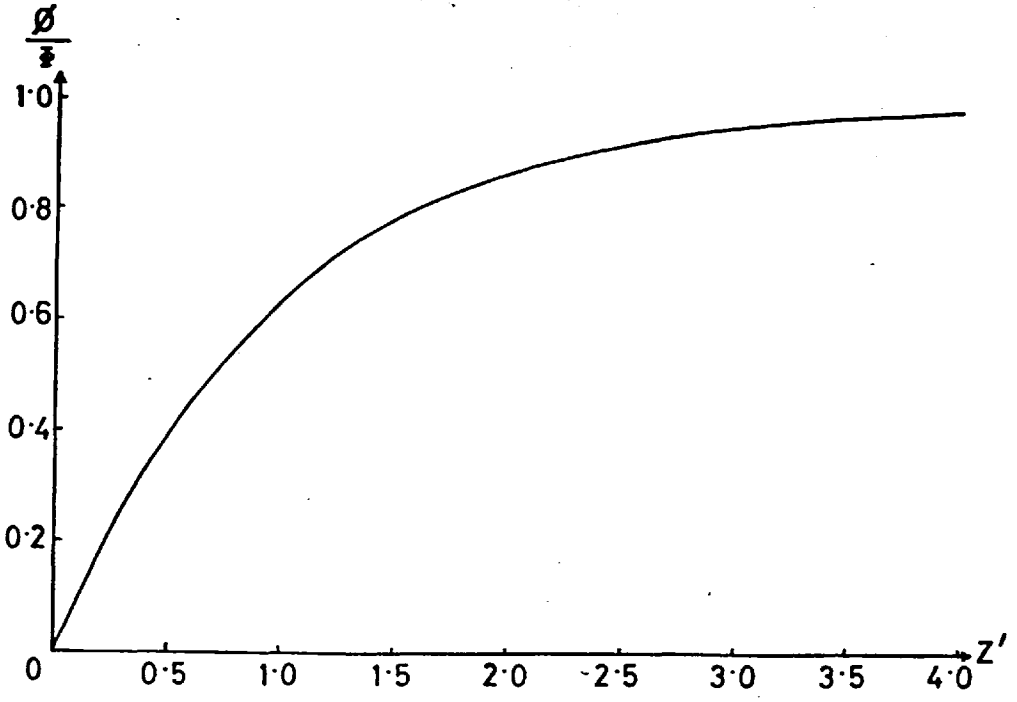

Figure 5.5(a)

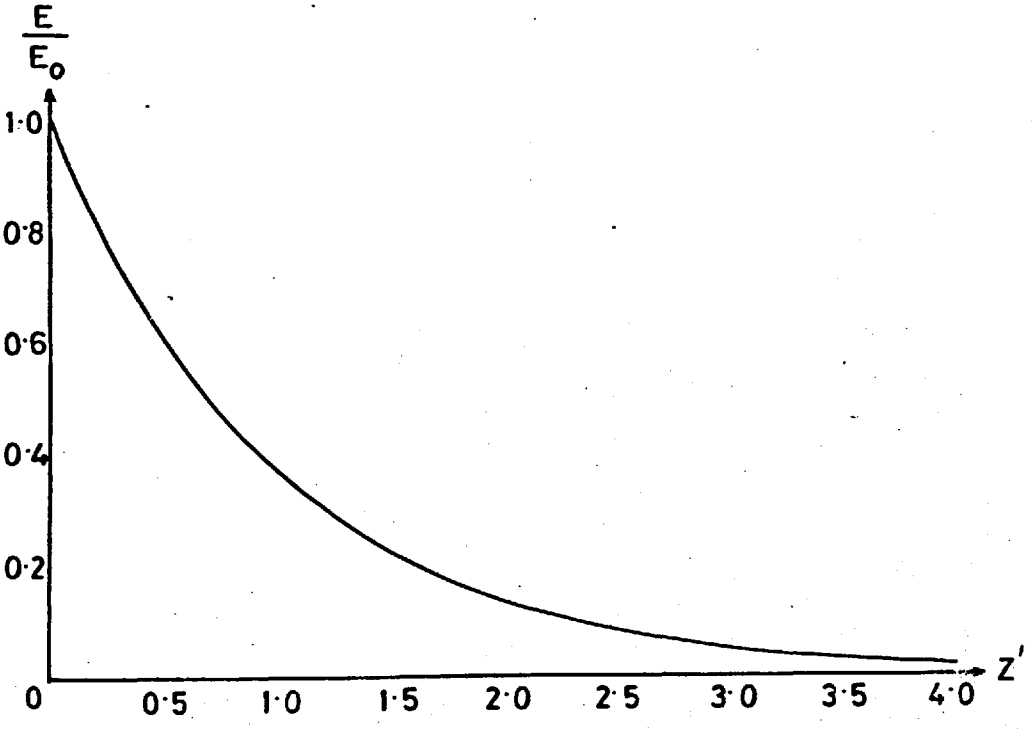

Figure 5.5(b)

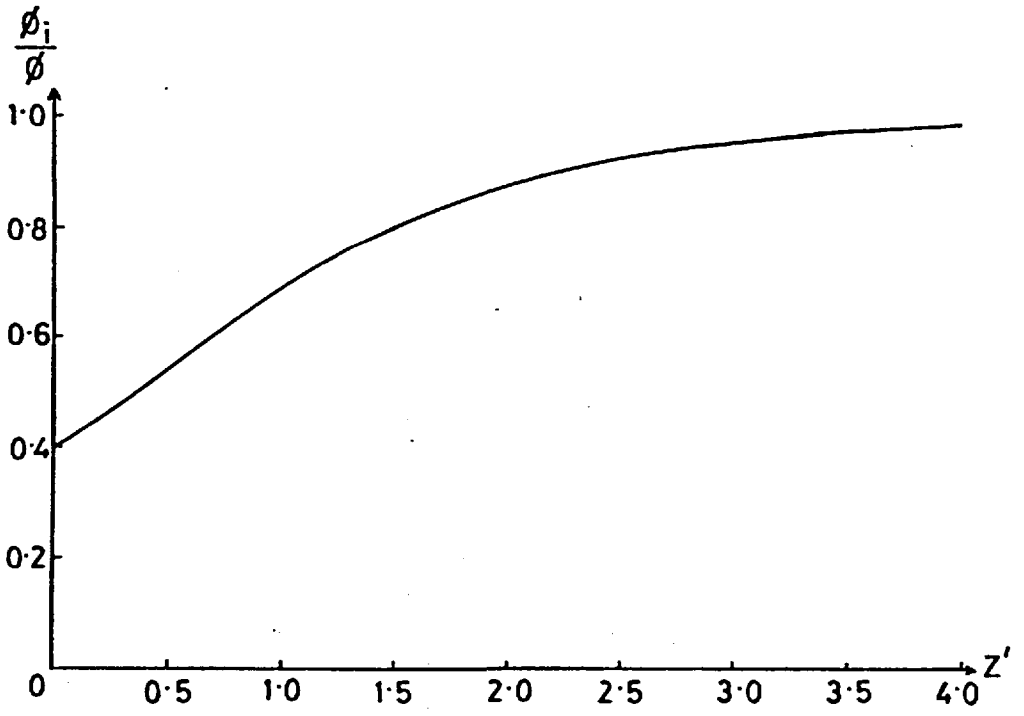

Figure 5.5(c)

Figure 5.5: (a) The potential ϕ/Φ versus r/L along the neutral sheet.

(b) The electric field E/E_0 versus r/L along the neutral sheet.

(c) The initial potential $\phi i/\Phi$ of incident particles at the neutral sheet versus r/L according to first order theory.

of their oscillations is expected to be

$$a \simeq (\sqrt{3} - \pi/3) \frac{v_p}{\Omega}$$

(for particles incident on a step in the magnetic field in the presence of a uniform electric field $E \simeq v_p B_o/c$) so that

$$\frac{a(r/L)}{L} \simeq 2(\sqrt{3} - \pi/3) K (\frac{E}{E_o}) \simeq 0.8 (\sqrt{3} - \pi/3) e^{-r/L}$$

This has also been plotted in Fig. 5.6 and can be seen to give general agreement with the computed orbits.

(iv) A Detailed Model of the Structure of the Proton Current Sheet.

We shall now look in more detail at the properties of the proton current sheet, separating the region of pure drift-flow from the layer containing oscillating non-adiabatic protons. The theory to be developed is an extension of that considered in Chapter 3, and uses the results of Chapter 4. We shall first calculate the surface density at potential ϕ of trapped, accelerating protons, when the incoming stream has flow energies comparable with $e(\Phi - \phi)$. (In Chapter 3 the incoming flow energies were assumed negligible). For simplicity we consider only the case where the incoming plasma far away from the sheet is uniform; the non-uniform case discussed in Chapter 4 represents only a straight forward extension to the theory presented here.

In the drift-flow region the particle velocity can be written as (equation (4.4))

$$\underline{v}_p = \frac{c\lambda}{eB} \frac{\underline{B}}{B} \wedge \underline{\nabla}(e\phi + \frac{m_p v_p^2}{2})$$

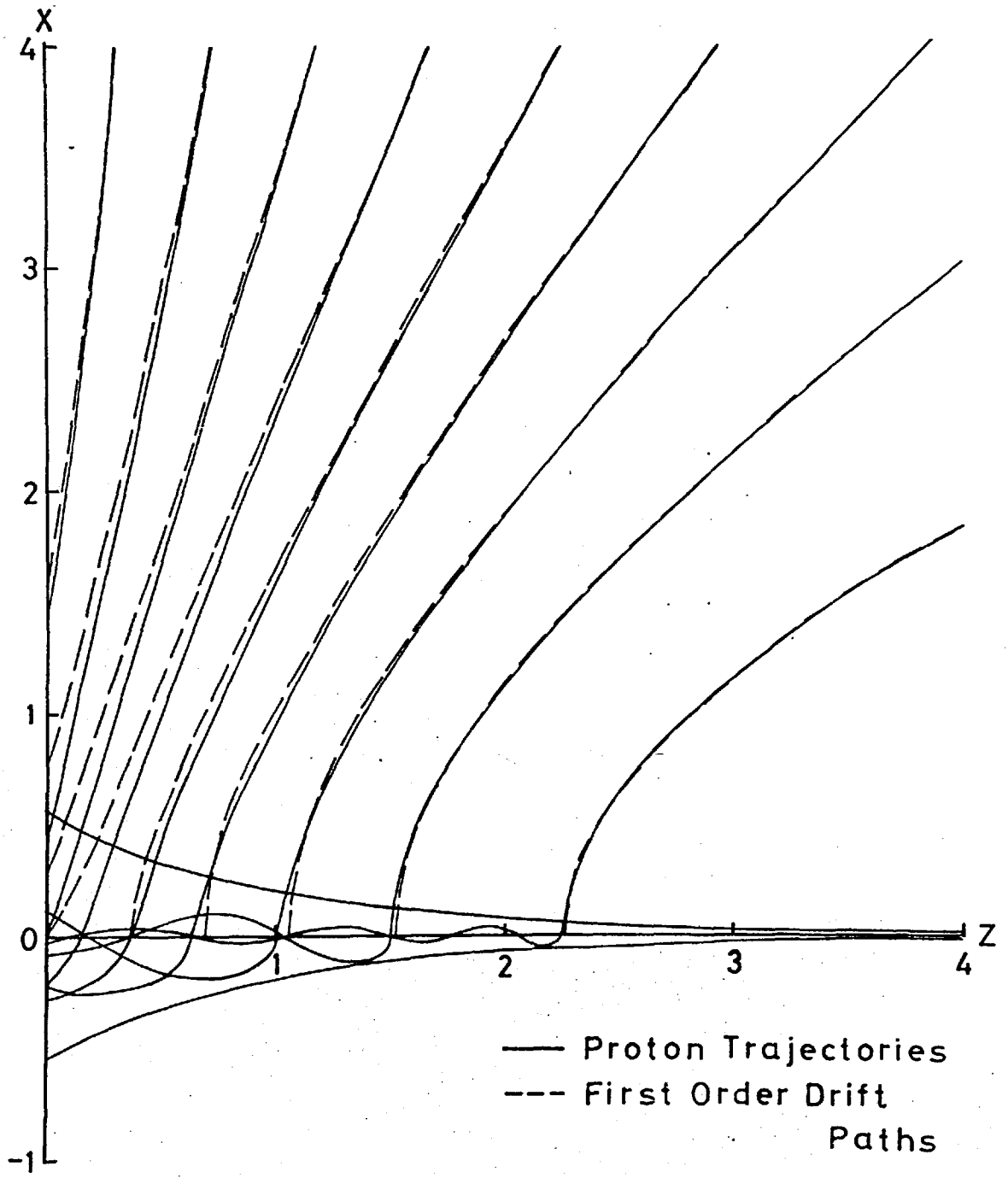

Figure 5.6: The computed proton orbits in the model field configuration (solid) compared with the first order drift lines (dashed). The initial amplitude of oscillation of the particles about the neutral sheet expected for near normal incidence on a magnetic field step is also shown.

and from (4.17)

$$\frac{N\lambda}{B} = \text{constant along a streamline.}$$

Thus the particle flux at any point is given by

$$\underline{F} = N\underline{v} = \frac{cN_o}{eB_o} \frac{\underline{B}}{B} \wedge \underline{\nabla} \left(e\phi + \frac{m_p v_p^2}{2}\right) \tag{5.21}$$

and the flux across a line element dL is

$$|\underline{F} \wedge \underline{dL}| = \frac{cN_o}{eB_o} \underline{dL}.\underline{\nabla} \left(e\phi + \frac{m_p v_p^2}{2}\right) = \frac{cN_o}{eB_o} d\phi_i \tag{5.22}$$

Let us consider the proton flow into the layer of non-adiabatic particles, where the velocity at a point on the boundary of the layer is $v_p(\phi)$, and

$$\phi_i(\phi) = \phi + \frac{m_p v_p^2}{2e} .$$

Since the particle orbits do not cross each other in the drift-flow $\phi_i(\phi)$ must be a monotonically increasing function of ϕ. This means that only the particles with initial potentials in the range

$$\phi_i(\phi) \leq \phi_i \leq \Phi$$

contribute to the surface density of trapped particles at ϕ, as they move towards the $\phi = 0$ boundary. By conservation of flux (from 5.22) the surface density of trapped protons at ϕ with initial potentials in the range ϕ_i to $\phi_i + d\phi_i$ is given by

$$d\sigma_p(\phi, \phi_i) = \frac{2cN_o \, d\phi_i}{B_o v_y(\phi, \phi_i)}$$

(multiplying by two for particle inflow from both sides of the sheet). Neglecting the velocity of the particle perpendicular to the sheet (i.e. in the oscillation) we have

$$v_y(\phi, \phi_i) = \{\frac{2e}{m_p}(\phi_i - \phi)\}^{\frac{1}{2}} .$$

Thus $\sigma_p(\phi)$ is given by

$$\sigma_p(\phi) = \frac{cN_o}{B_o}(2m_p e)^{\frac{1}{2}} \int_{\phi_i = \phi + \frac{m_p v_p^2}{2e}}^{\phi_i = \Phi} \frac{d\phi_i}{(\phi_i - \phi)^{\frac{1}{2}}}$$

$$= 4\frac{ecN_o}{B_o}\left(\frac{m_p}{2e}\right)^{\frac{1}{2}}\left\{(\Phi-\phi)^{\frac{1}{2}} - \left(\frac{m_p v_p^2}{2e}\right)^{\frac{1}{2}}\right\} \qquad (5.23)$$

If we neglect the incoming flow energy at potential ϕ, then (5.23) simply reduces to the corresponding equation in Chapter 3 (equation (3.38)). Note that we have assumed that the protons, on entering the sheet are moving with $v_y \geq 0$ (towards $\phi = 0$), and so continue to be accelerated by the electric field. This should be true for the field configuration we have here, as evidenced by our computed particle trajectories.

A similar calculation could be performed for electrons, but, as we have seen, if $m_p v_p^2 \sim e\Phi$, then $m_e v_e^2 << e\Phi$ and the expression for the trapped electron density derived in Chapter 3 should be valid. Thus, for the trapped particle we have

$$\sigma(\phi) = \frac{4ecN_o}{P_o}\left(\frac{m_p}{2e}\right)^{\frac{1}{2}}\{(\Phi-\phi)^{\frac{1}{2}} - \left(\frac{m_p v_p^2}{2e}\right)^{\frac{1}{2}} - \left(\frac{m_e}{m_p}\right)^{\frac{1}{2}}\phi^{\frac{1}{2}}\} \qquad (5.24)$$

We shall assume that once the protons enter this region they become non-adiabatic and are uniformly accelerated by the electric field, so that the only proton charge present is due to non-adiabatic particles, and given by equation (5.23). However, electrons are clearly adiabatic throughout the region, except very near the neutral sheet and to calculate their contribution to the charge at a given ϕ in the layer we need a model of the magnetic field. The thin electron current layer is again approximated by a 'step' in the magnetic field, of magnitude

$$B_1(\phi) = \frac{\phi}{\Phi} B_o .$$

The magnetic field at the boundary of the trapped proton layer is given by equation (4.27) in terms of the proton velocity in the drift-flow at potential ϕ

i.e.

$$\frac{B_2(\phi)}{B_o} = 1 - \frac{m_p}{2e\Phi} (v_p^2(\phi) - v_o^2) \qquad (5.25)$$

Assuming a linear variation for simplicity, we then have

$$B(\phi,z) \simeq B_o \{\frac{\phi}{\Phi} + \frac{z}{a} \{(1 - \frac{\phi}{\Phi}) - \frac{m_p(v_p^2(\phi)-v_o^2)}{2e\Phi}\} \} \qquad (5.26)$$

for $z \leq a$, where a is the half-thickness of the non-adiabatic proton layer. Then the surface density of adiabatic electrons is given by

$$\sigma_{ae} \simeq -2eN_o \int_o^a dz \frac{B(\phi,z)}{B_o} = -eaN_o \{1 + \frac{\phi}{\Phi} - \frac{m_p(v_p^2-v_o^2)}{2e\Phi}\}$$

$$= -eaN_o \{\frac{B}{B_o} + \frac{\phi}{\Phi}\} \qquad (5.27)$$

Since 'a' is the thickness of the region of oscillating protons at potential ϕ, it must be related to the incoming proton gyrolengths. For example, near $\phi = 0$, where we may expect a nearly linear field reversal we found in Chapter 3 that for consistency between the sheet thickness and the amplitude of oscillations that

$$a \simeq \frac{v_p}{\Omega}$$

If we go to the other extreme and have a step in the magnetic field (like near $\phi = \Phi$) then elementary analysis shows

$$a \simeq (\sqrt{3} - \pi/3) \frac{v_p}{\Omega} \simeq 0.7 \frac{v_p}{\Omega} .$$

Thus we write for some $\chi(\phi) \sim \mathcal{O}(1)$ that

$$a(\phi) = \chi \frac{v_p(\phi)}{\Omega(\phi)} = \chi \frac{v_p(\phi)}{\Omega_o} \frac{B_o}{B} \qquad (5.28)$$

where B is the field value at the boundary of the trapped proton zone, given by equation (5.25).

Then

$$\sigma_{ae}(\phi) \simeq -eaN_o \{\frac{B}{B_o} + \frac{\phi}{\Phi}\} = eN_o\chi\frac{v_p(\phi)}{\Omega_o}\{1 + \frac{\phi}{\Phi}\frac{B}{B_o}\} \qquad (5.29)$$

The charge-neutrality condition is then obtained by equating equations (5.24) and (5.29). The charge-neutrality of the thin electron current layer will be considered separately later, and we neglect it here to obtain

$$2\{(\frac{2e(\Phi-\phi)}{m_p})^{\frac{1}{2}} - v_p(\phi)\} = \chi v_p(\phi)\{1 + \frac{\phi}{\Phi}\frac{B_o}{B}\}$$

or

$$v_p(\phi) = \frac{\left(\frac{2e\ (\Phi-\phi)}{m_p}\right)^{\frac{1}{2}}}{\{1 + \frac{\chi}{2}(1 + \frac{\phi}{\Phi}\frac{B_o}{B})\}} \qquad (5.30)$$

Thus the charge-neutrality condition (or plasma approximation) determines $v_p(\phi)$ at the boundary of the proton current layer, although the right-hand side of (5.30) has a hidden dependence on $v_p(\phi)$ through B/B_o in the denominator. However, by using an iterative procedure starting with $B/B_o = 1$, calculating $v_p(\phi)$ then substituting into (5.25) for a new value of B/B_o etc., we can obtain $v_p(\phi)$ for various values of χ. These are shown in Fig. 5.7 where we have normalized $v_p(\phi)$ to $\sqrt{2}\ V_A$, the velocity of a particle after acceleration from rest through the potential Φ ($m_p v^2/2 = e\Phi$, $m_p V_A^2 = e\Phi$ $\therefore$ $v = \sqrt{2}\ V_A$). The corresponding values of B/B_o against ϕ/Φ are shown in Fig. 5.8.

The thickness of the region of oscillating protons is given by

$$a = \frac{\chi v_p(\phi)}{\Omega(\phi)} = \frac{\chi v_p(\phi)}{\Omega_o}\ \frac{B_o}{B} \qquad (5.31)$$

which may be rewritten as (since $\frac{V_A}{\Omega_o} = \lambda\!\!\!^{-}_p$)

$$a = \sqrt{2}\ \lambda\!\!\!^{-}_p\ \left(\frac{v_p}{\sqrt{2}\ V_A}\right)\ \left(\frac{\chi B_o}{B}\right) \qquad (5.32)$$

We have plotted $(a/\lambda\!\!\!^{-}_p)$ in Fig. 5.9 for various values of χ, also included in the figure is $(a/\lambda\!\!\!^{-}_p)$ from the momentum calculation. Near $\phi \simeq 0$ we have from (5.30)

$$\frac{m_p v_p^2(o)}{2e} \simeq \frac{\Phi}{(1 + \chi/2)^2}$$

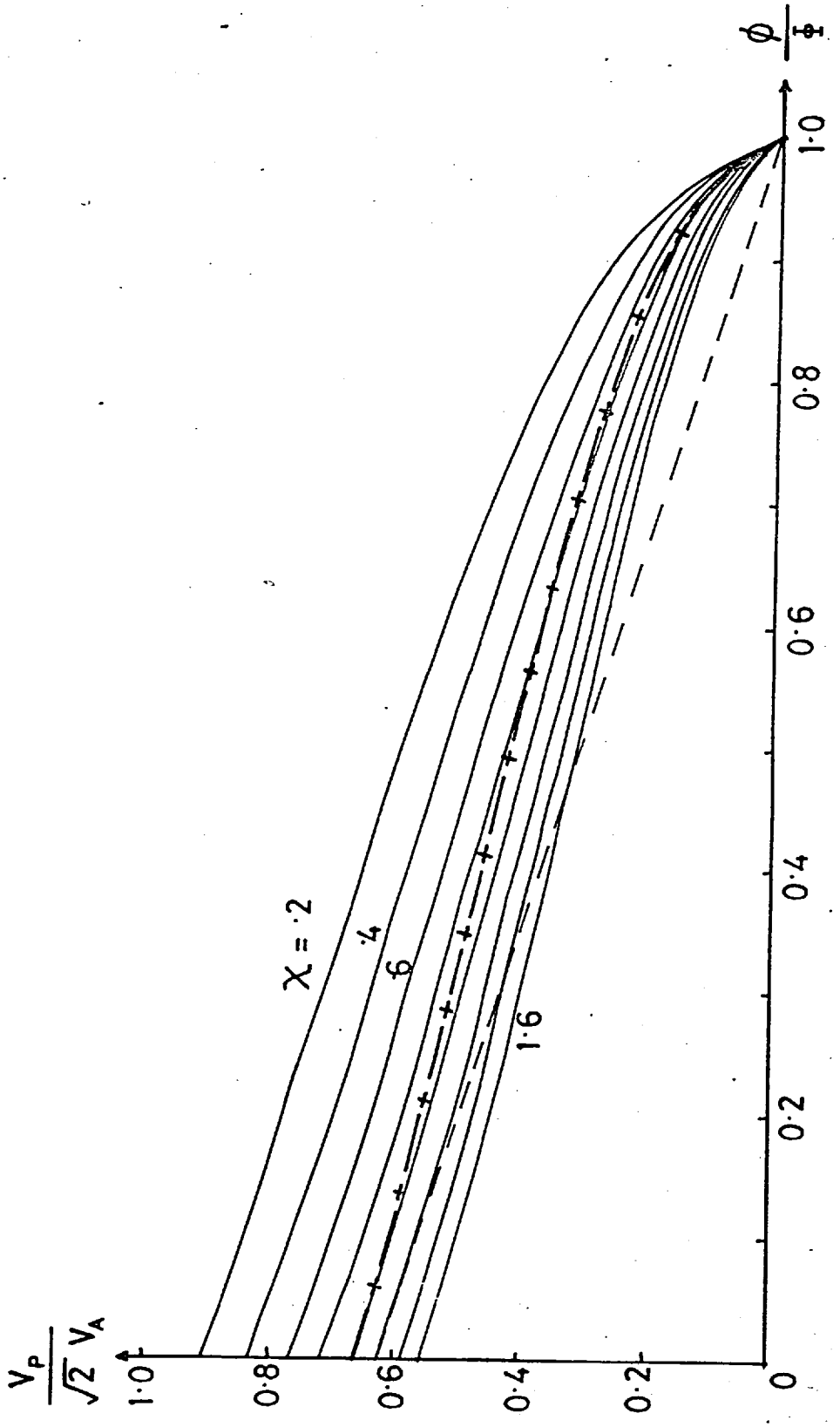

Figure 5.7: The values of incoming proton velocity $v_p(\phi)$ as a function of ϕ/Φ (normalized to $\sqrt{2}\ V_A$) for charge neutrality in the trapped proton beam. The thickness of the beam was taken as $a = \chi\ {}^{v}p/_{\Omega}$, and results are shown for χ = 0.2, 0.4, ..., 1.4, 1.6. The line marked with crosses results from taking χ to be linearly varying from a value of 1.0 at ϕ=0 to a value of $(\sqrt{3} - {}^{\pi}/_{3})$ at ϕ/Φ=1.0. Shown dotted is the value of ${}^{v}p/_{\sqrt{2}}\ V_A$ versus ϕ/Φ used in the trajectory studies in model fields (section 5-iii).

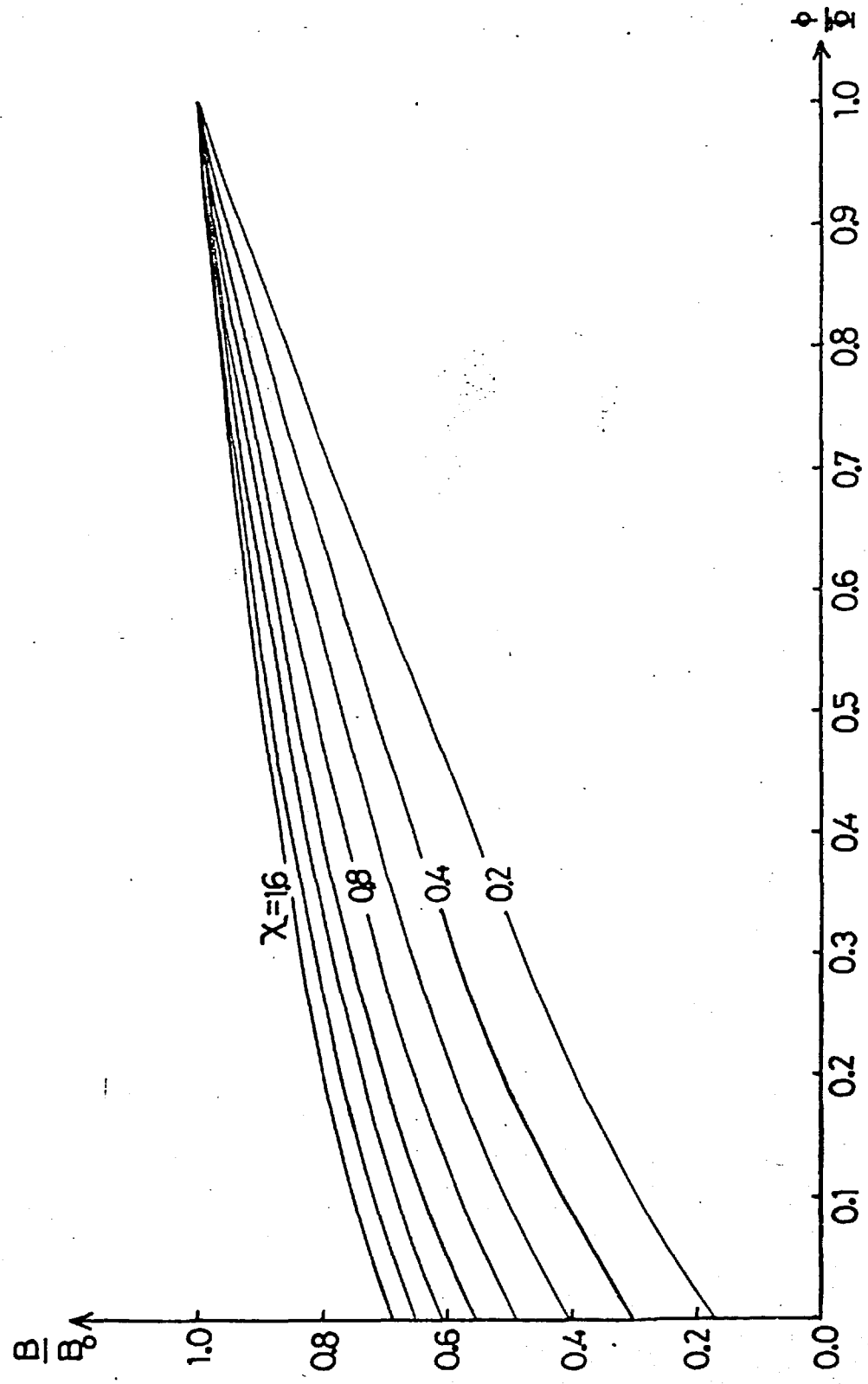

Figure 5.8: The values of P/P_o as a function of ϕ/ϕ at the boundary of the trapped proton beam, corresponding to the values of $v_p(\phi)$ in Fig. 5.7.

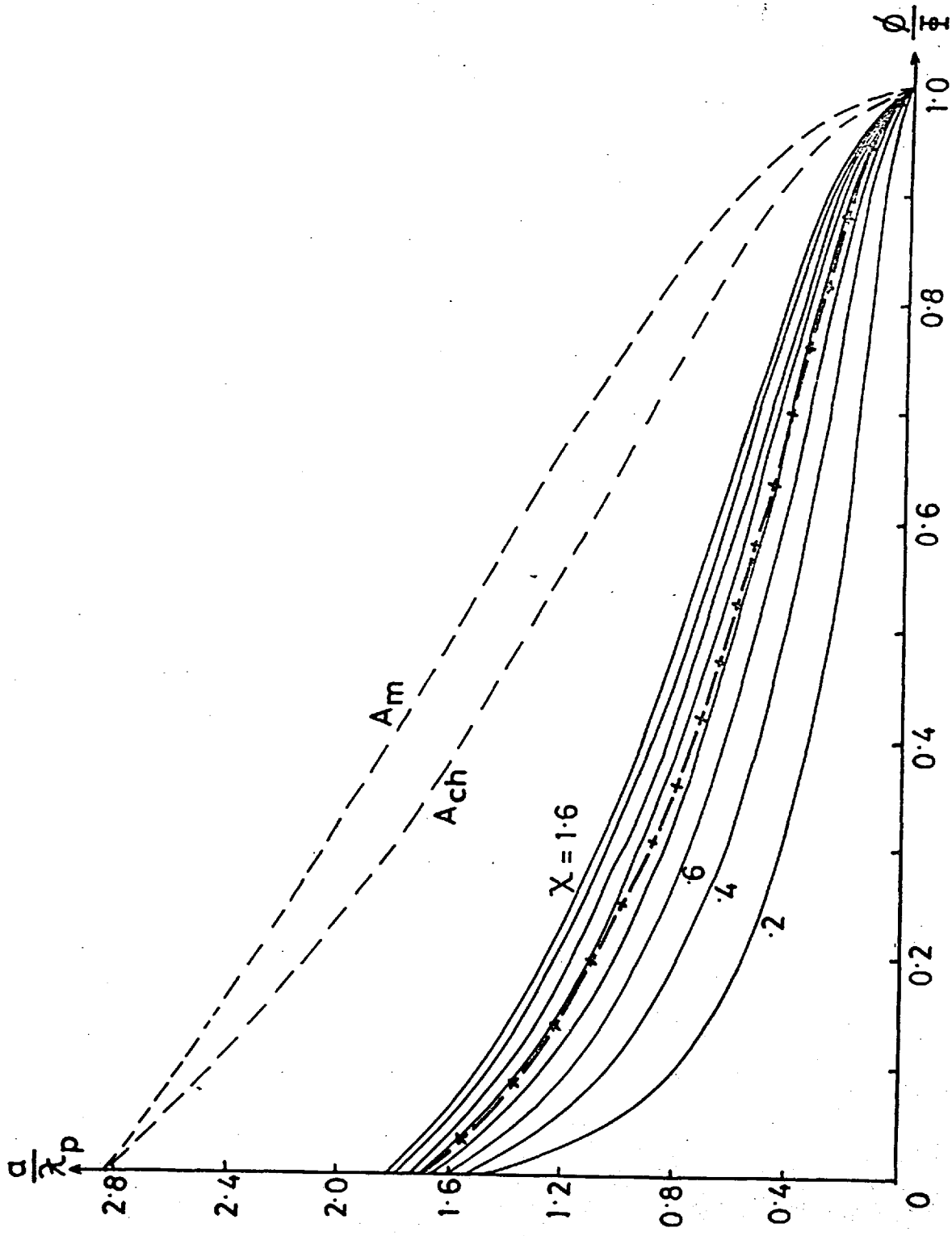

Figure 5.9: The values of $a/\lambda_p = \frac{\chi\, v_p(\phi)}{\Omega}$ (the half-thickness of the trapped proton beam) versus ϕ/ϕ along the neutral sheet. The line marked by crosses represents the linear variation of χ (as in Fig. 5.7). Shown by dotted lines are the half thicknesses of the total proton current region (trapped beam plus drift-flow) obtained from the momentum and charge neutrality calculations of section (5-ii).

so that $B/B_o \simeq 1 - \frac{m_p v_p^2}{2e\Phi} \simeq 1 - \frac{1}{(1 + \chi/2)^2}$

Thus, for $\chi \simeq 1$, $B/B_o \simeq 5/9$ and hence

$$a(\phi \simeq 0) \simeq \sqrt{2}\, \pi_p \left(\frac{\chi}{1 + \chi/2}\right) \left(1 - \frac{1}{(1 + \chi/2)^2}\right)^{-1} \simeq \frac{2.4}{\sqrt{2}}\, \pi_p$$

which is somewhat less than the value $a(\phi \simeq 0) = \frac{4}{\sqrt{2}}\, \pi_p$ for the whole current region (drift-flow plus non-adiabatic layer) given by the momentum calculation.

However, a more significant parameter than $v_p(\phi)$ is ϕ_i/Φ as a function of ϕ/Φ, given by

$$\frac{\phi_i}{\Phi} = \frac{\phi}{\Phi} + \frac{m_p v_p^2(\phi)}{2e\Phi} = \frac{\phi}{\Phi} + \frac{(1 - \phi/\Phi)}{\{1 + \frac{\chi}{2}(1 + \frac{\phi}{\Phi}\frac{B_o}{B})\}^2} \qquad (5.33)$$

which is shown in Fig. 5.10. As we stated before, this should be a monotonically increasing function of ϕ; for a given χ this is only true for $\chi \gtrsim 1$. When $d\phi_i/d\phi < 0$ in terms of the present theory, we have a negative flux of particles into the sheet, which in the present context has no physical meaning. However, if $\chi = \chi(\phi)$ then this difficulty can be removed for $\chi \lesssim 1$, for example if χ decreased with increasing potential. We previously argued from simple ideas that χ should vary between $\chi \simeq 1$ at $\phi = 0$ and $\chi \simeq (\sqrt{3} - \pi/3) \simeq 0.7$ at $\phi \simeq \Phi$, and if this occurs in a roughly linear fashion, we then obtain the dashed line in Fig. 5.10, which, as can be seen has $d\phi_i/d\phi > 0$ for all ϕ/Φ.

Near $\phi = 0$ we find

$$\frac{\phi_i}{\Phi} \simeq \frac{1}{(1 + \frac{\chi}{2})^2}$$

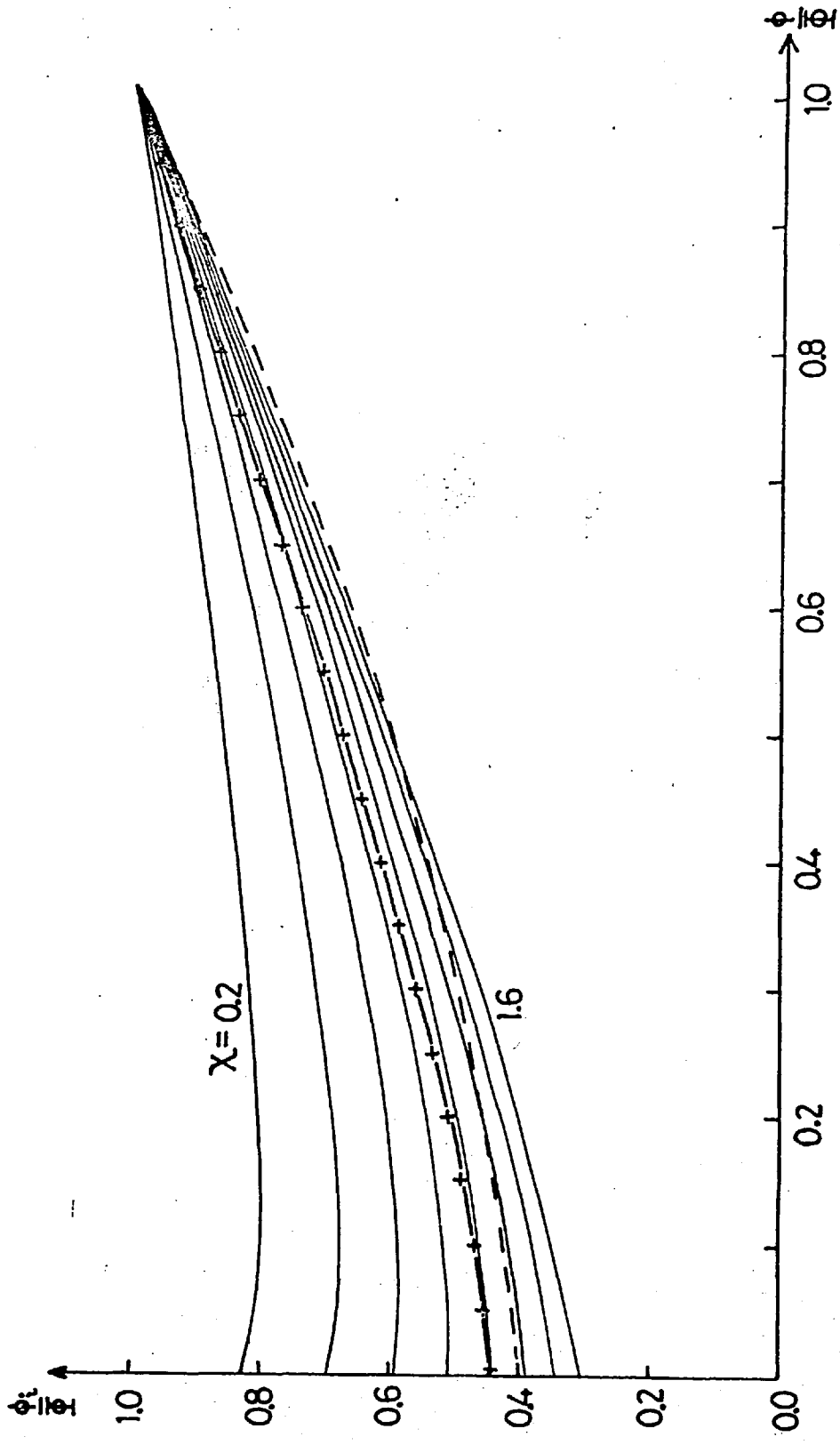

Figure 5.10: The values of $\dot{\phi}_i/\phi$ versus $\dot{\phi}/\phi$ for various values of χ. The line marked by crosses represents the result for the linear variation of χ from 1 to $(\sqrt{3} - \pi/3)$, while the dashed line shows $\dot{\phi}_i/\phi$ (first order) versus $\dot{\phi}/\phi$ for the model fields of section (5-iii).

so that for $\chi \approx 1$ we have $\phi_i/\Phi \approx 4/9$. Thus protons with initial potentials in the range

$$0 \leq \phi_i \leq \frac{4\Phi}{9}$$

do not enter the region of oscillating protons, but cross the $\phi = 0$ boundary in the drift-flow region.

Finally, if $v_p(\phi) \approx cE(\phi)/B(\phi)$ we can obtain $E(\phi)$ which is shown in Fig. 5.11 in the form of

$$\frac{v_o}{\sqrt{2}\, v_A}\left(\frac{E}{E_o}\right) \quad \text{versus} \quad \phi/\Phi \,. \quad (E_o = \Phi/d)$$

We have

$$\frac{v_o}{\sqrt{2}\, v_A}\left(\frac{E(\phi)}{E_o}\right) = \left(\frac{v_p(\phi)}{\sqrt{2}\, v_A}\right)\frac{B(\phi)}{B_o}$$

so that near $\phi \approx 0$ $\dfrac{v_o}{\sqrt{2}\, v_A}\dfrac{E(\phi)}{E_o} \approx \dfrac{1}{(1 + \chi/2)}\left\{1 - \dfrac{1}{(1 + \chi/2)^2}\right\}$

and for $\chi \approx 1$

$$\frac{v_o}{\sqrt{2}\, v_A}\frac{E(\phi)}{E_o} \approx \frac{10}{27} \approx 0.37 \qquad (5.34)$$

In order to obtain a rough idea of the potential structure near the boundary of the proton current layer from this electric field as a function of ϕ/Φ, we have (by trial and error) constructed a boundary potential $\phi(y)$ which gives the required $E(\phi) = (E_y^2 + E_z^2)^{\frac{1}{2}}$ when Laplace's equation is solved with rectangular boundary conditions (as in Chapter 4). We remember that we found that the solutions for the potential structure given by Poisson's equation for the drift-flow when

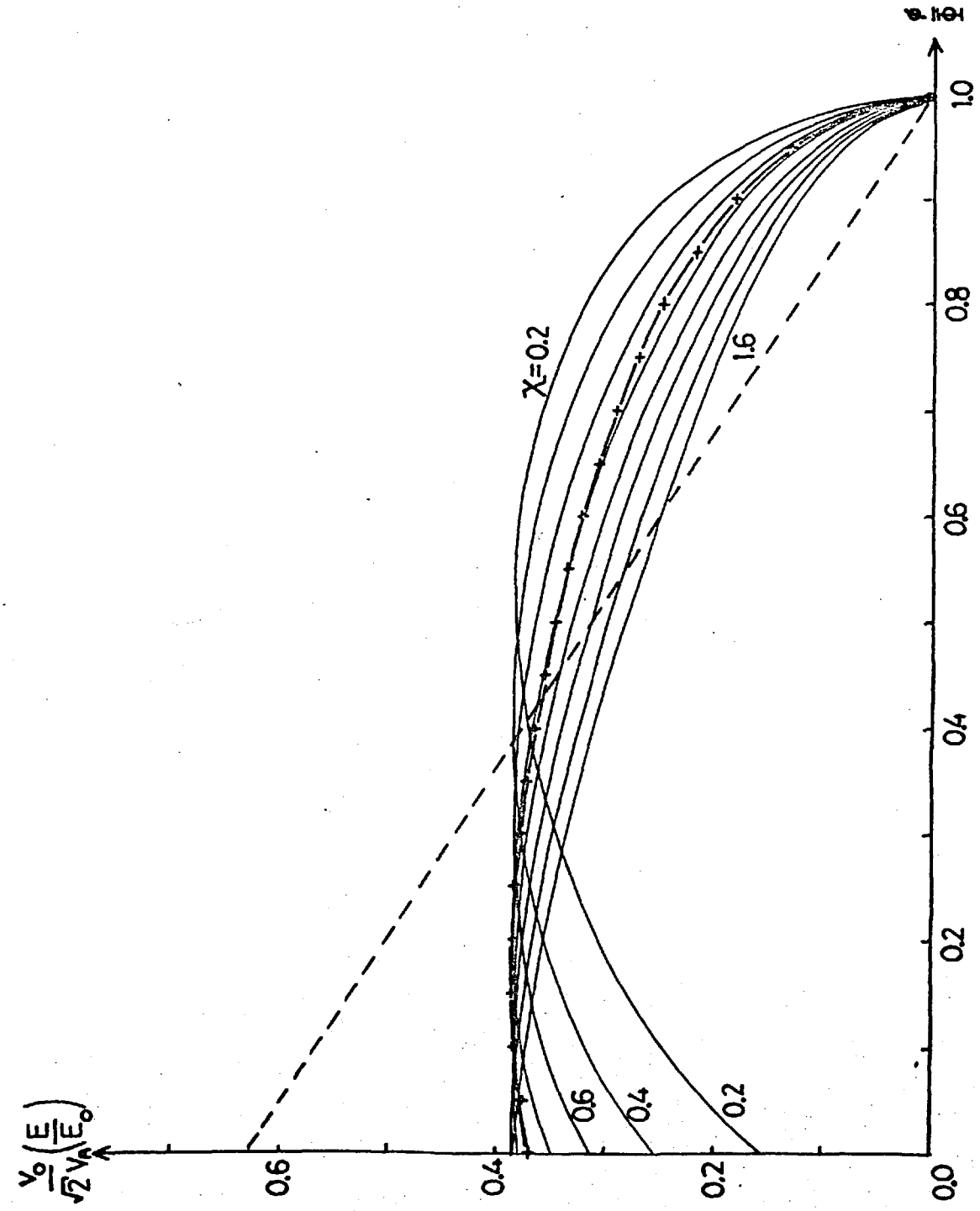

Figure 5.11: The values of $\frac{v_o}{\sqrt{2}\, V_A} \frac{E}{E_o}$ versus ϕ/ϕ (the electric field near the boundary of the trapped proton beam) for various values of χ. The line marked by crosses represents the result for linear variation of χ, while the dashed line shows the model field of section (5-iii).

the incoming flow is uniform do not differ appreciably from the solutions of Laplace's equation with the same boundary conditions. The electric field considered was that for $\chi = 1.2$ (see Fig. 5.11), and (E/E_o) was taken as 100 at $\phi = 0$. Thus from (5.34) we imply that

$$\frac{\sqrt{2}\, V_A}{v_o} \simeq 270$$

or equivalently $\left(\frac{2e\Phi}{m_p v_o^2}\right)^{\frac{1}{2}} \simeq 270$. Since $\left(\frac{\lambda_p}{d}\right) = \left(\frac{m_p v_o^2}{e\Phi}\right)^{\frac{1}{2}}$ we have, furthermore

$$\left(\frac{\lambda_p}{d}\right) \simeq \frac{\sqrt{2}}{270} \simeq 0.005$$

The result of ϕ/Φ versus z/d is shown in Fig. 5.12 and as expected we find that the total potential falls across a region whose characteristic length is a few times λ_p. The equipotential structure in the drift-flow is essentially the same as those shown in Chapter 4, the boundary potential used in the latter calculations is shown as a dotted line in Fig. 5.12.

Also shown in Figs. 5.7, 5.10 and 5.11 are the corresponding values of $v_p(\phi)/\sqrt{2}V_A$, $\phi_i(\phi)/\Phi$ and $v_o/\sqrt{2}V_A$ (E/E_o) which were used in the above proton trajectory calculations, given by

$$\frac{V_p}{\sqrt{2}V_A} = \left(\frac{m_p c^2 E^2(o)}{2B_o^2 e\Phi}\right)^{\frac{1}{2}}\left(\frac{E}{E(o)}\right) = (0.4)^{\frac{1}{2}}\left(1 - \frac{\phi}{\Phi}\right)$$

$$\frac{\phi_i(\phi)}{\Phi} = \frac{\phi}{\Phi} + 0.4\left(1 - \frac{\phi}{\Phi}\right)^2$$

$$\frac{V_o}{\sqrt{2}V_A}\left(\frac{E}{E_o}\right) = \left(\frac{m_p c^2 E^2(o)}{2e\Phi\, B_o^2}\right)^{\frac{1}{2}}\left(\frac{E}{E(o)}\right) = (0.4)^{\frac{1}{2}}\left(1 - \frac{\phi}{\Phi}\right)$$

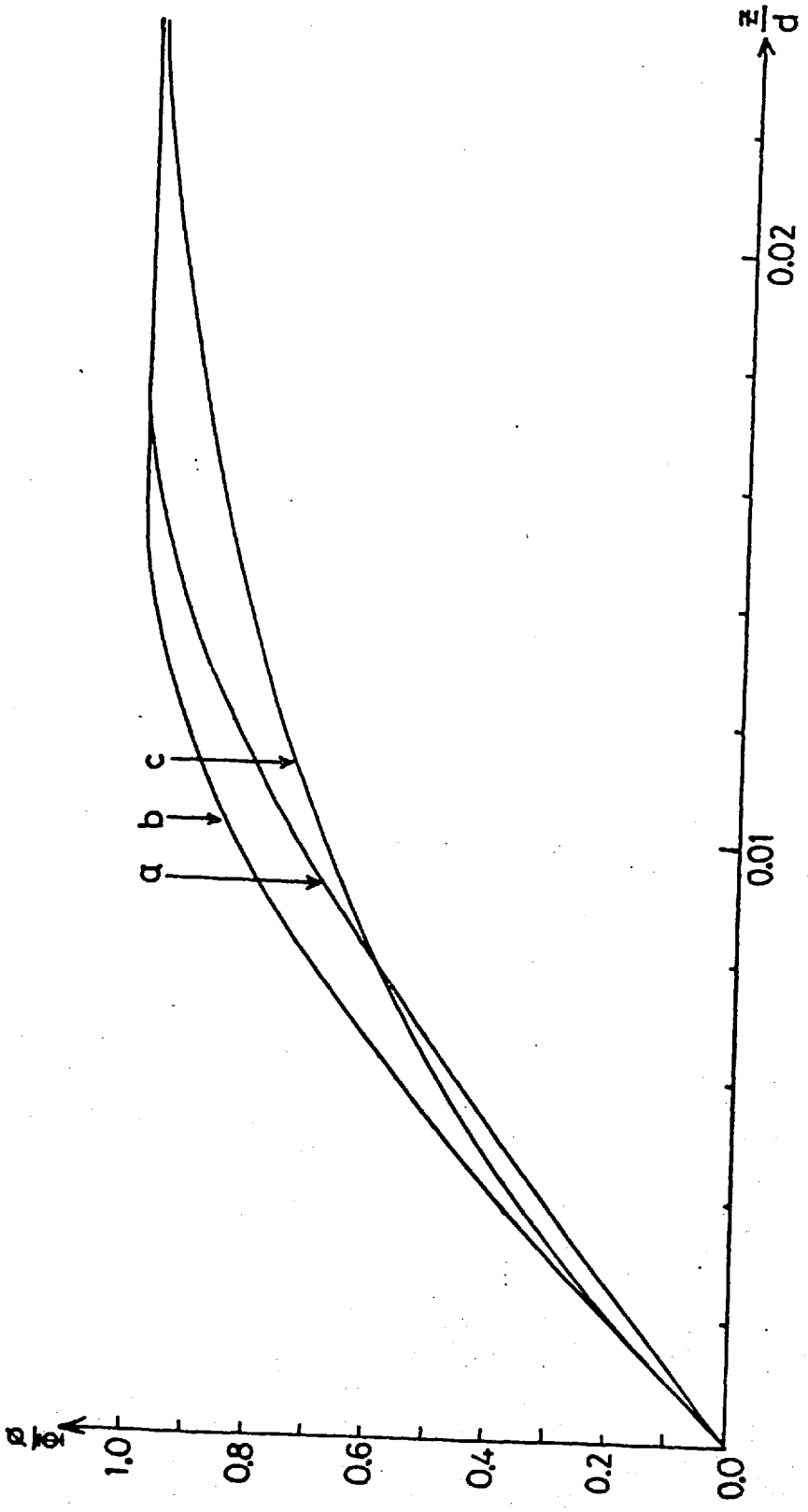

Figure 5.12

Figure 5.12(a): The potential structure along the neutral sheet which gives the required $|E|=E(\phi)$ (for $\chi=1.2$ of Fig. 5.11) at the lower boundary when Laplace's equation is solved in a rectangle (as in Chapter 4). E/E_o was taken as 10^2 at $\phi/\Phi = 0$.

(b): The boundary potential along the neutral sheet used for calculating drift-flow equipotential structures in Chapter 4, i.e. $\phi/\Phi = \sin(\frac{-z'}{p})$ with $p = 100$.

(c): The potential along the neutral sheet of the model field of section (5-iii) where we have taken $E(r=0) = 100\ E_o$, or equivalently $L = d/100$.

On Fig. 5.12 we also show the potential of the model field along the neutral sheet, taking $E(r=o) = 100\ E_o = 100\ \phi/d$ as above we obtain

$$\phi = (1 - e^{-100\ z/d}) .$$

Thus we see that the model fields correspond fairly well to the general results presented here, so that Fig. 5.6 gives us a good qualitative idea of the fields and particle motions to be expected.

(v) A Critism of the Above Current Sheet Theory

In the above theory it was assumed that the protons become non-adiabatic immediately on entry into the region of trapped particles, and so immediately start to be 'linearly accelerated' by the electric field (i.e. as though $\underline{B} = \underline{0}$). Consequently the only contribution to the positive charge of the layer considered was that due to the uniformly accelerating trapped proton beam, this being neutralized by the density of adiabatic electrons drifting towards the neutral sheet through the beam. The thickness of the slab was taken as

$$a = \chi \frac{v_p(\phi)}{\Omega_p(\phi)} \quad \text{with} \quad \chi \sim \mathcal{O}(1) .$$

However, merely by writing $a \simeq v_{p/\Omega}$ as a valid estimate of the thickness of the trapped proton beam and hence of the proton current layer, we do not necessarily guarantee that the

incoming protons become non-adiabatic on entry into the layer. This is due to the 'step' in the magnetic field produced by the thin electron beam. For example, if the magnetic field at the boundary of the layer is $B_1(\phi) \lesssim B_o$, the expected magnetic field structure at potential ϕ is

$$B(\phi,z) \simeq B_o \{\frac{\phi}{\Phi} + \frac{z}{\chi(\frac{v_p}{\Omega})} \{\frac{B_1}{B_o} - \frac{\phi}{\Phi}\}\} \qquad (5.35)$$

and hence the scale length in the direction of the incoming particles (roughly the z direction) in the current layer is

$$L_B \simeq \frac{B(\phi,z)}{(\frac{dB}{dz})} \simeq \chi \frac{\left\{\frac{\phi}{\Phi} + \frac{z}{\chi(v_p/\Omega)}\left(\frac{B_1}{B_o} - \frac{\phi}{\Phi}\right)\right\}\left(\frac{v_p}{\Omega}\right)}{\left\{\frac{B_1}{B_o} - \frac{\phi}{\Phi}\right\}} \qquad (5.36)$$

For example, at $\phi/\Phi \simeq 0.9$, $B_1 \simeq B_o$ and hence

$$L_B \simeq 9 \left(\frac{v_p}{\Omega}\right) .$$

In Fig. 5.13 we show $L_B(\phi)/(\frac{v_p(\phi)}{\Omega(\phi)})$ at the boundary of the trapped proton layer, i.e. $z = \chi(v_p(\phi)/\Omega(\phi))$

$$\frac{L_B(\phi)}{(\frac{v_p(\phi)}{\Omega(\phi)})} \simeq \frac{\chi \, B_1/B_o}{\{\frac{B_1}{B_o} - \frac{\phi}{\Phi}\}}$$

from equation (5.36), where we have taken χ to be linearly varying between $\chi = 1$ at $\phi = 0$ and $\chi = (\sqrt{3} - \pi/3)$ at $\phi = \Phi$. For $L_B(\phi)/(v_p/\Omega) > 1$ the protons remain adiabatic as they move into the beam as far as the magnetic gradient concerned. At the centre of the proton beam (i.e. the edge of the thin electron current layer, $z = 0$ in equation 5.36) we have

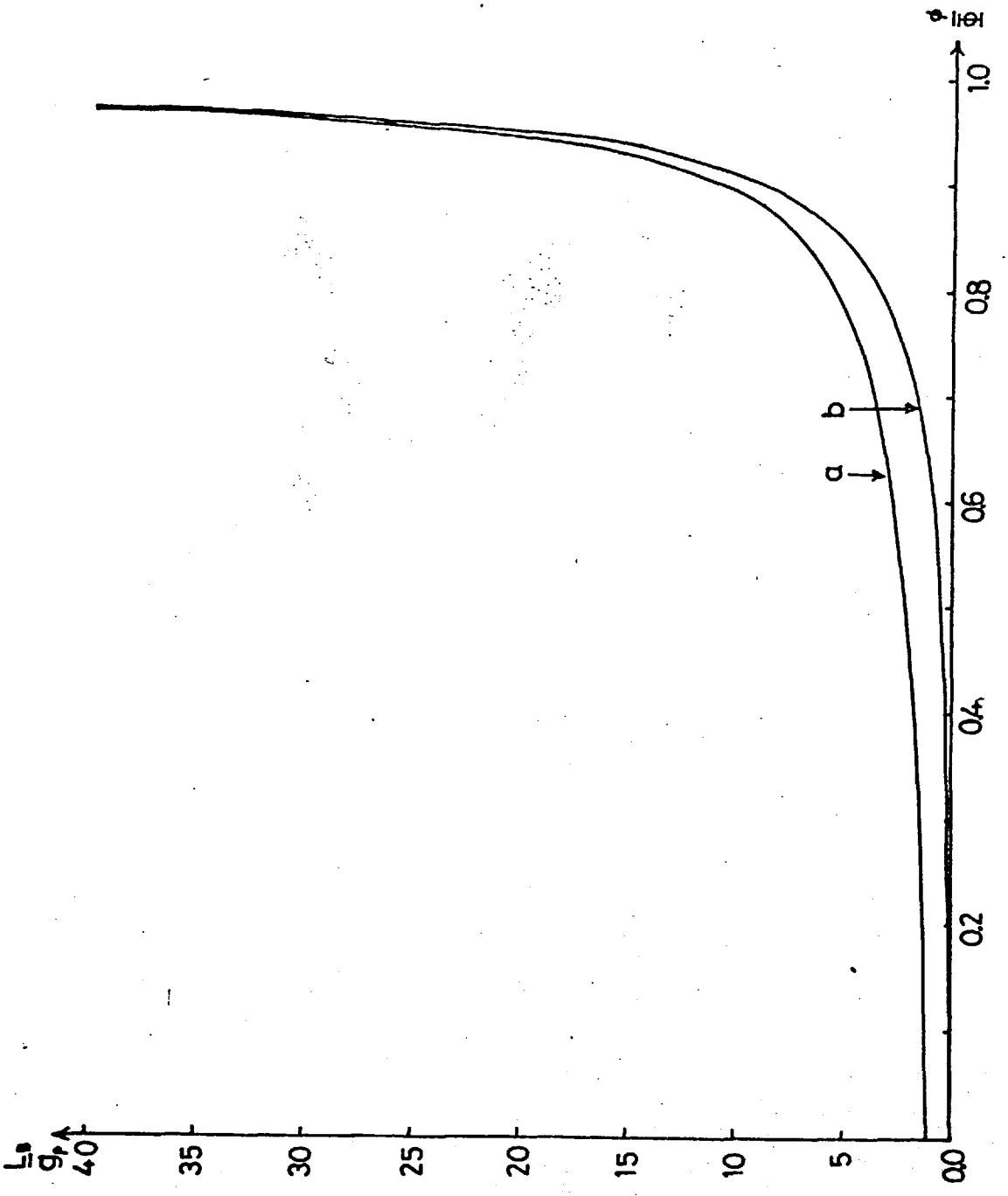

Figure 5.13: The ratio of the magnetic field scale length over the particle gyrolength at
(a) the boundary of the trapped proton zone, and at
(b) the boundary of the electron current sheet.

$$L_B \simeq \frac{\chi\ \phi/\Phi}{\{\frac{B_1}{B_o} - \frac{\phi}{\Phi}\}} \quad (\frac{v_p(\phi)}{\Omega(\phi)})$$

while the appropriate gyrolength is

$$\frac{v_p(z\simeq 0)}{\Omega(z\simeq 0)} \simeq \frac{m_p c^2 E\ (\phi)}{e\ B_o^2\ (\frac{\phi}{\Phi})^2} \simeq \frac{v_p(\phi)}{\Omega(\phi)}\ (\frac{B_1}{B_o})^2\ (\frac{\Phi}{\phi})^2$$

Hence

$$\frac{L_B(z=0)}{(\frac{v_p(z\simeq 0)}{(z\simeq 0)})} \simeq \frac{\chi\ (\phi/\Phi)^3}{(\frac{B_1}{B_o})^2\ (\frac{B_1}{B_o} - \frac{\phi}{\Phi})}$$

which is also shown in Fig. 5.13 taking the linearly varying χ. Again, if $L_B/(\frac{v_p}{\Omega}) > 1$ the protons are adiabatic at the centre of the beam, before they cross the neutral sheet, as far as magnetic gradients are concerned.

The scale lengths of the electric field may be estimated from

$$E\ L_E \lesssim \Phi$$

so that

$$L_E \sim (\frac{2e\Phi}{m_p v_p^2})(\frac{v_p}{\Omega}) \simeq (\frac{\sqrt{2}\ V_A}{v_p})^2\ (\frac{v_p}{\Omega}) \qquad (5.37)$$

Typically, near $\phi \simeq 0$ we obtain $\frac{m_p v_p^2}{2e\Phi} \sim \frac{1}{2}$ (see Fig. 5.7) so that

$$L_E \simeq 2\ (\frac{v_p}{\Omega})$$

while for higher values of ϕ/Φ, say, near $\phi/\Phi \simeq 0.9$, $v_p/\sqrt{2}\ V_A \simeq 0.2$, giving

$$L_E \simeq 25 \left(\frac{v_p}{\Omega}\right) .$$

We have plotted $L_E(\phi)/\left(\frac{v_p}{\Omega}\right)$ against ϕ/ϕ from equation (5.37) in Fig. 5.14.

Thus, from the model, the scale lengths of the electric and magnetic fields are of order (v_p/Ω) near $\phi \simeq 0$, while for higher values of ϕ/ϕ, we expect the protons to obey the drift-equations as they move through the trapped proton zone towards the neutral sheet. It is only after they cross the neutral sheet and become truly non-adiabatic that we can count them as being part of the trapped beam. However, the density of these adiabatic protons flowing through the trapped beam can be different from that of the adiabatic electrons, since

$$N_p = \frac{N_o B}{B_o \lambda_p} \quad \text{while} \quad N_e = \frac{N_o B}{B_o \lambda_e}$$

where λ_e is very nearly unity. Outside the beam the neutrality condition is simply $\lambda_p = 1$ (for the case of uniform inflow), giving Poisson's equation for the drift-flow derived in Chapter 4. If N_B is the beam density at some point, the new neutrality condition within the layer becomes

$$\frac{1}{\lambda_p} = \left(1 - \frac{N_B}{N_o} \frac{B_o}{B}\right)$$

or

$$\frac{c}{\Omega} \operatorname{div} \left(\frac{E}{B}\right) \simeq \frac{N_B}{N_o} \frac{B_o}{B}$$

where $\Omega = eB/m_p c$.

On a more qualitative basis, since λ_p is a power series in $g_p/L = v_p/\Omega L$ we may expect it to have the properties of

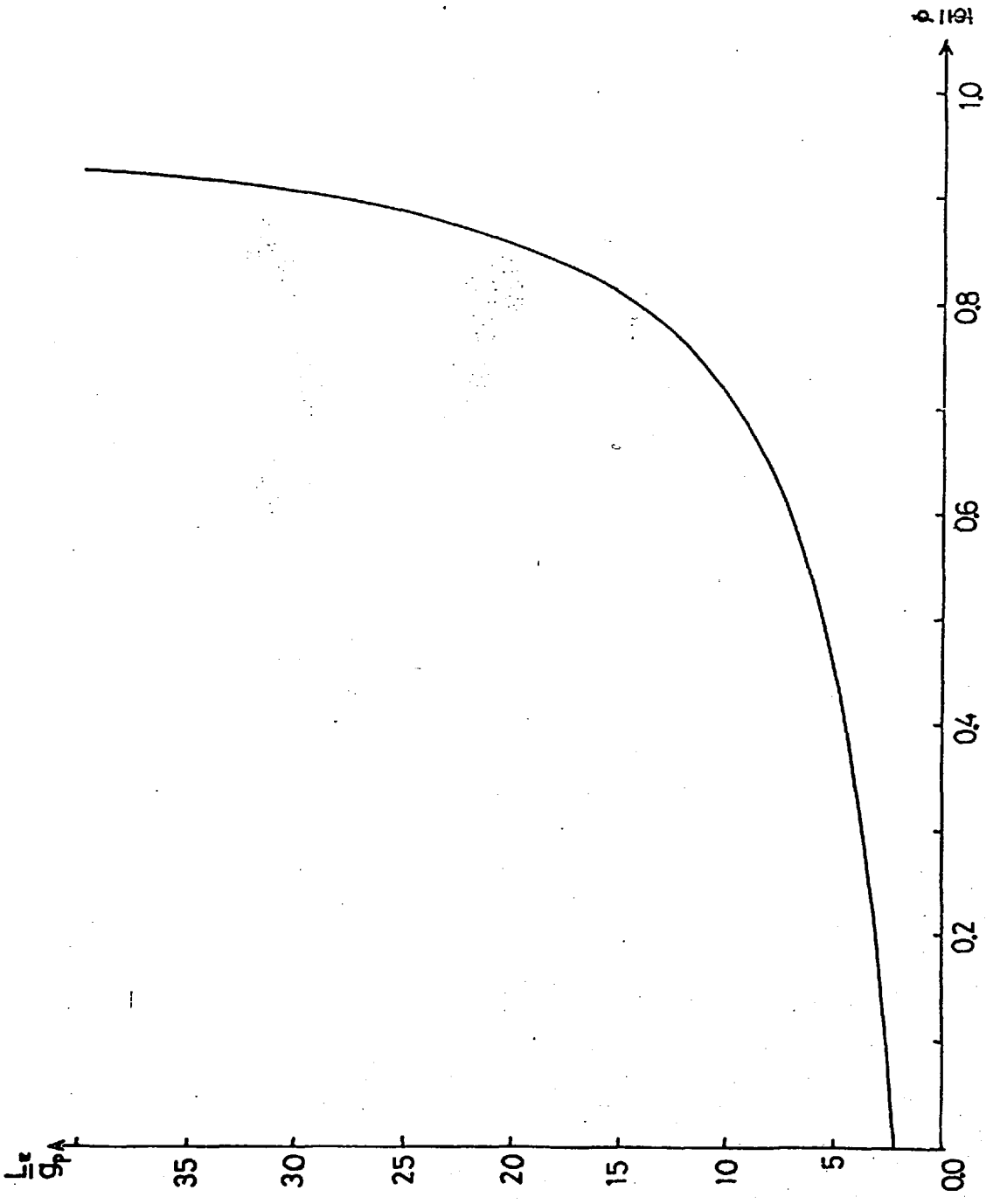

Figure 5.14: The ratio of the electric field scale length over the particle gyrolength at the boundary of the trapped proton zone.

$$\frac{1}{(1 - g/L)} \approx 1 + \frac{g}{L} + \left(\frac{g}{L}\right)^2 + \ldots \quad .$$

Thus, the net negative charge density of adiabatic particles in the layer is

$$(N_e - N_p)_{ad} = \frac{N_o R}{B_o} \left(g_{p/L}\right) ,$$

whereas in the above theory, we assumed $g_{p/L} \approx 1$ upon entry, and neglected the adiabatic protons.

A detailed calculation of the properties of the sheet based on these ideas has not yet been carried out. However, since we are now attempting to balance the beam density against the density difference between adiabatic protons and electrons, rather than electrons alone, the result must be an increase in the electric field and sheet thickness and a decrease in beam density over the results obtained above. Qualitatively there can be little difference.

We have, however, neglected one possibility in this discussion, which would validate the above theory, but this has not been investigated in sufficient depth to raise it above the level of a suggestion. There may exist electric fields localized in the trapped proton layer arising from differing density distributions between the trapped beam and the adiabatic particles. Such an electric field would redistribute the densities within the thickness of the layer in order to satisfy the plasma approximation. These electric fields are on the scale length $v_{p/\Omega}$, the thickness of the beam, and may be of sufficient strength to make the protons become non-adiabatic immediately on entry into the layer.

If we consider the adiabatic electron density within the trapped proton beam, this is a maximum at the boundary,

and decreases with the magnetic field towards the centre of the sheet. Since $v_p(\phi)$ decreases with increasing ϕ/ϕ, and oscillation amplitude decreases as particles accelerate along the sheet, particles in the beam at potential ϕ coming from higher potentials will tend to have amplitudes of oscillation less than $v_p(\phi)/\Omega(\phi)$. We may expect therefore, that the beam density will be larger nearer the sheet centre, or at least relatively constant across the thickness of the beam. It is thus sensible to consider the effects of a positive potential localized within the beam, the form of which is shown in Fig. 5.15.

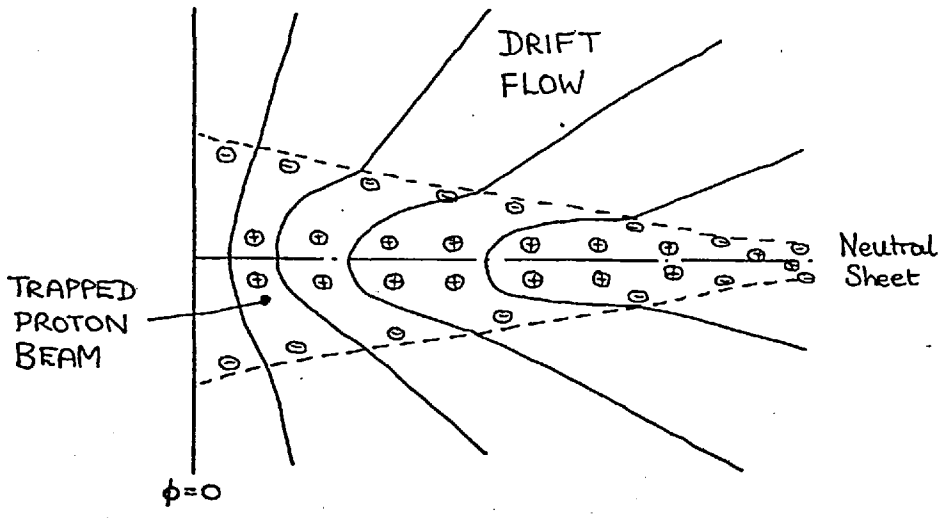

Figure 5.15

Incoming protons are reflected out of the sheet by the electric field E_z, so long as

$$\Delta\phi > \frac{m_p v_p^2}{2e}$$

where $\Delta\phi$ is the potential difference between the centre and edge of beam at a given y. They are then turned round (back into the sheet) by the magnetic field, gaining energy, and

then penetrate further into the sheet, only to be reflected again. Protons thus oscillate about the line where the electric force E_z, and magnetic force $v_y B_x/c$ balances. We expect the velocity along the sheet to increase uniformly as it is accelerated by F_y, the velocity in the oscillations remaining roughly constant at the incoming (perpendicular) particle velocity. When v_y has increased so much that the electric field E_z can no longer balance the Lorentz force, the particle crosses the neutral sheet and oscillates symmetrically about it, continuing to accelerate in the electric field. Thus a positive potential has the effect of redistributing the protons in the manner desired, and should also cause them to become non-adiabatic at the edge of trapped proton beam.

We have studied these effects by computing some proton trajectories in model field configurations, where the electric field was taken as

$$E_y = E_o \qquad E_z = \begin{cases} \frac{\alpha E_o \pi}{2} \sin\left(\frac{\pi z}{a}\right) & |z| \leq a \\ 0 & |z| \geq a \end{cases}$$

so that the potential field is given by

$$\phi = \begin{cases} -E_o y + \frac{\alpha E_o a}{2}\left(\cos\left(\frac{\pi z}{a}\right) + 1\right) & |z| \leq a \\ -E_o y & |z| \geq a \end{cases}$$

where we have taken the $y = 0$ equipotential outside the sheet as the arbitrary zero. This equipotential crosses the neutral sheet at $y = \alpha a$ (see Fig. 5.16).

The protons are assumed to be moving adiabatically towards the

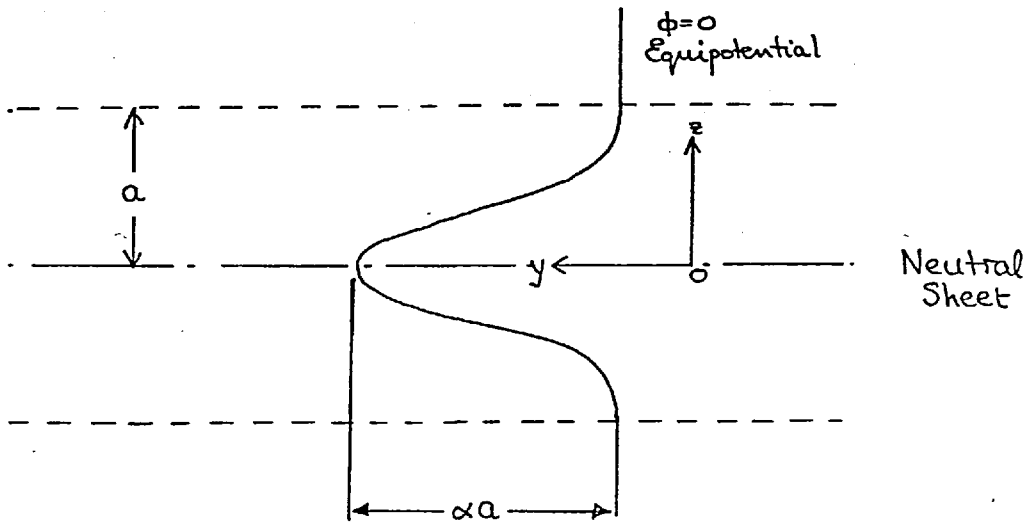

Figure 5.16

sheet, with velocity $v_p = cE_o/B_o$, and hence having energy $\varepsilon = \frac{m_p c^2 E_o^2}{2\ B_o^2}$. They will thus be reflected by the localized potential if $e\alpha E_o a > \frac{m_p c^2 E_o^2}{2\ B_o^2}$ or $\alpha \gtrsim \frac{1}{2}$ if we put $a \simeq \frac{v_p}{\Omega} \simeq \frac{m_p c^2 E_o}{e\ B_o^2}$.

As our example we take $B_x = B_x(z) = B_o\ \mathrm{sgn}(z)$ so that the line about which the particles oscillate is given by

$$\alpha\ E_o\ \frac{\pi}{2}\ \sin\ (\frac{\pi z}{a}) \quad = \quad \frac{v_y B_o}{c}$$

where $v_y \simeq \{(\frac{2e}{m_p})\ \{-\ \frac{\alpha E_o a}{2}\ (\cos\ (\frac{\pi z}{a}) + 1) + E_o\ y\}\}^{\frac{1}{2}}$

assuming that we start the particle at $y = 0$ with $|z| \geq a$. Thus the line is

$$y/g_o = \left(\frac{\alpha\pi}{2} \sin\left(\frac{\pi z}{a}\right)\right)^2 + \frac{\alpha a}{2g_o}\left(\cos\left(\frac{\pi z}{a}\right)+1\right) \qquad (5.39)$$

where g_o is the initial gyrolength of the particles,

$$g_o \quad = \quad \frac{m_p c^2 E_o}{e B_o^2}\ .$$

The computed particle trajectories are shown in Fig.

5.16 for $\alpha = 0, 2, 4$. When $\alpha = 0$ (no localized potential) the particle moves adiabatically towards the sheet, and the initial amplitude of the oscillation is $(\sqrt{3} - \pi/3)\, g_o \simeq 0.685\, g_o$, as expected for the cycloidal motion in uniform, crossed electric and magnetic fields. This amplitude defines the sheet thickness in this region, so we put $a = (\sqrt{3} - \pi/3) g_o$ in the equation for $E_z(z)$ when $\alpha \neq 0$.

The orbits for $\alpha = 2, 4$ are also plotted in Fig. 5.16[a], and show the anticipated oscillations about the line where E_z and $v_y B_x/c$ balances, given by equation (5.39); this is also plotted in the figure. This motion may be further understood by considering the effective potential for the motion perpendicular to the neutral sheet. If we write

$$m_p \frac{dv_z}{dt} = - \frac{\partial V}{\partial z} \quad \text{where} \quad \frac{\partial V}{\partial z} = - e\left(E_z - \frac{v_y B_x}{c}\right)$$

then the equivalent potential $V(z,t)$ in the sheet is given by

$$V(z,t) - V(o,t) = e\left\{\phi(z,y(t)) - \phi(o,y(t)) + \frac{v_y}{c}\int_o^z B_x(z)\,dz\right\}$$

where we consider v_y to be independent of z. We define the value of $V(o,t)$ such that $V(z,t) = 0$ when $v_y = 0$ and $z = a$, so that the particle is incident on the sheet at zero potential, i.e.

$$V(o,t) = e\left\{\phi(o,y) - \phi(a,y)\right\} .$$

Then

$$V(z,t) = e\left\{\phi(z,y(t)) - \phi(a,y(t)) + \frac{v_y}{c}\int_o^z B_x(z)\,dz\right\}$$

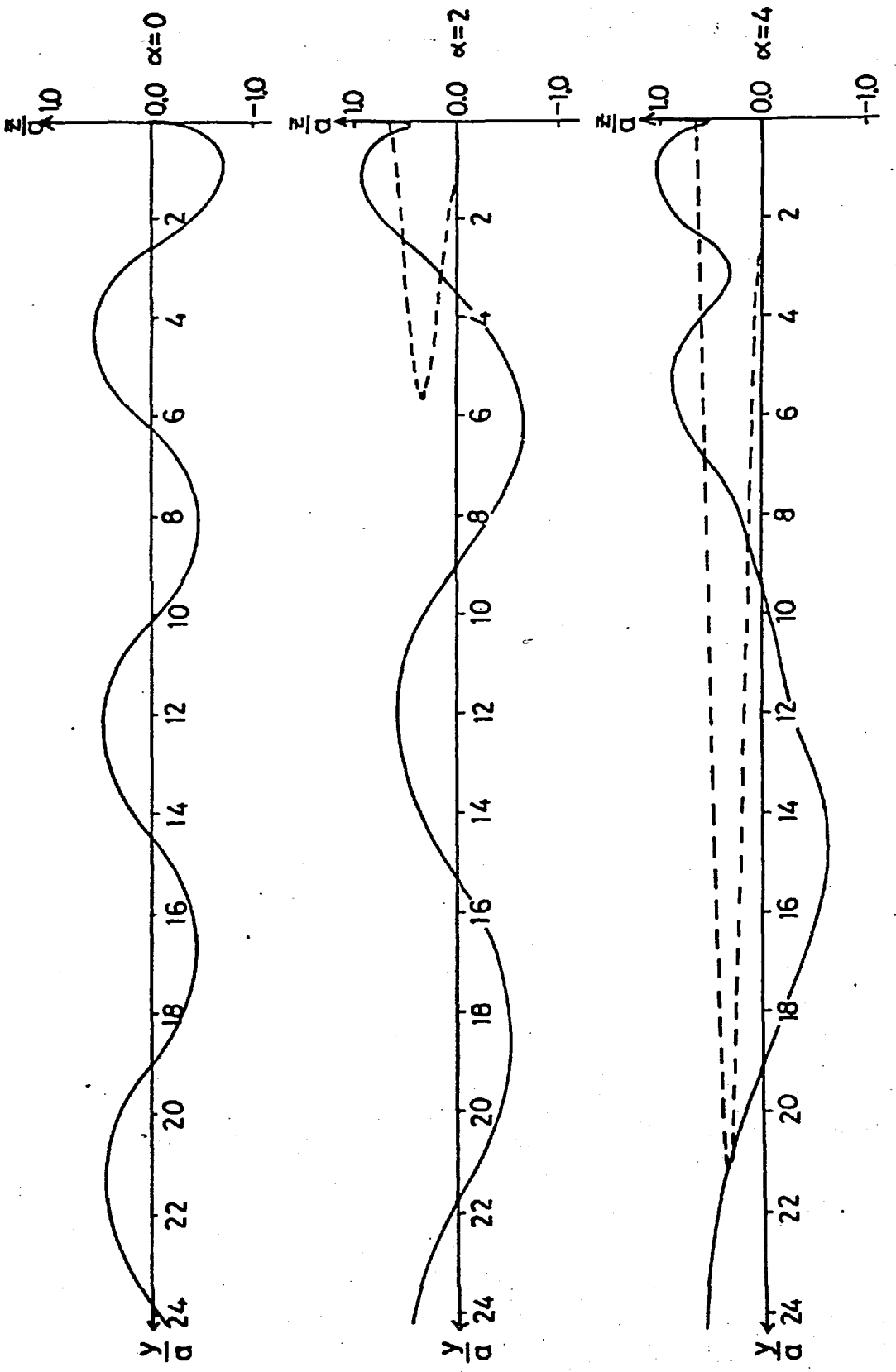

Figure 5.16: Computed proton trajectories in the model fields of section (5-v) for $\alpha = 0,2,4$. The dotted line is the line along which the electric and magnetic forces balance for the incoming particle, and about which the particles initially oscillate.

and using the given fields

$$V(z,t) = ea\left\{\frac{\alpha E_o}{2}\left(\cos\left(\frac{\pi z}{a}\right)+1\right) + \frac{v_y B_o}{c}\left(\frac{z}{a}\right)\mathrm{sgn}(z)\right\} \qquad (5.40)$$

The first term is simply the electrostatic potential which repels the protons from the sheet, while the second term, produced by the magnetic force, turns the particles back into the sheet when $v_y > 0$. If we write $v_y = \beta(t)\, cE_o/P_o$ for some value of β, and normalize $V(z,t)$ to the initial kinetic energy of the proton $\varepsilon_o = m_p c^2 E_o^2/2B_o^2$ we then find that

$$\left(\frac{g_o}{a}\right)\frac{V(z,t)}{\varepsilon_o} = \left\{\alpha\left(\cos\left(\frac{\pi z}{a}\right)+1\right) + 2\beta\left(\frac{z}{a}\right)\mathrm{sgn}(z)\right\}$$

and this is plotted for $\alpha = 4$, for various values of β in Fig. 5.17. It shows the minimum in the effective potential about which the proton oscillates; it also shows that there exist two solutions of $E_z = v_y B_x/c$ for a range of β corresponding to

$$\frac{\alpha a}{2g_o}\left(\cos\left(\frac{\pi z}{a}\right) + 1\right) \leq y/g_o \leq \frac{y_{max}}{g_o}$$

in equation (5.39), (see also Fig. 5.16(a)). However we now see that the solution with the higher value of z at a given y represents a minimum in the effective potential about which the particle can oscillate, while the lower z solution is a maximum in the potential about which the particles cannot oscillate. As v_y increases (β increases), the minima move towards $z = 0$, and become less deep, such that the particle eventually has sufficient energy to escape from the potential well and start to oscillate symmetrically about the neutral

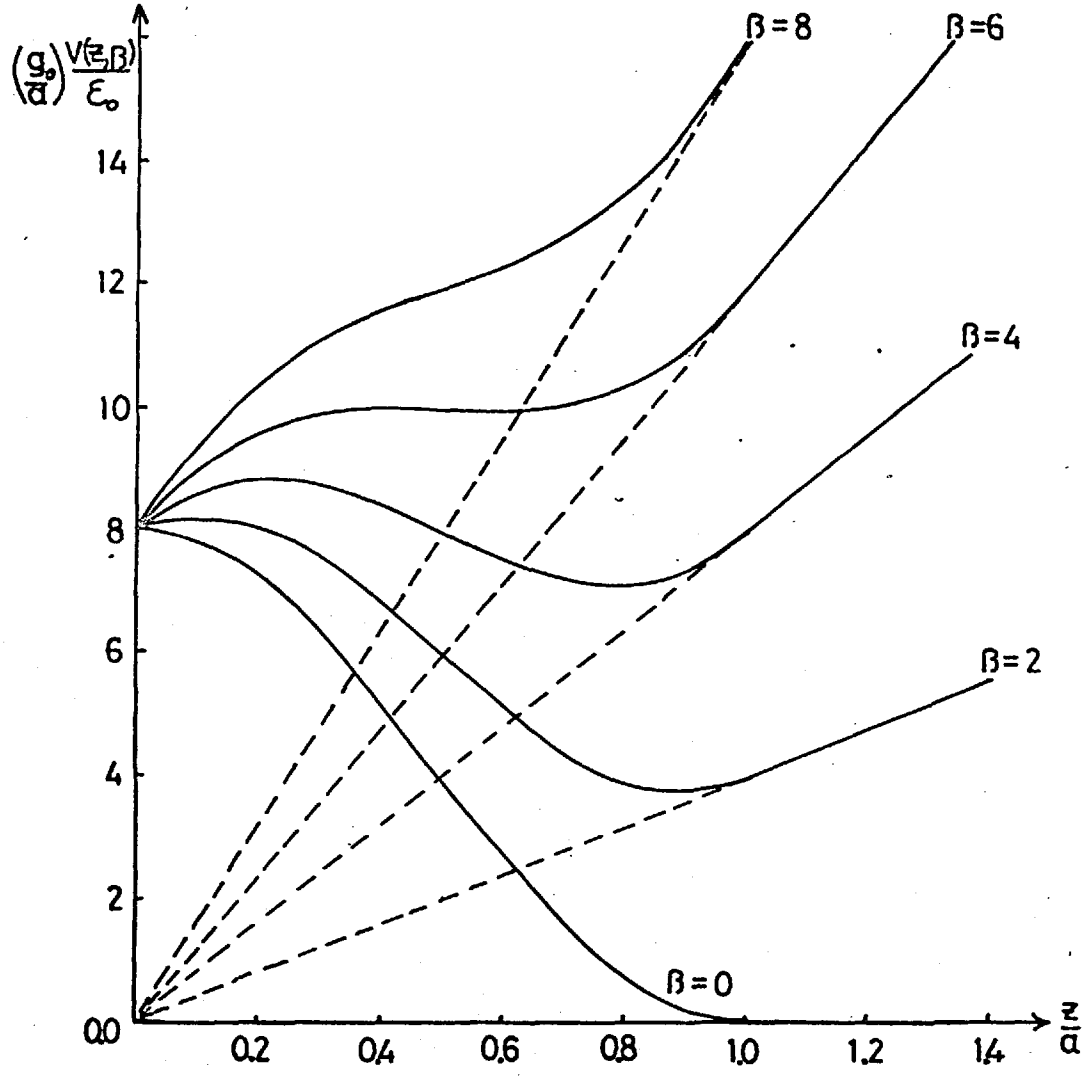

Figure 5.17: The effective potential of the electromagnetic field near the neutral sheet for the model fields (α=4) of section (5-v) for various values of $\beta = \frac{v_y}{(\frac{cF_o}{P_o})}$. As the particle accelerates along the sheet (β increases) the minimum in the potential about which the particle oscillates becomes shallower, and eventually it is able to escape and move symmetrically about the neutral line.

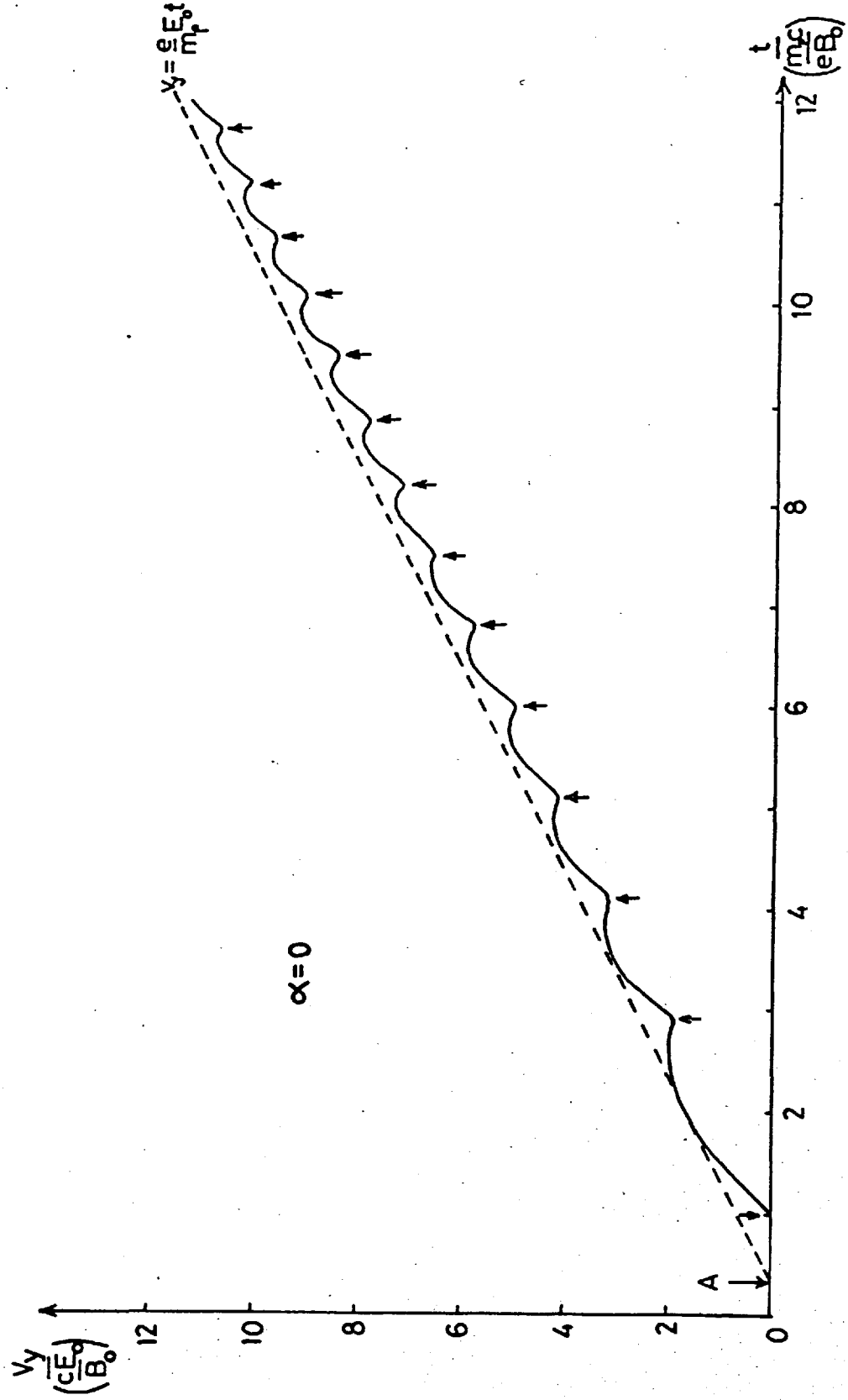

Figure 5.18(a)

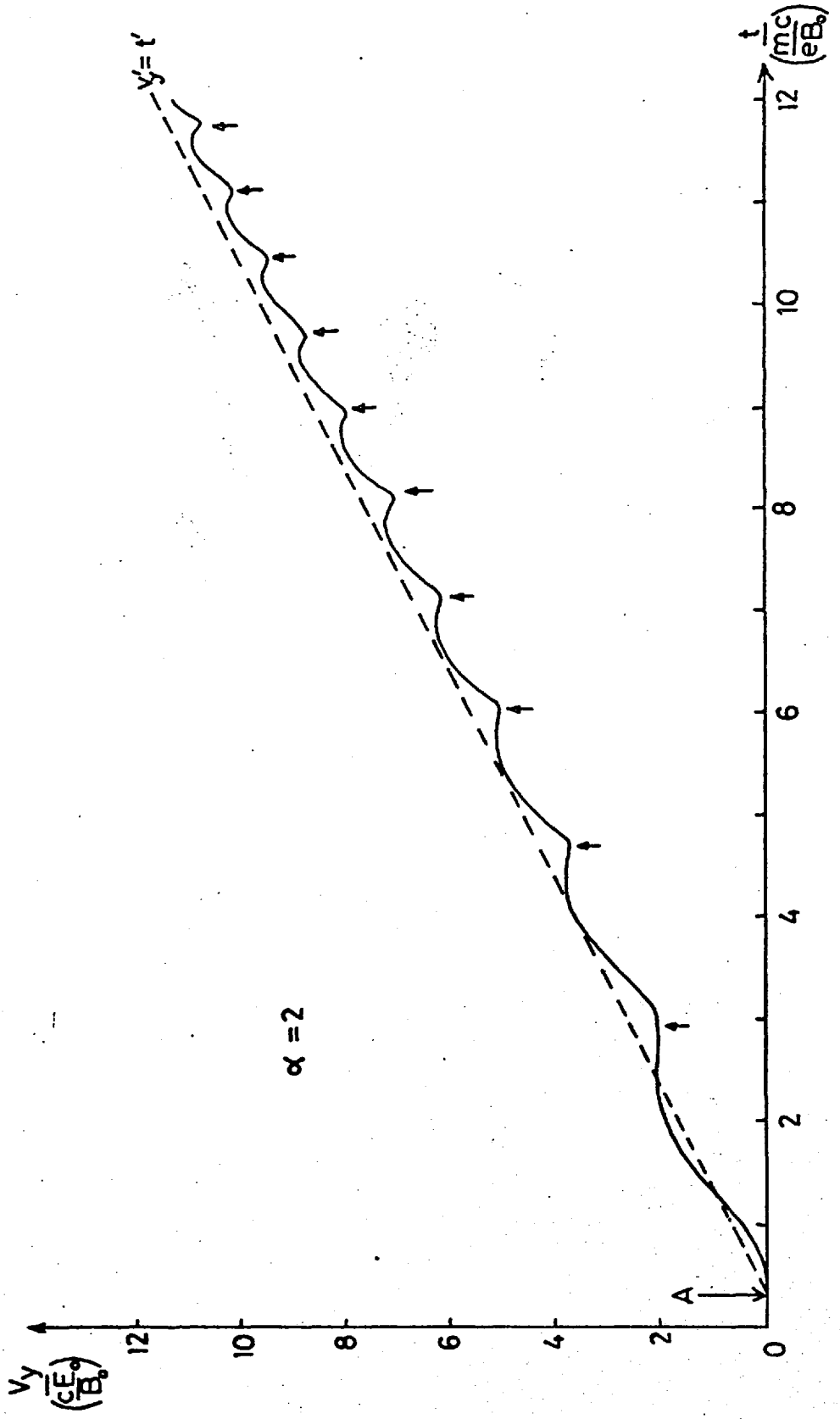
$v_y = t'$
$\alpha = 2$
A
$v_y \left(\frac{cE_0}{B_0}\right)$
$\frac{t}{\left(\frac{mc}{eB_0}\right)}$
0
2
4
6
8
10
12

Figure 5.18(b)

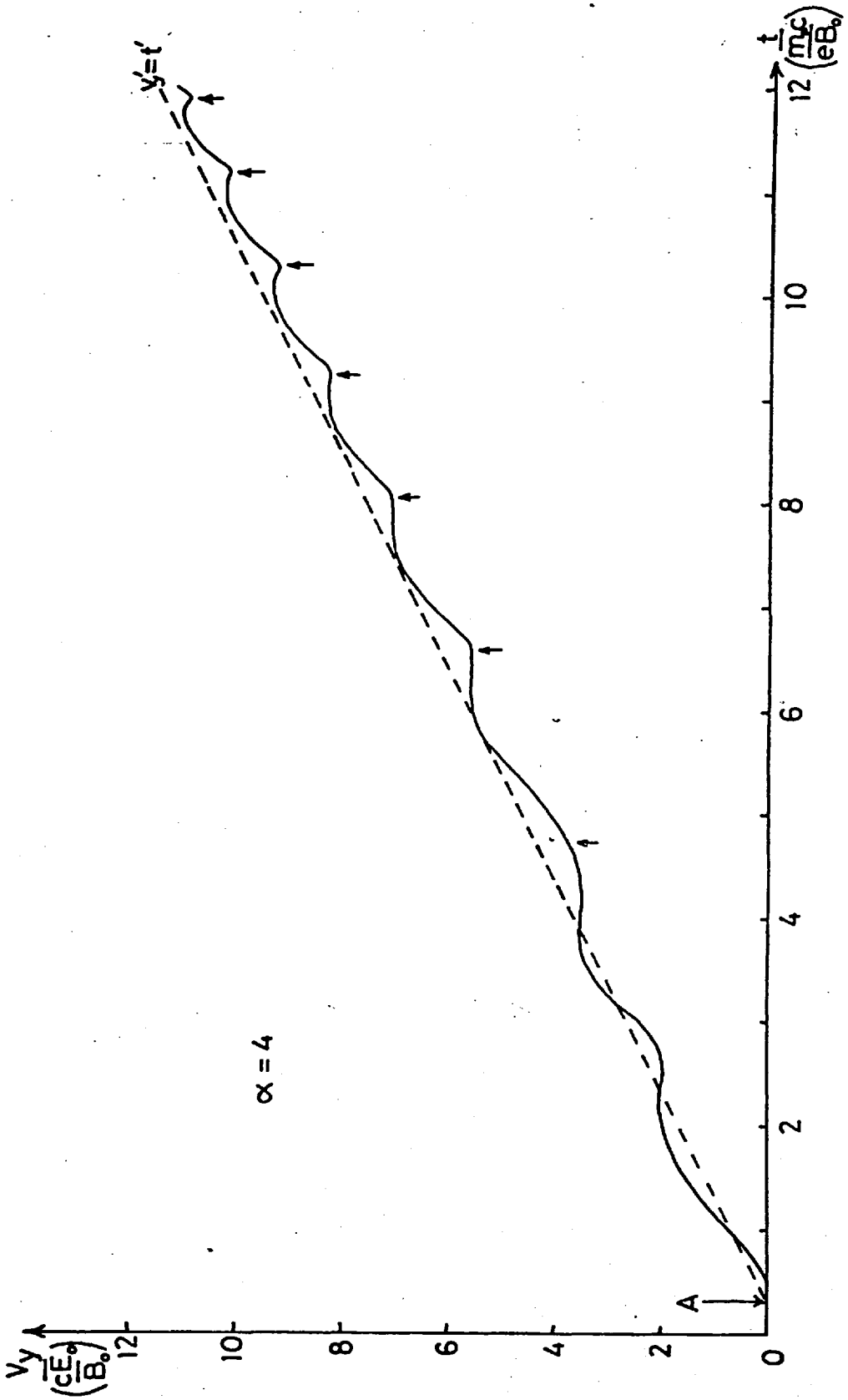

Figure 5.18: Proton velocity parallel to the neutral sheet versus time from entry into the trapped beam (marked with the letter A) for the computed proton trajectories of Fig. 5.16 and section (5-v). Neutral sheet crossings are marked by an arrow. The trajectories are compared with that of a particle uniformly accelerating in the electric field from rest,

i.e. $$\frac{v_y}{(\frac{cE_o}{B_o})} = \frac{t}{(\frac{m_p c}{eB_o})}$$

sheet.

In Fig. 5.18 we have plotted v_y against time, which shows the expected result that for $\alpha \neq 0$ the particles start to accelerate along the sheet immediately on entry, while for $\alpha = 0$, we have adiabatic motion until the neutral sheet is reached. For uniform acceleration from rest in the field E_o we would obtain the straight line $v_y = e\, E_o/m_p t$, while for uniform acceleration from an initial velocity cE_o/P_o, $v_y = e\, E_o/m_p t + \frac{cE_o}{P_o}$ and these lines are also shown in Fig. 5.18 for comparison. ($t = 0$ is the time of entry of the particle into the trapped proton layer, $z = (\sqrt{3} - \pi/3)\, g_o$).

Finally, we note that the trapped protons are redistributed about the sheet by the potential such as to tend to neutralize the assumed charge densities.

(vi) <u>The Properties of the Thin Electron Peam</u>

The majority of the present work has been devoted to the study of the proton current sheet of dimension $\lambda_p << d$, across which falls the Alfvén potential Φ. All the plasma entering the sheet enters in this region, and it produces a thin beam of electrons moving towards $\phi = \bar{\Phi}$ which provides the current for the remainder of the neutral sheet. Within the proton current sheet we have assumed that the electrons remain adiabatic until very close to the neutral sheet, where adiabaticity breaks down due to the scale lengths of the magnetic field. We have not been lead to suggest the existance of electric fields whose scale lengths are comparable with v_e/Ω_e, such that $m_e v_e^2 \sim e\Phi$. If this is true, the WKB

theory used in Chapter 3 should be adequate to describe the properties of the electron current sheet. However, the detailed structure of the sheet still poses considerable problems, bearing in mind that the electrons enter the sheet with widely different initial conditions, depending on ϕ/ϕ. Consequently we shall restrict ourselves to a much simpler problem in our investigation of the self-consistent magnetic structure. We shall consider the problem of the self-consistent magnetic field structure set up by a beam of electrons entering the sheet at potential ϕ_i and being accelerated along the sheet up to the potential Φ. If, for instance we take $\phi_i = \Phi/2$ then the results of this problem should give a good indication of the structure to be expected. From Chapter 3 we recall that the oscillation amplitude and velocity amplitude of particles in a magnetic field structure of the form

$$B(z(t)) = \frac{B_1(t)\ z(t)}{a(t)}$$

is given by

$$\hat{z}(t) = \frac{\hat{z}_o}{\left(\frac{m_e c v_y(t)}{a(t) e B_1(t)}\right)^{\frac{1}{4}}} \qquad \hat{v}_z(t) = \hat{v}_{z_o} \left(\frac{m_e c v_y(t)}{a(t) e B_1(t)}\right)^{\frac{1}{4}} \qquad (5.41\ a,b)$$

We see that $\hat{z} = \hat{z}_o$ and $\hat{v}_z = \hat{v}_{z_o}$ when

$$\frac{v_y(t)}{\Omega(t)} \simeq a \qquad (5.42)$$

For consistency, the initial amplitude of the particle oscillations must be equal to the sheet thickness and from Chapter 3, we found that

$$a(t=o) \simeq \frac{v_{z_i}(\phi_i)}{\Omega(t=o)}$$

where $t = 0$ is the time of entry of the particle into the sheet. For times $t > 0$, v_y increases, and as a first approximation

$$v_y(t) \approx \{\frac{2e}{m_e}(\phi(t) - \phi_i)\}^{\frac{1}{2}} >> \hat{v}_z(t)$$

whereas, from (5.41a) the oscillation amplitude, and hence $a(t)$, decreases. Thus (5.42) is only satisfied when $v_y(t) \approx v_{z_i}(\phi_i)$ i.e. very near $t = 0$. Thus, in the formulae (5.41a,b) $\hat{z}_o$ and $\hat{v}_{z_o}$ are the initial amplitude and velocity of the oscillatory motion on injection into the sheet, given by

$$\hat{z}_o = a(t=o) \approx \frac{v_{z_i}(\phi_i)}{\Omega(t=o)}$$

$$\hat{v}_{z_o} = v_{z_i}(\phi_i)$$

and we put $v_y \approx a(\phi)\ \Omega(\phi) \approx v_{z_i}(\phi_i)$ at $t \approx 0$.

We also have $B_1(t) \approx \frac{\phi(t)}{\Phi} B_o$, so that

$$\hat{z}(t) \simeq \frac{v_{z_i}(\phi_i)}{\left(\frac{\phi_i}{\Phi}\right)\Omega_o} \cdot \frac{1}{\left(\frac{v_y(t)}{a(t)\left(\frac{\phi(t)}{\Phi}\right)\Omega_o}\right)^{\frac{1}{4}}} \tag{5.43}$$

and

$$\hat{v}_z(t) \approx v_{z_i}(\phi_i)\ \left(\frac{v_y(t)}{a(t)\left(\frac{\phi(t)}{\phi}\right)\Omega_o}\right)^{\frac{1}{4}} \tag{5.44}$$

where $\Omega_o = \frac{eP_o}{m_e c}$. If the magnetic field structure is to be consistent with this beam of particles then $a(t) \approx \hat{z}(t)$, so that for consistency we obtain from (5.43)

$$a \approx \left(\frac{v_{z_i}(\phi_i)}{\left(\frac{\phi_i}{\phi}\right)\Omega_o}\right)^{4/3} \left(\frac{\left(\frac{\dot{\phi}}{\phi}\right)\Omega_o}{v_y(t)}\right)^{1/3}$$

$$\text{or} \qquad a \simeq \frac{V_{z_i}(\phi_i)}{\left(\frac{\phi_i}{\Phi}\right)\Omega_o}\left(\frac{\phi}{\phi_i}\,\frac{V_{z_i}(\phi_i)}{V_y(t)}\right)^{1/3}$$

$$\simeq \frac{V_{z_i}(\phi_i)}{\left(\frac{\phi_i}{\Phi}\right)\Omega_o}\left(\frac{\phi}{\phi_i}\,\frac{V_{z_i}(\phi_i)}{\left(\frac{2e}{m_e}(\phi-\phi_i)\right)^{1/2}}\right)^{1/3}$$

From the properties of the proton current sheet where the electrons enter the sheet, the initial velocities $v_{z_i}(\phi_i)$ are such that

$$\frac{m_p\, v_{z_i}^{\,2}}{2} \simeq Ke\Phi$$

giving $$\frac{v_{z_i}}{\Omega_o} \simeq \left(\frac{m_e}{m_p}\right)^{1/2} (2K)^{1/2}\, \lambda_p$$

Thus

$$a \simeq \left(\frac{m_e}{m_p}\right)\frac{(2K)^{1/2}}{\left(\frac{\phi_i}{\Phi}\right)}\left(\frac{\phi}{\phi_i}\right)^{1/3}\left\{\frac{m_e K\Phi}{m_p(\phi-\phi_i)}\right\}^{1/6}\lambda_p$$

$$\simeq \left(\frac{m_e}{m_p}\right)^{7/6}\frac{(2K)^{1/2}}{\left(\frac{\phi_i}{\Phi}\right)}\left(\frac{\phi}{\phi_i}\right)^{1/3}\left\{\frac{K\Phi}{(\phi-\phi_i)}\right\}^{1/6}\lambda_p \qquad (5.45)$$

and when $\phi = \Phi$, and taking $\phi_i = \Phi/2$, $K = 0.2$ (from Fig. 5.10), we finally arrive at the thickness of the electron current sheet on emergence from the proton current layer

$$a \simeq \left(\frac{m_e}{m_p}\right)^{7/6}\lambda_p \,.$$

Now $(m_p/m_e)^{7/6} \simeq 6 \times 10^3$, and $\lambda_p \simeq 600$ Km for $N_o \simeq 0.1$ cm^{-3} and $\lambda_p \simeq 2000$ Km for $N_o \simeq 0.01$ cm^{-3}. Thus, from the theory we arrive at the following estimates of the sheet thickness

$$a \approx 0.1 \text{ Km} \quad \text{for} \quad N_o \approx 0.1 \text{ cm}^{-3}$$

$$a \approx 0.3 \text{ Km} \quad \text{for} \quad N_o \approx 0.01 \text{ cm}^{-3} .$$

Before leaving the problem of the self-consistent magnetic field structure we should like to show that the procedure adopted above to determine the sheet thickness i.e. matching $a(t)$ to $\hat{z}(t)$ of the WKB solution gives results consistent with a more usual 'fluid'-like approach, based on 'pressure balance'. For hydromagnetic equilibrium

$$\frac{\underline{j} \wedge \underline{B}}{c} = \underline{\nabla} p \qquad (5.46)$$

and writing $\underline{j} = nev_y$, and $\underline{\nabla} p \approx \frac{nv_z^2}{a} m_e$ we have

$$\frac{nev_y B_o}{c} = \frac{nv_z}{a} , \quad \text{or} \quad a \approx \frac{v_z^2}{\Omega_o v_y} \qquad (5.47)$$

From the 'self-consistent' WKB theory we have

$$v_z = v_{z_o} \left(\frac{v_y}{a\,\Omega_o}\right)^{\frac{1}{4}} \qquad z = \frac{z_o}{\left(\frac{v_y}{a\,\Omega_o}\right)^{\frac{1}{4}}} \qquad (5.48\ a,b)$$

taking $B_1(t) = B_o$ for simplicity. Thus $v_z z \approx$ constant. For self consistency we put $z = a$ and $z_o \approx \frac{v_{z_o}}{\Omega_o}$ hence obtaining

$$a = \frac{v_{z_o}^2}{\Omega_o v_z} \qquad (5.49)$$

Thus, if (5.49) and (5.47) are to be consistent we require that $v_z^3 = v_{z_o}^2 v_y$ from the WKB theory.

From (5.48) we have

$$v_z^3 = v_{z_o}^3 \left(\frac{v_y}{a\,\Omega_o}\right)^{\frac{3}{4}}$$

while from (5.48b) we have for consistency between the oscillation amplitude and sheet thickness a

$$a^{\frac{3}{4}} = \frac{z_o}{\left(\frac{v_y}{\Omega_o}\right)^{\frac{1}{4}}} = \frac{v_{z_o}}{\Omega_o} \frac{1}{\left(\frac{v_y}{\Omega_o}\right)^{\frac{1}{4}}}$$

Thus $v_z^3 = v_{z_o}^3 \left(\frac{v_y}{\Omega_o}\right)^{\frac{3}{4}} \left(\frac{\Omega_o}{v_{z_o}}\right) \left(\frac{v_y}{\Omega_o}\right)^{\frac{1}{4}} = v_{z_o}^2 v_y$, the required result.

Finally, we turn to the question of the charge neutrality of the beam. At a potential ϕ in the sheet its surface charge density is given by

$$\sigma_e(\phi) = -\frac{4ecN_o}{B_o} \left(\frac{m_e}{2e}\right) \phi^{\frac{1}{2}}$$

which, while a factor of $\left(\frac{m_e}{m_p}\right)^{\frac{1}{2}}$ smaller than typical values of the trapped proton density, still requires the plasma approximation to be valid. The only source of neutralizing positive charge is trapped protons moving towards $\phi = 0$, whose density is given by

$$\sigma_p(\phi) = \frac{4ecN_o}{B_o} \left(\frac{m_p}{2e}\right) (\Phi - \phi)^{\frac{1}{2}}$$

(the flow energies into the sheet outside of the 'proton current sheet' must be much smaller than $e\Phi$). Thus, for charge neutrality we simply obtain

$$\phi = \frac{\Phi}{\left(1 + \frac{m_e}{m_p}\right)}$$

for the electron current sheet. We interpret this result as

indicating that a potential drop of $\Phi/(1+m_e/m_p)$ occurs across the proton current sheet of dimention λ_p, rather than Φ, and the remainder falls across a small region near the other boundary, where a small flux of protons enter the sheet, neutralizing the electron beam as they flow towards $\phi = 0$ (see Fig. 5.19). These particles must be contained wholly within the electron current sheet which, as we have seen, is expected to be of dimension

$$a \simeq \left(\frac{m_e}{m_p}\right)^{7/6} \lambda_p .$$

This can happen provided that this sheet thickness is of order v_p/Ω_p for the incoming protons.

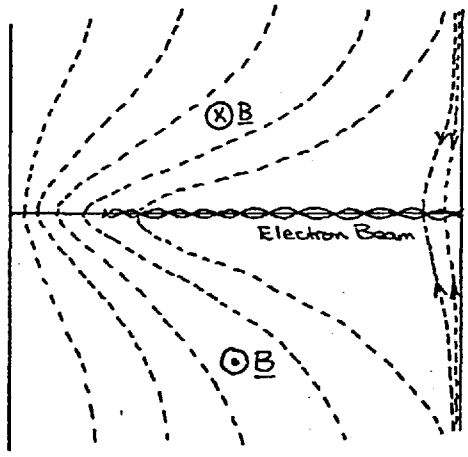

Figure 5.19

Thus

$$v_p \simeq \left(\frac{m_e}{m_p}\right)^{7/6} \Omega_p \lambda_p$$

or

$$E \simeq \frac{B_o}{c} \Omega_p \left(\frac{m_e}{m_p}\right)^{7/6} \lambda_p .$$

On this basis the characteristic length of the region of in-

coming protons should be given by

$$L \simeq \frac{m_e}{m_p}\frac{\Phi}{E} \simeq \left(\frac{m_e}{m_p}\right)^{1/6} \lambda\!\!\!^{-}_p \simeq 3\lambda\!\!\!^{-}_p$$

which is again much smaller than d.

We also have $\frac{E}{E_o} \simeq \left(\frac{m_e}{m_p}\right)^{7/6} \left(\frac{d}{\lambda\!\!\!^{-}_p}\right)$

so that

$$\frac{E}{E_o} \simeq 0.1 \quad \text{for} \quad N_o \simeq 0.1 \text{ cm}^{-3}$$

and $$\frac{E}{E_o} \simeq 0.03 \quad \text{for} \quad N_o \simeq 0.01 \text{ cm}^{-3}.$$

Conclusions

The basic properties of the system may be summarized as follows.

(i) Nearly all the potential drop across the sheet occurs near the boundary where the protons leave the system. The characteristic dimension of this region is $\lambda\!\!\!^{-}_p$, so that

$$\frac{m_p v_p^2}{2e\Phi} \simeq \frac{m_p c^2 \Phi}{2P^2 e \lambda\!\!\!^{-}_p{}^2} \sim \mathcal{O}(1) .$$

Thus drifting protons in this region have energies comparable with $e\Phi$, and hence many drift out of the system before reaching the neutral sheet.

(ii) Those protons reaching the sheet and performing the non-adiabatic oscillation about it, form a trapped proton beam near the neutral sheet, the charge density of which must be neutral-

ized by electrons adiabatically drifting through the beam towards the neutral sheet. The thickness of the sheet is again of order λ_p.

(iii) Over most of the sheet the current is carried by electrons which are neutralized by a few protons entering the sheet near the $\phi = \Phi$ boundary. The thickness of this current sheet has been estimated as a few times $(\frac{m_e}{m_p})\ \lambda_p$.

CHAPTER 6

DISCUSSION, CONCLUSIONS AND SUGGESTIONS FOR FURTHER WORK

This thesis represents a first attempt to consider the self-consistent properties of a neutral sheet, where the current is provided by a collisionless plasma surrounding the field reversal region. It can now be seen that evaluating the currents by simply writing an Ohms law of the form

$$\underline{E} + \frac{\underline{\underline{v}} \wedge \underline{B}}{c} = \underline{j}/\sigma$$

with a constant conductivity σ, as in the 'fluid' theories, effectively suppresses all the interesting physics of the collisionless system. However, since this has been a first attempt at a somewhat unorthodox plasma physics problem the methods used to analyse the system have had to be specially developed for the purpose. Even where previous theories have existed (e.g. the drift-flow of cold plasma, the WKB approximation for particle motion in a neutral sheet) considerable extensions were found to be necessary before they could be applied to the problem. Even so, the approach has necessarily been rather crude, for example by considering the plasma approximation for the 'surface charge density' in the trapped particle beams, rather than a detailed point by point $n_p = n_e$. However, we feel that the qualitative results we have obtained should be valid, if not the details of the quantitative answers, since these rely on several approximations, and a little intuition.

A criticism of the theory developed here has already been given in Chapter 5, its shortcomings (within its own terms) being pointed out and discussed. While these comments and suggestions for improvement might be considered with some profit, it seems likely that extensions of the sort of analytic work we have been investigating here will not yield considerably more understanding of the basic principles involved. Significant improvements of understanding will probably only be possible by conducting a computer simulation of the system in all its complexity, and this is quite a formidable problem. However, direct extensions of the theory in several directions are possible.

Firstly, it should be possible to extend the theory given here to include a thermal (rather than cold) external plasma. For instance, in the drift-flow region we should be able to write

$$\underline{v}_d = \frac{c\lambda}{q} \frac{\underline{B}}{B^2} \wedge \underline{\nabla} \left(q\phi + \frac{mv^2}{2} + W_{th} \right)$$

where W_{th} is the thermal energy of the particle, which becomes a function of position through the conservation of the first adiabatic invariant (the magnetic moment μ to first order). The first order thermal drift term is then

$$\underline{v}_d = \frac{c\mu}{q} \frac{\underline{B}}{B^2} \wedge \underline{\nabla} B$$

i.e. the well-known $\underline{\nabla}B$-drift. However, the modification to the theory by including thermal effects should be small unless $W_{th} \gtrsim m_p v_d^2/2$, and since $m_p v_d^2/2 \sim e\phi$ in the interesting regions, this becomes $W_{th} \gtrsim e\phi$. The problem then becomes

less interesting from the plasma-energization point of view.

A much more interesting problem would be to consider the effects of a small component of magnetic field perpendicular to the current sheet. As we have seen, this has the effect of turning particles around in the sheet as they are accelerated along it by the electric field, until they are ejected along the magnetic field lines. As a first problem we might consider a normal magnetic field small enough to leave protons uneffected but strong enough to significantly modify the electron trajectories. If the electrons <u>are</u> ejected from the sheet, this immediately raises questions about the current system and charge neutralization of the ejected particles, and at the present time it seems unwise to make firm predictions as to the probable answers. However, it is possible that even with such a normal magnetic field, electrons may be prevented from leaving the current sheet by the magnetic mirror effect or a potential drop along the field lines near the current sheet, or a combination of both. Some interesting future work along these lines seems promised, especially as it is likely to be the situation appropriate to the geomagnetic tail quite close to the Earth during substorms. (Chapter 2, section (iv)).

Another question which we have not considered yet in great depth is the magnetospheric consequences of the results obtained, notably the localization of the potential drop in the current sheet near the dusk boundary of the tail (over a distance ~ 1 R_E) which is demanded for self-consistency.

Figure 6.1 shows the Earth's north polar cap during quiet times, where we have plotted (a) the precipitating

electron 'soft zone' for $K_p \leq 2$ (adapted from Hoffman and Berko (1971)); (b) the region of 'transverse magnetic disturbances' for $K_p \leq 2+$ (Zmuda et. al., 1970); and (c) the region of open field lines. We recall from Chapter 2 that the dayside soft zone is associated with magnetosheath plasma entering via the dayside neutral line (or lines), while it was argued that the nightside soft zone is associated with the tail plasma sheet. The region shown in Fig. 6.1 is that for which there is greater than 40% probability of observing soft-zone fluxes (with $K_p \leq 2$). Being a statistical distribution, however, it should be noted that the width of the region at any local time will be rather narrower than shown, and as a warning we have plotted along the noon meridian typical extents and positions of the dayside soft zone for $K_p = 0$ to 1 and $K_p = 1$ to 2 (taken from Hoffman (1972)). In addition we have plotted on the midnight meridian the latitudinal extent of the plasma sheet during quiet times as indicated by the magnetic field studies of Fairfield and Ness (1970).

The soft-zone fluxes produce enhanced ionization in the ionosphere, and lead to the formation of high conductivity strips (the dayside and nightside auroral zones), which are broad in longitude, but narrow in latitudinal extent. Magnetospheric electric fields can drive Hall or Pedersen currents either north-south or east-west along these strips, and we assume, in accordance with many recent authors, that current continuity is maintained by field-aligned currents flowing in or out near the boundaries of the strip (Bonnevier et. al. (1970), Heppner et. al. (1971), Coroniti and Kennel (1971)). If the conductivity gradients are more gentle than we have

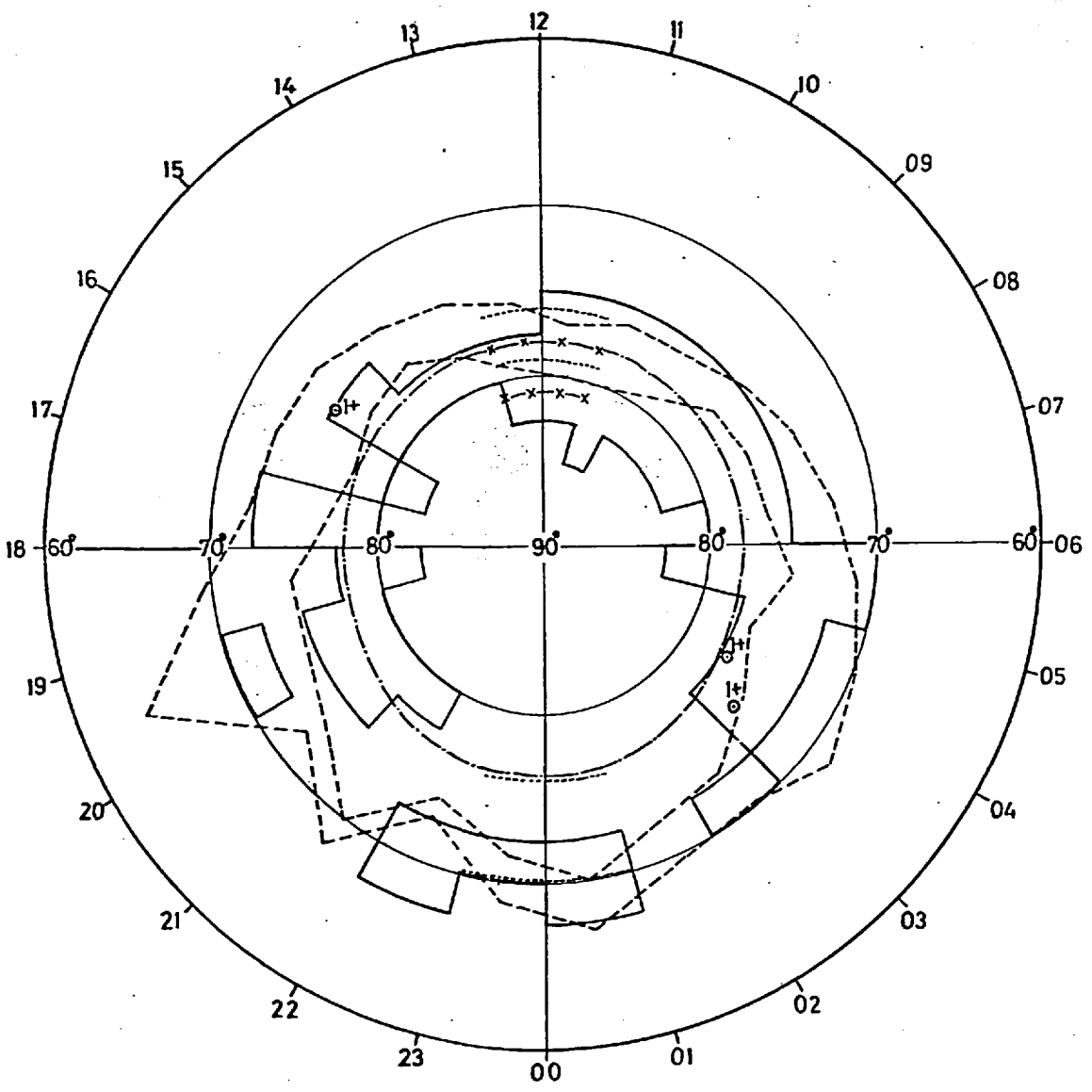

Figure 6.1: The north polar cap for quiet times showing (see text for full description)

——— Electron soft-zone. — — — Region of 'transverse magnetic disturbances'.

x—x—x Typical noon meridian extent of soft zone for K_p = 0 to 1.

-------- Typical noon meridian extent of soft zone for K_p = 1 to 2.

------- Midnight meridian extent of quiet-time plasma sheet.

⊙|+ K_p value and position of electric field reversals ($K_p \leq 2^+$).

.—.—. Estimated boundary of open field lines for quiet times.

implied here, then field-aligned current densities will become correspondingly more distributed. The north-south currents and their field-aligned continuity currents form a system similar to a long solenoid (Fig. 6.2(a)); this system produces little magnetic perturbation outside the region enclosed by the currents (i.e. on the ground), but the field inside becomes 'tipped' in the east-west direction. Such 'transverse magnetic disturbances' are assumed to be those observed by Zmuda et. al. (1966, 1967, 1970) and Armstrong and Zmuda (1970), and should thus be associated with the soft zones as shown in Fig. 6.1 On a smaller scale, such current systems are associated with the enhanced conductivity inside an individual quiet-time nightside auroral arc (length, several thousand Km east-west, width ~ 10 Km north-south), as has been shown by Cloutier et. al. (1970) and Park and Cloutier (1971). A current driven <u>along</u> the strip, with its field-aligned continuity currents, as shown in Fig. 6.2(b), <u>will</u> cause ground perturbations, and is assumed to correspond to the current systems of the substorm expansion eastward and westward electrojets, as has been suggested by Bonnevier et. al. (1970), Heppner et. al. (1971), and shown to be the case by Kisabeth and Rostoker (1971). In both current systems (Figs. 6.2(a,b)) the field-aligned currents are assumed to close in the magnetosphere.

The region of open field lines in the polar cap (Fig. 6.1) has been drawn to coincide with the equatorward boundary of the soft-zone at noon for K_p = 0 to 1, and with the poleward boundary of the plasma sheet at midnight. Thus at noon the boundary latitude is $\Lambda \sim 78^{o}$, which agrees

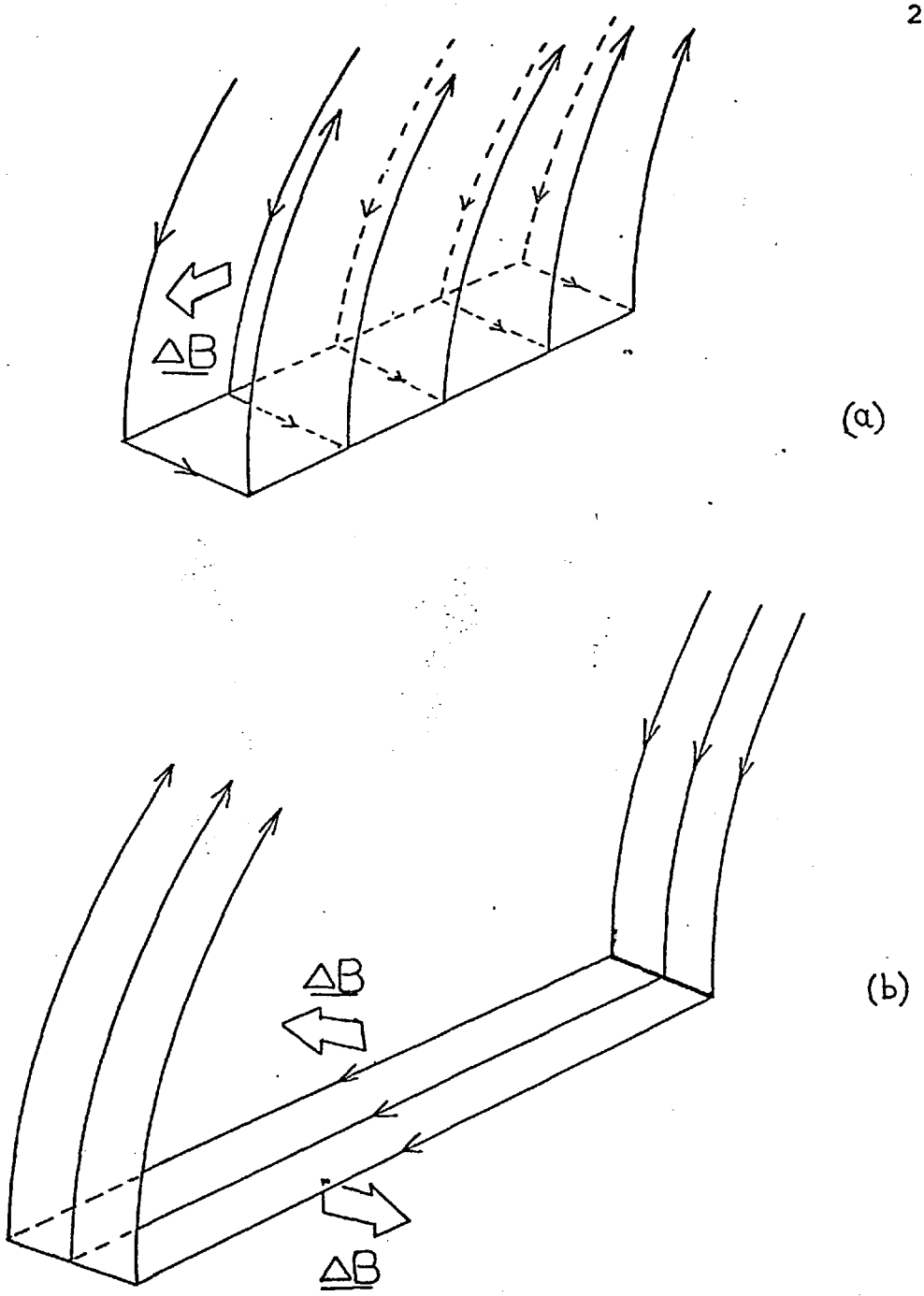

Figure 6.2: (a) The solenoid system produced by currents driven across the high-conductivity soft zone ionosphere.
(b) The electrojet system produced by currents driven along the high-conductivity soft zone ionosphere.

with the field lines mapping into the magnetopause, according to the magnetic model of Fairfield (1968), and also with the lower boundary of the dayside auroral oval of Feldstein (1966) for K_p = 0 to 1. At midnight the boundary is at $\Lambda \sim 76^o$, and is just polewards of the plasma sheet soft zone poleward boundary if these particles are produced by acceleration in the X-neutral field configuration in the tail (Holzer (1971)). In the dusk and dawn quadrants the boundary of open field lines maps into the magnetopause along the tail flanks, and this will be approximately an equipotential, being a boundary between oppositely directed flows, towards the sun in the magnetosphere, and antisolar in the magnetosheath. Thus in the polar cap the direction of the electric field reverses across this boundary, as has been observed by Cauffman and Gurnett (1971) and Maynard (1972). The observed positions of this reversal of the electric field direction in the dusk and dawn quadrants for northern hemisphere passes with K_p = 0 to 2+ has also been plotted in Fig. 6.1

The flux contained within the region of open field lines thus obtained is approximately 4×10^{16} maxwells (gauss-cm^2), which is also the flux in one of the tail lobes at the lunar distance (diameter $\simeq$ 50 R_E, B $\simeq$ 10 γ).

In Fig. 6.3 we show the expected region of open field-lines prior to substorm breakup, which has been determined on the above bases from the position of the dayside soft zone for K_p = 4 to 5 (Hoffman (1972)) and the plasma sheet soft zone for the substorm growth phase indicated by Fairfield and Ness (1970). The noon boundary latitude of

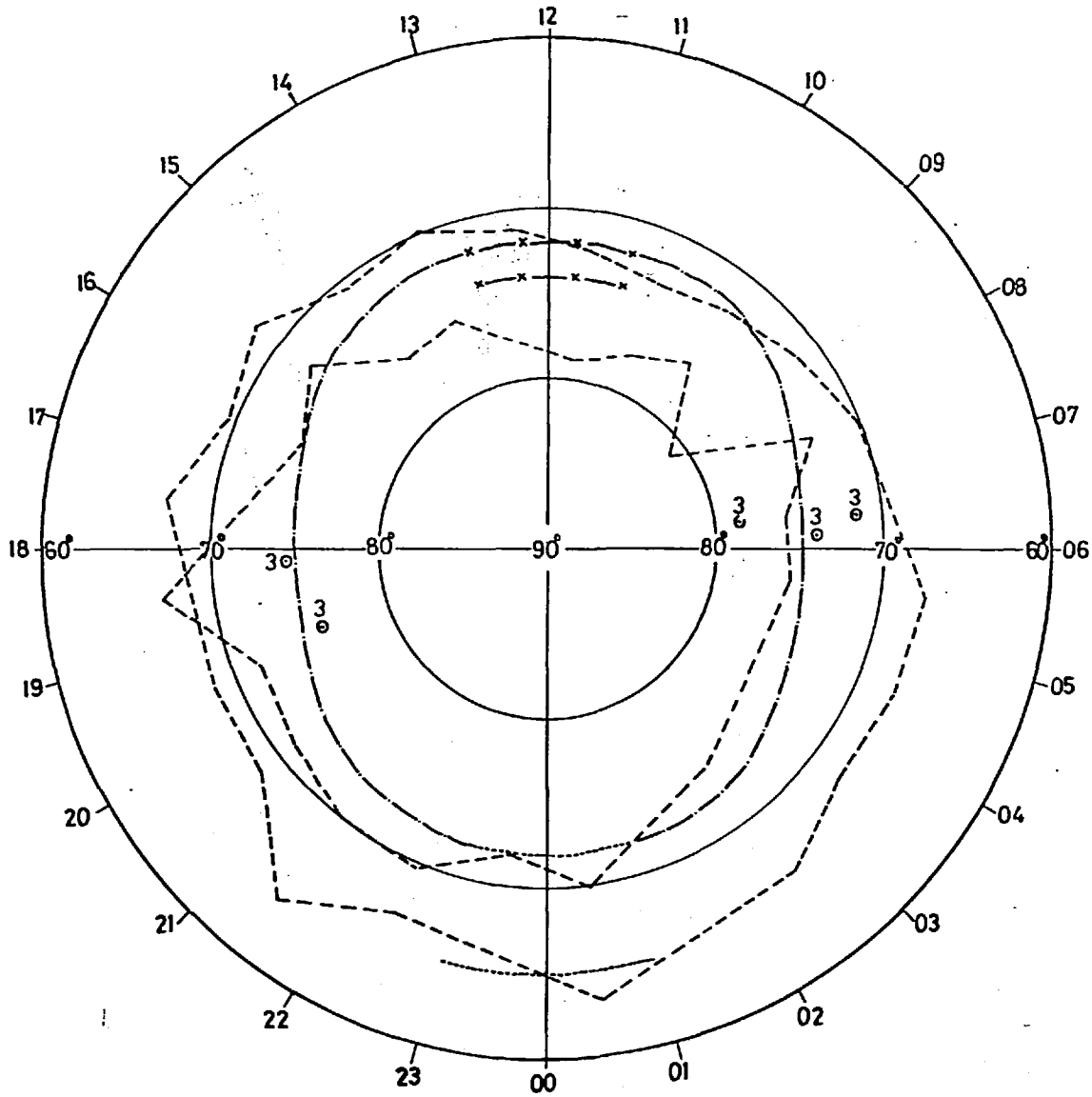

Figure 6.3: The north polar cap prior to substorm expansion, key as for Fig. 6.1. The soft zone data for disturbed times are not currently available, but its position is indicated by the region of transverse magnetic disturbances.

~ 72° is corroborated by the results of Akasofu (1971), who showed that the dayside auroral forms can move 5° to 7° equatorwards from Λ ~ 78° to 80° as flux is removed from the dayside magnetopause during the growth phase. This is consistent with inward displacements of the dayside magnetopause by 1 to 2 R_E observed by Meng (1970) and Aubry et. al. (1970). In this diagram (Fig. 6.3) we also show the region of 'transverse magnetic disturbances' for K_p = 3- to 5+ (Zmuda et. al. (1970)) which relates to the position of the soft zone as above, and the position of the electric field reversals in the dawn and dusk quadrants for $K_p \geq 3$ from Cauffman and Gurnett (1971) and Maynard (1972).

The flux contained within the region of open field-lines is now $\approx 6 \times 10^{16}$ maxwells, such that $\approx 2 \times 10^{16}$ maxwells have been transfered from the dayside magnetopause into the open-field-line region (tail) during the growth phase. This is in agreement with Aubry et. al.'s (1970) data, which indicate a flux transfer of $\approx 10^{16}$ maxwells.

In Fig. 6.4 we have redrawn the region of open field lines in the north polar cap for disturbed periods as described above, and then schematically indicated the paths of the feet of the field lines (i.e. the equipotentials) within this region as required by our analysis of the tail electric field structure for the straight field-line model. We have also indicated how the equipotentials are expected to close at lower latitudes, assuming that the localization of the potential drop near the dusk boundary of the tail neutral sheet relaxes towards a uniform electric field closer to the Earth. Our straight field-line model, as discussed in

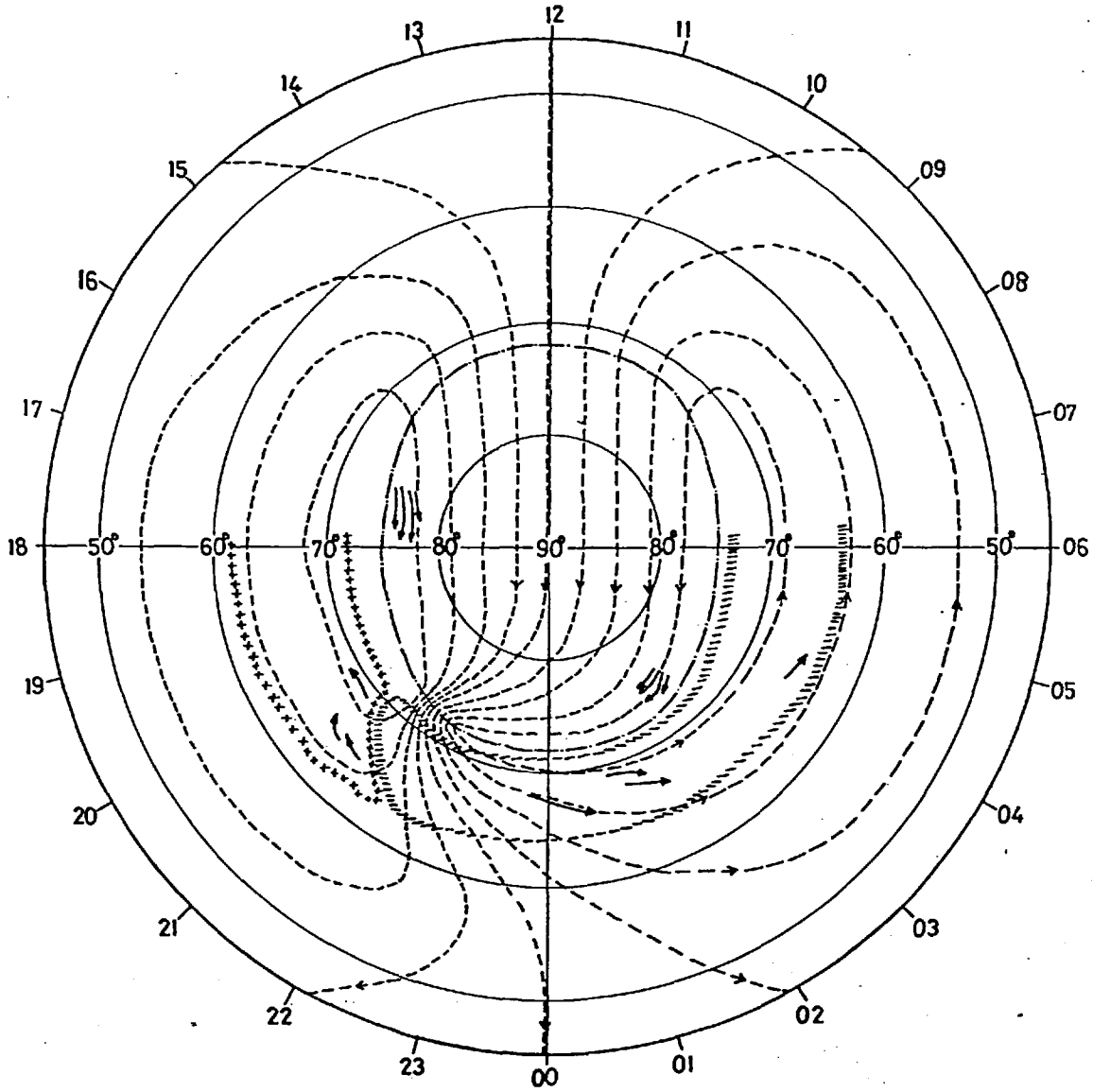

Figure 6.4: Schematic diagram of polar cap flow required by our analysis of the tail electric field structure. In addition we show the polar cap B_a^+ cloud tracks of Heppner et. al. (1971), and selected auroral zone tracks from Haerendel and Lust (1970). Regions of positive (++++) and negative (----) bay disturbances are also indicated.

Chapter 2, is valid only in a region where B_z is small enough such that particles entering the current sheet and accelerating along it, exit into the magnetosheath rather than along a tail field-line towards (or away from) the Earth. The region of the tail where protons have the former history, may be of considerable extent ($X \lesssim -20\ R_E$) during the growth phase, since we only require $B_z \lesssim 0.5\ \gamma$ (Chapter 2). It is reasonable to assume that the localized potential drop should exist with this region, since in the straight field-line model it results from all incoming protons flowing in the current sheet towards dusk boundary (we have not considered the electron motion for such large B_z values, however). Closer to the Earth where B_z is significantly larger, the proton orbits in the sheet become small compared with the tail width, and in such a case there is no a priori reason to believe that the electric field should be non-uniform. This is where the plasma sheet should form, and as we have drawn in Fig. 6.4, we assume that the localized potential drop relaxes towards a uniform electric field in this region. We should note that the localized potential drop may exist in an extensive region of the tail; this maps into an extremely thin latitudinal strip on the polar cap, since the amount of flux involved is very small ($\lesssim 10^{15}$ maxwells).

It can be seen that our model predicts considerable effects in the polar cap and auroral zone flow pattern. We shall interpret these in terms of observations during substorm breakup and expansion phases, to which they clearly apply. Firstly, the polar cap (open field-line) flow should be basically antisolar in the daytime and evening sectors

(i.e. a dawn to dusk electric field), but should be nearly westwards in the midnight-morning region (i.e. a northward electric field in the region above the auroral zone). The only vector electric field measurements for the polar cap region so far published have been via three Ba^+ vapour releases ($\Lambda \sim 75^o$), and a balloon-bourne double probe ($\Lambda \sim 78^o$). The barium releases (Heppner et. al. (1971)) were conducted during substorms (with $K_p \simeq 3$), in the local time sectors 17:00 to 18:00 and 02:00 to 03:00, and directly confirm the flow pattern we find here. The Ba^+ cloud tracks have been drawn in Fig. 6.4 for comparison; electric field strengths were 20 to 40 mV/m. The balloon data (Mozer and Manka (1971)) indicate that in the local morning sector of the polar cap a (growth phase) westward electric field is replaced by a northward electric field of ~ 20 mV/m at substorm expansion, which also agrees with our result.

In the night-side auroral zone (which we identify with the lowish latitude region of the soft zone), the flow is predominantly eastwards (i.e. a southward electric field) in a region extending from late evening into late morning, and is westward (i.e. a northward electric field) from late afternoon to early evening. It has been consistently shown from rocket-bourne double probes (Mozer and Bruston (1967), Mozer and Fahleson (1970), Kelley et. al. (1971), Potter and Cahill (1969), Potter (1970)), Ba^+ vapour releases (Föppl et. al. (1968), Harendel and Lüst (1970), Wescott et. al. (1969), (1970)) and balloon-bourne double probes (Mozer and Serlin (1969), Mozer and Manka (1971), Kelley et. al. (1971 (a)), Mozer (1971)) that northward and southward electric fields are to be found during substorm expansions in the

regions indicated. The balloon-bourne experiments have further shown explicitly that during the growth phase, the electric field develops a westward component (i.e. DP2 activity), with the north-south field associated only with substorm expansion. This latter field component drives strong Hall currents along the highly conducting soft zone strip, leading to negative bay disturbances in the region of southward electric field and positive bay disturbances where the field is northward, as shown by the barium vapour experimenters. These currents are, of course, the eastward and westward electrojets. However, it has also been shown that the strength and position of the electrojets are more highly dependent on the ionospheric conductivity profiles, rather than on the electric field strength. Thus the electrojets form where the conductivity is high, rather than where the electric field is high. Conductivity, produced by precipitating particles on the nightside, will be low for field lines connected to rapidly convecting regions of the magnetosphere where the magnetospheric particle lifetimes are much longer than flow times (even in the strong diffusion limit), but becomes much enhanced (two orders of magnitude perhaps) for ionospheric regions connected to slower flow, where loss times are comparable with flow times (Kennel (1969)). Thus we expect the conductivity to peak near the equatorward boundary of the plasma sheet electron soft zone ($\Lambda \sim 65^{o}$) if we interpret this as such a precipitation boundary. This then, is the region where the electrojets will initially form, as shown by Kisabeth and Rostoker (1971).

In the late evening to late morning auroral zone, the

electric field will have westward and southward components, with $E_{west} \simeq 10$ to 30 mV/m, $E_{south} \simeq 10$ to 100 mV/m (Mozer (1971)). According to Föppl et. al. (1968) the height-integrated Pedersen conductivity is about half the height-integrated Hall conductivity in the night-side auroral zone. The westward electric field drives Pedersen currents and the southward field Hall currents westwards along the oval, forming the westward electrojet, as above (Fig. 6.2(b)). The Hall current should be about four times the strength of the Pedersen current since $E_s/E_w \sim 2$, and $\Sigma_H/\Sigma_p \sim 2$. However, the Pedersen current to the south driven by E_s, should be approximately the same strength as the Hall current driven to the north by E_w. Thus the direction of the field-aligned current system of Fig. 6.2(a) in the negative bay region is likely to be rather variable, certainly difficult to predict. We note that Zmuda et. al. (1966, 1967, 1970) were unable to discuss the direction of the currents producing the 'transverse magnetic disturbances', since the satellite orientation was unknown.

We conclude this thesis with an interpretation of the magnetospheric substorm in terms of the results we have found, and discussed above. We are not able to comment on auroral effects, since it is not certain how or where they are produced. No investigations have yet been carried out attempting to relate concurrent auroral data with particle measurements of the soft zone, hard zone or $E_e > 45$ keV 'trapping boundary'.

In Chapter 2 we found that magnetospheric changes during the growth phase were directly attributable to field-line merging at the dayside magnetopause, adding flux to the tail. The tail current system is enhanced, the magnetic field

component perpendicular to the current sheet becomes steadily smaller and the plasma sheet thins. We interpret this as a 'closing up' of the X-neutral field-line configuration in the tail. Although we have not considered such a system, we postulate that for large angles of the 'X', a localized potential drop does not occur across the dusk boundary of the tail current sheet. This is reasonable, even at the neutral line, because particle motion along the line is unstable to perturbations in the X_{SM} direction. Thus, during the growth phase it is probable that few protons are able to completely cross the tail, implying that the localized potential drop does not exist as is indicated by the form of the DP-2 flow system. However, as the X-neutral configuration closes up, there will come a time when protons will be able to travel the whole distance across the tail in a considerable spatial region, and the localized potential drop will develop. The minimum time scale for such a configuration to be set up can be estimated by considering a system with uniform electric field and large B_z. If we 'switch off' B_z at a given time, the information that this has happened will travel with the trapped protons across the current sheet. The typical proton velocity in the current sheet is the Alfvén velocity of the external medium (Chapter 1), so that the minimum time scale for the setting up of the localized potential should be $t \sim d/V_A$ (d is the tail diameter). With $V_A \sim 10^3$ km/sec, we find a characteristic time of about five minutes. The data of Fairfield and Ness (1970) indicate that the normal field component ($X_{SM} \sim -30\ R_E$) decreases at a rate of about 5 to 10 γ/hr during the growth phase, so that the time required for the tail to change from a

uniform electric field system (B_z ~ 1 γ say) to one of small enough B_z to allow the escape of protons at this distance ($B_z \lesssim 0.2\ \gamma$) is 5 to 10 minutes. We thus argue that on a time-scale of 5 to 10 minutes the X-neutral configuration can change from one where few protons can escape into the magnetosheath (uniform electric field), to one where protons escape over a rather large spatial region. The localized potential drop near the dusk boundary is then set up. We identify this with the onset of the substorm expansion phase.

During the 5 to 10 minutes that the localized potential is forming, the developing southward ionospheric electric field region propagates westwards across the nightside oval until the configuration of Fig. 6.4 is set up. The region of strong electric fields, which separates the northward and southward directed electric field regions at lower latitude (i.e. positive and negative bay regions) will thus form in the premidnight zone and appear to propagate towards the evening. This is clearly identifiable with the westward travelling surge. It is satisfying that no similar effect is anticipated, or observed, in the morning hours. As reconnection of field lines in the tail proceeds, leading to a contraction of the region of open field lines, the precipitation of plasma sheet particles moves to higher latitudes (i.e. the northward expansion) as shown in Fig. 6.5. The westward surge will also move to higher latitudes, although its motion in local time is more difficult to anticipate. The plasma sheet then 'expands'. In relation to the ground magnetic perturbations, DP2 during the growth phase is explicable only in terms of uniform convection. The DP-1 equivalent current system (shown in Chapter

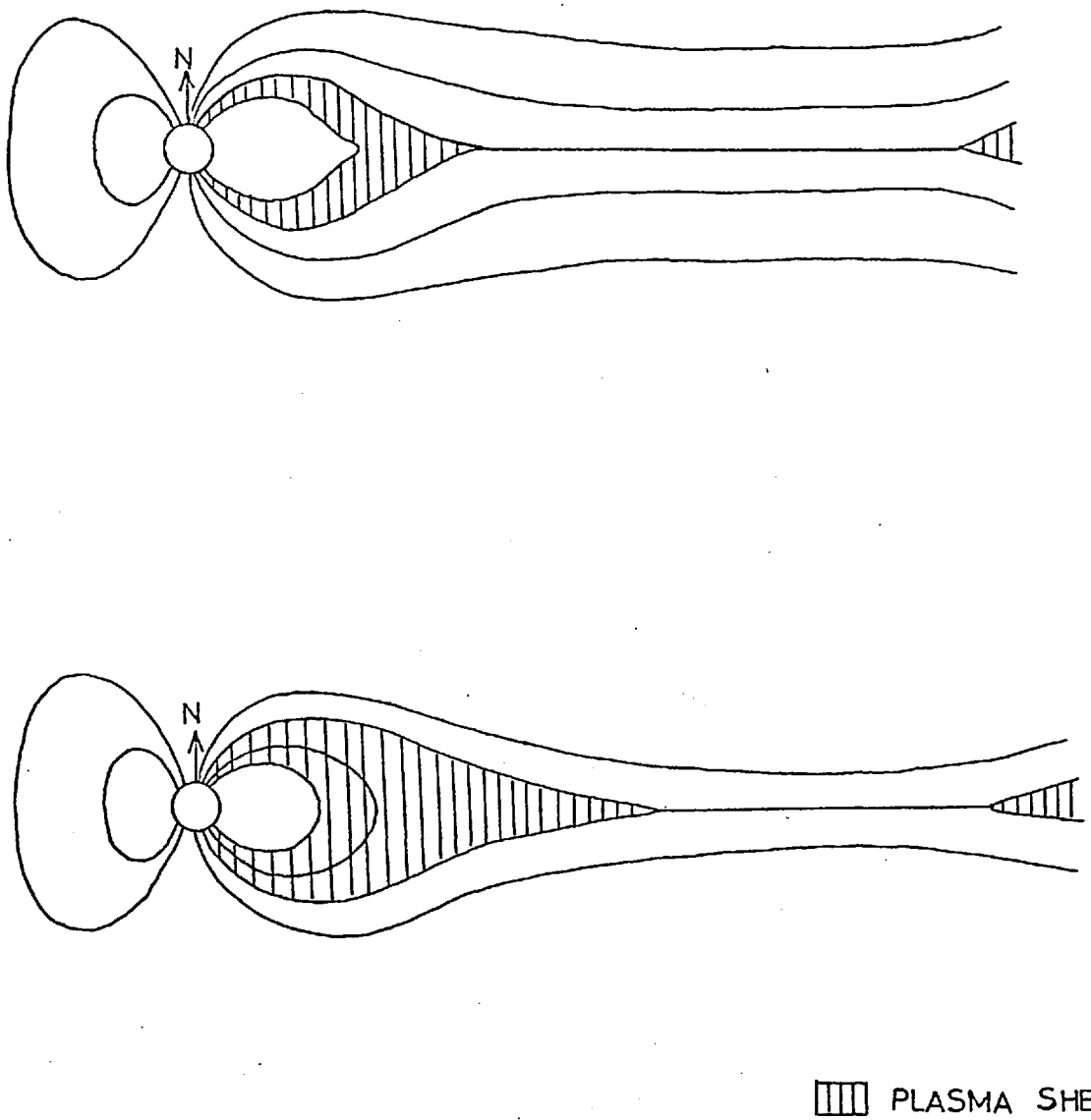

Figure 6.5: Showing the northward expansion of the soft zone (auroral zone) and the thickening of the plasma sheet which occurs during the expansion phase, when the tail merging rate exceeds the dayside merging rate.

2) consists of the eastward and westward electrojets and their supposed 'return' currents across the polar cap and at lower latitudes. Interpreted as ionospheric Hall currents driven by magnetospheric convection electric fields, the indicated flow does not agree with the flow model we have presented here. However, as we have already said, the polar cap magnetic disturbances and those at a somewhat lower latitude than the auroralzone, have been shown to be consistent with the field-aligned current continuity models of Fig. 6.2(a) and (b), by Kasabeth and Rostoker (1971) and Heppner et. al. (1971). Smaller ionospheric currents produced by the electric fields of Fig. 6.4 outside the soft zone (i.e. low conductivity regions) are masked by such effects. We expect that at very low latitudes, however, the ionospheric currents should resemble DP2 activity even during substorm expansion (as indicated in Fig. 6.4), which has been found to be true by Nishida (1971).

References

Akasofu, S.-I. 1971. Midday aurora at the south pole during magnetospheric substorms. Preprint, Geophysical Institute of Alaska.

Aubry, M.P., Russell, C.T. and Kivelson, M.G. 1970. Inward motion of the magnetopause before a substorm. J. Geophys. Res., 75, 7018-7031.

Armstrong, J.C. and Zmuda, A.J. 1970. Field-aligned current at 1100 Km in the auroral region measured by satellite. J. Geophys. Res., 75, 7122-7127.

Bonnevier, B., Boström, R., and Rostoker, G. 1970. A three-dimensional current system for polar magnetic substorms. J. Geophys. Res., 75, 107-122.

Cauffman, D.P. and Gurnett, D.A. 1971. Double probe measurements of dc electric fields with the Injun-5 satellite. J. Geophys. Res., 76, 6014-6027.

Cloutier, P.A., Anderson, H.R., Park, R.J., Vondrak, R.R., Spiger, R.J. and Sandel, B.R. 1970. Detection of geomagnetically aligned currents associated with an auroral arc. J. Geophys. Res., 75, 2595-2600.

Coroniti, F.V. and Kennel, C.F. 1971. Magnetospheric substorms. UCLA preprint, PPG-98. To be published (1972) in Proc. of Conference on Cosmic Plasma Physics, ESRIN, Frascati, Italy.

Dungey, J.W. 1968. Polar substorms: Theoretical Review. Space Research, 8, (Ed. A.P. Mitra, L.G. Jacchia and W.S. Newman), 1291-1298, Academic Press, New York.

Fairfield, D.H. 1968. Average magnetic field configuration of the outer magnetosphere. J. Geophys. Res., 73, 7329-7338.

Fairfield, D.H. and Ness, N.F. 1970. Configuration of the geomagnetic tail during substorm. J. Geophys. Res., 75, 7032-7047.

Feldstein, Y.I. 1966. Peculiarities in the auroral distribution and magnetic disturbance distribution in high latitudes caused by the asymmetrical form of the magnetosphere. Planetary & Space Sci., 14, 121-130.

Föppl, H., Haerendel, G., Haser, L., Lüst, R., Melzner, F., Meyer, B., Neuss, H., Rabben, H.-H., Rieger, E., Stöcker, J. and Stoffregen, W. 1968. Preliminary results of electric field measurements in the auroral zone. J. Geophys. Res., 73, 21-26.

Haerendel, G. and Lüst, R. 1970. Electric fields in the ionosphere and magnetosphere. In Particles & Fields in the Magnetosphere, (Ed. McCormac), 213-228. D. Reidel Publishing Co., Dordrecht-Holland.

Heppner, J.P., Stolarik, J.D. and Wescott, E.M. 1971. Electric-field measurements and the identification of currents causing magnetic disturbances in the polar cap. J. Geophys. Res., 76, 6028-6053.

Hoffman, R.A. 1972. Properties of low energy particle impacts in polar domain in the dawn and dayside hours. In Magnetosphere-Ionosphere Interactions, University of Oslo Press, Oslo.

Hoffman, R.A. and Berko, F.W. 1971. Primary electron influx to the dayside auroral oval. J. Geophys. Res., 76, 2967-2976.

Holzer, T.E. 1971. Formation of the plasma sheet (abstract). EOS Trans. Am. Geophys. Union, 52, 905.

Kelley, M.C., Starr, J.A. and Mozer, F.S. 1971a. Relationship between magnetospheric electric fields and the motion

of auroral forms. J. Geophys. Res., 76, 5269-5277.

Kelley, M.C., Mozer, F.S. and Fahleson, U.V. 1971b. Electric fields in the nighttime and daytime auroral zone. J. Geophys. Res., 76, 6054-6066.

Kennel, C.F. 1969. Consequences of a magnetospheric plasma. Rev. Geophys., 7, 379-419.

Kisabeth, J.L. and Rostoker, A. 1971. Development of the polar electrojet during polar magnetic substorms. J. Geophys. Res., 76, 6815-6828.

Maynard, N.C. 1972. Electric fields in the ionosphere and magnetosphere. In Magnetosphere-Ionosphere Interactions University of Oslo Press, Oslo.

Meng, C.-I. 1970. Variations of the magnetopause position with substorm activity. J. Geophys. Res., 75, 3252-3254.

Mozer, F.S. 1971. Origin and effects of electric fields during isolated magnetospheric substorms. J. Geophys. Res., 76, 7595-7608.

Mozer, F.S. and Bruston, P. 1967. Electric field measurements in the auroral ionosphere. J. Geophys. Res., 72, 1109-1114.

Mozer, F.S. and Serlin, R. 1969. Magnetospheric electric field measurements with balloons. J. Geophys. Res., 74, 4739-4754.

Mozer, F.S. and Fahleson, U.V. 1970. Parallel and perpendicular electric fields in an aurora. Planetary & Space Sci., 18, 1563-1571.

Mozer, F.S. and Manka, R.H. 1971. Magnetospheric electric field properties deduced from simultaneous balloon

flights. J. Geophys. Res., 70, 1697-1712.

Nishida, A. 1971. DP2 and polar substorm. Planetary and Space Sci., 19, 205-221.

Park, R.J. and Cloutier, P.A. 1971. Rocket-based measurement of Birkeland currents related to an auroral arc and electrojet. J. Geophys. Res., 76, 7714-7733.

Potter, W.E. 1970. Rocket measurements of auroral electric and magnetic fields. J. Geophys. Res., 75, 5415-5431.

Potter, W.E. and Cahill, L.J. Jr., 1969. Electric and magnetic field measurements near an auroral electrojet. J. Geophys. Res., 74, 5159-5160.

Wescott, E.M., Stolarik, J.D. and Heppner, J.P. 1969. Electric fields in the vicinity of auroral forms from motions of barium vapour releases. J. Geophys. Res., 74, 3469-3487.

Wescott, E.M., Stolarik, J.D. and Heppner, J.P. 1970. Auroral and polar cap electric fields from barium releases. In Particles & Fields in the Magnetosphere, (Ed. McCormac), 229-238. D. Reidel Publ. Co., Dordrecht-Holland.

Zmuda, A.J., Martin, J.H. and Heuring, F.T. 1966. Transverse magnetic disturbances at 1100 Km in the auroral region. J. Geophys. Res., 71, 5033-5045.

Zmuda, A.J., Heuring, F.T. and Martin, J.H. 1967. Dayside magnetic disturbances at 1100 Km in the auroral oval. J. Geophys. Res., 72, 1115-1117.

Zmuda, A.J., Armstrong, J.C. and Heuring, F.T. 1970. Characteristics of transverse magnetic disturbances observed at 1100 kilometers in the auroral oval. J. Geophys. Res., 75, 4757-4762.

Appendix : Growing Plasma Oscillations for Symmetrical Double-Humped Velocity Distributions

The problem considered here is that of growing longitudinal waves which propagate in a hot plasma parallel to any magnetic field which may be present (i.e. the magnetic field is neglected in the Vlasov equation). Here it is shown that for any symmetrical double-humped velocity distribution, all growing waves with real wave-number have phase velocity equal to the velocity at the minimum of the distribution function. Distributions made up of parabolae are convenient for calculation, and growth rates are obtained for several symmetrical distributions made up of parabolae.

The dispersion relation for growing waves (i.e. $\mathcal{I}_m(\omega) > 0$, where the electric field varies as $e^{i(kz-\omega t)}$) was obtained by Vlasov (1938)

$$\left(\frac{k}{\omega_p}\right)^2 = \int_{-\infty}^{\infty} \frac{\partial f_o(v)}{\partial v} \frac{dv}{v-W} \qquad - (A.1)$$

where $W = \frac{\omega}{k}$, $f_o(v)$ is the normalized combined velocity distribution function for all species of particles present, and ω_p is the plasma frequency. We shall consider the special case of $f_o(v)$ symmetrical about $v = 0$ with two maxima, at $v = \pm v_m$. Then from the symmetry of $f_o(v)$, (A.1) becomes

$$\left(\frac{k}{\omega_p}\right)^2 = 2 \int_{o}^{\infty} \frac{\partial f_o(v)}{\partial v} \frac{v dv}{v^2 - W^2}$$

and writing $W = (\omega_r + i\omega_i)/k = \alpha + i\beta$ and separating real and imaginary parts we must solve simultaneously (for $\beta > 0$)

$$2\int_0^\infty \frac{\partial f_o}{\partial v}\,\frac{v(v^2-\alpha^2+\beta^2)\,dv}{(v^2-\alpha^2+\beta^2)^2+4\alpha^2\beta^2} = \left(\frac{k}{\omega_p}\right)^2 \qquad - (A.2)$$

$$\alpha\int_0^\infty \frac{\partial f_o}{\partial v}\,\frac{v\,dv}{(v^2-\alpha^2+\beta^2)^2+4\alpha^2\beta^2} = 0 \qquad - (A.3)$$

If $\alpha \neq 0$, then the integral in (A.3) must vanish and (A.2) becomes

$$\int_0^\infty \frac{\partial f_o}{\partial v}\,\frac{v^3\,dv}{(v^2-\alpha^2+\beta^2)^2+4\alpha^2\beta^2} = \tfrac{1}{2}\left(\frac{k}{\omega_p}\right)^2 \qquad - (A.4)$$

Then multiplying the integral in (A.3) by v_m^2 and subtracting from (A.4) gives

$$\int_0^\infty \frac{\partial f_o}{\partial v}\,\frac{v(v^2-v_m^2)\,dv}{(v^2-\alpha^2+\beta^2)^2+4\alpha^2\beta^2} = \tfrac{1}{2}\left(\frac{k}{\omega_p}\right)^2 \qquad - (A.5)$$

But the product $(v^2-v_m^2)\,\partial f_o/\partial v$ is always negative while the other factors in the integrand are positive over the range of integration. Thus the integral must be negative and hence an unacceptable solution, since we require k to be real.

The only other solution to (A.3) is $\alpha = 0$, when (A.2) becomes

$$2\int_0^\infty \frac{\partial f_o}{\partial v}\,\frac{v\,dv}{v^2+\beta^2} = \left(\frac{k}{\omega_p}\right)^2 \qquad - (A.6)$$

which may give a positive result for k^2. Thus the only growing waves have zero phase velocity, the velocity at the minimum of the distribution function. This result is in contrast to that of the 'bump-in-the-tail' problem, where waves in a range of phase velocities may grow, with growth rate proportional to

$(\frac{\partial f_o}{\partial v})_{v=\omega r/k}$.

Growth rate calculations are made using (A.6) for $f_o(v)$ constructed from three parabolae, so that $\partial f_o/\partial v$ is linear in v. The parameters of the distribution are s and W as shown in figure A-1, and $K = 1 - \frac{f_{min}}{f_{max}}$. It is found convenient to define $r = W/s$ and use the parameters r, s and K. We also write $t = (1 - Kr^2)$.

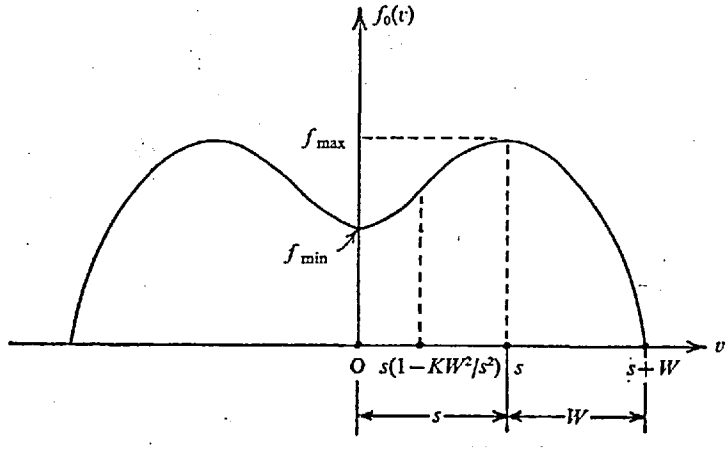

Figure A-1

Then $f_o(v)$ and its first derivative for $v \geq 0$ is taken to be

$f_o(v)$	$\partial f_o/\partial v$	Range
$f_{max}\left\{\begin{array}{l}\frac{Kv^2}{s^2t} + (1-K)\\ (1-\frac{1}{r^2})+\frac{2v}{sr^2}-\frac{v^2}{s^2r^2}\\ 0\end{array}\right.$	$f_{max}\left\{\begin{array}{l}\frac{2Kv}{s^2t}\\ 2(\frac{1}{sr^2}-\frac{v}{s^2r^2})\\ 0\end{array}\right.$	$0 \leq v \leq st$ $st \leq v \leq s(1+r)$ $v \geq (1+r)s$

Normalization of $f_o(v)$ gives

$$f_{max} = \left(\frac{3}{2s}\right) \left(K^2r^2 + 2r - 2K + 3\right)^{-1}.$$

We note that for fixed $r = {}^{W}/_{s}$, K cannot be arbitrarily changed. If $r > 1$ then K can take on its full range $0 \leq K \leq 1$; but for $r < 1$, there is an upper limit for K, i.e. $K \leq \frac{1}{r^2}$, and hence $0 \leq K \leq \frac{1}{r^2}$ (Fig. A-2). At this upper limit the central parabola disappears, there is a cusp at $v = 0$ in the distribution function and effectively a discontinuity in ${}^{\partial f_0}/_{\partial v}$ (Fig. A-3). Conversely, for a given K, the maximum value of r is $\frac{1}{\sqrt{K}}$, and its minimum value is, of course, zero, i.e. $0 \leq r \leq \frac{1}{\sqrt{K}}$.

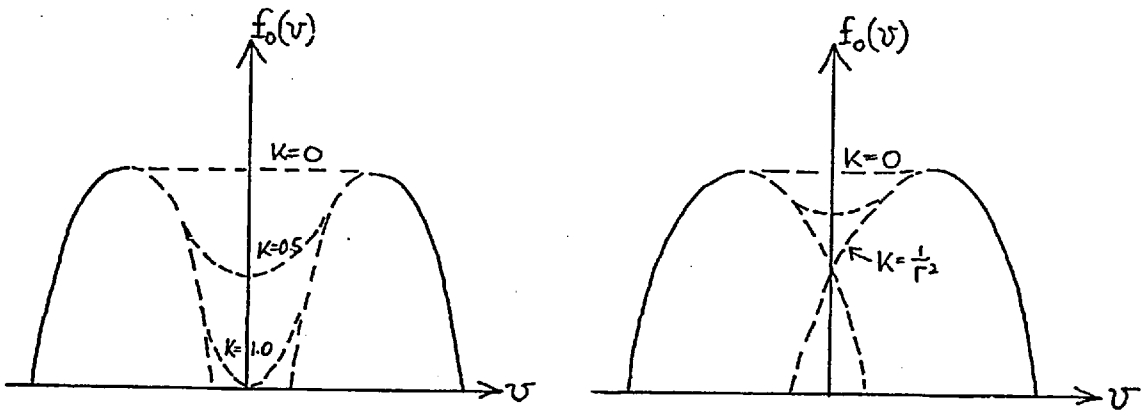

$r < 1$, allowing $0 \leq K \leq 1$.

$r > 1$, showing the upper limit to K at $K = 1/r^2$

Figure A-2

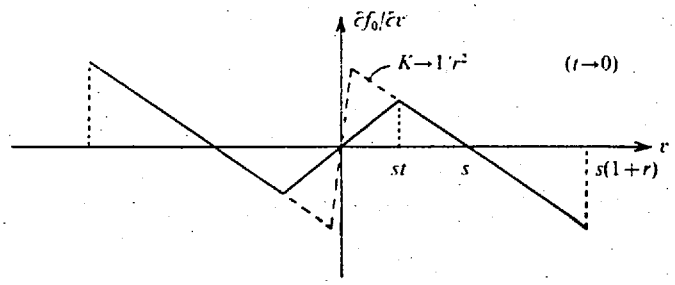

Figure A-3

Substituting $\frac{\partial f_o}{\partial v}$ into (A.6) and rearranging into dimensionless form we have

$$\left(\frac{ks}{\omega_p}\right)^2 = \frac{6}{(K^2r^2+2r-2K+3)} \left\{\frac{K}{t}\int_o^t \frac{v'^2dv'}{(v'^2+\varepsilon^2)} + \frac{1}{r^2}\int_t^{1+r} \frac{(1-v')v'dv'}{(v'^2+\varepsilon^2)}\right\}$$

or

$$\left(\frac{ks}{\omega_p}\right)^2 = \frac{6}{r\,(K^2r^2+2r-2K+3)} \left\{\tfrac{1}{2}\log\left(\frac{(1+r)^2+\varepsilon^2}{t^2+\varepsilon^2}\right)+\varepsilon\left\{\tan^{-1}\frac{(1+r)}{\varepsilon} - \frac{1}{t}\times\right.\right.$$

$$\left.\left.\times\tan^{-1}\frac{t}{\varepsilon}\right\} - r\right\} \quad - (A.7)$$

where $v' = v/s$ and $\varepsilon = \beta/s = \omega_i/ks$.

The right-hand side of (A.7) is evaluated for given values of K, r, and ε. For given K there is a range of r for which there is a range of ε which gives a positive result, as required. Within this range of r, the right-hand side of (A.7) is positive for $\varepsilon = 0$, goes to zero as ε increases and never again is positive (it approaches zero as $\varepsilon \to \infty$). If $\left(\frac{ks}{\omega_p}\right)^2 > 0$ for $\varepsilon = 0$, then this corresponds to $\omega_i = 0$ at finite $k = k_{max}$. As $\left(\frac{ks}{\omega_p}\right)^2$ decreases as ε increases, we have thus a range of $k \leq k_{max}$ for which ω_i is positive. As $\left(\frac{ks}{\omega_p}\right)$ goes zero when ε is finite, this corresponds to $\omega_i \to 0$, as $k \to 0$ such that $\omega_i/k \to$ constant. However, for some ranges of r at given K we find that the right-hand side of (A.7) is negative for all ε. This is true if $\left(\frac{ks}{\omega_p}\right)^2 \leq 0$ for $\varepsilon = 0$ (i.e. $k_{max}^2 \leq 0$).

For $\varepsilon = 0$ equation (A.7) becomes

$$\left(\frac{k_{max}\,s}{\omega_p}\right)^2 = \frac{6}{r^2(K^2r^2+2r-2K+3)} \left\{\log\left(\frac{1+r}{1-Kr^2}\right) - r\right\} \quad - (A.8)$$

and the r.h.s. is positive if $K > \frac{e^r - (1+r)}{r^2\ e^r}$. The latter expression is monotonically decreasing with increasing r, its maximum value (for r positive) is 0.5, at $r = 0$. Thus for $K \geq 0.5$ there is a range of $(\frac{ks}{\omega_p})$ for which $\omega_i > 0$, since $k_{max} \geq 0$, for all $0 \leq r \leq \frac{1}{\sqrt{K}}$. However, for $K \leq 0.5$, there exists a minimum value of $r = r_{min}$ (given by the solution of $K = \frac{e^r - (1+r)}{r^2\ e^r}$) below which $(\frac{k_{max}s}{\omega_p})^2 < 0$. The range of $r_{min} \leq r \leq \frac{1}{\sqrt{K}}$ for which there exists a range of $0 \leq k \leq k_{max}$ for which $\omega_i > 0$ for given K is shown in Fig. A-4. For example, for $K = 0.2$, a range of k exists $(0 \leq k \leq k_{max})$ for $1.5 \leq r \leq \frac{1}{\sqrt{0.2}} \approx 2.24$. As r approaches 1.5 from above, k_{max} decreases to zero, and no solutions occur for $r \leq 1.5$, since $(\frac{ks}{\omega_i})^2$ is negative for all $\varepsilon \geq 0$. We also note that for the case $r = \frac{1}{\sqrt{K}}$ we have (equation (A.8) $k_{max} = \infty$, so that $\omega_i > 0$ for $0 \leq k \leq \infty$.

The results of the numerical calculation are plotted in the form of $\frac{\omega_i}{\omega_p}$ versus $(\frac{ks}{\omega_p})$, obtained from $\frac{\omega_i}{\omega_p} = \varepsilon\sqrt{f(\varepsilon,K,r)}$ where $f(\varepsilon,K,r)$ is the value of the r.h.s. of equation (A.7). Fig. A-5 shows the growth rates for distributions with a shallow minimum ($K = 0.2$), and a deep minimum ($K = 1.0$). For $K = 0.2$, we find $\omega_{i_{max}} \sim 0.03\ \omega_p$ at $k \approx 0.26\ \omega_p/s$; while for $K = 1.0$, $\omega_{i_{max}} \sim 0.3\ \omega_p$ with $k \approx 0.7\ \frac{\omega_p}{s}$.

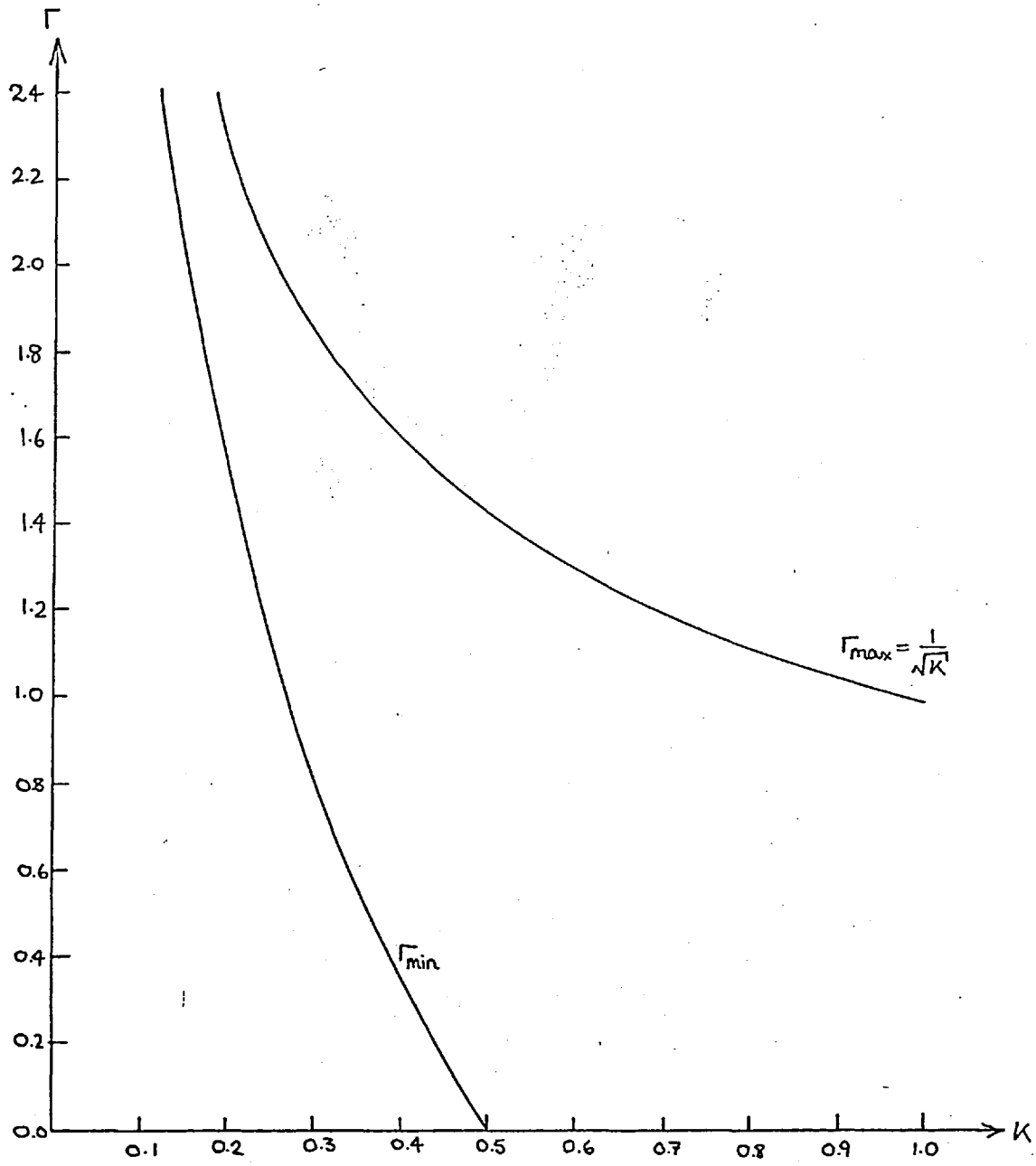
Γ
2.4
2.2
2.0
1.8
1.6
1.4
1.2
1.0
0.8
0.6
0.4
0.2
0.0
0.1
0.2
0.3
0.4
0.5
0.6
0.7
0.8
0.9
1.0
K
$\Gamma_{max} = \frac{1}{\sqrt{K}}$
Γ_{min}

Figure A-4

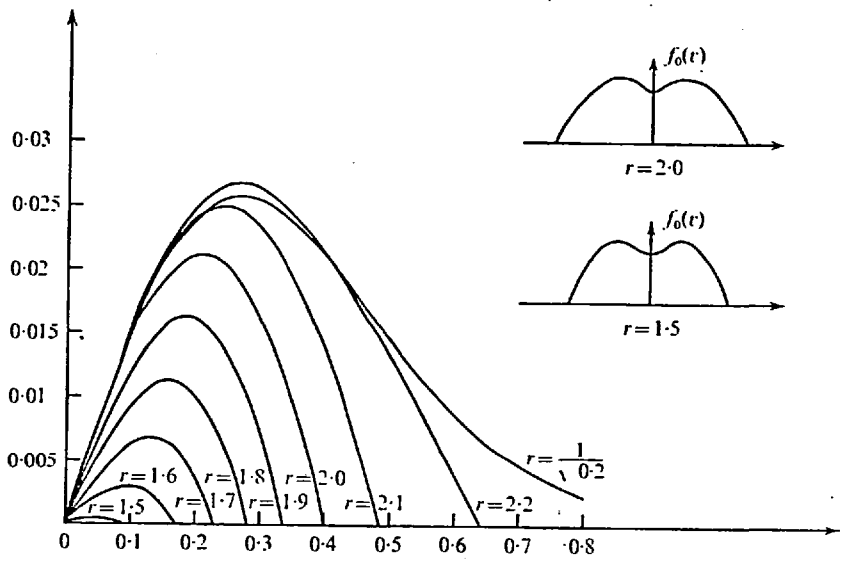

Figure A-5(a)

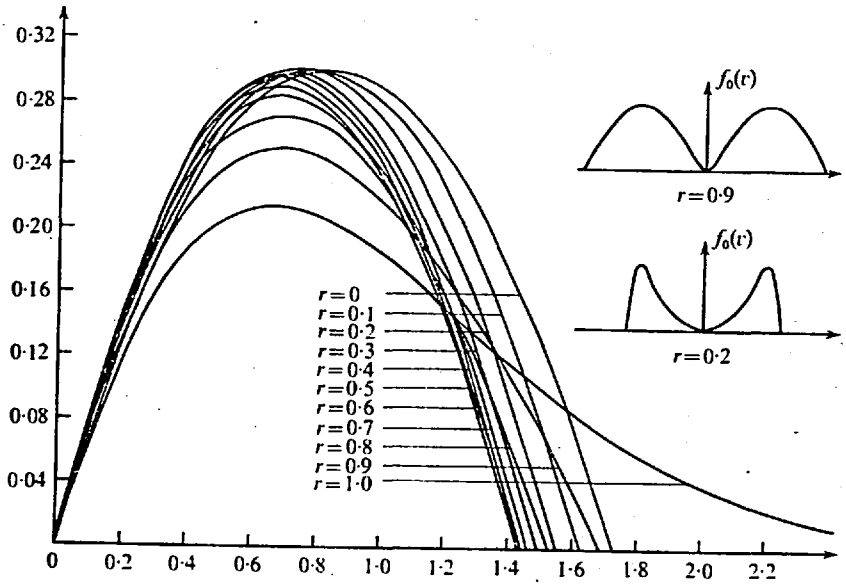

Figure A-5(b)

This may be compared with the growth rates for two cold counter-streaming beams, i.e. $f_o = \frac{1}{2}\{\delta(v-s) + \delta(v+s)\}$. From equation

(A.6) we have, integrating by parts

$$\left(\frac{ks}{\omega_p}\right)^2 = 2\int_o^\infty \frac{\partial f_o}{\partial v}\frac{vdv}{v^2+\beta^2} = 2\left[f_o \frac{v}{v^2+\beta^2}\right]_o^\infty - 2\int^\infty f_o \frac{\beta^2-v^2}{(v^2+\beta^2)^2}\,dv$$

$$= 2\int_o^\infty f_o \frac{(v^2-\beta^2)}{(v^2+\beta^2)}\,dv$$

and substituting for f_o we have

$$\frac{2-(\varepsilon^2+1)}{(\varepsilon^2+1)^2} = \left(\frac{ks}{\omega_p}\right)^2 .$$

Thus

$$\left(\frac{\omega_i}{\omega_p}\right)^2 = \tfrac{1}{2}\left\{\sqrt{1+8\left(\frac{ks}{\omega_p}\right)^2} - \left(1+2\left(\frac{ks}{\omega_p}\right)^2\right)\right\} .$$

The maximum growth rate occurs at $k = \frac{1}{2}\sqrt{\frac{3}{2}}\frac{\omega_p}{s} \approx 0.61\,\frac{\omega_p}{s}$ with growth rate $\omega_i = \frac{\omega p}{2\sqrt{2}} \approx 0.35\ \omega_p$. The results of our calculation with distributions made up of parabolae are very similar to these when K approaches unity.

References

Cowley, S.W.H. 1970. Growing plasma oscillations for symmetrical double-humped velocity distributions. J. Plasma Phys., 4, part 2, 297-300.

Vlasov, A.A. 1938. The oscillation properties of an electron gas. Zhur. Eksp. i Teoret. Fiz., 8, 291.